Study of ^{2} Tl background rejection influence on the $0\nu\beta\beta$ decay sensitivity, characterisation of SuperNEMO demonstrator calorimeter timing performance

Cloé Girard-Carillo

université
PARIS-SACLAY

Study of ^{208}Tl background rejection influence on the $0\nu\beta\beta$ decay sensitivity
Characterisation of SuperNEMO demonstrator calorimeter timing performance

Thèse de doctorat de l'Université Paris-Saclay

École doctorale n° 576 Particules, Hadrons, Énergie et Noyau : Instrumentation, Imagerie, Cosmos et Simulation (PHENIICS)
Spécialité de doctorat : physique des particules
Unité de recherche : Université Paris-Saclay, CNRS, IJCLab, 91405, Orsay, France.
Référent: : Faculté des sciences d'Orsay

Thèse présentée et soutenue à Orsay, le 11 décembre 2020, par

Cloé GIRARD-CARILLO

Composition du jury:

Achille STOCCHI Professeur, Université Paris-Saclay	Président
Alessandra TONAZZO Professeure, Université Paris-Diderot	Rapportrice & examinatrice
Mark C. CHEN Professeur, Queen's University	Rapporteur & examinateur
Christine MARQUET Chargée de recherche, CENBG	Examinatrice
Laurent SIMARD Maître de conférence, Université Paris-Saclay	Directeur de thèse
Mathieu BONGRAND Chargé de recherche, Subatech	Co-encadrant

Thèse de doctorat

NNT: 2020UPASP097

Acknowledgement

Je remercie mes rapporteurs, Alessandra Tonazzo et Mark Chen pour avoir accepté de lire en détails mon manuscrit de thèse, pour leurs commentaires éclairés et leurs corrections fort utiles. Merci aussi à Achille d'avoir présidé avec brio mon jury de thèse, malgré ton emploi du temps chargé. Je glisse aussi un petit remerciement à Valérie Le Port sans qui mon second dépôt de thèse n'aurait pas pu avoir lieu. Christine, merci également d'avoir accepté de faire partie de mon jury de thèse. Mais évidemment merci pour ces trois ans de conseils, et d'aide dans mon travail. Merci aussi de m'avoir soutenue dans les moments de doute, de m'avoir montré avec Manu le premier signal de PM, et pour m'avoir appris à manier la Black Mamba, toujours avec parcimonie ;) Merci aussi infiniment pour tes commentaires à la fin de ma soutenance, qui m'ont beaucoup touchés.

Merci aussi Laurent et Mathieu, pour le jury certes, mais surtout pour ces plus de trois ans de thèse. Merci à Mathieu, c'était incroyablement motivant de bosser avec toi sur ces premières données, j'ai énormément appris, et on s'est bien marré, au labo, aux réunions de collab, et à Modane. Laurent, la première fois que j'ai entendu parler de toi, c'était Ana en stage de M2 qui m'a dit "tu vas voir, au téléphone il n'est pas très alaise, mais il est super sympa". Maintenant je vois de quoi elle parlait ;) Merci pour ton humour qui s'est débridé au fil de la thèse. Merci pour ton suivi, au jour le jour, malgré tes innombrables responsabilités. Pour les bonnes tartes et les bons gâteaux aussi ! Les derniers mois de rédaction auront été intenses, merci d'avoir été présent malgré le confinement.

Je n'oublie évidemment pas toute l'équipe du LAL, équipe étendue bien sûr (Xavier qui nous a semi-quitté, semi car il était quand même toujours là pour raconter des blagues toujours très fines et chercher des ragots, et on ajoute aussi l'équipe Delight qui était aussi souvent présente dans le bureau du café... euh... des thésards pardon) ! On s'est bien régalé avec tous ces gâteaux, bien marré aussi, vous êtes vraiment une équipe incroyable, je ne pourrai jamais assez vous remercier, c'est aussi grâce à vous que je garde un super souvenir de cette thèse. Merci aussi aux *disparus* de l'équipe, Steven, grâce à qui j'ai pu comprendre pas mal de trucs sur le soft de SuperNEMO, et qui m'a introduit aux soirées film. Merci aussi à Luis, pour tes fausses traditions, la grimpe, la course... et merci Delphine pour ce temps passé en tête à tête dans le bureau. Avec, quand même, un spécial big up pour Noë ! AH!! C'était quelque chose ces moments passés

ensemble ! Le thé, la bouffe, l'enseignement, une playlist musicale en or, un temps non-négligeable passé à essayer de faire de beaux plots avec Root, rigoler des chefs (parce que quand même on est aussi là pour ça, j'espère que Mathieu ne lira pas cette phrase avant ta soutenance...). Je regrette évidemment que ce temps ait été écourté par le confinement, mais je garde tout ce qu'on a vécu bien précieusement, bon courage pour les mois qui viennent, tu vas voir, c'est violent ! Thanks also to Malak, good luck for this second part of your PhD.

Il y a aussi plein de gens au LAL que je voudrais remercier pour ces discussions de couloir et de cafet, je ne les citerai pas tous, mais j'espère qu'ils se reconnaîtront. Toute l'équipe des responsables étudiants notamment, une équipe sur-motivée, entre ptits dej' étudiants, talks inter-labos, bières... Merci à vous tous et bonne chance pour la suite ! Le service méca du LAL, meilleur service méca du monde !! C'est grâce à vous que j'ai pu si bien connaître et comprendre le détecteur, et Modane et ses alentours. Vous êtes de supers gars, je suis contente d'avoir pu partir avec vous autant de fois à Modane. Et tous les anciens thésards/post-docs du LAL et labos alentours, adeptes des soirées film, encore une fois je ne donnerai pas de noms pour ne pas les compromettre, mais merci pour tous ces super moments, à chanter, à manger des fajitas et à (PAS) boire de bières, à accessoirement regarder des films, pas toujours très bons :p

Et parmi tous les trucs chouettes qui sont arrivés pendant la thèse, je ne peux pas oublier les Suri4 !! Meilleur groupe de musique des labos de la vallée ! Ses nombreux membres, occasionnels ou acharnés, Catherine, Christelle, Christian, Eli, Elsa, François, Henri, Hugues, Laurent, Louis, Lucien, Michel, Momo, Rémy, Valérie. Merci à tous pour ces supers moments, dire que tout a commencé pour moi après une chansonnette poussée du haut d'un échafaudage en étalant de la Black Mamba à la truelle... merci Claude François. J'ai découvert les joies de la musique en groupe avec vous, et quelle entrée en matière !! On a eu de supers moments, de supers concerts, de supers ratés, toujours dans la bonne humeur ! Merci les copains, j'espère qu'on rejouera ensemble quand je serai de passage à Paris, c'est triste que le confinement m'ai empêché de continuer cette aventure avec vous encore quelques mois.

Merci aussi à toute la collab de SuperNEMO, une collab vraiment au top, dans le travail comme dans la déconnade, et puis un peu dans la picolade aussi... En remote ou en réunion de collab, ça me faisait toujours plaisir de discuter avec vous, notamment pendant les fameux meetings du jeudi matin. Axel, Hichem et Christophe, merci aussi à vous trois, vous êtes une des raisons pour laquelle j'ai survécu à cette thèse, avec nos messages d'urgences lancés à 3h du mat pour parler de Root et de segmentation fault, et aussi pour rigoler un peu des chefs, désolée ;) Tantôt à Bordeaux, tantôt à Marseille ou à Paris (et ailleurs), on se sera bien poilés, en plus de la super école CodinGame !! Quoi que nous fassions tous les trois, j'espère qu'on continuera à rigoler et à partager notre passion pour la bière et pour Boby Lapointe.

Je ne peux pas citer tout le monde ici, j'en suis déjà à ma quatorzième page de remerciements... mais évidemment il y a tous les gens croisés en dehors de la thèse, les copains de toutes ces années d'études (et de danse) sans qui tout ceci n'aurait pas eu la même saveur. Les copains du Deblé pour ne pas les citer... entre

souloulouille et autres, c'était quelque chose aussi !! Mais ça, c'est pas fini j'espère ;) La Casa Del Amor On Fire... vous êtes géniaux, ces années passées avec vous ont été incroyables, VOUS êtes incroyables !

Et puis bon... Les meilleurs pour la fin ! Merci à ma famille, Papa pour m'avoir donné le goût de la physique en m'expliquant le fonctionnement du système solaire avec des oranges et des pamplemousses dans la cuisine de Noé... Je n'aurai pas fait astrophisicienne (astrologue pour les connaisseurs) finalement. Merci Maman, pour tout, le soutient, l'amour, la vie. Coline et Roméo, meilleure fratrie/sororie ever, je vous aime très fort tous les deux, et je pleure en écrivant ça, on est vraiment une famille de chialeurs ! Cœurs cœurs. Marion et Benoît aussi, parce que bon, on a quand même été élevés dans les mêmes baraques de l'amour et de la teuf ! Et toute la smallah (des cousinades notamment), je vous oublie pas, mais on est trop nombreux pour tous vous citer ! Ma vie ne serait pas la même si je ne vous avais pas rencontrés, avec vos guitares et vos anisettes de l'enfer !

Je crois que je n'oublie personne... ;)

Sylvain, Sly2000 pour les intimes. Il me faudrait 14 pages supplémentaires. Merci mon amoureux, pour un milliers de raisons différentes. Croisé dans les couloirs du LAL pendant que tu allais déposer une structure rocambolesque à la cafet et que j'étais à la bourre dans mes papiers administratifs, ça n'a pas beaucoup changé 3 ans après ! La vie qui va venir va être (et est déjà) hors du commun, pleine de saltimbanquerie, de physique, d'amour.

Merci à vous tous qui avez parsemé ma vie de choses incroyables. Des nouvelles aventures sont à venir...

“Moi aussi, je ne me sens pas dans mon assiette,
j’ai jamais beaucoup aimé les tunnels.”
Bohort – Kaamelott

Contents

Acknowledgement **3**

dedication **7**

Contents **9**

Introduction **13**

1 Phenomenology of particle physics and experimental status **15**
1.1 The Standard Model of particle physics 16
1.1.1 Particle content 16
1.1.2 Where the Standard Model ends 17
1.2 Going beyond the Standard Model with neutrinos 18
1.2.1 Neutrino flavors and oscillations 18
1.2.2 Neutrino masses and nature 21
1.2.3 Double beta decays 26
1.3 $0\nu\beta\beta$ experimental status 30
1.3.1 Experimental design criteria 30
1.3.2 $0\nu\beta\beta$ direct search experiments 31
1.3.3 Bolometers 33
1.3.4 Time projection chambers 34
1.3.5 Liquid scintillators 36
1.3.6 Tracking calorimeters 37
1.3.7 Summary 38
1.4 Conclusion 38

2 The SuperNEMO demonstrator **41**
2.1 The SuperNEMO technology 42
2.1.1 Detection principle 42
2.1.2 The source foils 44
2.1.3 The tracker 47
2.1.4 The calorimeter 51
2.1.5 Interaction of particles in the SuperNEMO scintillators . . . 56

2.1.6 The magnetic coil and the shieldings . . . 58
2.1.7 Calibration strategy . . . 59
2.1.8 Detector cabling . . . 61
2.1.9 Electronics . . . 63
2.1.10 Detector gas tightness . . . 66
2.2 Backgrounds . . . 67
2.2.1 Internal background . . . 68
2.2.2 External background . . . 70
2.2.3 Radon background . . . 71
2.2.4 Background reduction . . . 72
2.3 The SuperNEMO software . . . 73
2.3.1 Simulation . . . 73
2.3.2 Reconstruction pipeline . . . 73
2.3.3 Analysis tools . . . 74
2.4 Summary . . . 77

3 Sensitivity of the SuperNEMO experiment to the $0\nu\beta\beta$ 79
3.1 The $0\nu\beta\beta$ signal and background model . . . 80
3.1.1 The $0\nu\beta\beta$ signal . . . 80
3.1.2 Inside detector backgrounds . . . 80
3.1.3 External backgrounds . . . 81
3.1.4 Expected number of decays . . . 81
3.2 Event selection . . . 82
3.2.1 Electron definition . . . 82
3.2.2 Total energy spectrum . . . 83
3.3 Demonstrator sensitivity to the $0\nu\beta\beta$ decay of ^{82}Se . . . 85
3.3.1 Sensitivity to the $0\nu\beta\beta$ half-life . . . 85
3.3.2 Limit on the effective neutrino mass . . . 87
3.4 Impact of sources contamination levels on the sensitivity . . . 88
3.4.1 Contamination levels . . . 88
3.4.2 Optimisation of event selection . . . 91
3.5 Impact of the magnetic field on the sensitivity . . . 97
3.5.1 Simulations of the magnetic field . . . 97
3.5.2 Impact of the magnetic field on signal and background selections . . . 98
3.5.3 Influence of the magnetic field on optical modules and reconstruction efficiency . . . 100
3.5.4 Simulations with a non-uniform magnetic field . . . 101
3.6 Searching for the ^{150}Nd $0\nu\beta\beta$ decay . . . 103
3.6.1 Searching for the $0\nu\beta\beta$ of other isotopes . . . 103
3.6.2 Sensitivity to the $0\nu\beta\beta$ of ^{150}Nd . . . 103
3.7 The final detector sensitivity . . . 105
3.8 Conclusion . . . 106

4 Improvement of the internal ^{208}Tl background rejection 109
4.1 Motivations . . . 109
4.2 The internal ^{208}Tl background . . . 110

4.2.1 The internal conversion process . . . 111
4.2.2 ^{208}Tl disintegrations in the 2e channel . . . 112
4.3 Simulated demonstrator performances . . . 112
4.4 Analysis tools to describe the ^{208}Tl internal background . . . 114
4.4.1 The internal probability . . . 114
4.4.2 The exponential probability . . . 116
4.5 Event selection . . . 118
4.5.1 Energy selection . . . 118
4.5.2 Time-of-flight cut-off . . . 119
4.5.3 Probability cut-off . . . 121
4.5.4 Influence of the calorimeter time resolution . . . 124
4.6 Impact of ^{208}Tl rejection on the experiment's sensitivity . . . 127
4.6.1 Sensitivity results . . . 127
4.6.2 Expected number of background . . . 129
4.7 Conclusion . . . 130

5 Calorimeter commissioning 133
5.1 Optical modules calibration . . . 133
5.1.1 Pulse shape studies . . . 133
5.1.2 Baseline studies . . . 134
5.1.3 Gain studies . . . 134
5.1.4 Energy calibration . . . 136
5.2 Light Injection System . . . 136
5.3 Calorimeter cabling network . . . 137
5.3.1 Motivations . . . 138
5.3.2 Experimental setup . . . 139
5.3.3 Pulse shape analysis . . . 140
5.3.4 Pulse timing . . . 142
5.3.5 Signal attenuation . . . 147
5.3.6 Summary . . . 148
5.4 Synchronisation of calorimeter FEBs . . . 149
5.5 Conclusion . . . 150

6 Characterisation of the calorimeter time resolution 153
6.1 Time response of optical modules . . . 153
6.1.1 Scintillator time dispersion . . . 154
6.1.2 Photomultiplier time dispersion . . . 156
6.2 Description of ^{60}Co nucleus . . . 156
6.3 Experimental design . . . 157
6.3.1 Setting up the experimental design . . . 157
6.3.2 Simulations and analysis pipelines . . . 159
6.4 Signal events selection . . . 159
6.5 Energy calibration . . . 161
6.6 Background estimation . . . 162
6.6.1 Types of background . . . 164
6.6.2 Background characterisation . . . 165
6.7 Determination of the optical modules timing resolution . . . 167

6.7.1 Time difference distributions 168
6.7.2 Coupled time uncertainties 170
6.7.3 Decoupling the Σ_t uncertainties 170
6.8 Conclusion 172

Conclusion **173**

Bibliography **175**

Résumé **179**

Introduction

It is always interesting to take a historical approach when talking about a scientific discovery. This allows us to put into perspective knowledge that is now considered to have been acquired.

The Standard Model of Elementary Particle Physics attempts to describe the world around us on scales that were inconceivable two centuries ago. A little over a hundred years ago, Henri Becquerel discovered what we today call radioactivity, with the observation of β decay. This historical discovery was nevertheless accompanied by profound questioning, since the β particle emitted during this decay, which turned out to be an electron, only carries away part of the available energy for the reaction. This observation was contrary to the first principle of thermodynamics on the energy conservation, and some scientists postulated that this fundamental law was being violated. It took 35 years for an eminent scientist by the name of Wolfgang Pauli to propose as a "desperate remedy" the existence of the *neutrino* (ν) – for small neutron in Italian – to explain the problem of missing energy. Three years later Enrico Fermi laid the foundations for the first mathematical formulation of what is today the Lagrangian of weak interaction. It was another 25 years, 60 years after the discovery of β radioactivity, before the neutrino was experimentally observed by Clyde Cowan and Frederick Reines. The neutrino adventure had only just begun.

Why is this particle, although abundantly produced in the sun in the atmosphere and in the earth, so difficult to detect? It is because of its very low interacting rate with the matter – electrons and quarks – that constitutes us, being sensitive only to the weak interaction (of short range), and to the gravitational force (very weakly since the mass of the neutrino is extremely low, so much that it was believed mass-less for a long time).

In the current model of particle physics, neutrinos are actually described as mass-less. It was Bruno Pontecorvo who proposed in 1957 that neutrinos could oscillate between their different mass states, based on the already known model of oscillation of neutral kaons. To be valid, this model then presupposed that neutrinos had a non-zero mass. It was the Super-Kamiokande experiment that first observed this phenomenon in 1998, demonstrating that at least two of the three neutrino mass eigenstates have a non-zero mass. The Standard Model of particle physics is then no longer sufficient to account for this particle properties, opening the way to physics beyond the Standard Model.

It now remains to be discovered how this particle acquires its mass. Indeed, having a neutral charge under the three fundamental interactions described by the Standard Model, two mass generation mechanisms are foreseeable. The first is to assume that, like all other fermions, the neutrino obtains its mass through the Higgs mechanism, leading irremediably to the assumption of the existence of

a sterile neutrino. The second, proposed by Ettore Majorana, assumes that the neutrino is its own antiparticle, giving the neutrino its mass with the addition in the Lagrangian of the Majorana mass term. If this assertion is the one that applies to neutrinos, then a disintegration, prohibited in the Standard Model, is possible. It is called *neutrinoless double beta decay* ($0\nu\beta\beta$), to contrast with the *two neutrinos double beta decay* ($2\nu\beta\beta$) allowed by the Standard Model and already observed for several isotopes. In the former disintegration, two simple β decays take place simultaneously in the same nucleus, in which the two neutrinos are absorbed, allowing the total energy of the reaction to be distributed between the two exiting electrons. For reasons that are detailed in the first chapter of this manuscript, which deals with the phenomenology of the neutrino, this disintegration is only possible if the neutrino is a Majorana particle.

Several experiments are dedicated to the search for this disintegration which, if it exists, is expected to be extremely rare. The SuperNEMO experiment, on which I conducted my PhD, is one of them. Successor of the NEMO experiments, it uses a unique combination of technologies, described in detail in the second chapter, allowing to trace the path of the electrons resulting from double β disintegrations – with a wire chamber –, and also to measure their energies – with a segmented electromagnetic calorimeter.

These experiments differ from one another in the technology they use, and also in the sensitivity they can achieve in the search for this decay. Within the framework of this PhD, I carried out a sensitivity study of this experiment presented in the third chapter, determining the influence that several characteristics of the detector can have on it.

All these experiments are designed to observe, should this process exist, an extremely rare physical event. They are thus constrained to focus on the background which may disturb the measurement and have a non-negligible impact on their sensitivity to this disintegration. In this perspective, the fourth chapter presents a new technique to identify the events resulting from one of the main background for this experiment, which is the natural disintegration of ^{208}Tl isotope inside the source.

When I joined the LAL team at Orsay (now IJCLab) as a PhD student, SuperNEMO was already largely built in the Modane underground laboratory. I had the opportunity to actively participate in the completion of its assembly, as well as in the analyses of the first commissioning data described in the fifth chapter, which made it possible to ensure that the calorimeter was working properly and to calibrate it to make it operational for the first data collection. On this occasion, I focus in the last chapter on a study aiming to provide a value for the time resolution of a large part of the segmented calorimeter, using a calibration source.

The demonstrator is fully assembled in the underground laboratory, remaining mainly the commissioning phase of the tracker before encapsulating it definitively in its external shielding.

Chapter 1

Phenomenology of particle physics and experimental status

> I have done a terrible thing: I have postulated a particle that cannot be detected.
>
> Wolfgang Pauli

The idea that our universe is composed of very small and indivisible particles is not new, and has its origins in various cultures. The word *atom*, which is derived from the Greek word *atomos*, also means *unbreakable*. Currently, the theory that brings together our understanding of matter, the *elementary particles*, and its interactions, the *forces*, is called the Standard Model of Particle Physics (SM). This model provides a unified picture where the forces between particles are themselves described by the exchange of particles. Remarkably, the Standard Model succeeds in describing most current experimental data and represents one of the triumph of modern physics. A brief review of this model is given in the first part of this chapter.

Nevertheless, some questions are still open, for which the SM does not provide answers, as the matter/antimatter asymmetry of the universe, the dark matter nature and the origin of neutrino masses. In order to account for these observational discrepancies, new physics models have to be investigated. If a satisfactory theory beyond the Standard Model emerges, it could greatly impact our comprehension of the fundamental mechanisms of the Universe. In particular, the third one, concerning the mass of neutrinos, is the one which ultimately motivated this PhD, and is therefore particularly described in the second part of this chapter. It could also have an impact on the comprehension of matter/antimatter asymmetry origin. The third part of this chapter aims at giving an overview of the current research of a non-standard decay, of which the detector I worked on is a part.

1.1 The Standard Model of particle physics

The Standard Model of particle physics describes the strong, weak and electromagnetic interactions, gauged by the symmetry group $SU(3)_C \times SU(2)_L \times U(1)_Y$, where C represents the colour, L the left-handed chirality and Y the hypercharge. The SM gauge bosons (the 8 gluons, Z_0, $W^{\pm}$ and the photon) mediate these interactions. The scalar Higgs field is at the origin of electroweak symmetry breaking (i.e. $SU(2)_L \times U(1)_Y \rightarrow U(1)_{em}$), and is responsible for giving masses to elementary particles.

1.1.1 Particle content

The particle content is presented in Fig. 1.1.

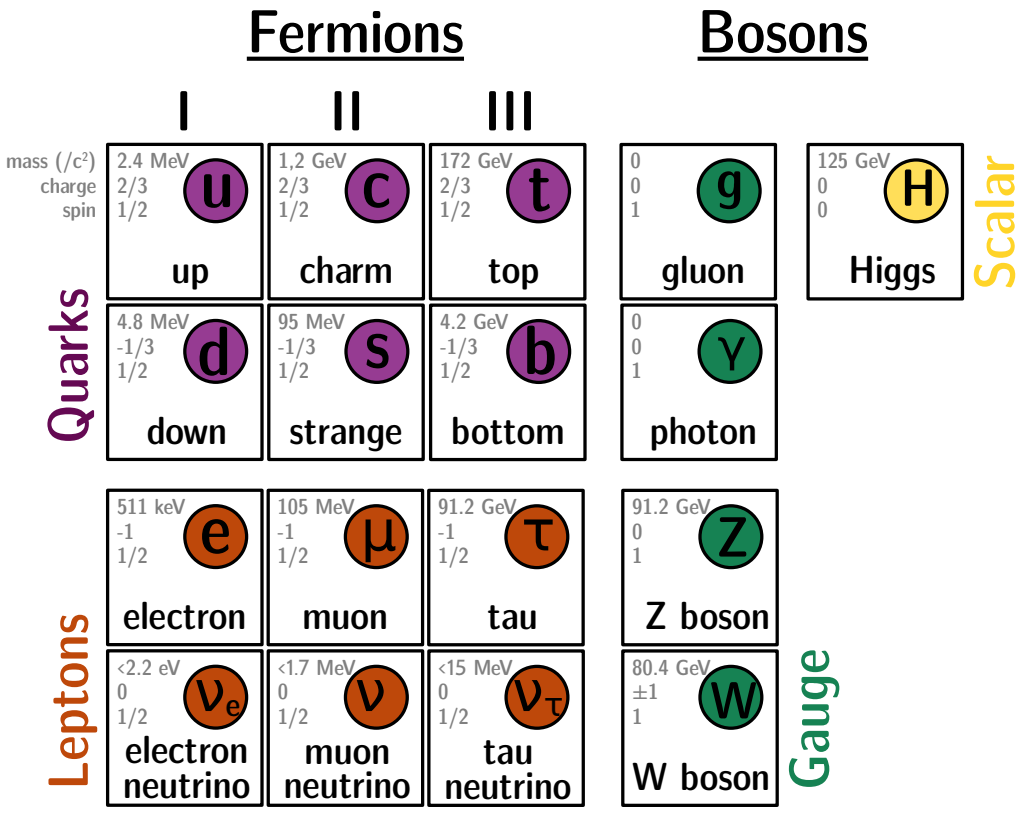

Figure 1.1: The Standard Model of elementary particles.

Fermions

Fermions are particles with half-integer spins, obeying to the Pauli exclusion principle. The properties of the 12 fermions of the Standard Model allow to classify them into categories, according to the forces to which they are sensitive. All fermions experience the weak force, while only 9 of them participate in the

electromagnetic interaction of QED, the neutrinos being electrically neutral. Only quarks feel the strong force, as they are the only ones carrying the QCD charge. The SM fermions are further classified in three generations.

To construct the electroweak $SU(2)_L \times U(1)_Y$ theory, the fermions field can be represented through their chirality properties. For one given generation, the left-handed chiral components of the fermion fields are grouped into $SU(2)$ doublets

$$L_L = \begin{pmatrix} \nu_L \\ l_L \end{pmatrix} \qquad \text{and} \qquad q_L = \begin{pmatrix} u_L \\ d_L \end{pmatrix}, \tag{1.1}$$

where L_L stands for the leptons and q_L for the quarks. The right-handed components of the other fermions are $SU(2)$ singlets, e_R, u_R and d_R. In the SM, neutrinos are assumed to have only left-handed components. The generalisation for three generations is not presented in this chapter.

Bosons

Bosons are particles with integer spins, described by the Bose-Einstein statistics. The elementary bosons of the SM, also called gauge bosons, have a spin 1 and mediate the interaction between elementary particles. The Higgs boson, with a spin 0, is a scalar boson.

1.1.2 Where the Standard Model ends

An ultimate Model of particle physics should theoretically predict and explain all particle masses and interactions, with few free parameters. Despite the success of the Standard Model in the explanation of particle behaviours, unanswered questions remain.

- Matter/antimatter asymmetry
  The beginning of the Universe should have produced the same quantity of matter and antimatter, simply because nor matter nor antimatter should be advantaged over the other. Nevertheless, from experimental evidences, we know that the former dominates over the latter. This is known as the Baryonic Asymmetry of the Universe (BAU). The amount of charge-parity (CP) violation observed in the quark sector being not sufficient to explain this asymmetry, the SM fails to explain this unbalance.

- Dark matter
  The known matter described by the SM represents only 5% of the Universe composition. Another 27% represents matter existing in a *non-luminous* form, called Dark Matter (DM), for which the Standard Model does not provide a viable candidate. Such matter is colourless and electrically neutral, and can only have weak and/or gravitational interactions. Early evidence for the existence of DM was provided by galaxy rotation curves: relying only on *luminous* matter, the velocity should decrease as $r^{-1/2}$, where r is the distance to the galaxy centre. This is in disagreement with observation, suggesting the existence of additional matter. The remaining 68% of the

universe composition is dark energy, an unknown form of energy introduced, among others, to explain the accelerated expansion of the universe.

- Neutrino masses
  Providing an explanation to neutrino masses, and understanding their smallness compared to other fermions, is an important question in modern particle physics. First proposed by Fermi in 1933 [1], neutrinos were believed to be mass-less, and in its original formulation, the SM included no neutrino mass term. Neutrino oscillations, which are confirmed by a plethora of experiments, provided evidence for neutrino masses. Given their unique neutral character, neutrinos can be either Dirac (particles and anti-particles are distinct) or Majorana (particles are their own anti-particles) fermions. Looking for neutrinoless beta decays is one of the preferred ways to probe the Majorana nature of neutrinos.

This is a non-exhaustive list, and other tensions exist between theory and observation, such as the anomalous magnetic moment of the muon, or the flavour universality violation in B and D meson decays.

1.2 Going beyond the Standard Model with neutrinos

1.2.1 Neutrino flavors and oscillations

The neutrinos are only detected through their weak interaction with matter, which defines the three neutrino flavours. For instance, an electron neutrino ν_e is defined through a charged-current weak interaction of an electron. In the same manner, the charged-current weak interaction of an electron neutrino produces an electron.

The first (and only) evidence that neutrinos are massive is the observation of neutrino oscillations, first predicted in 1957 by Pontecorvo [2]. In 1998 emerged from the Super-Kamiokande experiment the confirmation for neutrino flavour changing: the deficit of muon neutrinos was inconsistent with expectations based on calculations of the atmospheric neutrino flux, suggesting that muon neutrinos oscillate with tau neutrinos [3].

Flavour and mass eigenstates

The neutrino oscillation is a quantum-mechanical effect, which can be understood in terms of the relationship between the three weak interaction eigenstates, ν_e, ν_μ and ν_τ that can be experimentally measured, and the three mass eigenstates, ν_1, ν_2 and ν_3, that propagate in space-time. If the neutrino mass is zero thus, in the charged lepton sector, a basis can always be defined such as the lepton mass matrix is diagonal. However, by introducing even small masses for the neutrinos, a common basis were the two lepton mass matrix are diagonal can't be found. The

neutrino interaction and mass eigenstate are related by the U_{PMNS} matrix such as

$$\begin{pmatrix} \nu_e \\ \nu_\mu \\ \nu_\tau \end{pmatrix} = \begin{pmatrix} U_{e1} & U_{e2} & U_{e3} \\ U_{\mu 1} & U_{\mu 2} & U_{\mu 3} \\ U_{\tau 1} & U_{\tau 2} & U_{\tau 3} \end{pmatrix} \begin{pmatrix} \nu_1 \\ \nu_2 \\ \nu_3 \end{pmatrix} , \tag{1.2}$$

where U_{e2} denotes the ν_2-component of the interaction eigenstate ν_e, for instance.

Oscillation probability

Considering two-flavour neutrino ν_α and ν_β, the oscillation probability is written as

$$\mathcal{P}_{\nu_\alpha \to \nu_\beta}(t) = \sin^2(2\theta) \sin^2\left(\frac{\Delta m^2}{4E} L\right) \qquad (\nu_\alpha \neq \nu_\beta) \tag{1.3}$$

where L is the source-detector distance, E is the neutrino energy and θ is the mixing angle with a value in the interval $0 \leq \theta \leq \pi/2$. In the particular case of two-neutrino mixing the squared mass difference Δm^2 is defined as

$$\Delta m^2 = \Delta m^2_{12} = m_2^2 - m_1^2 \,, \tag{1.4}$$

where m_1 and m_2 are the masses of the states ν_1 and ν_2 defined as $m_1 < m_2$ so that $\Delta m^2 > 0$. The first observation coming with Eq. (1.3) is that if neutrino masses were not degenerated, oscillations would not be possible. A direct consequence of this statement is that if neutrinos are mass-less, they cannot oscillate. Then, we only need two non-zero neutrino masses for neutrino oscillation to be observed.

Neutrino mixing is a quantum effect: an interaction state ν_α is produced in a well-determined state, which is a linear combination of the three mass eigenstates. When the neutrino propagates through space-time, these coefficient are free to evolve as long as the neutrino is not detected and therefore measured. The neutrino is then no more determined as ν_α. When the neutrino is detected, an eigenstate is determined in the interaction basis, corresponding to ν_e, ν_μ or ν_τ. Thus ν_α can be measured as another neutrino state, with the probability given in Eq. (1.3).

Neutrinos mass ordering

The sensitivity to Δm^2 of an experiment is the value of Δm^2 for which $\Delta m^2 L/2E \sim 1$, allowing to classify neutrino experiments.

Atmospheric neutrinos are created by the interaction between the cosmic rays and the nuclei in the earth's atmosphere: protons of the cosmic rays interact with atmospheric nuclei, mostly producing pions. Pions mainly decay into muons and muon neutrinos in the energy range of $[0.5 - 10^2]$ GeV. Atmospheric neutrino experiments, with a source-detector distance about 10^4 km, are then sensitive to $\Delta m^2 \sim 10^{-4}$ eV^2, above the order of magnitude of Δm^2_{32} , which allow to rename $\Delta m^2_{32} = \Delta m^2_{atm}$.

In nuclear fusion processes, protons are transformed into neutrons through a weak process, producing electron neutrinos with an energy about $[0.2 - 15]$ MeV. Since the sun-earth distance is about 1.5×10^{11} km, solar neutrino experiments are sensitive to $\Delta m^2 \sim 10^{-12}$ eV^2. Comparing this sensitivity with Δm^2_{12}, one can

write $\Delta m^2_{12} = \Delta m^2_{sol}$. The study of neutrino mixing allows us to have access to precise values of squared mass differences Δm^2_{sol} and Δm^2_{atm}.

Thanks to matter effects in the Sun, we know that $\Delta m^2_{sol} > 0$. Since Δm^2_{atm} is essentially measured via neutrino oscillations in vacuum, which exclusively depend on its absolute value, its sign is unknown at the moment. Therefore, the neutrino masses can be ordered in two ways: normal ordering (NO) if $\Delta m^2_{atm} > 0$ and inverted ordering (IO) if $\Delta m^2_{atm} < 0$. Both orderings are presented in Fig. 1.2. Indirect constraints may come from the observation of the neutrinoless double beta decay or from cosmological bounds on the sum of the neutrino masses.

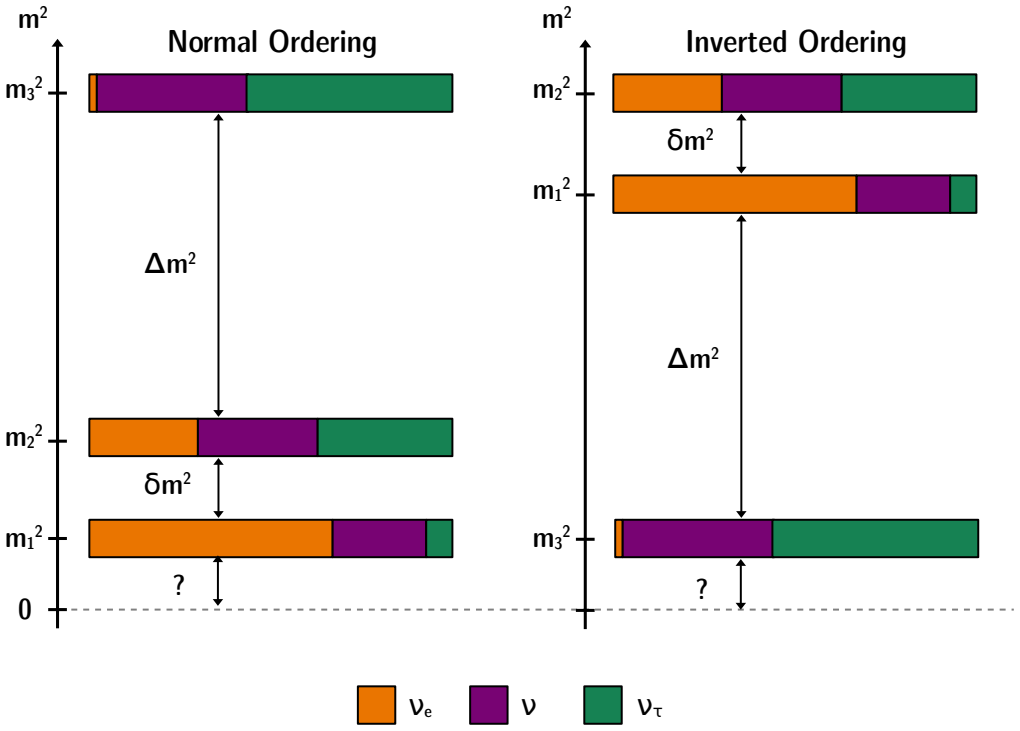

Figure 1.2: Graphic view of the probability of finding one of the flavor eigenstates if the neutrino is in a certain mass eigenstate. Normal and inverted orderings are presented. $\delta m^2 = m_2^2 - m_1^2$ and $\Delta m^2 = m_3^2 - (m_1^2 + m_2^2)/2$.

Oscillation data

The leptonic mixing matrix defined in Eq. (1.2) can be parameterised as

$$U_{PMNS} = \begin{pmatrix} c_{12}c_{13} & s_{12}c_{13} & s_{13}e^{-i\delta_{CP}} \\ -s_{12}c_{23} - c_{12}s_{23}s_{13}e^{i\delta_{CP}} & c_{12}c_{23} - s_{12}s_{23}s_{13}e^{i\delta_{CP}} & s_{23}c_{13} \\ s_{12}s_{23} - c_{12}c_{23}s_{13}e^{i\delta_{CP}} & -c_{12}s_{23} - s_{12}c_{23}s_{13}e^{i\delta_{CP}} & c_{23}c_{13} \end{pmatrix} \quad (1.5)$$

where $c_{ij} = \cos\theta_{ij}$, $s_{ij} = \sin\theta_{ij}$ and δ_{CP} is the Dirac CP violating phase. Tab. 1.1 sums up the latest best fit values of U_{PMNS} parameters [4].

Parameter	Hierarchy	Best fit
Δm^2_{12} (10^{-5}eV^2)	NO or IO	7.37
$\sin^2\theta_{12}$ (10^{-1})	NO or IO	2.97
Δm^2 (10^{-3}eV^2)	NO	2.52
Δm^2 (10^{-3}eV^2)	IO	2.50
$\sin^2\theta_{13}$ (10^{-2})	NO	2.15
$\sin^2\theta_{13}$ (10^{-2})	IO	2.15
$\sin^2\theta_{23}$ (10^{-1})	NO	4.22
$\sin^2\theta_{23}$ (10^{-1})	IO	5.90
δ_{CP}/π	NO	1.40
δ_{CP}/π	IO	1.30

Table 1.1: Best fit values of neutrino oscillation parameters, for inverted and normal orderings (IO and NO, respectively) [4]. $\Delta m^2 = m_3^2 - (m_1^2 + m_2^2)/2$ with $+\Delta m$ for NO. The CP violating phase is taken in the interval $0 \leq \delta_{CP}/\pi \leq 2$.

Fig. 1.3 pictures the relative different contributions of quark and neutrino matrix elements. Unlike the CKM matrix for the quark sector, the neutrino mixing angles are found to be large.

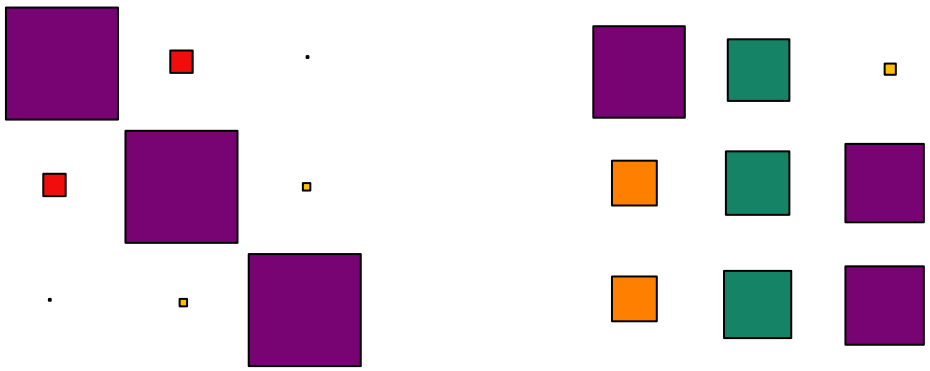

(a) CKM matrix. (b) PMNS matrix.

Figure 1.3: Comparison between the relative contributions of quark and neutrino matrix elements. The square areas stand for the square of the corresponding matrix element.

1.2.2 Neutrino masses and nature

As neutrinos are neutral particles, several mass terms can be introduced in the SM Lagrangian, depending on their nature.

1.2.2.1 Neutrino Dirac masses

In the SM, fermions are Dirac particles, meaning particles and anti-particles are different. Their masses arise with the Higgs mechanism, through the coupling of

left- and right-handed fields with the Higgs doublet. One can imagine the same mechanism arises for neutrinos.

In the SM, only left handed leptons participate in the charged weak interaction. As it is the only force through which neutrinos interact, only the left-handed component is described in the SM for neutrinos. Then, adding a Dirac term in the Lagrangian comes with introducing a right-handed chiral neutrino field, so-called sterile neutrino. They are named that way in order to distinguish them from known left-handed active neutrinos.

Dirac spinors

In the Standard Model, fermions are described by Dirac quantised fields $\psi(x)$, 4-component spinors which are a solution of the Dirac equation,

$$(i\partial\!\!\!/ - m)\psi(x) = 0\,, \tag{1.6}$$

with m the mass of charged leptons. $\partial\!\!\!/ \equiv \gamma^\mu \partial_\mu$ where there is an implied summation over the values of the twice-repeated index $\mu = 0, 1, 2, 3$, and ∂_μ is the 4-gradient. We can describe a Dirac field in term of chiral fields as

$$\psi = \psi_R + \psi_L\,, \tag{1.7}$$

with ψ_R and ψ_L the eigenvectors of the γ^5 chirality projector matrix. ψ_R and ψ_L are called Weyl spinors. Then the Lagrangian for a free fermion field is written as

$$\mathcal{L} = (\overline{\psi_R} + \overline{\psi_L})(i\overleftrightarrow{\partial\!\!\!/} - m)(\psi_R + \psi_L)\,. \tag{1.8}$$

It results from Eqs. (1.6) and (1.7) that ψ_R and ψ_L have independent kinetic terms, but coupled mass terms:

$$i\gamma^\mu \partial_\mu \psi_L = m\psi_R\,, \tag{1.9}$$
$$i\gamma^\mu \partial_\mu \psi_R = m\psi_L\,. \tag{1.10}$$

Consequently, the two chiral component fields are independent only if $m = 0$.

Dirac mass term

Charged leptons are massive in the SM with the Dirac mass term in the Lagrangian:

$$\mathcal{L}^l_Y = -\frac{v}{\sqrt{2}}\,\bar{l}_L\, Y^l\, l_R + h.c.\,, \tag{1.11}$$

where Y^l is the Yukawa matrix for charged leptons, and v is the vacuum expectation value (vev) for the Higgs field. In the SM Lagrangian, there is no mass term for neutrinos, and the lepton Yukawa couplings can be diagonalised without leading to flavour violation in charged lepton currents. Thus the lepton flavour is conserved in the SM.

In the Standard Model, neutrinos only undergo weak interactions. But weak interactions are described by the $SU(2)_L$ group, whose elements act only on left-handed chiral components of the fermion fields. So weak interaction "see" only the

LH components of fields. If one goes beyond the SM, one can add a right handed neutrino ν_R, singlet under all gauge interactions ($SU(3)_C \times SU(2)_L \times U(1)_Y$ gauge groups). In this case, and as occurred for the quark and charged lepton sectors, neutrino masses can be generated by the Higgs mechanism, with a Dirac mass term:

$$\mathcal{L}_Y^\nu = -\frac{v}{\sqrt{2}}\,\overline{\nu}_L\, Y^\nu\, \nu_R + h.c.\,. \tag{1.12}$$

Thus to have a Dirac mass term in the Lagrangian, we need to introduce right handed neutrinos ν_R, called sterile neutrinos, because they do not interact through weak interaction, unlike active neutrinos. If neutrinos and leptons are both massive, one cannot have Y^ν and Y^l simultaneously diagonal. Then the leptonic charged currents are not diagonal anymore, leading to lepton flavour violation. That leads to new processes including neutrino oscillations.

It is important to notice that for Dirac neutrinos, and even if their masses are described by the same mechanism responsible for all other SM fermion masses, the corresponding Yukawa couplings are extremely tiny, many orders of magnitude below Y^l and Y^q (the Yukawa matrix for quarks).

1.2.2.2 Neutrino Majorana masses

Majorana neutrinos

As we have seen in the previous sub-section, 4-component Dirac spinors are used to describe fermion fields. As Eqs. (1.9) and (1.10) are coupled, we could derive one simple expression if we find a link between ψ_R and ψ_L. In the 1930's Ettore Majorana suggested such a link by writing $\psi_R = C\overline{\psi}_L^T$, where C is the charge conjugation matrix and $\overline{\psi} = \gamma^0\psi$. Therefore $C\overline{\psi}_L^T$ is right-handed. We thus have the Majorana condition for fields

$$\psi = C\overline{\psi}^T\,, \tag{1.13}$$

since we have the chiral description for fermion fields in Eq. (1.7). With this condition, fermion fields are now described by a 2-component spinor. Thus a Majorana field has half the number of degree of freedom of a Dirac field. As $C\overline{\psi}_L^T$ is equivalent to ψ_L^C [5], the Majorana condition in Eq. (1.13) can be written as $\psi = \psi^C$. This further implies that a Majorana particle is its own antiparticle. Therefore, Majorana and Dirac particles are fundamentally different particles.

Majorana mass term

An effective field theory (EFT) is an "approximation" of a more general theory. It is used when a physical process is studied at such low energies (or long distances) that we cannot probe the underlying phenomenon that occurs (one says that the heavy fields at the origin of such interactions are "integrated out"). Fermi first described the weak interaction of beta decay with an EFT, when only leptons and hadrons were known. This so-called Fermi theory describes a contact interaction between 4 SM fields. In a more general manner, an effective Lagrangian, which

generalises the SM one, has an infinite number of terms as

$$\mathcal{L}_{eff} = \mathcal{L}_{SM} + \sum_{d} \frac{1}{\Lambda^{d-4}} C^d O^d \,, \tag{1.14}$$

with $d > 4$. C represents the couplings at the effective vertex, and O is an effective non-renormalisable operator with a dimension above 4, which contains only SM fields. For the neutrino case, we want to write a mass term involving only SM fields, that means with the only left-handed neutrino field ν_L. The operator with the lowest dimension - which respects the SM symmetries - to describe neutrino masses in the SM (without RH neutrinos) is a dimension-5 operator, called the Weinberg operator, which can be represented as in Fig. 1.4 and defined as

$$\mathcal{L}_5 = \frac{1}{2} \frac{g^{eff}}{\mathcal{M}} (\overline{L}_L^c \sigma^2 \phi)(\phi^T \sigma^2 L_L) + h.c. \,, \tag{1.15}$$

where g^{eff} is a dimensionless coefficient corresponding to a new effective coupling and σ the Pauli matrices. L_L is defined by Eq. (1.1) and ϕ represents the Higgs field. In Eq. (1.15), the coefficient C is here identified with $g^{eff}/2$, and O is represented by the [LH][LH] operator. This Lagrangian respects all the SM symmetries, except for the total lepton number conservation. After the electroweak symmetry breaking, the following Lagrangian stands for the neutrino fields

$$\mathcal{L}_5 = \frac{1}{2} \frac{g^{eff} v^2}{\mathcal{M}} \overline{\nu}_L^c \nu_L + h.c. \,, \tag{1.16}$$

where $\mathcal{M}$ denotes a mass scale at which new degrees of freedom arise, corresponding to new physics. A Majorana mass term for neutrinos can be defined as

$$m_\nu = \frac{g^{eff} v^2}{\mathcal{M}} \,. \tag{1.17}$$

The dimension-5 operator in Eq. (1.15) is not renormalisable. Nevertheless, it is natural to think that the actual SM theory is not the final theory, but an effective theory, as a reminiscence of a more complete one. Neutrino masses can then be seen as a low energy manifestation of this physics beyond the Standard Model. There exist many other higher dimension operators, for example, the Fermi operator is a dimension-6 effective operator, as are the operators responsible for charged lepton flavour violation. Notice that the higher the dimension is, the harder is the observation of the corresponding new physics effects.

1.2.2.3 Neutrino mass term

In the two previous sub-sections the Dirac and Majorana nature of neutrinos were reviewed. Assuming a right-handed chiral field exists, it is possible to combine the Dirac and Majorana descriptions. A Dirac-Majorana mass term is derived for one generation of neutrinos, for the minimal model where an additional right-handed neutrino is added to the particle content.

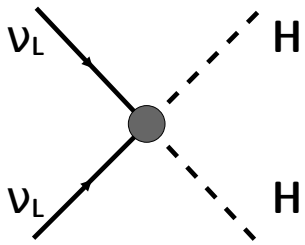

Figure 1.4: Weinberg operator diagram. The grey circle pictures a new physics interaction.

Dirac-Majorana mass term

After Eq. (1.12), a Dirac mass term for neutrinos in the Lagrangian can be defined as

$$\mathcal{L}_D = -m_D \overline{\nu}_L \nu_R + h.c.\,, \tag{1.18}$$

with $m_D = \frac{v}{\sqrt{2}} y^\nu$ in the case of one generation of neutrinos, where y^ν embeds the Yukawa coupling. In addition, one can define a Majorana mass term for the right-handed neutrino field as

$$\mathcal{L}_R = \frac{1}{2} m_R \overline{\nu}_R^c \nu_R + h.c.\,, \tag{1.19}$$

with m_R defined in the same manner as in Eq. (1.17). Thus, in general, it is possible to have a Dirac-Majorana mass term in the Lagrangian:

$$\mathcal{L}_{D+M} = \mathcal{L}_D + \mathcal{L}_R = -m_D \overline{\nu}_L \nu_R + \frac{1}{2} m_R \overline{\nu}_R^c \nu_R + h.c.\,. \tag{1.20}$$

This term can be re-written as

$$\mathcal{L}_{D+M} = \frac{1}{2} n_L^T C^\dagger \mathbb{M} n_L + h.c.\,. \tag{1.21}$$

with $n_L = (\nu_L \nu_R^c)^T$, and the non-diagonal matrix

$$\mathbb{M} = \begin{pmatrix} 0 & m_D \\ m_D & m_R \end{pmatrix}. \tag{1.22}$$

For one generation of neutrinos, $\mathbb{M}$ is a (2×2) matrix. In the more general case of three generations, m_D and m_R are (3×3) diagonal matrices. The matrix $\mathbb{M}$ has to be diagonalised in order to have masses for ν_R and ν_L. $\mathbb{M}$ is diagonalised by $U^T \mathbb{M} U$ with U the mixing matrix from interaction to mass basis

$$U = \begin{pmatrix} \cos\theta & \sin\theta \\ -\sin\theta & \cos\theta \end{pmatrix} \begin{pmatrix} \eta_1 & 0 \\ 0 & \eta_2 \end{pmatrix} \tag{1.23}$$

with η_1 and η_2 two phases called Majorana phases, ensuring that masses, eigenvalues of $\mathbb{M}$, are positive. Thus, after diagonalisation, we have the two masses

$$m_{1,2} = \frac{1}{2} \left(m_R \mp \sqrt{m_R^2 + 4 m_D^2} \right) \eta_{1,2}^2\,, \tag{1.24}$$

with $\eta_1 = i$ and $\eta_2 = 1$. Here we note the role of Majorana phases: η_1 guarantees the positiveness of the m_1 solution. Other models, including a Majorana mass term m_L for the ν_L field exist, and allow to describe pure Dirac or pure Majorana conditions.

See-saw mechanisms

The Standard Model forbids a mass term for the ν_L field but predicts nothing for the ν_R field. Considering the case were $m_D \ll m_R$ (and $m_L = 0$) would allow to explain how neutrinos acquire their small masses, through the see-saw mechanism. Indeed, the two mass eigenstates can be re-written as

$$m_1 \simeq \frac{m_D^2}{m_R} \qquad \text{and} \qquad m_2 \simeq m_R \,. \tag{1.25}$$

If a large value is considered for m_R and a small one for m_D, the light neutrino has a mass m_1 corresponding to the observed active one, while the heavy neutrino has a mass m_2 and corresponds to the sterile singlet. This realisation of the see-saw mechanism is the best known, but others exist.

To introduce a Weinberg operator, leading to a Majorana mass term in the Lagrangian, one can consider the most general form $[LHLH]$, composed of Higgs fields H and lepton fields L, and try to combine it in order to have gauge invariant operators.

- It is possible to combine lepton and Higgs fields to have an $SU(2)$ fermion singlet. The corresponding Feynman diagram is represented in Fig. 1.5a. This realisation of the see-saw mechanism was already presented above, where one RH neutrino field gives rise to a mass for one LH neutrino field. In that case, the addition of three RH fields to the model would be sufficient to give masses to the three active neutrinos.

- We can also consider a combination giving a heavy scalar triplet $\xi = (\xi^{++}, \xi^{+}, \xi^{0})$. The corresponding Feynman diagram is presented in Fig. 1.5b. This is a mechanism which does not require right-handed neutrinos.

- The last way to combine lepton and Higgs fields in order to have a gauge invariant Lagrangian consists in introducing a fermionic triplet $\Sigma = (\Sigma^{+}, \Sigma^{0}, \Sigma^{-})$, not to be confused with the baryon of the same name. The Feynman diagram is pictured in Fig. 1.5c.

These three possibilities are in fact the only possible realisations to obtain the effective Weinberg operator, using only renormalisable interactions. They correspond to the so-called type I [6], II [7] and III [8] seesaw mechanisms, respectively.

1.2.3 Double beta decays

Even though it is not protected by a symmetry, the total lepton number is conserved in the SM. If the neutrino is found to be a Majorana particle it

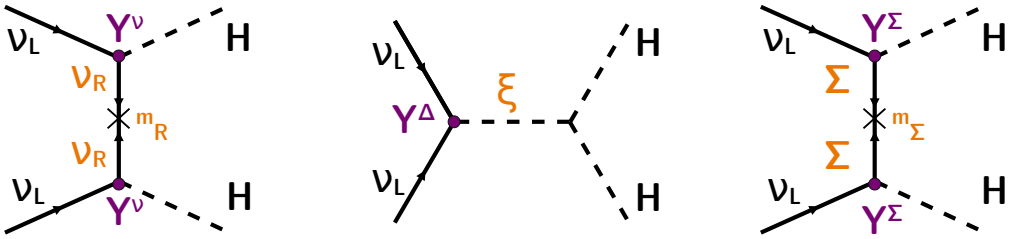

(a) See-saw type I. (b) See-saw type II. (c) See-saw type III.

Figure 1.5

could open leads for the explanation of lepton number violation (LNV), the small masses of the neutrinos through the see-saw mechanism and the matter/antimatter asymmetry in the Universe through Leptogenesis. The neutrino mass term leads to LNV with $\Delta L = 2$, and the best known process able to probe it is neutrinoless double beta decay [9].

Standard double beta decay

Let us first introduce the double beta decay proposed by Goeppert-Mayer in 1935 [10] as

$$(A, Z) \rightarrow (A, Z+2) + 2e^- + 2\overline{\nu}_e\,, \tag{1.26}$$

describing two simultaneous β decays of two nucleons of the same nucleus. This decay is physically possible for nuclei with an even-even number of nucleons, for whose a simple beta decay would not be favourable: the energy of the daughter nucleus would be higher than the parent one (see Fig. 1.6). In some cases (as the ^{48}Ca nucleus) the simple β decay is suppressed because of transition spin considerations. The double beta decay is then strongly suppressed, which makes it the rarest known nuclear decay. It is allowed by the Standard Model for 35 isotopes, and despite its rarity, has already been observed for numerous of them like ^{100}Mo, ^{82}Se, ^{136}Xe and ^{76}Ge, with typical half-lives ranging from 10^{18} to 10^{24} years. The Feynman diagram illustrating this process is given in Fig. 1.7.

Neutrinoless double beta decay

In 1939, Furry proposed the double beta decay without neutrino production as

$$(A, Z) \rightarrow (A, Z+2) + 2e^-\,, \tag{1.27}$$

in which two neutrons simultaneously decay into protons [12].

The existence of such a decay would have deep implications for various physics research. Firstly, as neutrinos are not emitted, this process implies the violation of the total lepton number by 2 units, thus making it forbidden in the SM. However, the lepton number conservation results from an accidental symmetry breaking of the SM, and thus its violation would not necessarily imply Physics beyond the Standard Model. But more than the LNV, the $0\nu\beta\beta$ would violate also the baryon - lepton number (B-L) which, on the contrary, is a fundamental symmetry of the SM. Hence such observation would have major contribution for theories trying to

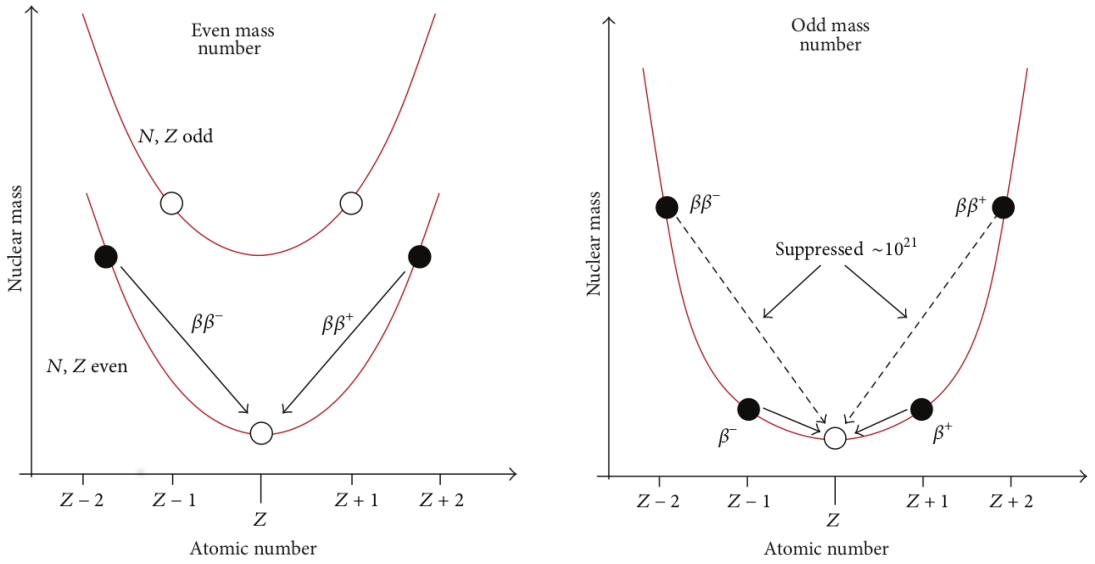

Figure 1.6: Nuclear mass as a function of the atomic number Z in the case of an isotope with A even (a) and A odd (b). Adapted from [11].

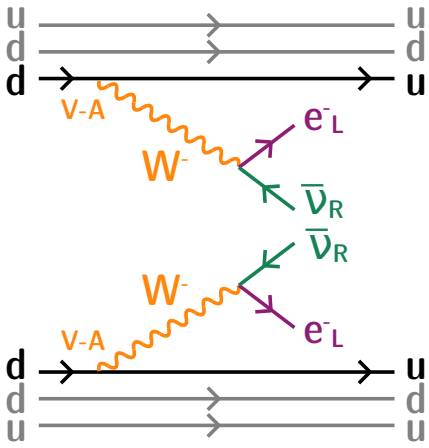

Figure 1.7: Standard double beta decay.

explain the matter/antimatter asymmetry of the Universe. Moreover, the $0\nu\beta\beta$ process is allowed only if neutrinos are massive Majorana particles. Therefore, the observation of this decay would point to the existence of a process that violates a fundamental symmetry of the Standard Model of Particle Physics, and would allow to establish the nature of neutrinos.

At the moment, no experiment has observed $0\nu\beta\beta$ processes, but various experiments, of which a non-exhaustive list is given in Sec. 1.3, have lead to precise limits on $0\nu\beta\beta$ half-life of $10^{25} - 10^{26}$ years. The future generation of $0\nu\beta\beta$ experiment is currently under construction.

The underlying mechanism through which the neutrinoless double beta decay would occur is not known, and several theories have been developed. The most

spread one is the exchange of light Majorana RH neutrinos, including dimension-5 operator, but other theories are described.

- Higher dimensional operators: it is possible to consider higher dimension operators (dimension 6 and 9 for instance), that are effective and non-renormalisable, respecting the gauge symmetry $SU(3)_C \times SU(2)_L \times U(1)_Y$.
- Heavy neutrino exchange considers the case where a heavy RH neutrino is exchanged during the $0\nu\beta\beta$ decay. This was historically the first case to be considered, including a dimension-9 operator, with constraints on the heavy neutrino mass coming from the mixing between left-handed neutrinos and the heavy neutrino.
- Right-handed currents include new RH gauge bosons W_R of a new $SU(2)_R$ gauge group. The corresponding operator would be of dimension-9 and highly suppressed, by 4 powers of the masses of the new gauge bosons.

If the $0\nu\beta\beta$ decay is observed, the underlying mechanism through it occurs would have to be determined. In Fig. 1.8 is given the Feynman diagram of the neutrinoless double β decay for the light Majorana neutrino exchange realisation.

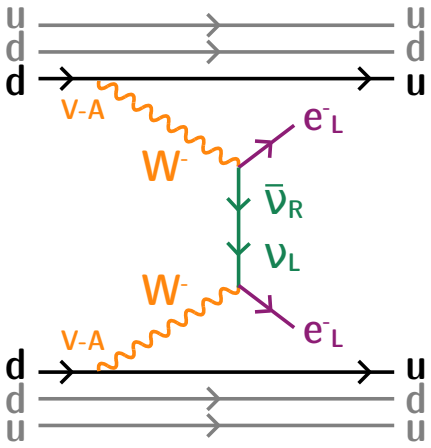

Figure 1.8: Neutrinoless double beta decay through light Majorana neutrino exchange.

Experimental search for $0\nu\beta\beta$

One of the experimental observable of the double β decays is the total energy spectrum of the 2 emitted electrons, given in Fig. 1.9. The $2\nu\beta\beta$ decay emits 4 leptons, the two electrons having an energy continuum between 0 and $Q_{\beta\beta}$, the total available energy of the reaction. In the case of the $0\nu\beta\beta$ decay, the two electrons would bring the total energy of the reaction, thus the expected signature would be an energy peak at $Q_{\beta\beta}$.

If existing, the $0\nu\beta\beta$ decay would be an extremely rare process. The decay rate of the light Majorana exchange is given by:

$$(T^{0\nu}_{1/2})^{-1} = g_A^4 G^{0\nu} |M^{0\nu}|^2 \left| \frac{m_{\beta\beta}}{m_e} \right|^2 , \tag{1.28}$$

where $G^{0\nu}$ is the phase space factor embedding the influence of the Coulomb field of the daughter nucleus on the emitted electrons/positrons. $M^{0\nu}$ is called the nuclear matrix element embedding the nuclear structure effects of the decaying nucleus. $m_{\beta\beta}$ is the effective neutrino mass defined as

$$\langle m_{\beta\beta} \rangle = \left| \sum_{i=1...3} m_i U_{ei}^2 \right| , \tag{1.29}$$

is summed over the three mass eigenstates. This effective mass depends on the U_{PMNS} matrix elements given in Eq (1.5), and thus is a function of the CP violating phases and of the mass ordering.

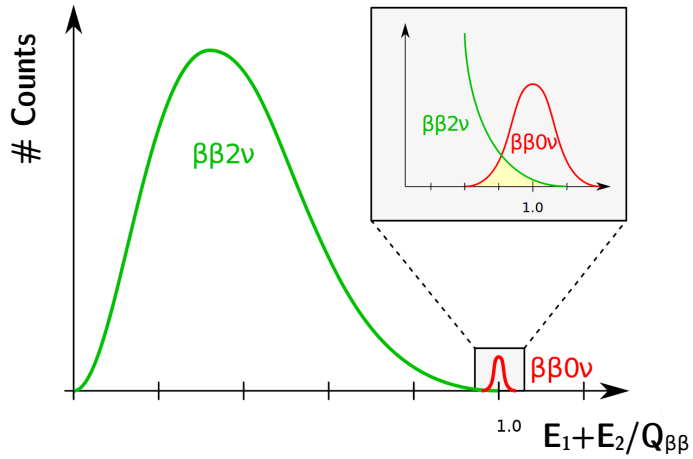

Figure 1.9: Electron energy sum spectrum for $2\nu\beta\beta$ and $0\nu\beta\beta$ decays.

1.3 $0\nu\beta\beta$ experimental status

The $0\nu\beta\beta$ decay has theoretically been proposed. Various experiments are searching for it, with various technologies, considering the experimental constraints coming with each technique.

1.3.1 Experimental design criteria

As no neutrinos are emitted in a $0\nu\beta\beta$ decay, the minimal observable in direct searches for $0\nu\beta\beta$ decay is the total energy of the two emitted electrons. In that case the signature of a $0\nu\beta\beta$ signal is an excess of events, compared to the expected background noise, in the total energy spectrum, near the $Q_{\beta\beta}$ released energy. The width of this peak depends on the energy resolution of the detector. Depending on experiment designs and purposes, individual electron energies and tracks also represent interesting observables.

The sensitivity to the $0\nu\beta\beta$ half-life $T_{1/2}^{0\nu}$ of a given experiment is detailed in Chapter 3, but a brief overview is given. It depends on the amount of enriched $\beta\beta$ source isotope of the experiment (with M its molar mass), as well as on its natural abundance a, on the detector efficiency ϵ, and on the data acquisition time t. The number of background events highly impacts this sensitivity, as

$$T_{1/2}^{0\nu,\lim} \propto \begin{cases} aM\epsilon t & \text{if no background is expected,} \\ a\epsilon\sqrt{\frac{Mt}{B\Delta E}} & \text{with background,} \end{cases} \tag{1.30}$$

where ΔE is the energy resolution and B is the background rate usually expressed in counts.keV^{-1}.kg^{-1}.y^{-1}, taking into account the energy range considered for the $0\nu\beta\beta$ search, the source mass, and the observation time. The advantage of a background free experiment clearly comes out: the $0\nu\beta\beta$ half life would increase linearly with the time of exposure t, while following a $\sqrt{t}$ law for an experiment with a non-negligible number of background events. Then, it is clear that the control and the discrimination of background is of high priority for such $0\nu\beta\beta$ direct search experiments.

As experiments aim at reaching the highest possible half-life sensitivities, choices have to be made concerning detector designs. An ideal isotope would have a high natural abundance and would be deployed with the highest mass possible in a detector with a high detection efficiency, a good energy resolution (small ΔE) under low-background conditions (small B). Of all the 35 isotopes capable of disintegrating through $2\nu\beta\beta$, none meets all the previous conditions. Experimenters will then have to find compromises, which are at the origin of the different detection strategies.

In the following, we detail different detection technologies, using either active source (the source is also the detector), or passive source (the source is decoupled from the detection volume).

1.3.2 $0\nu\beta\beta$ direct search experiments

1.3.2.1 Semiconductors

Various semiconductor technologies are employed in the detection of $0\nu\beta\beta$ decay. The ^{76}Ge $\beta\beta$ emitter ($Q_{\beta\beta}$ = 2039 keV) is historically important as it has been adopted since the 1960s in $0\nu\beta\beta$ decay searches, acting as active source, which enhances the detection efficiency. ^{76}Ge-enriched high purity Germanium detectors (HPGe) offer both high energy resolution and extremely high radiopurity (as impurities are removed in the crystal growing process). These characteristics allow, once external background contribution is minimised, to reach high sensitivity on $0\nu\beta\beta$ decay, which makes this category of detectors one of the most promising for ton-scale experiments. Since the last generation (IGEX and Heidelberg-Moscow), HPGe detectors had been improved to reach an ultra low background rate, making way for the current generation of $0\nu\beta\beta$ detectors – GERDA, MAJORANA demonstrator and LEGEND.

GERDA experiment [13] (GERmanium Detector Array) is located at the Laboratori Nazionali del Gran Sasso (LNGS), Italy. GERDA phase I was running

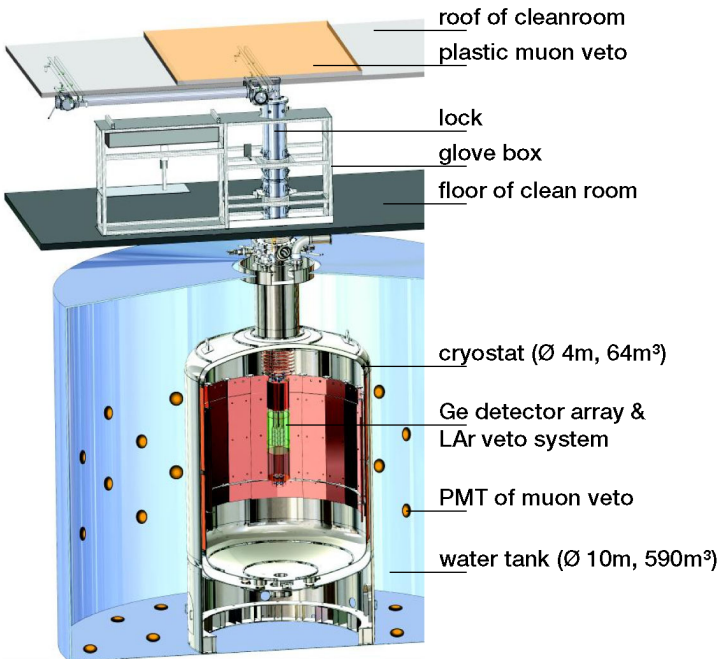

Figure 1.10: Scheme of the GERDA experiment.

from 2011 to 2013 with 17.8 kg of enriched active source detectors from the HEIDELBERG-MOSCOW and IGEX experiments. Its first aim was to put to the test the controversial result of HEIDELBERG-MOSCOW experiment given in 2001, announcing the first evidence for $0\nu\beta\beta$ signal at a 4.2σ confidence level. With an exposure of 21.6 kg.y, the absence of signal in the GERDA-I experiment refuted the previous result, setting a limit $T^{0\nu}_{1/2} > 2.1\,10^{25}$ y. Since 2015, the GERDA experiment is in the second phase (see Fig. 1.10), with a total of 35.8 kg enriched detectors, 20 kg of which is Broad Energy Germanium (BEGe) detectors that have been deployed for GERDA-II, providing a better energy resolution and pulse shape discrimination. The active source is deployed inside a liquid Argon (LAr) augmented with light sensors, acting as an active external shield as well as a cooling down system. The total is surrounded by a water tank. The underground laboratory provides 3500 m water equivalent to reduce the external cosmic background. The aim is to reach a 10^{26} y sensitivity with 100 kg.y exposure, and a background rate less than 10^{-3} counts.keV^{-1}.kg^{-1}.y^{-1}. In 2020, a combined analysis for GERDA phases I and II has resulted in a half-life limit of $T^{0\nu}_{1/2} > 1.8 \times 10^{26}$ years (90% C.L.) under the no signal hypothesis, with a total exposure of 127.2 kg.y [14].

MAJORANA demonstrator [15] is an array of enriched germanium detectors searching for the $0\nu\beta\beta$ decay of the ^{76}Ge isotope, using High Purity Germanium (HPGe) detectors. The Majorana Demonstrator is located at the Sanford Underground Research Facility (SURF) in Lead, USA. It is composed of 58 HPGe detectors divided into 2 cryostats with 7 strings each. Each string is an assembly of 3, 4 or 5 detectors. The total mass of HPGe crystals is 44.1 kg, 29.7 kg of which is enriched to 88% ^{76}Ge. The observed lower limit is $T^{0\nu}_{1/2} > 2.7 \times 10^{25}$ years at

90% CL [16]. A combined limit from the two Ge-based experiments GERDA and MAJORANA would exceed 10^{26} years.

LEGEND stands for Large Enriched Germanium Experiment for Neutrinoless Double-Beta Decay [17]. After the encouraging results of the MAJORANA Demonstrator and GERDA, the LEGEND collaboration has been formed to pursue a tonne-scale ^{76}Ge experiment, with discovery potential at a half-life beyond 10^{28} years. The collaboration aim to use existing material from GERDA, especially the cryostat, and perform additional R&D to build the detector.

1.3.3 Bolometers

Bolometers are high energy resolution (few keV) and high detection efficiency calorimeters operating at low temperatures ($\simeq 10-20$ mK), by measuring the heat increase, quantified by phonons, generated by particles interaction in the crystal. The crystals are both the source and the detector, which is particularly suitable for $0\nu\beta\beta$ searches, and provides the possibility to build large-scale experiments. As the two electrons topology is not available, analyses of the pulse shapes can be performed in order to discriminate the signal from the electronics noise and the natural radioactivity events.

CUORE for Cryogenic Underground Observatory for Rare Events [18], is an experiment based at Laboratori Nazionali del Gran Sasso in Italy. The feasibility of the project has been proved by Cuoricino, the pilot experiment taking data from 2003 to 2008 with 62 TeO2 cryogenic detectors, for a total of 19.75 kg.y exposure, achieving a lower limit of $T^{0\nu}_{1/2} > 2.8 \times 10^{24}$ years at 90% CL. The next step towards the final experiment CUORE is CUORE-0 which aims at improving the background reduction. The data took place from 2013 to summer 2015, showing the α background were reduced by a factor 6. The final CUORE detector consists of an array of 988 TeO2 crystals arranged in a cylindrical structure of 19 towers. The first results of the CUORE experiment had been published in 2018, where no evidence for $0\nu\beta\beta$ were found. Combining their results with the earlier experiments Cuoricino and CUORE-0, a lower limit of $T^{0\nu}_{1/2} > 1.5 \times 10^{25}$ years at 90% CL were achieved. Latest results of the CUORE collaboration in 2020 reported a sensitivity of $T^{0\nu}_{1/2} > 1.7 \times 10^{25}$ years [19].

CUPID for CUORE Upgrade with Particle IDentification [20], uses the expertise acquired with the CUORE facility, with a background level improved by a factor 100 as the particle identification is a powerful tool for background rejection. This technology uses scintillating bolometers, and is based on the principle that different particles produce different amount of light, providing a good discrimination between γ and α background events. The first CUPID-0 detector uses 24 crystals enriched at 95% with ^{82}Se, for a total mass of 5.17 kg, coupled with 31 Germanium light detectors. It is hosted in the CUORE-0 cryostat at LNGS. With an exposure of 9.95 kg.y, the CUPID-0 collaboration presented the first results with a lower limit of $T^{0\nu}_{1/2} > 3.5 \times 10^{24}$ years at 90% CL. These are encouraging for the next

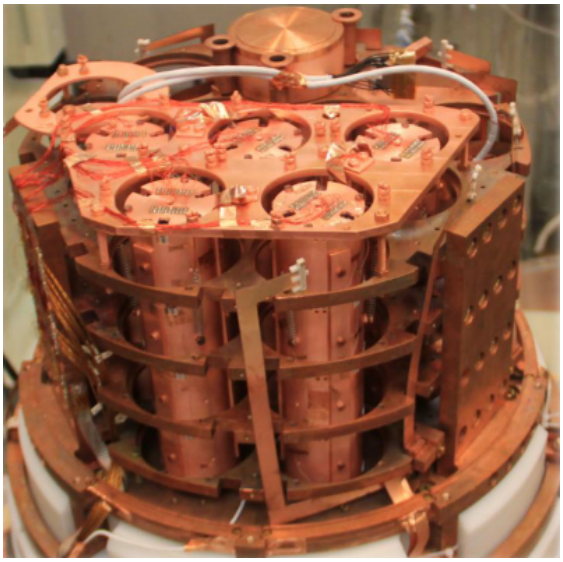

Figure 1.11: Picture of the CUPID-Mo project.

CUPID project by showing a high α rejection. The ^{82}Se material is however not suitable for CUPID, making the crystal growth complicated and showing a high internal contamination in natural isotopes. The next project CUPID-Mo was commissioned in 2019 and is already taking data at Laboratoire Souterrain de Modane in France, with 210 g of $Li_2^{100}MoO_4$ crystals, divided into 5 towers of 4 modules each (see Fig. 1.11). Preliminary results have been presented and show a high energy resolution (about 5 keV FWHM), a good γ/α discrimination, and a high internal radiopurity, demonstrating that the CUPID technology is ton-scalable.

1.3.4 Time projection chambers

Time Projection Chambers (TPC) detectors use a medium producing two ways to measure the electron energies: a *scintillation* (ultra-violet light) prompt signal, and a *ionisation* delayed signal. When a particle crosses the detector, a scintillation light is emitted, the energy of the scintillation peak depending on the medium. Scintillation photons, travelling at speed of light in the medium, are detected by photo-sensors, giving the *zero-time* of the event. The crossing particle ionises the medium all along its way, creating electrons drifting to a collection system (an electric field is applied between cathode and anode), allowing the precise measurement of the electron production location in a 2D plane. The drift time measurement gives access to the third coordinate of the interaction point. Therefore, combining the two consecutive signals allows precise position and energy reconstructions. For $0\nu\beta\beta$ searches, ^{136}Xe-enriched isotope in liquid phase is often used, offering a maximal source density (more compact detectors) and a good position resolution. Unfortunately, the energy resolution is worse than that of the gas-phase TPCs detectors[1]. Noble elements are natural radiation detectors,

[1]Two-phase liquid-Xenon detectors are developed for Dark Matter searches and could be exploited for $0\nu\beta\beta$ direct searches with the DARWIN project.

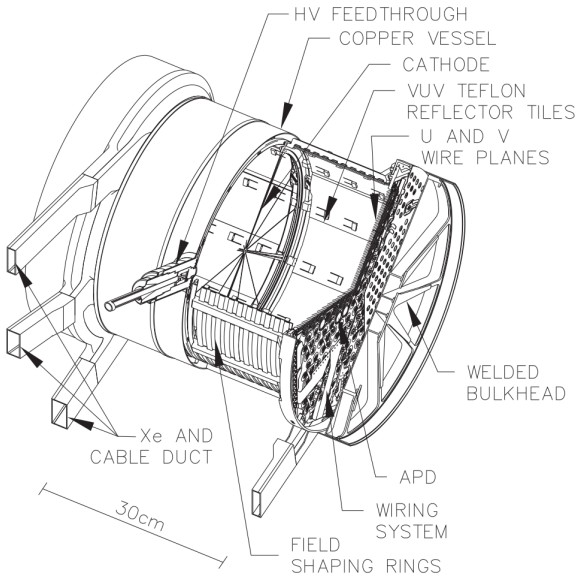

Figure 1.12: Cross-section of the EXO-200 TPC detector

avoiding the need for excess materials that could generate extra radioactive backgrounds. ^{136}Xe-enriched is the only noble element capable to $2\nu\beta\beta$ decay, with $Q_{\beta\beta} = 2457.8$ keV. This isotope has a relatively high natural abundance (9%) and can be enriched to highly pure concentrations, making it interesting for large-scale TPCs $0\nu\beta\beta$ experiments.

EXO-200 experiment [21] is a prototype of the Enriched Xenon Observatory (EXO) project, currently operating in a room under an overburden of 1624 m.w.e, at the Waste Isolation Pilot Plant (WIPP), USA. The detector is shaped as a cylinder, with two back-to-back cylindrical TPCs. A high negative voltage grid cathode holds at the mid plane of the detector (40 cm diameter), and two anodes are located on both sides, at ground potential. A cross-section of the detector is displayed in Fig. 1.12. The detector is held at 167 K in a cryogenic bath. With 110 kg of enriched ^{136}Xe in liquid phase, the phase I of this TPC detector has measured for the first time the Xenon $2\nu\beta\beta$ decay with $T^{0\nu}_{1/2} = 2.165 \times 10^{21}$ y. Between phase I and IIa, the detector was upgraded with improved low-noise electronics, a Radon suppression system, and the impurities contents of the Xenon were reduced by a factor ten. The current detector performance shows an energy resolution of 2.90% (FWHM) at the decay Q-value and a background rate of 1.6×10^{-3}counts.keV^{-1}.kg^{-1}.y^{-1}. EXO-200 phase IIa data placed a new limit of $T^{0\nu}_{1/2} > 1.8 \times 10^{25}$ y (90% C.L.). The final analysis allowed to reach 5.0×10^{25} years at 90% CL with a 234.1 kg.y exposure [22].

nEXO [23] is the successor of EXO-200 searching for the $0\nu\beta\beta$ decay of ^{136}Xe with a target half-life sensitivity of $\sim 10^{28}$ years using 5×10^3 kg of enriched liquid-xenon in a time projection chamber. This limit would be reached by using an increased mass of enriched ^{136}Xe, and an active R&D program, aimed primarily at improving the active medium homogeneity.

NEXT for Neutrino Experiment with a Xenon TPC is searching for the $0\nu\beta\beta$ decay of ^{136}Xe isotope at the Canfranc underground laboratory in Spain [24]. This technology uses high-pressure gaseous Xenon at 15 bar with using electroluminescence to amplify the signal (HPXe). The gas medium allows to obtain longer particle tracks than with liquid Xenon and thus confers the ability to reconstruct the trajectory of the two emitted electrons, contributing to the suppression of backgrounds. The NEXT-100 project, which deploys 100 kg of enriched Xenon, aims to demonstrate the feasibility of such an experiment and its usefulness for the $0\nu\beta\beta$ searches.

PandaX-III also searches for the $0\nu\beta\beta$ of ^{136}Xe with a high 10 bar pressure gas TPC [25]. It is installed at the China Jin Ping underground Laboratory (CJPL) and contains 200 kg of 90% enriched ^{136}Xe. The previous PandaX-II detector is a dark matter direct detection experiment.

1.3.5 Liquid scintillators

In this section are presented two large-scale detectors, first designed to measure the solar neutrino oscillations. By adding $\beta\beta$ isotopes to their large detection volume, they now both aim at searching for the $0\nu\beta\beta$ decay. The main drawbacks of these detectors are the poor energy resolution as well as the absence of event topology reconstruction. This is nevertheless compensated by the high exposure, as they both contain the highest quantities of $\beta\beta$ isotopes, allowing to reach high $T^{0\nu}_{1/2}$ limits. We also review two new liquid scintillator technologies.

KamLAND-ZEN for Kamioka Liquid Scintillator Antineutrino Detector - Zero Neutrino Double Beta Decay Search, is located in the underground neutrino detection facility in Japan. It uses the original design of KamLAND detector that precisely measured 2 cycles of neutrino oscillations. This detector searches for the $0\nu\beta\beta$ decay of the ^{136}Xe isotope, by installing a mini-balloon at the centre of KamLAND (Fig. 1.13). The chosen isotope, enriched at 91%, is dissolved in a liquid scintillator, and a purification method is well-established for both of them, allowing to reach low internal background levels. The first phase, the KamLAND-Zen 400 project, was already terminated and its latest limit for half life of $0\nu\beta\beta$ is $T^{0\nu}_{1/2} > 1.07 \times 10^{26}$ years at 90% CL [26]. This result confirmed the feasibility of such high-scale technology, and KamLAND-Zen 800 has started taking data in January 2019 with 745 kg of ^{136}Xe, planning a ~ 5 years data acquisition.

SNO+ is an experiment using the existing SNO detector located in SNOLAB (6000 m.w.e.) in Canada, by replacing the water volume with a liquid scintillator. This offers the possibility to search for the $0\nu\beta\beta$ decay by loading 800 kg of ^{130}Te isotope into 780 tons of scintillating solution. The huge quantity of isotope loaded into SNO+ gives a significant advantage over other $0\nu\beta\beta$ experiments. This technology aims at reaching a lower limit on the $0\nu\beta\beta$ half-life of 9×10^{25} years after 5 years.

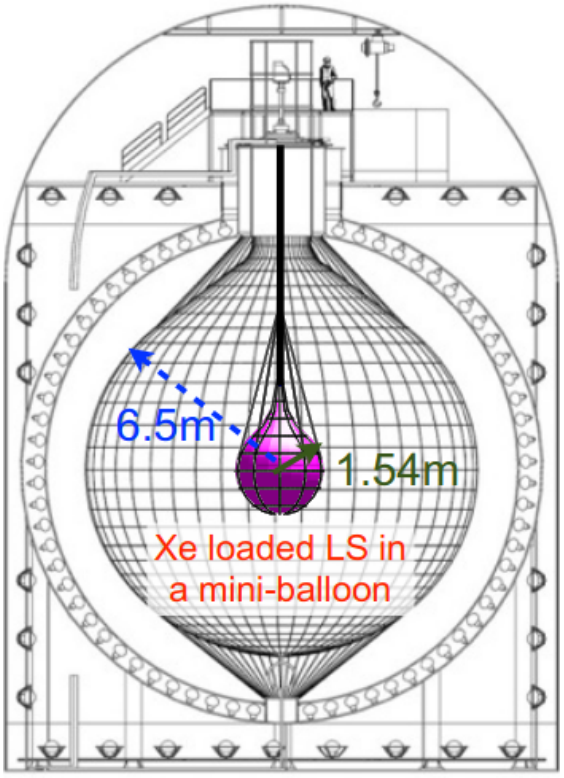

Figure 1.13: Sketch of the KamLAND-ZEN detector.

ZICOS is a new experiment using a liquid scintillator loaded with enriched zirconium. The goal is to use 865 kg of ^{96}Zr enriched at 50% to reach a sensitivity of $\sim 1 \times 10^{27}$ years. This sensitivity would be achieved by an efficient ^{208}Tl background reduction using the information of Cherenkov light.

CANDLES is a project searching for $0\nu\beta\beta$ with ^{48}Ca installed at the Kamioka underground laboratory. The chosen isotope has an advantage of the highest $Q_{\beta\beta}$ of 4.27 MeV. The 96 CaF2 scintillator detectors, for a total mass of 305 kg, are immersed in a liquid scintillator. Scintillation light from the CaF2 scintillators and from the liquid scintillator are measured by 62 photomultiplier tubes (see Fig. 1.14).

1.3.6 Tracking calorimeters

Tracking calorimeters technology, instead of using a *source-as-detector*, employ a passive source shaped as thin source foils of enriched $\beta\beta$ emitters. Sources are placed at the detector centre, surrounded by two trackers allowing for particle identification (between electrons, positrons, γ and α particles) and vertex reconstruction to improve the background rejection. The whole is sandwiched between calorimeters enabling individual particle energy reconstruction. This passive source tracking calorimeter technology provides topological information on angular emissions of the two electrons from $\beta\beta$ decay, making possible to distinguish between underlying mechanisms for $0\nu\beta\beta$ decay in case of a discovery.

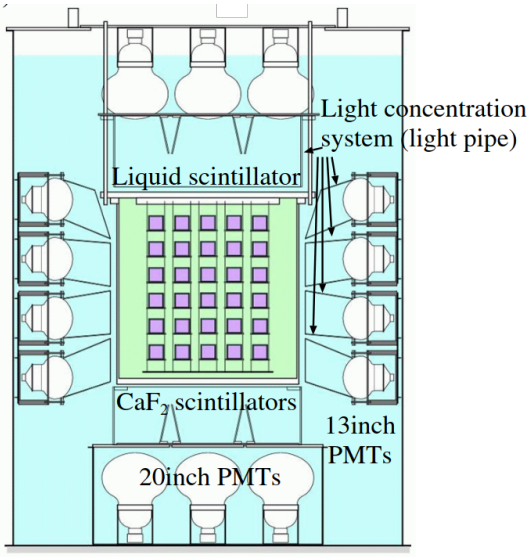

Figure 1.14: Sketch of the CANDLES detector.

NEMO for Neutrino Ettore Majorana Observatory was installed in LSM and has taken data from 2003 to 2011 with 7 different $\beta\beta$ isotopes. This detector has set limits on the $0\nu\beta\beta$ half-life of these 7 isotopes between 0.9×10^{19} and 1.1×10^{24} years.

SuperNEMO experiment is a next-generation of detector, inheriting the lineage of the NEMO experiments. It aims at searching for the $0\nu\beta\beta$ decay of several isotopes as ^{82}Se, ^{150}Nd and ^{96}Zr, with about 100 kg of enriched material. The detector will be composed of 20 modules of $\sim$ 5 kg of source each. Giving its low isotope mass, SuperNEMO might not be the first experiment to observe the searched decay, but would identify the underlying mechanism responsible for this decay, thanks to its tracking capabilities. The first module, aiming at demonstrate the scalability of such a technology, is on the commissioning phase, with 6.23 kg of enriched ^{82}Se.

1.3.7 Summary

All experiments presented above aim at searching for the $0\nu\beta\beta$ decay with specific features. Various approaches have been reviewed in this section, and a non-exhaustive list of experiment has been given. The results of the current generation of detectors will make it possible to determine which technologies are the best suited for the search for $0\nu\beta\beta$ decay.

1.4 Conclusion

This chapter presented the questions that are still open around the physics of the neutrino. This particle, discovered relatively late in the history of physics, could allow us to explore physics beyond the Standard Model, and to get closer

to a more global theory of physics. Notably, the observation of the $0\nu\beta\beta$ decay would prove that the neutrino is a Majorana particle, while demonstrating that the lepton number is not a symmetry of physics. Beyond the physics of the neutrino, such an observation would have great implications in many fields of physics, and this is why a multitude of experiments are looking for this disintegration. The SuperNEMO detector, on which I worked during my PhD, is one such experiment.

Chapter 2

The SuperNEMO demonstrator

> It doesn't matter how beautiful your theory is, it doesn't matter how smart you are. If it doesn't agree with experiment, it's wrong.
>
> Richard Feynman

The Neutrino Ettore Majorana Observatory (NEMO) is an international collaboration of scientists searching for the yet never-observed $0\nu\beta\beta$ decay. This collaboration began in 1989 with a first device based on an innovative technology coupling a charged particles tracking chamber and a calorimeter measuring their energies. Since then, 3 detectors based on the same technology were installed and collected data in the Modane Underground Laboratory (Laboratoire Souterrain de Modane in French, LSM in short), a subterranean laboratory located in the Fréjus road tunnel, below the Fréjus peak. In particular, the third generation of detector, the so-called NEMO-3 experiment, which had been operating from 2003 to January 2011, derived a lower limit on the half-life of $0\nu\beta\beta$ decays of enriched Molybdenum (^{100}Mo) of $T^{0\nu}_{1/2} > 1.1 \times 10^{24}$ years at the 90% Confidence Level, under the hypothesis of light Majorana neutrino exchange. Depending on the model adopted for calculating nuclear matrix elements, the limit for the effective Majorana neutrino mass lies in the range $\langle m_{\beta\beta} \rangle < [0.33 - 0.62]$ eV for this detector. Therefore, if existing, the $0\nu\beta\beta$ decay would remain an extremely rare event. The NEMO experiments have then been designed to be ultra-low background detectors, by reaching high radiopurity levels and efficiently removing background events thanks to the tracko-calo technology.

Based on a similar principle, the SuperNEMO detector stands as the successor of NEMO-3, and is expected to set a lower limit of $T^{0\nu}_{1/2} > 1 \times 10^{26}$ years with 100 kg of enriched Selenium (^{82}Se) in 5 years of data acquisition. In order to prove the NEMO technology is scalable to such considerable masses of isotope, while remaining an ultra-low background detector, the SuperNEMO demonstrator had been designed with a reduced mass of $\beta\beta$ isotope, being 6.23 kg of ^{82}Se. Installation has begun at LSM in 2015. Since then, sources have been installed, the tracker and calorimeter were assembled, and all calibration systems have been deployed.

I have been involved in the work that has been carried out since 2017 on the demonstrator, since I participated in several missions to Modane. During the first

year of my PhD, I passed all the security and first aid training required to become one of the people in charge of security on site. It was an honour to personally participate in the detector closure, the 22 November 2018 (Fig. 2.1). The demonstrator is currently in the commissioning phase and almost fully calibrated, pending the start of tracker calibration phase which will begin in the course of the year 2020.

Figure 2.1: Last picture of the SuperNEMO demonstrator before closing it, the 22 November 2018. The picture is taken from one side of the detector, facing the other side. We can distinguish on the right the front of one of the two calorimeter main walls, and on the left one of the two tracker chambers.

2.1 The SuperNEMO technology

The SuperNEMO demonstrator, in the manner of NEMO-3, combines tracking and calorimetry technologies to record the full event kinematics and measure the particle energies. It is designed to search for the $0\nu\beta\beta$ decay which, if observed, would reveal the Majorana nature of the neutrino particle, opening the door of physics beyond the Standard Model, with huge implications for physics research. The SuperNEMO demonstrator is 6 meters long, 3 meters tall and 2 meters large. It is the first of the 20 modules that will make up the final detector. This unique technology allows the experiment to characterise with a significant performance its own background, placing the detector in the ultra-low background category of experiments.

2.1.1 Detection principle

In Fig. 6.13 is drawn a simplified scheme of the SuperNEMO demonstrator. In order to ease the naming of the different areas of the detector, the collaboration

has decided to label each part as *French*, *Italian*, *tunnel* or *mountain* sides, given with respect to the orientation of the detector in the underground laboratory.

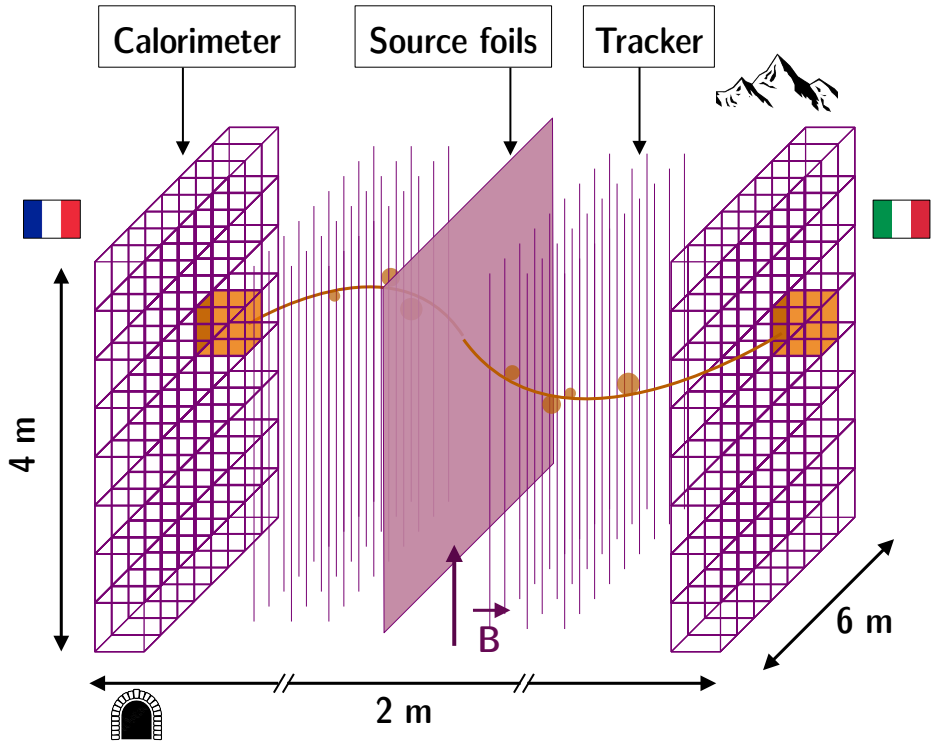

Figure 2.2: Scheme of an open view of the SuperNEMO demonstrator (not to scale). An example of emission from the source foils of two negatively charged particles is drawn. Each side of the tracker is labelled as French, Italian, tunnel or mountain side.

The $\beta\beta$ isotope is distributed within ultra thin foils, at the centre of the detector. Therefore, for the same detector size, the mass of isotopes studied with this technology is lower than for experiments using liquid scintillators or TPCs. But as the source is separated from the detection volume, various $\beta\beta$ isotopes can be studied as long as they can be set up in solid thin foils, making this technology very interesting for the search for the $0\nu\beta\beta$ decay.

An emission of two negatively charged particles[1] from the source is also schematised, exiting in opposite directions for this particular case. The design of SuperNEMO as successive layers of sub-detectors makes it possible to collect a variety of information on the emitted particle. When crossing the wire chamber, the charged particle ionises the gas, and the arrival time of the signals on the anode and copper rings allows the track reconstruction. The detector is surrounded by a copper coil, delivering a magnetic field inside the wire chamber. The few MeV particle trajectories are bent, allowing to discriminate electrons from positrons. Muons have too much energy for their trajectory to be bent by a magnetic field of this intensity. The α particles interact too quickly for their track to be curved,

[1]By convention, a negatively curved track has the curvature of an electron going from the foil to the scintillator main wall.

but can still be recognised precisely because of this short length (a few cells long). Therefore, the tracking technology makes it possible to discriminate electrons from positrons (with the trajectory curvature), to identify γ particles (corresponding to an energy deposit inside the calorimeter without any associated track), and to tag α particles (characterised by a short delayed track inside the wire chamber). Thus, although the SuperNEMO energy resolution and detection efficiency are modest compared to germanium or bolometer experiments, it is compensated by the powerful particle identification allowing to identify events coming from natural radioactive decays in dedicated channels. Particles end up in scintillator blocks, where the collection of deposited charge by a photomultiplier tube allows the incident particle energy measurement. Electric signals are sent to electronic boards where they are sampled and recorded for off-line analyses.

In addition to the search for the $0\nu\beta\beta$ decay, the SuperNEMO technology is suitable for the search for other processes like double beta decays to excited states of the daughter nucleus that can be studied in dedicated channels (two-electrons and one/two gamma particles). Thanks to the topological informations brought by the successive sub-detectors (two single electron energies and emission angle between them), if the $0\nu\beta\beta$ signal is observed, the SuperNEMO technology would also have the ability to discriminate between different hypothesised underlying mechanisms, allowing to investigate physics beyond the Standard Model.

In the following we describe in detail the successive layers of the SuperNEMO technology, from the $\beta\beta$ emitter source foils to the electronic boards where the signal is sampled.

2.1.2 The source foils

Choice of isotope

There are about 30 double beta emitters, some of which can be created in laboratory if an enrichment technique exists, for physics research purposes. The choice of the isotope is directed by several factors and experimental constraints. Although this choice is specific to each detector, some constraints are common to all $0\nu\beta\beta$ experiments.

- The energy transition $Q_{\beta\beta}$: a significant background coming from natural radioactivity is the 2.615 MeV-γ emitted after the Thallium-208 (^{208}Tl) β disintegration. Also, Bismuth-214 (^{214}Bi) isotope disintegrations have a high available energy with $Q_\beta = 3.27$ MeV. Therefore, a high $Q_{\beta\beta}$ would help to guaranty the experiment to be free from radioactive background.

- The phase space factor and the nuclear matrix elements: as described in Chapter 1, the $0\nu\beta\beta$ half-life depends on these two parameters. The higher they are, the more signal events are expected for a given data acquisition time. Unfortunately, the uncertainties that exist on nuclear matrix element calculations prevent from reaching a clear conclusion on the isotope choice.

- The $2\nu\beta\beta$ half-life: this process represents an unavoidable background for the search for $0\nu\beta\beta$. Then, the higher the half-life of this process, the less $2\nu\beta\beta$ events are expected.

- The natural abundance: the higher it is, the more we can produce substantial quantities of the enriched isotope.

- Ease of enrichment: although it is not a measurable quantity as previous requirements, known purification techniques must be applicable to the isotope considered to reach high quantities of $\beta\beta$ emitter.

In Tab. 2.1 are given these characteristics for some of the $\beta\beta$ emitters used for current $0\nu\beta\beta$ searches. ^{82}Se was chosen for SuperNEMO because of its high transition energy, and preferred to ^{100}Mo because of its higher $2\nu\beta\beta$ half-life (by a factor ~ 13). Its nuclear phase space factor and natural abundance are satisfying and its enrichment is feasible using classical technique (centrifugation).

Isotope	$Q_{\beta\beta}$ (MeV)	$G_{0\nu}$ (10^{-15} y^{-1})	$T^{2\nu}_{1/2}$ (y)	η (%)
^{48}Ca	4.273	24.81	6.37×10^{19}	0.187
^{76}Ge	2.039	2.363	1.926×10^{21}	7.8
^{82}Se	2.995	10.16	9.6×10^{19}	9.2
^{96}Zr	3.350	20.58	2.35×10^{19}	2.8
^{100}Mo	3.035	15.92	6.93×10^{18}	9.6
^{116}Cd	2.809	16.70	2.8×10^{19}	7.6
^{130}Te	2.530	14.22	6.9×10^{20}	34.5
^{136}Xe	2.458	14.58	2.165×10^{21}	8.9
^{150}Nd	3.367	63.03	9.11×10^{18}	5.6

Table 2.1: $\beta\beta$ emitters used in current $0\nu\beta\beta$ experiments. $Q_{\beta\beta}$, phase space factors, $2\nu\beta\beta$ half-lives and natural abundances are given.

Source foils production

The ^{82}Se isotope is enriched and purified by the ITEP laboratory in Russia. Two purification techniques have been employed, given in Tab. 2.2. Approximate isotope quantities are given for each technique. About 6.5 kg of ^{82}Se powder have been produced and purified. The ^{82}Se is then ground to a fine powder (50 μm grains) and mixed with a radio-pure glue.

Enrichment technique	^{82}Se quantity (kg)	Number of foils
Double distillation	$\sim$ 2+1.5	$\sim$ 11+8
Reverse chromatography	$\sim$ 3	$\sim$ 15

Table 2.2: Different purification techniques and corresponding approximate quantities of ^{82}Se isotope produced. Two batches of ^{82}Se have been produced through double distillation.

To shape the ^{82}Se powder into the final SuperNEMO source foils, two distinct designs have been tested, one by ITEP and the other by the LAPP laboratory in Annecy (Fig. 2.3).

- ITEP implemented the same technique as for NEMO-3 source foils, by smearing the ^{82}Se+glue mixture between two 12 μm thick Mylar backing films, creating 3 meters long foils. The Mylar is perforated by irradiation, allowing the mixture to dry and better adhere to the film. However this technique could contaminate the source, which encouraged the development of an alternative technique.

- The LAPP team split up the foils in several pads: two Mylar sheets are heat welded together to host the several pads.

The principal interest in designing the sources that thin is to maximise the chances of the electrons produced inside the source to escape it, to be detected by the successive sub-layers. Moreover, thinner sources reduce electron energy losses inside the source, and thus their fluctuations, which contributes to the improvement of the detector global energy resolution. In addition, the collaboration made this design choice in order to leave the possibility of easy isotope change in the future. Finally, 6.23 kg of ^{82}Se have been distributed into 34 source foils each of them measuring 135.5 $\times$ 2700 mm. The thickness of the produced sources were precisely measured at 300 μm by the collaboration.

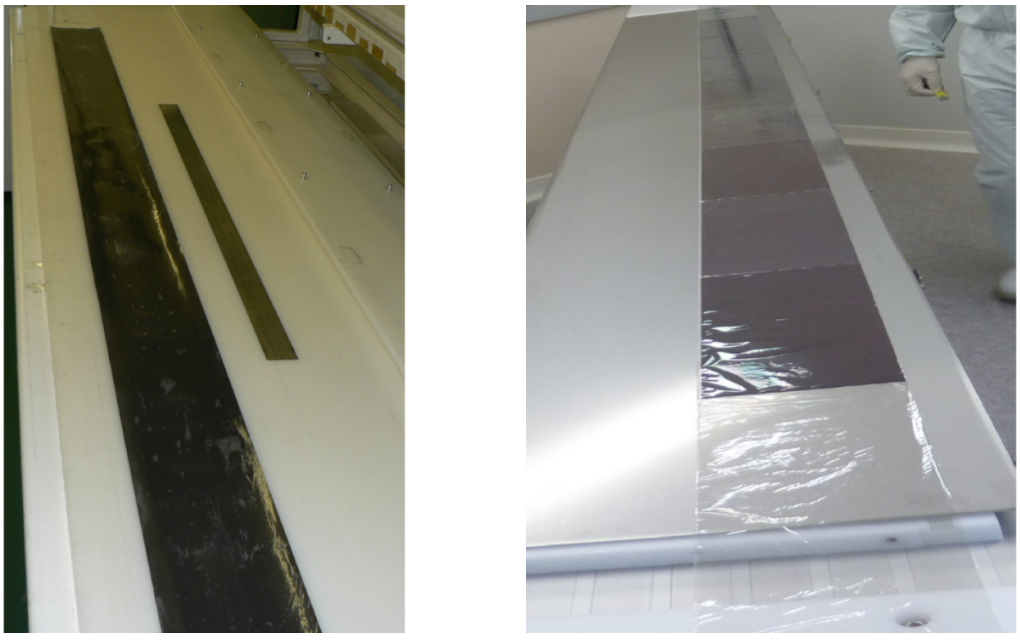

(a) ITEP style foils. (b) LAPP style foils.

Figure 2.3: Two designs of source foils, ITEP (left) and LAPP (right).

Source foils installation

The 24 September 2018, each strip was fasten to a frame measuring 4.857 meters large and 2.7 meters high. The original plan was to place the ITEP sources next to each other and to do the same for the LAPP sources. Unfortunately, some of the sources had to be relocated because of source shape issues (in particular, some sources were in contact with the Bismuth calibration sources described in Sec. 2.1.7). The final position decided for the source foils are pictured in Fig. 2.4, where we can see the alternation of ITEP and LAPP sources. ITEP sources appear slightly curved on the picture, what probably happened during the glue drying step. We can also distinguish the presence of the vertical wires of the tracker before the sources, discussed in next sub-section. Each source curvature have been precisely measured using a laser tracking system, for a future precise description of the sources geometry and its integration in the simulation software. I was part of the team that carried out the first curvature measurements right after sources integration in Modane.

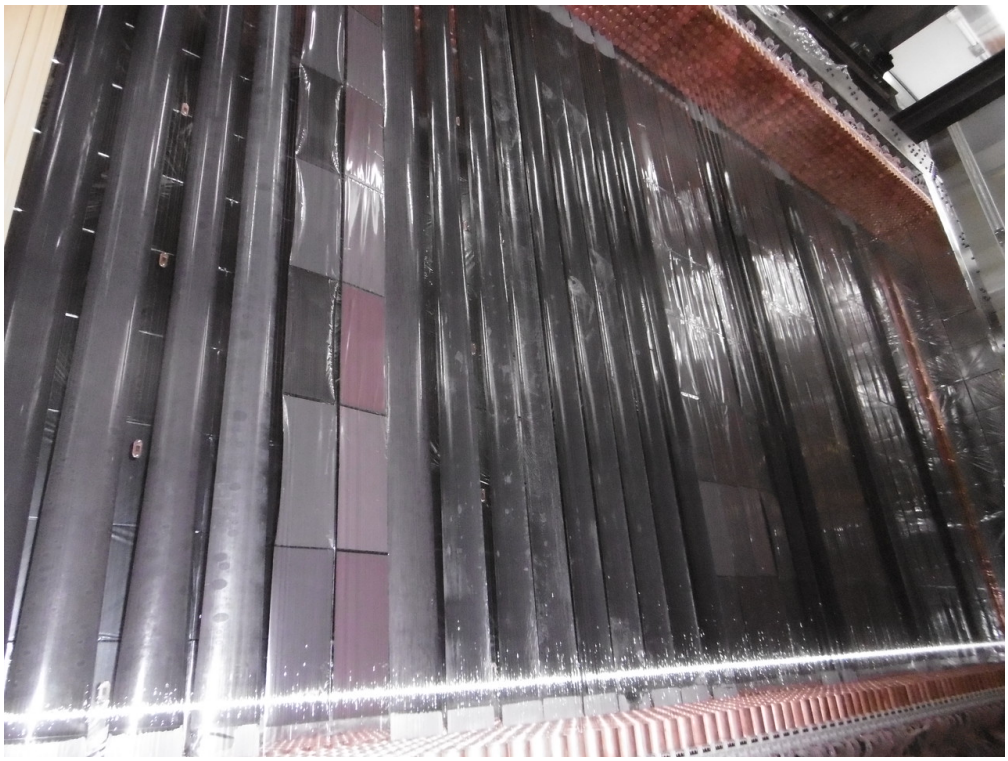

Figure 2.4: Source foils final position. The ITEP foils (one-piece long foils) and LAPP foils (divided in pads) are easily distinguishable.

2.1.3 The tracker

The tracker is a detector aiming at measuring the charged particle three-dimensional trajectories, through their electromagnetic interaction with the gas filling the tracking chamber. This sub-detector allows for efficient background rejection through the identification of particles, by making sure the event is

composed of exactly two electrons. The reconstruction of the vertices on the source makes it possible to identify highly contaminated areas, the so-called *hot spots* of the experiment, and to reject them with appropriate cut-offs. The SuperNEMO tracker is divided into two halves, one on each side of the source frame, to measure particles exiting from it in all possible directions. These are two drift chambers filled with a gas mixture and operating in Geiger mode.

Geiger counters

In Fig. 2.5 is schematised the basic operation principle of a Geiger cell. When a particle goes through the gas in which the cell is immersed, it ionises it all along its path, creating positive charges on one hand (heavy ions) and negative on the other hand (electrons). A high electric potential is applied, allowing the freed electrons to drift towards the anodic wire, and the ions towards the field wire. When ionisation electrons come close to the anodic wire, the electric field becomes so high that the accelerated electrons can themselves ionise the gas, creating electronic avalanches until the wire is reached. Other avalanches are created all along the anode wire by de-excitation and recombination of UV photons. The Geiger mode is reached when the avalanches created by the electrons are saturated: increasing the voltage does not increase the collected charge. This is the so-called *Geiger plateau*, which provides a very high detection efficiency ($> 99\%$). The longitudinal position is obtained with the time needed for these avalanches to reach both ends of the wire.

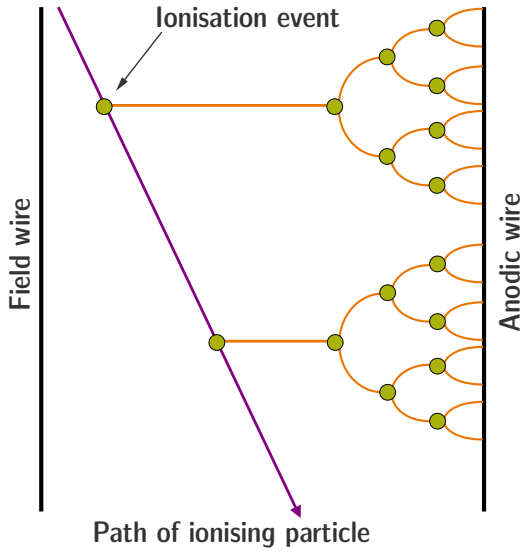

Figure 2.5: The principle of a Geiger cell illustrated with one central anodic wire and one field wire. Electrons (orange) drift to the anodic wire.

SuperNEMO cells

A minimal amount of material is required inside the tracker chambers, for the particles to freely cross it with limited energy losses and reduced multiple

scatterings. However, a minimal distance between the tracker wires is required in order to efficiently collect the charges coming from gas ionisation. Taking into account the tracker spatial resolution needs and the constraints on gas mixture composition, the decision was made to design Geiger cells as in Fig. 2.6, with one central anodic wire (stainless steel, 40μm in diameter) and 12 surrounding field wires (stainless steel, 50μm in diameter). Each cell has a diameter of 4.4 cm. Two copper rings, of 4 cm diameter and 4 cm long, are placed on both ends of each cell, allowing the cessation of the avalanches. In total, the tracker chamber is composed of 2034 Geiger cells of 3 m long, divided in 9×113 layers, parallel to the source strips. The minimal distance between the ionising particle and the anode, called *radial distance*, is given by the anodic signal. The interaction point along the cell axis, called *longitudinal position*, is obtained with the time needed for the avalanches to reach both ends of the cell. In the SuperNEMO operating conditions, a few micro seconds elapse between the creation of the first ionisation electron and the creation of the first avalanche, after which the avalanche is expected to spread through a cell in about 40 μs [27]. The final reconstructed times at which a charge particle passes nearby successive tracker cells are defined using the particle arrival time in the calorimeter as a reference.

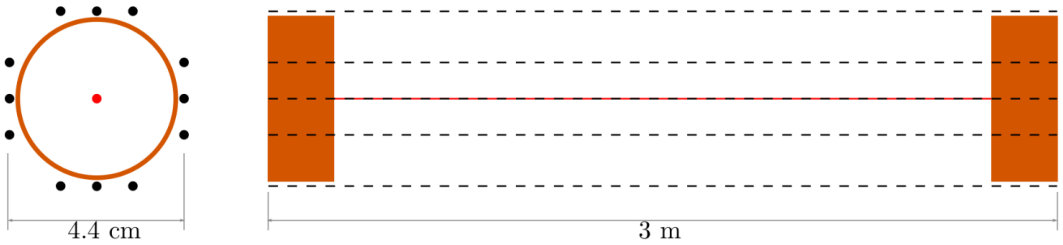

Figure 2.6: Sketch of a SuperNEMO Geiger cell, in transverse view (left) and side view (right, the sketch is rotated of 90° as the Geiger cells are vertical in the SuperNEMO demonstrator). The anodic central wire is represented at the centre in red. Field wires, in black, surround it to form 4.4 cm large and 3 m long Geiger cells. On the right the copped rings are also represented by orange stripes at both ends of the wires.

As we said, the behaviour of a Geiger cell depends on the voltage applied. For the SuperNEMO cells, the Geiger plateau is located around 1800 V and is $\sim$ 300 V-wide [28]. However, the exact voltage to be applied to each cell depends on their individual properties, and will have to be determined and set up after the tracker commissioning phase.

Gas mixture

The tracker gas composition is decisive for the wire chamber operation. For the SuperNEMO demonstrator, it is composed as follows:

- Helium is the main component, which is ionised by incident radiations. As an inert gas, it does not react with the detector sensitive parts.

- Argon (1%) enhances the propagation of avalanches along the anode wires thanks to its lower ionisation energy.
- Ethanol (4%) is used as a quenching agent, stopping the successive discharges.

This gas composition guarantees a medium with a low Z number in order to minimise the energy losses and particle multiple scatterings.

Tracker installation

Each of the tracker halves is itself divided into two C-sections (named in this way according to the C-shape of each section) assembled at UCL's Mullard Space Science Laboratory. They were delivered individually and integrated in Modane to form the two tracker chambers. In Fig. 2.7 is given a picture of the tracker after its integration to the detector. The bottom copper rings are noticeable and indicate the presence of the Geiger cells whose wires are too thin to be visible on the picture. After installation, some meticulous work were achieved to remove few wires damaged during transport.

Figure 2.7: Inside view of the tracker (with me standing in the foreground), before detector closing, on the day of the wire check, looking for possible broken wires at the base of the copper rings.

Gas sealing

A constant over-pressure is kept inside the tracker, which is imperative to maintain the right gas mixture, without infiltration of outside air. Indeed, if atmospheric

air enters the gas detector, its properties can be disturbed. For example, the quenching may become too strong and the signal can not be properly transmitted through the gas. Therefore, once the tracker was integrated into the detector, a huge effort was achieved by the entire collaboration to seal it. In the case of SuperNEMO, it is also necessary that the detector is sealed to prevent helium from escaping and penetrating into the vacuum tubes of the PMs. As a PhD student in the collaboration, I had the opportunity to participate in much of this work. The different techniques used to seal the detector are discussed in detail in Sec. 2.1.10.

The tracking part of the demonstrator enters the commissioning phase in November 2020. Among other, each cell will have to be characterised, and is expected to have a 0.7 mm radial and 1 cm vertical spatial resolutions.

2.1.4 The calorimeter

The $2\nu\beta\beta$ is an irreducible background for the $0\nu\beta\beta$ decay. Both of them have the same signature in the tracker, with the emission of two electrons from the source foils. The only way for the SuperNEMO technology to distinguish them is to measure the two electrons individual energies. In order to achieve the target sensitivity, the calorimeter R&D program for SuperNEMO has covered three main areas of study: geometry, energy resolution and radiopurity. The two firsts are discussed in this sub-section, while the last one is detailed in Sec. 2.2.1 and 2.2.2.

- As shown in Fig. 6.13, the SuperNEMO calorimeter is segmented to measure the individual energies. A compromise has been reached between a high granularity and the minimisation of dead zones. Also, mainly for financial considerations, the number of electronic channels had to remain reasonable.

- The lower the energy resolution, the more $2\nu\beta\beta$ and $0\nu\beta\beta$ energy spectra can be discriminated. In order to achieve the target sensitivity, the energy resolution of the SuperNEMO calorimeter is required to be around 8% FWHM at 1 MeV for electrons. The requirement for the time resolution is set to be $\sigma_t = 400$ ps at 1 MeV for external background rejection purposes (to discriminate between two-electron internal events from those that originate outside of the detector and then cross its active volume to imitate $0\nu\beta\beta$ events).

Each individual optical module (OM) is made of the association between two sub-detectors, a scintillator and a photomultiplier (PM).

Scintillators

The material chosen for the SuperNEMO scintillators is an organic, polystyrene-based material, doped with 0.05% of POPOP (1.4-bis(5-phenyloxazol-2-yl) benzene), a scintillator used as a wavelength shifter, and 1.5% of p-Terphenyl (p-TP), a secondary wavelength shifter. This composition fulfils the requirements of high light yield, low electron back-scattering (because of its low Z), high radiopurity, good timing and a relatively low cost. Four main geometries have been considered for the scintillator blocs during the R&D phase, all presented in Fig. 2.8.

What all these forms have in common is that they can be stacked to form a compact active detection volume, thanks to their entrance face shapes. Tapered geometries have been considered in order to reduce the amount of material. The hexagonal shape was designed to get closer to a cylindrical shape and thus to limit edge effects on light propagation inside the scintillator. However, Monte-Carlo simulations and measurements were carried out, showing the best energy resolutions are reached for hexagonal and cuboid 256×256 mm^2 shapes. As these two geometries give similar energy resolution results, the cuboid block has been chosen for the final design to ease the manufacturing. A two dimensional drawing, as well as a picture of a cuboid scintillator is given in Fig. 2.9. The scintillator block is hollowed out to receive the photomultiplier bulb. The SuperNEMO scintillator blocks are designed thicker compared to that of NEMO-3 to enhance the γ detection and thus improve the background rejection. In order to increase the collection light efficiency, each scintillator block is wrapped in radio-pure Teflon (on its sides) and aluminised Mylar (on its sides and front face). The latter also protects the scintillators against the UV photons coming from the tracker chamber and other surrounding optical modules.

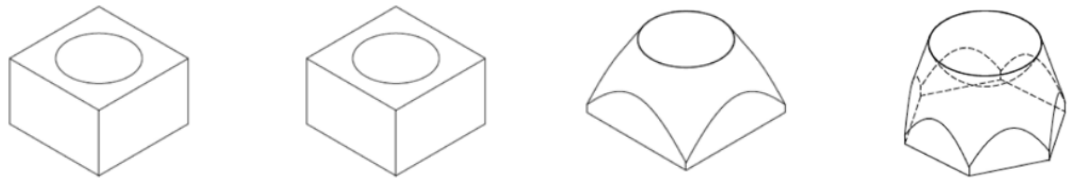

(a) Cuboid shape 256×256 mm^2. (b) Cuboid shape 308×308 mm^2. (c) Tapered shape 308×308 mm^2. (d) Hexagonal shape ø 276 mm.

Figure 2.8: Scintillator shapes considered for the SuperNEMO demonstrator. The first one had been selected.

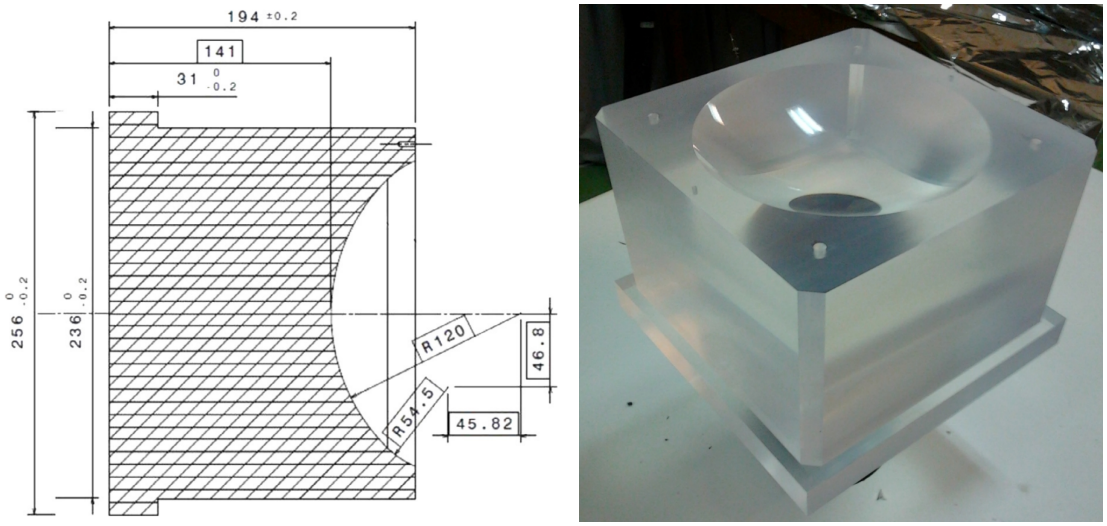

Figure 2.9: Geometry of a polystyrene cuboid scintillator block designed for the SuperNEMO demonstrator. The polystyrene is hollowed out to receive the photomultiplier bulb.

The incoming particles (electrons, positrons or photons) enter the plastic scintillator and interact by ionisation. The scintillator thus emits scintillation photons proportionally to the deposited energy, propagating through the scintillating medium. Wave-length shifters ensure the light is not re-absorbed by the scintillator material. Some of the scintillation photons are then collected by the photomultiplier photocathode.

Photomultipliers

The SuperNEMO calorimeter requires a PM with a high quantum efficiency, a good photoelectron collection efficiency, a linear gain with energy, a high radiopurity, a good time resolution and low dark currents. The PM used for the NEMO-3 experiment were mainly Hamamatsu 5 inch types. For the SuperNEMO demonstrator, 8 inches PMs (R5912-MOD Hamamatsu) were chosen in order to match de designed scintillators. They also allow to reduce the number of electronic channels, as well as to increase the photo-detection surface compared with its predecessor, to improve the energy measurement.

When reaching the photocathode, some of the scintillation photons are absorbed and photoelectrons are emitted through the photoelectric effect (Fig. 2.10). These electrons drift to the first dynode under the influence of a high electric potential difference. Electrons ionise this dynode when reaching it, amplifying the number of electrons which will in turn drift into the next dynode. This drift/ionisation cascade amplifies the initial amount of charge collected by the last dynode, creating a measurable electric current. The gain reached by 8 inches SuperNEMO PMs is 10^6.

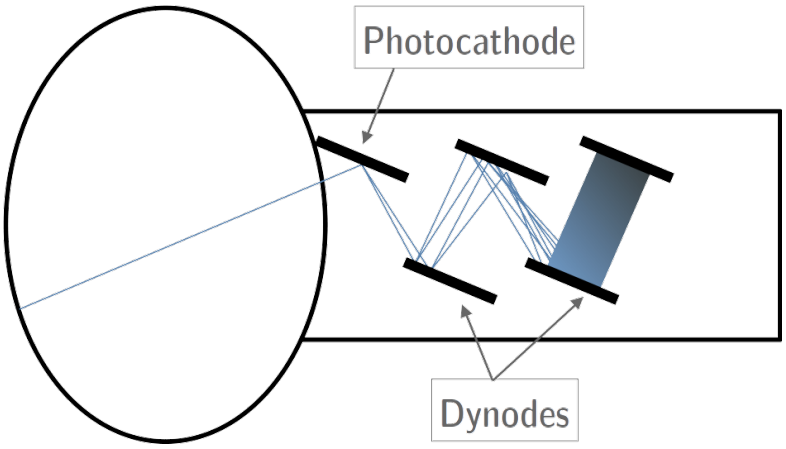

Figure 2.10: Basic operation principle of a photomultiplier. A scintillation photon enters the glass bulb of the PM and reaches the photocathode. The photoelectrons created through photoelectric effect are then multiplied by several dynodes under the influence of a high electric field.

The quantum efficiency of the chosen photomultipliers were optimised for 400 nm wave-lengths (that of the photons arriving on the photocathode) and is equal to 35% (compared to the 25% for NEMO-3). The photoelectrons collection

efficiency and linearity were also improved, increasing the number of photoelectrons to $\sim$ 1000 for 1 MeV electrons in order to reach the 8% energy resolution at 1 MeV.

Optical modules and mechanical design

Scintillators and photomultipliers are assembled together by the CENBG team (Bordeaux) to constitute so-called *optical modules* (Fig. 2.11). They are joined together using RTV615 glue. A surface polishing and an optical gel with a refractive index comprised between the indices of the PM glass and the scintillator also helps the optical coupling. Each optical module is protected by a magnetic shielding, whose usefulness is detailed in Sec. 2.1.6. Groups of 8 optical modules are pre-assembled for easy transport. Finally, the calorimeter was assembled in its entirety at LSM during the summer 2016 (Fig. 2.12).

Figure 2.11: A scintillator coupled with a PM. The shiny wrapping around the scintillator is the aluminised Mylar.

The calorimeter of SuperNEMO is divided into three distinct sections.

- Two main calorimeter walls (one French side and one Italian side), parallel to the source foils, one on each side of the detector. Each wall is composed of 13×20 blocks, for a total of 520 optical modules. The first and last optical module rows are built with 5 inches PMs recovered from NEMO-3, while others are 8 inches. NEMO-3 PMs have a worse resolution than 8 inches but they will detect almost no electrons as these rows are mainly screened by the cathode rings in front of the scintillators. However, they insure a complete coverage for the detection of γ particles.

- Gamma-Veto optical modules are located at the top and bottom of the demonstrator: 2 columns of 16 on each side of the source, for a total of 64. They are only used as a veto system against γ's.

(a) Back view of one calorimeter main wall.

(b) Front view of one calorimeter main wall.

Figure 2.12: Installation at LSM of one of the two main walls of the SuperNEMO calorimeter (summer 2016).

- X-walls are located on each detector side: 2 columns of 16 are located on the mountain side, same on the tunnel side, for a total of 128 optical modules. They are directly exposed to the tracker volume.

The optical modules constituting the X-walls and Gamma-Vetos are directly fixed on the tracker frame. As they are composed of 5 inches PMs, their energy resolution is more modest than the rest of the calorimeter (12% FWHM at 1 MeV for the X-wall blocks and 15% FWHM at 1 MeV for the veto blocks). Nevertheless, they ensure a 4π calorimetric coverage for γ particles.

The commissioning of the SuperNEMO calorimeter started in 2018 and is almost fully achieved (a scientific paper is currently being prepared). During my PhD, I actively participated in this crucial phase for the detector development.

2.1.5 Interaction of particles in the SuperNEMO scintillators

Understanding how particles interact in the SuperNEMO scintillators is essential. The calorimeter part of the demonstrator mainly aims to detect electrons and photons. In the following we review how these two particles interact inside the polystyrene scintillators.

Interaction of electrons

Electrons interact with matter through one of two processes: elastic scattering on a nucleus, or inelastic scattering on an atomic electron. Inelastic scatterings are dominant for polystyrene scintillators and occur through two different forms: coherent scattering with the electron cloud, and radiative energy losses (the so-called bremsstrahlung effect). In Fig. 2.13a is displayed the stopping power of electrons in polystyrene for these two processes. Electrons detected in the SuperNEMO calorimeter should deposit a minimal energy of 50 keV (the acquisition low energy threshold) and a maximal energy of few MeV (depending on the $2\nu\beta\beta$ isotope). In this energy range, collisions with the electron cloud are preponderant compared with radiative energy losses. In Fig. 2.13b, we give informations about the mean free path of an electron in polystyrene. In particular, we observe that an electron of 1 MeV penetrates, on average, several millimetres into a polystyrene scintillator.

Interaction of photons

Photons travelling in matter can interact with the electronic cloud, through three main processes, whose contributions are presented in fig. 2.14a, depending on their energies. Low-energy photons mainly interact with the electron cloud, either through photoelectric effect (γ radiation is fully absorbed by an electron of the cloud), or through coherent (so-called Rayleigh) scattering. But the dominant effect, for energies between 10 keV and 10 MeV, is the Compton inelastic scattering of a γ with an atomic electron. In Fig. 2.14b, we display the mean attenuation

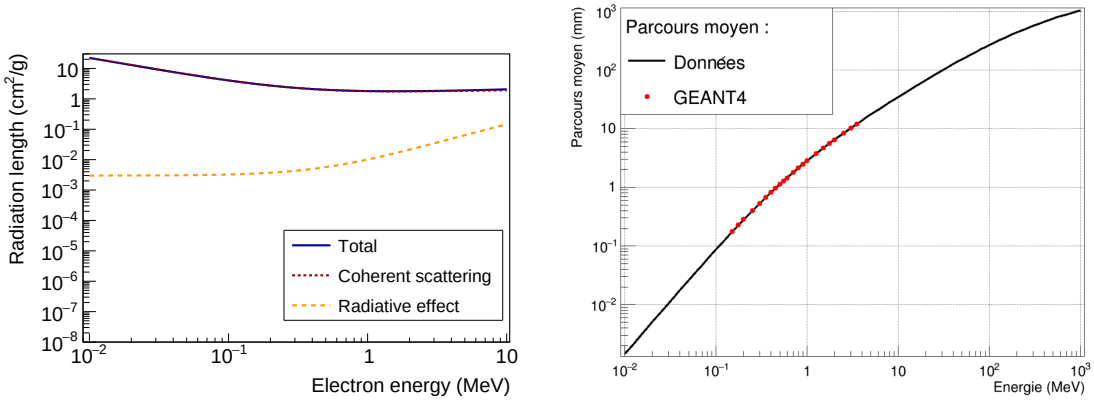

(a) (b)

Figure 2.13: Stopping power (a) and mean free path (b) for electrons in polystyrene. (a) Energy losses through radiative effect (orange dashed line) and coherent scattering (red dashed line), which is the dominant process for the considered energy range [29]. (b) At 1 MeV, the mean free path of an electron is about 3 mm. Adapted from [30].

length of a γ radiation in polystyrene scintillators, with energy. Thus, most of 1 MeV γ radiations will interact around 10 cm inside the scintillating material.

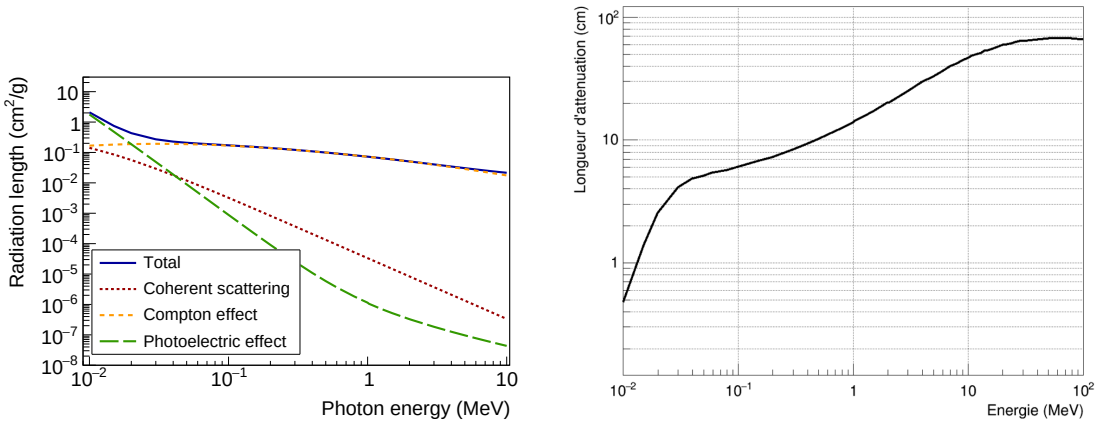

(a) (b)

Figure 2.14: Linear attenuation coefficient (a) and attenuation length (b) for γ radiations in a plastic scintillator made of polystyrene. (a) In the considered energy range of 10 keV − 10 MeV, γ radiations interact with matter mainly through Compton diffusion [31]. (b) The attenuation length of a γ radiation is about 10 cm at 1 MeV. Adapted from [30].

At the considered energy range (10 keV − 10 MeV), the interaction of photons with matter is dominated by Compton effect, while the electrons interact mainly through coherent scattering. The SuperNEMO scintillators are designed to detect such particles. Photons have a high probability to interact inside the volume of the scintillator, while electrons are stopped in the first few millimetres.

2.1.6 The magnetic coil and the shieldings

After a neutron capture outside the detector, high energy gammas can be created and can cross the detector volume. Electron/positron pair creation can then occur in the source, the two emitted particles sharing the energy of the initial photon. If an electron/positron discrimination is impossible, this category of event can be harmful for the search for the $0\nu\beta\beta$ decay. For that reason, in the manner of NEMO-3, the SuperNEMO demonstrator will be equipped with a copper coil that will deliver a vertical (parallel to the wires) magnetic field inside the tracker chamber, in order to bend the charged particle trajectories.

The SuperNEMO magnetic field

A three-dimensional representation of the SuperNEMO demonstrator is given in Fig. 2.15 with the coil circled in red. A study led by the collaboration allowed to determine that the optimal intensity for the magnetic field would be 25 Gauss, allowing to bend the few MeV particle trajectories, thus providing a useful discrimination between electrons and positrons.

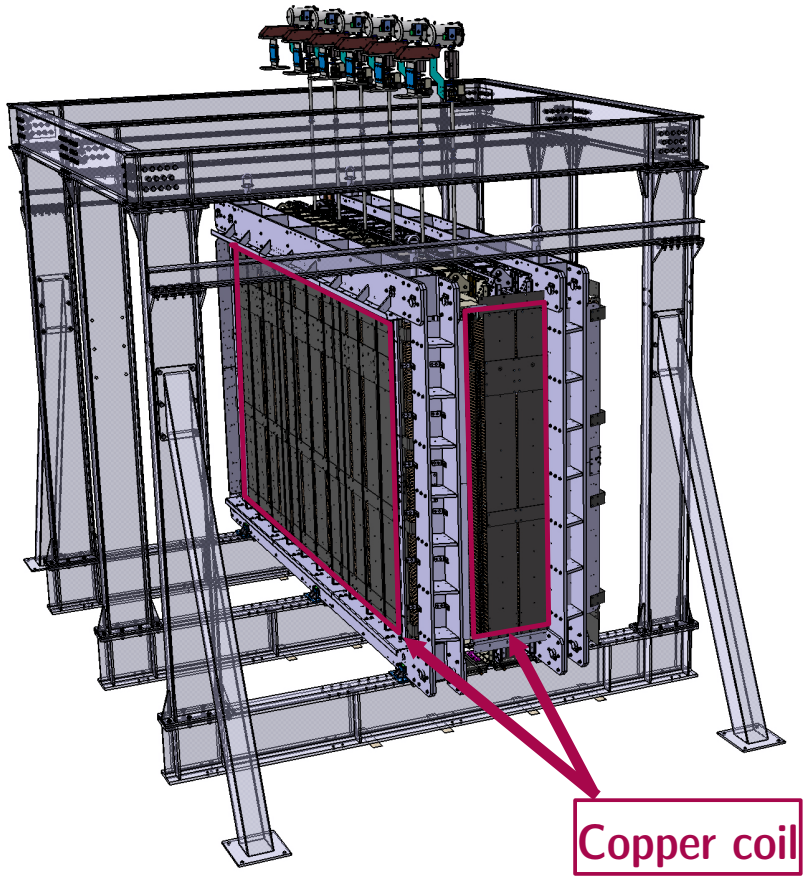

Figure 2.15: 3D representation of the SuperNEMO demonstrator, without the external iron shielding. The copper coil is circled in red.

The copper coil is constituted of copper rods recycled from NEMO-3 and reshaped by the mechanics team at LAL to surround the demonstrator (Fig. 2.16).

The coil is made of 200 turns with 16 mm steps, which makes it possible to generate the desired magnetic field while limiting the amount of heat produced. The overall dimensions are $6097 \times 2198 \times 3483$ mm^3 and are supported by iron plates, for a total weight of 9 tons. The copper coil was planned to be installed by March 2020 but was delayed due to the world health situation.

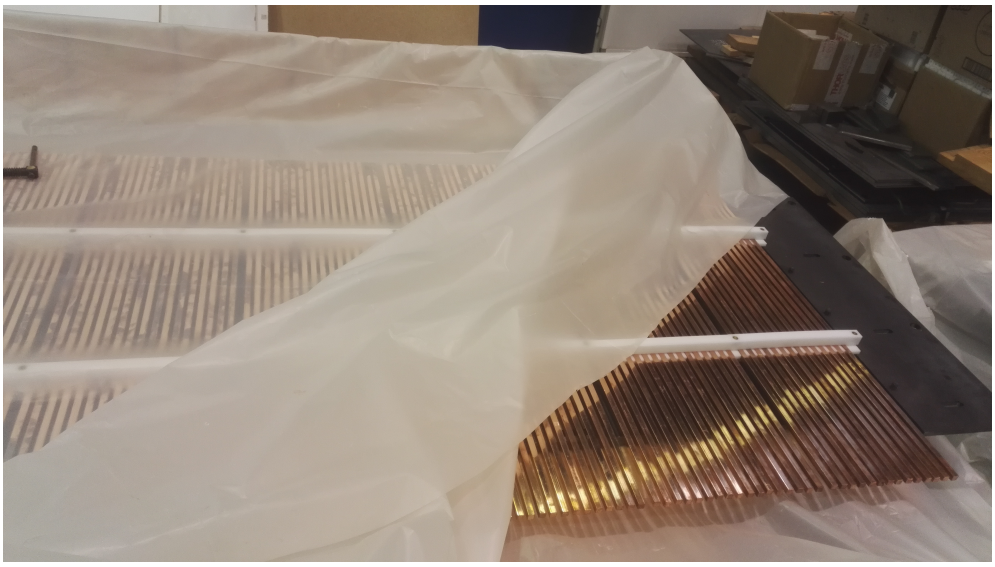

Figure 2.16: One of the coil panel, recycled from NEMO-3.

Magnetic shieldings

Unfortunately, the PMs are highly sensitive to the presence of a magnetic field inside the detector and their performances could be greatly impacted [32, 33]. Indeed, even a magnetic field as low as 1 Gauss can prevent the low energy photoelectrons from reaching the first dynode and thus impact the PM energy resolution. Therefore, 3 mm thick pure iron shieldings have been designed to surround the optical modules and protect them from the magnetic field (Fig. 2.17). The magnetic shieldings are separated by 10 mm acrylic spacers (PMMA). As done for NEMO-3, better shieldings would have been achieved with mu-metal, but this material is much more expensive and unfortunately less radio-pure. Some of these mu-metal shields have however been recovered to protect the few 5-inch PMs from X-wall and Gamma-Vetos which contribute less to the total radioactive isotope budget.

2.1.7 Calibration strategy

The SuperNEMO demonstrator is designed to have a long exposure time. In this context, calibration systems are necessary to control regularly and calibrate the response of the detector.

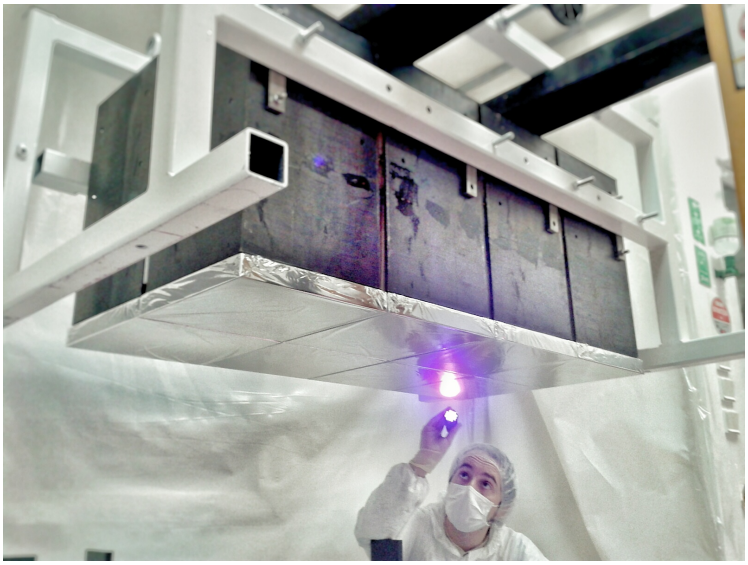

Figure 2.17: A block of 8 optical modules grouped together for installation at LSM. The magnetic shields are the black boxes surrounding the optical modules.

Source deployment system

The ^{207}Bi isotope decays almost exclusively through electron capture to excited states of ^{207}Pb. The decay is followed by ^{207}Pb de-excitation with γ-ray emission (the decay scheme is given in Fig. 2.18). The γ-ray can convert in K,L or M electrons with a given probability through the internal conversion process, which is described in detail in Chapter 4. The three corresponding electron energies are 976 keV (7.1% probability), 1050 keV (1.8% probability) and 1060 keV (0.4% probability).

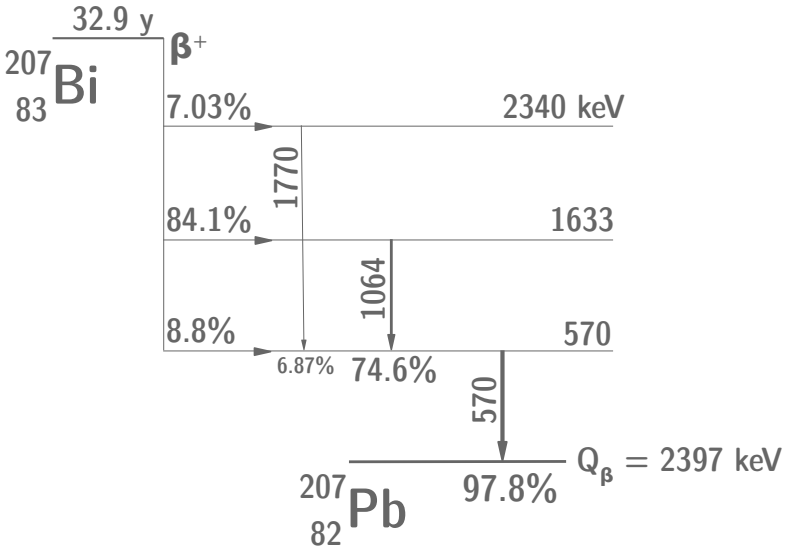

Figure 2.18: Simplified decay scheme of the ^{207}Bi isotope.

^{207}Bi sources are used for SuperNEMO absolute energy calibrations: the three

different electron energy peaks can be measured helping to follow and thus correct the response of the calorimeter modules with time. In total 42 sources (7 columns and 6 rows) of around 130 Bq are integrated to the so-called *deployment system*, which is in charge of the automatic deployment of the calibration sources between the source foils (Fig. 2.19). To do so, the Bismuth sources are attached at seven fixed points of six different stainless steal wires. Each wire is wrapped around a wheel on top of the detector which may be rotated by a stepper motor, making it possible to introduce the sources into the detector source frame. Daily runs are being considered to monitor the optical module gains with the conversion electrons.

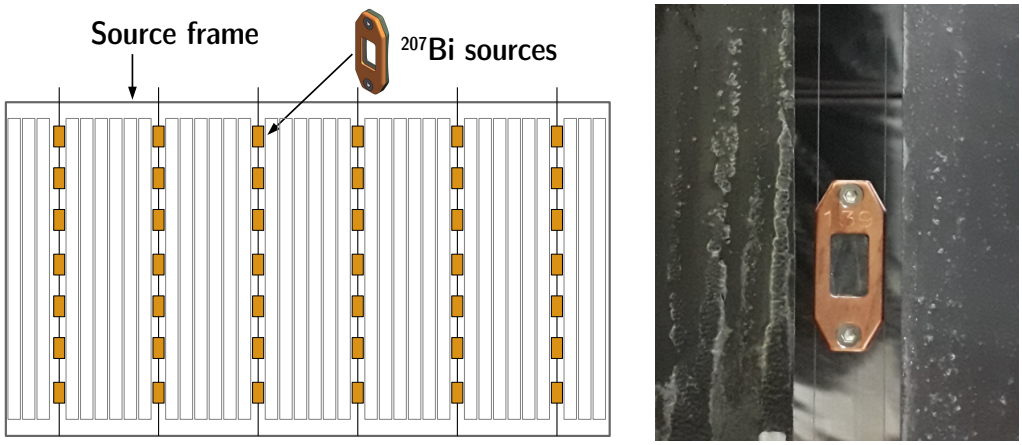

Figure 2.19: ^{214}Bi calibration sources in the automatised deployment system. Sketch of the sources deployed (left) and picture of one of the sources, between two ITEP source foils (right).

Light Injection System

The so-called *Light Injection* (LI) System will monitor the stability of the calorimeter response in energy during the data acquisition time ($\sim$ 2.5 years). A scheme of the complete LI calibration system is given in Fig. 2.20. Twenty Light Emitting Diodes (LED) at 385 nm will inject light in each scintillator block via optical fibers. A set of reference optical modules, receiving light from both LEDs and ^{241}Am sources, monitors the stability of the LEDs. This system is fully installed and entered in the commissioning phase in 2019. I participated in the analysis of the first LIS commissioning data taken discussed in Chapter 5.

2.1.8 Detector cabling

During the R&D program, special attention has been paid to the total number of electronic channels needed for the demonstrator. Indeed, this number must remain reasonable in order to control the total cost of the experiment, but must be high enough so that the granularity of the detector is sufficient to search for the $0\nu\beta\beta$ decay. Indeed, a good background events rejection where two electrons and a gamma particle are emitted can be ensured if they are detected in different optical modules.

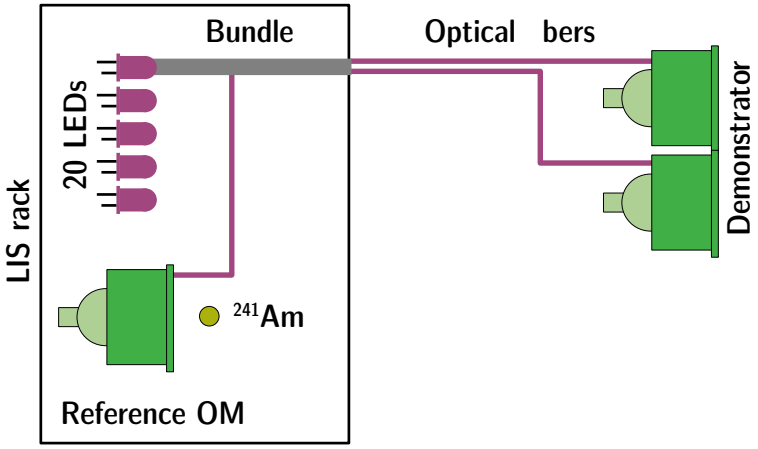

Figure 2.20: A scheme of the Light Injection (LI) calibration system. More than 1300 fibers, distributed in 20 bundles, carry the light from 20 LEDs to each scintillator block of the demonstrator. Reference OMs coupled with ^{241}Am sources monitor the LED light.

Ultimately the detector will be enclosed in an anti-radon tent, which is described in Sec. 2.2.4. In order to ensure that this external envelope is leak-tight, a patch panel (PP) has been designed to allow cables to pass the tent, from the inside to the outside. Cables coming from the detector, called *internal cables*, are connected to a specific location on the patch panel. So-called *external cables* are connected on the other side and allow the signal transmission to electronics.

Calorimeter cabling

The basic operation principle of a SuperNEMO photomultiplier has been discussed in Sec. 2.1.4. For this sub-detector to amplify the signal a potential difference is applied between its dynodes. To do so, a high voltage (HV) must be provided to the PM. Therefore, each PM divider is connected to a so-called *high voltage* cable. The voltage applied depends on the individual optical module characteristics and is about $\sim$ 1500 V for the 8 inches and $\sim$ 1100 V for the 5 inches. After the electrons have reached the last dynode, the charge is transported by *signal cables* to the electronics. Finally, each PM divider is connected to two cables, one for the high voltage and one for the signal. A back view of one of the fully cabled main calorimeter wall is given in Fig. 2.21.

A global sketch of the calorimeter cabling is given in Fig. 2.22, picturing all internal, external, high voltage and signal cables. External HV cables are grouped in 26 bundles, and each HV channel corresponds to a given pin on the bundle connector. External signal cables are independently routed from patch panel to electronics, as it is the case for internal HV and signal cables.

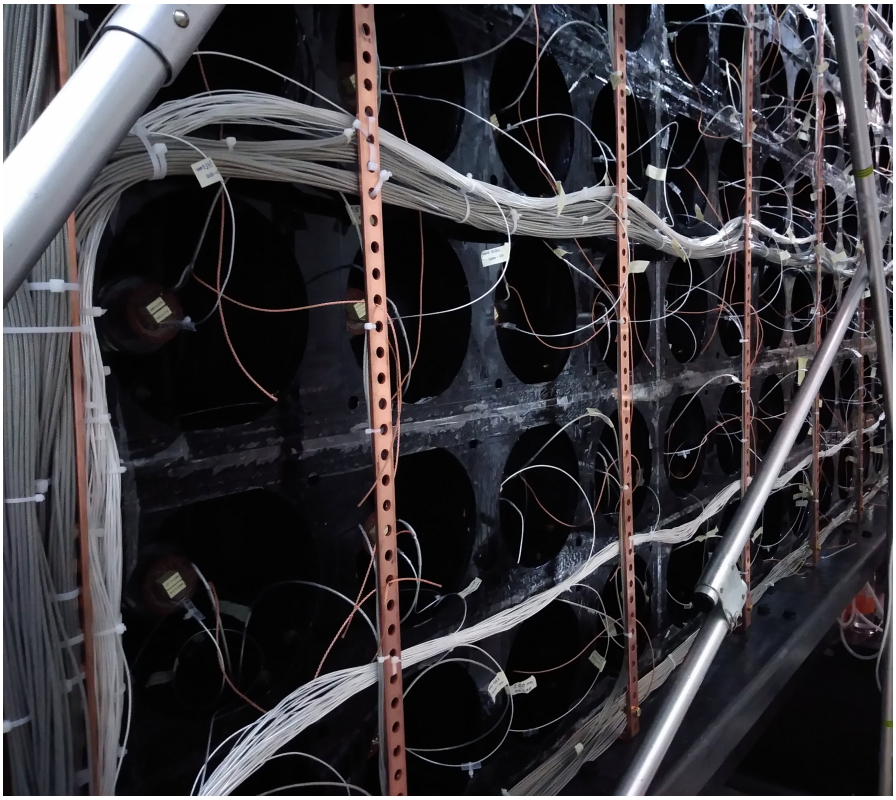

Figure 2.21: Back view of one main calorimeter wall. Signal cables are white and thin, HV cables are grey and thick.

Tracker cabling

The same internal and external pattern applies to the tracker cables. Geiger cells are connected via cables to the patch panel, where external cables, several tens of metres long, are linked to the electronics.

The routing of tracker and calorimeter lasted several months and required an enormous amount of work and involvement from the whole of the collaboration.

2.1.9 Electronics

Dedicated electronics has been developed for the SuperNEMO demonstrator. Six racks arranged next to the detector contain all it. The racks have been organised in separate areas - called crates - to accommodate the hardware dedicated to the calorimeter, tracker and calibration systems. The calorimeter electronics were realised at LAL while the tracker electronics were developed jointly by the French and English teams.

The triggering and acquisition electronics are based on a three-levels architecture: the front-end boards (FEB), the control boards (CB) and the trigger boards (TB). From the analogue signal generated in one part of the detector to its storage, a complex communication pattern takes place between these three structures.

1. The FEBs receive, process and digitise the primary analogue signals from the

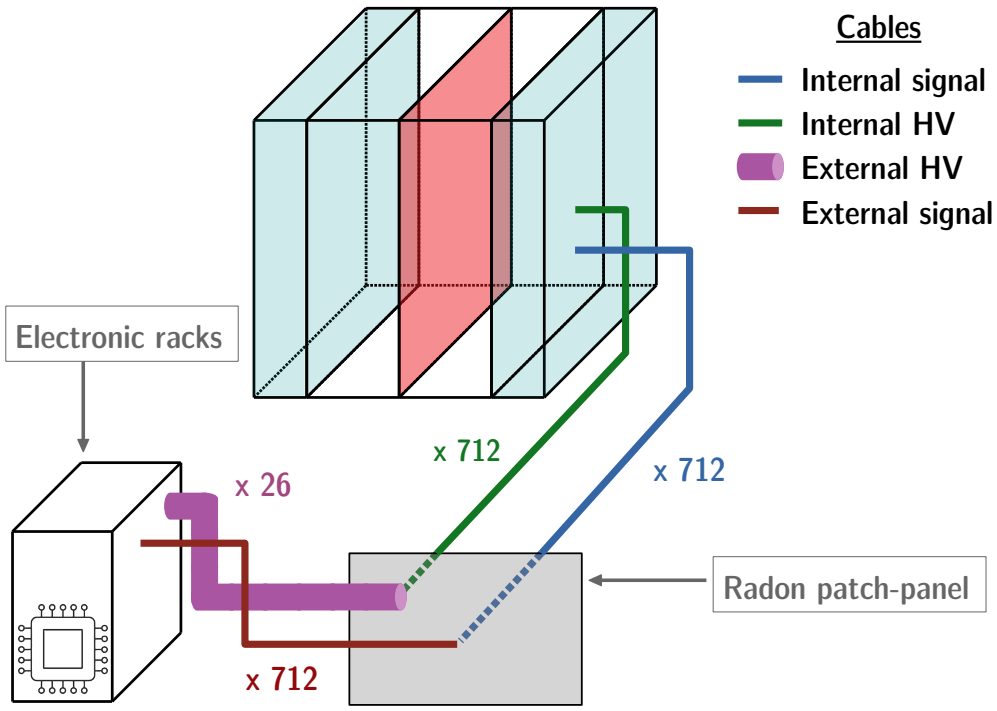

Figure 2.22: A scheme of the calorimeter cabling. Internal signal and HV cables go from the calorimeter to the patch-panel. External cables link the patch-panel to the electronic racks.

optical modules and the Geiger cells. The digitisation of the pulses by the FEBs is an innovation for SuperNEMO compared to NEMO-3 where only the ADC (analogue-to-digital converter) and TDC (time-to-digital converter) were calculated. This would permit to distinguish two successive interactions in the same electronic pulse. Part of this information is transmitted directly to the control board. Other data are stored in the FEBs as long as the central controller system has not validated or invalidated their acquisition. There are two types of FEBs, one for the calorimeter and one the tracker.

2. The control boards receive, centralise and forward signals coming from distinct locations of the detector (i.e. distinct FEBs). The calorimeter and tracker control boards have the same design and only differ by the firmware.

3. Once the acquisition decision is taken by the trigger board, the control boards propagate the information to calorimeter and tracker FEBs for the acquisition to begin.

4. After the acquisition has been taken, all digitised data are sent via the control boards to the data acquisition system (DAQ).

The electronics commissioning has begun in June 2018 at Manchester and is fully completed. I participated in the timing calibration of the front-end boards, which I discuss in Chapter 5.

Dedicated calorimeter electronics

In total, three crates are dedicated to the signal acquisition of the calorimeter. Each of them houses 20 front-end boards and one control board placed in the centre of the crate. A picture of one fully cabled calorimeter crate is given in Fig. 2.23. All the photomultipliers of a calorimeter wall are connected to front-end boards of a unique crate. Each front-end board collects the output PM signals of one column of optical modules of the calorimeter wall.

- For each of the main walls, 20 front-end boards are needed, each board corresponding to 13 output PM signals.
- For X-Walls and Gamma-Vetos, only 12 front-end boards are needed (8 for X-Walls and 4 for Gamma-Vetos). One front-end board corresponds to 16 output PM signals.

In total, all the 52 FEBs needed for the calorimeter electronics were designed at LAL with 16 channels each, collecting all the signals from the 712 optical modules.

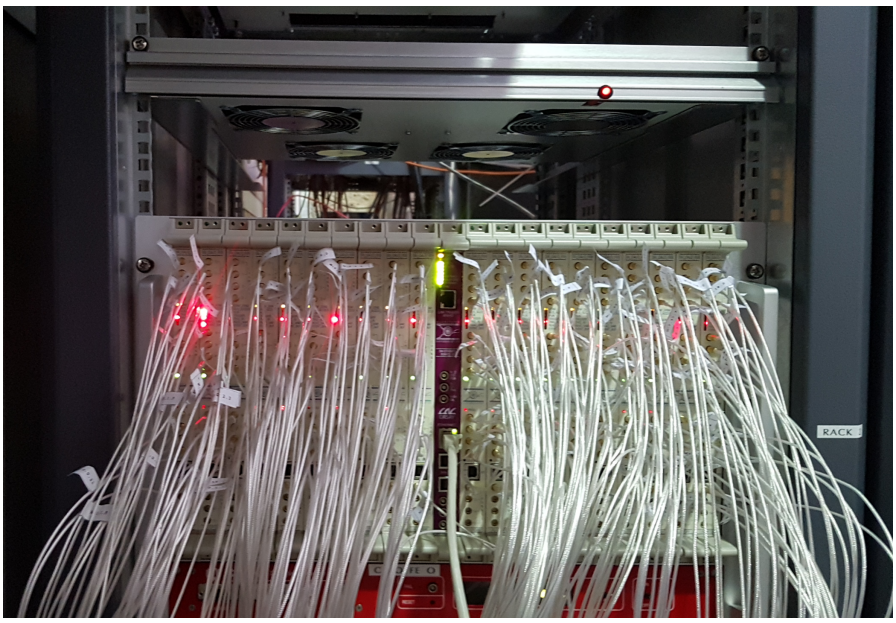

Figure 2.23: Picture of a calorimeter crate for one of the main wall.

Dedicated tracker electronics

Three crates are dedicated to the tracker electronics, with 680 Geiger cells per crate (for a total of 2040 cells). In each crate, there are 19 tracker front-end boards, called tracker FEBs. Each FEB therefore contains 108 electronic channels. A control board is located in the centre of each crate and centralises the information from the FEBs. A total of 57 FEBs and 3 CB are then needed to collect the signal of all the anodic and cathodic analogue signals from the wire chamber.

Calibration racks

Two racks are dedicated to the electronics and informatics of the demonstrator's calibration systems (one for the deployment system, one for the light injection system).

2.1.10 Detector gas tightness

An important part of the SuperNEMO detector is filled with a Helium-based gas mixture. As described in Sec. 2.1.3 it is essential for the proper functioning of the tracker that the detector is gas tight. As with the NEMO-3 detector, a major effort is therefore made to ensure that the detector is sealed to prevent external contaminants from infiltrating. Different techniques are deployed during and after the detector assembly (Fig. 2.24).

- The pre-assembled blocks of 8 optical modules were wrapped in a radio-pure nylon film. Additional patches of nylon film were glued on the calorimeter back side on each gap between these groups of 8 optical modules.
- After the calorimeter walls assembly, copper bars have been installed on the back side at the gap between the calorimeter and the structure supporting the detector.
- A piece of nylon was mounted on the front side of each main wall before the detector was closed (Fig. 2.25) in order to prevent the Radon from emanating from the calorimeter to the tracker.
- Different leak-sealing radio-pure materials (SBR, RTV, Stycast and Black Mamba glues) have been applied on different detector areas (mainly inside the optical module shieldings, tracker frame and source frame).

I took part in several of these operations, and my first shift to Modane was one of them.

After these operations, remaining leaks can still occur through two interfaces:

- through the nylon film. Indeed, one of the two films (Italian side) was damaged during the detector closure leading to possible gas leaks between the tracker volume and the optical modules buffer volume,
- through optical module magnetic shieldings (in the area of the clamping screws) leading to leaks between the buffer volume and the detector outside.

In order to reduce these leaks, several sealing operations have been carried out. They consist in injecting a gas inside the tracker via the gas injection system and detect possible leaks with a gas probe. In case of major leaks, helium gas could infiltrate the PMs vacuum by diffusing through the glass. Therefore the gas chosen for the first leaks checks is Argon. Every major leak is then fixed using the more suitable radio-pure glues presented above (depending on the size and location of the leak). The first over-pressure in the tracker was successfully obtained in September 2019 showing that a reasonable gas-tightness was achieved.

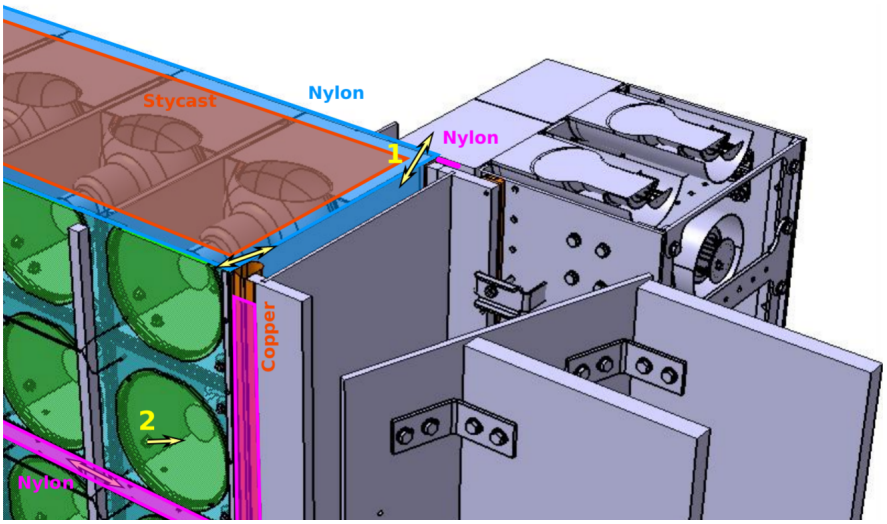

Figure 2.24: Demonstrator gas tightness plan. Back view of one of the calorimeter main walls.

Figure 2.25: Piece of radio-pure nylon film installed on the front face of each calorimeter main walls.

After all major leaks were detected, Helium can be injected inside the tracker to identify smaller leaks without any danger for the PMs.

2.2 Backgrounds

The SuperNEMO experiment seeks, if it exists, an extremely rare signal. It is therefore necessary to know and reduce as much as possible the possible sources of background that could degrade the observation of the signal in question. The

energies involved in the double beta process imply that this type of experiment is sensitive to several sources of background.

2.2.1 Internal background

We refer to *internal background* as the background being generated from inside the sources, where trace quantities of naturally-occurring radioactive isotopes can occasionally produce two-electron events and thus mimic $\beta\beta$-decay events. The largest contributions come from isotopes of the natural decay chains of ^{238}U and ^{232}Th.

Two-electrons signature processes

Following a beta disintegration, mainly three processes are likely to mimic a double beta disintegration with two electrons exiting the source foil as a signature, as shown in Fig. 2.26.

- An electron resulting from an internal conversion is ejected from the atom in addition to the electron beta. An X-photon can also be emitted without being detected by the calorimeter. This process will be described in detail in Chapter 4.
- The initially emitted electron can scatter in the source on another electron through the so-called Møller scattering, and emit a second electron of significant energy.
- The photon can eject an electron from the source by the Compton effect. If the scattered photon is not detected in the calorimeter, this decay may present a two-electron signature.

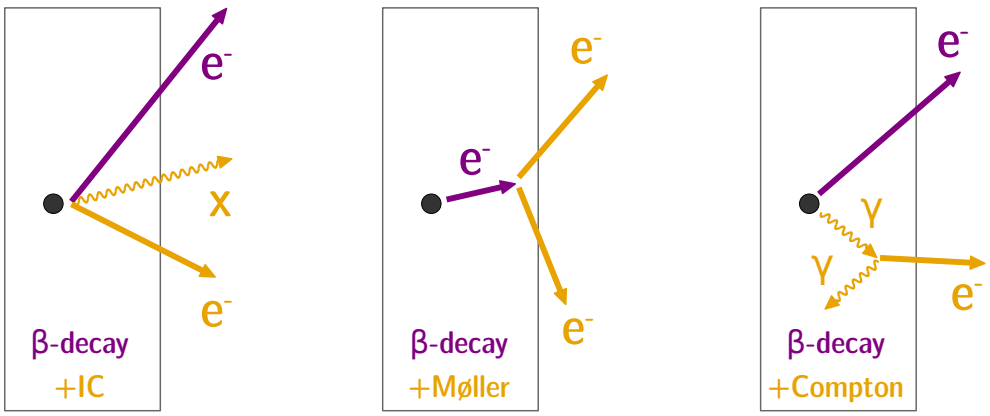

(a) (b) (c)

Figure 2.26: (a) β decay followed by internal conversion: radioactive nucleus performs a β decay, then an electron is emitted after internal conversion of the γ-ray. (b) β decay followed by Møller scattering. (c) β decay followed by Compton diffusion: radioactive nucleus β decays to an excited state, then the photon performs a Compton diffusion.

Characterisation of background

The ^{208}Tl and ^{214}Bi contaminations inside the source foils are harmful backgrounds for the neutrinoless double beta decay. One of the key features of the SuperNEMO demonstrator remains its ability to measure its own background in dedicated channels with large statistics, which are independent from the channel used to search for the signal.

After a β disintegration, ^{208}Tl emits between 1 and 3 γ's. Consequently, the $1e1\gamma$, $1e2\gamma$ and $1e3\gamma$ channels can be used to discriminate internal ^{208}Tl events, and measure the activity of the source. For ^{214}Bi disintegrations, between 0 and 2 γ's are expected after the β decay thus a significant contribution to the $1e1\gamma$ channel is also expected from ^{214}Bi. ^{214}Bi decays via β^- to ^{214}Po (the so-called *BiPo events*) which decays via the emission of an α particle with a half-life of 164 μs. Therefore one can measure BiPo events in the $1e1\alpha(\gamma)$ channel.

Internal activities

The collaboration established recommendations for maximum levels of the internal backgrounds, expressed in number of disintegrations per second, for a unit mass of $\beta\beta$ isotope, or for a unit volume of gas. These *specified activities* have been calculated in order to achieve the expected sensitivity of the final detector of $\sim 1 \times 10^{26}$ years.

The ^{82}Se demonstrator source is segmented in 34 foils, whose production was the responsibility of different laboratories (Dubna, LAPP and Tomsk). The sources have undergone different purification treatments, in order to investigate new techniques, and to compare them with those of NEMO-3. After the sources production and purification, preliminary measurements have been performed with the BiPo-3 detector to determine the actual ^{208}Tl and ^{214}Bi contamination levels inside the foils [34]. BiPo-3 is a detector installed in the Canfranc underground laboratory in Spain, dedicated to the measurement of the radiopurity in ^{208}Tl and ^{214}Bi of NEMO sources before their installation. It measures the Bismuth-Polonium cascade (electron emission followed by a delayed α). It is made of 2 modules of 40 PMs and scintillator blocks each that takes the source foils in sandwich.

We summarise measured contamination levels in Tab. 2.3, and give a comparison with initial specifications. The targeted ^{208}Tl level is not reached, being almost 27 times higher than expected, and 3.0×10^4 internal Thallium events are expected in 2.5 years in the total energy range. Nevertheless, on average, the activity of the sources was improved by a factor of 2 compared to the ^{100}Mo sources of NEMO-3 which is encouraging. In addition, valuable information has been accumulated on the different production techniques, which are of great importance for the final detector construction. In particular, the two best ^{208}Tl sources activities were reached by inverse chromatography, reaching a 20 ± 10 μBq/kg level, an improvement by a factor 5 compared to NEMO-3. This encourages for further investigations in this direction. The sensitivity of BiPo-3 detector only allowed to give an upper limit on the level of internal ^{214}Bi (an activity of 290 μBq/kg would correspond to 1.6×10^5 internal Bismuth events in

2.5 years). Precise additional measurements are expected from the demonstrator calibration.

	Specified activities	Measured activities
^{208}Tl	2 μBq/kg	54 μBq/kg [26 - 102]
^{214}Bi	10 μBq/kg	< 290 μBq/kg

Table 2.3: Measured and specified activities for the SuperNEMO demonstrator. The limit on ^{214}Bi contamination is provided by BiPo-3 measurements for a 90% CL [34].

2.2.2 External background

External background sources

Different processes originating from outside the detector can mimic $\beta\beta$ decays.

- External high energy γ's emitted after the disintegration of natural radioactive isotopes (mostly ^{208}Tl, ^{214}Bi and ^{40}K) occurring outside the detector (typically the lab rocks).
- Neutrons resulting from the spallation of nuclei by cosmic muons.
- Contamination of detector materials by natural radioactive nuclei (mostly in PM glass).

The three types of processes listed above can be the cause of a photon interaction inside the source and lead to a $\beta\beta$ topology, though different possible processes (Fig. 2.27).

- Interaction of such a high-energy photon ($>$ 1.022 MeV) can induce a creation of an electron/positron pair. The presence of a magnetic field in the SuperNEMO experiment allows the discrimination between a positron and an electron thanks to the curvature of their trajectories and thus reduce this background.
- Two successive Compton scattering can occur, the last gamma escaping detection.
- After a first Compton scattering, the emitted electron can make a Møller diffusion on another electron in the source, the gamma being not detected.

Radiopurity

A huge work has been done by Hamamatsu to control the photomultipliers contamination compared with NEMO-3, in order to reduce the total radioactive isotope budget for the experiment. In Tab. 2.4 is presented the total activities

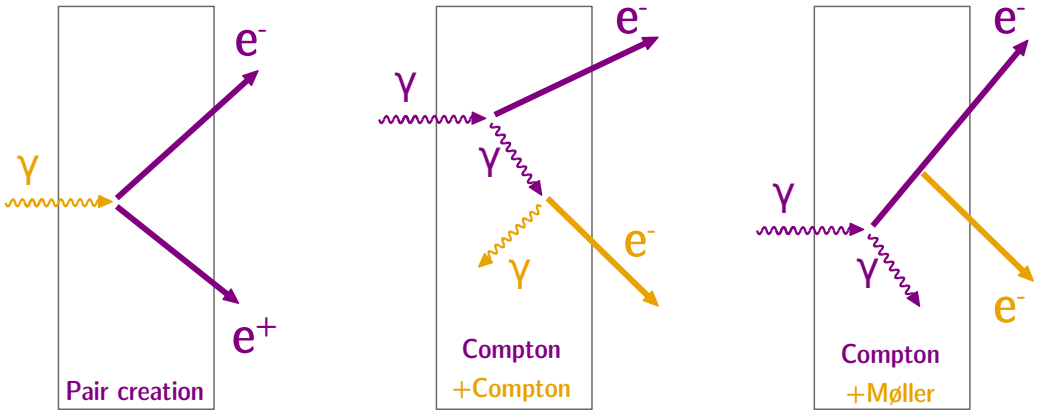

(a) (b) (c)

Figure 2.27: (a) External γ undergoes an electron/positron pair creation. (b) Two successive Compton scatterings. (c) Compton scattering followed by a Møller scattering.

Experiment	^{40}K	^{226}Ra	^{232}Th
SuperNEMO demonstrator [35]	540	197	124
NEMO-3 [36]	832	302	50

Table 2.4: Total activity in Bq of SuperNEMO and NEMO-3 PMs in ^{40}K, ^{226}Ra and ^{232}Th isotopes.

measured for 8 and 5 inches PMs [35]. The radiopurity is smaller than for NEMO-3 for ^{40}K and ^{226}Ra (leading to ^{214}Bi contamination) by $\sim 35\%$ but is worse for ^{232}Th (^{208}Tl) by $\sim 150\%$.

The NEMO-3 experiment set a limit on the external background number of counts, of < 0.2 events in the $2e$ topology, for the energy range [2.8;3.2] MeV (two electrons energy sum), for an exposure of 34.3 kg·y, with ^{100}Mo sources [37]. This could lead us to think that the external background contribution for SuperNEMO could be higher than that of NEMO-3 because of the higher level of ^{208}Tl measured. Hopefully, on that level, the most notorious difference between the two detectors is the fact that the SuperNEMO scintillator blocks are thicker than those of NEMO-3. Therefore, a gamma emitted from a PMT glass is more likely to be detected before crossing the source foils, such that it would be rejected and would not contribute to the background in the $2e$ channel. Even if the regions of interest are slightly different between these two experiments, it produces a negligible increase on the external background contribution[2].

2.2.3 Radon background

Radon is a noble gas which occurs as an indirect decay product of uranium and thorium, which is a daughter of uranium. Radon contaminations inside the tracker

[2] A study conducted by the SuperNEMO collaboration showed that at most 0.73 additional external background events would have been expected for the NEMO-3 detector, if instead of taking the [2.8;3.2] MeV energy range, we would have considered the [2.7;3.15] MeV region of interest.

volume is a major background to rare event experiments such as SuperNEMO. Due to its chemical properties, radon has a long diffusion length in solids, making it difficult to remove. This isotope is outgased in the surrounding air from the rock walls of the laboratory and detector materials and can enter the detector. The potential sources of radon are

- gas contamination at the tracker entrance,
- emanation of the tracker materials,
- radon diffusion from the detector material to the tracker,
- radon diffusion from the laboratory to the tracker.

Simulations show that, to achieve the designed sensitivity for the final SuperNEMO detector, the level of radon must not exceed 0.15 mBq/m^3 since its decay daughter ^{214}Bi can mimic a $0\nu\beta\beta$ event. The level of radon emissions inside the tracker was extrapolated by the collaboration for each of the four C-section, revealing an expected total activity of 0.15 ± 0.02 mBq/m^3 (67% CL), assuming the combination of an anti-radon tent and an air-flushing method (2 m^3/h gas flow rate) [38]. These levels were measured using a concentration line where the detector materials are enclosed in a chamber in which they emanate Radon. The gas from the vessel is then sent to a Radon trap in order to measure the concentration of this isotope.

2.2.4 Background reduction

The underground laboratory

The LSM is located under the Fréjus mountain besides the road tunnel of the same name that links France and Italy. This laboratory is one of the deepest in the world with a maximal rock thickness of 1700 m, or 4800 meter water equivalent. At this depth, the flow of cosmic muons is reduced by a 10^6 compared to the surface (the muon flux is measured at ~ 4 muons/m^2/day in the laboratory).

External shield

In order to reduce the contribution of external gamma background, ultra-pure iron plates 20 cm thick form a shield surrounding the anti-radon tent. In addition,the detector will be protected from neutrons by a final shield consisting of water tanks (on the sides of the detector) and borated Polyethylene plates (top and bottom).

Radon background reduction

A wide variety of means are employed by the collaboration to combat this contamination.

- Radon trap: the gas in the tracker is constantly recycled. On this occasion, the gas (without ethanol) is sent into a radon trap before being re-injected into the tracker.

- The emanations of the tracker materials were measured in Manchester with the concentration line before the installation of the chambers.

- The gas flow can be reasonably increased to have a sufficiently low Radon level.

- The huge effort deployed for the detector gas tightness (Sec. 2.1.10) is one of the means to reduce radon contamination.

- The detector will be encapsulated in its entirety in a Radon Tent made of High Density Polyethylene (HDPE) panels preventing radon from the laboratory from entering the detector by possible tiny gaps.

2.3 The SuperNEMO software

The SuperNEMO collaboration developed its own simulation, reconstruction and analysis environment. The Falaise software, specifically designed by and for the SuperNEMO collaboration, holds the `C++` library for the event reconstruction and analysis of simulated and real data. Especially, it contains the geometry, the detector material, the event data model, the reconstruction algorithms and the data analysis. Finally, the SNFee software is a tool package for the configuration, control and monitoring of the SuperNEMO front-end electronics.

2.3.1 Simulation

The Falaise software handles the simulation of events based on the Monte-Carlo method implemented in GEANT4. The event generation, the detector geometry and its materials are simulated. The process to be simulated ($2\nu\beta\beta$, radioactive isotope decays...), its location (source foils, PM glass...), as well as the detector configuration (on/off magnetic field, presence or absence of external shield...) can be set by using configuration files. After the Monte-Carlo simulations, the detector performances and characteristics (optical module energy resolutions, Geiger cell spatial resolution...) are implemented in order to reproduce the behaviour of the detector as faithfully as possible.

2.3.2 Reconstruction pipeline

The Falaise Software of SuperNEMO is made up of successive algorithms allowing to characterise the events stored after a data acquisition or a simulation.

The tracker clustering is in charge of clustering individual Geiger cell hits to form continuous traces and thus identify the number of charged particles of an event.

The tracker trajectory fitting fits the reconstructed traces with two patterns: a helix (well adapted to the identification of electrons and positrons of a few MeV that have a curved trajectory in the magnetic field of the experiment) and with a line (rather adapted to muons and alpha particles). The fit with the best χ^2/ndf is then selected.

The charged particle tracking: previous algorithms are suitable for any experience with a thread chamber. The present one adapts informations to the SuperNEMO specific geometry. It extrapolates the charged particles trajectories to associate a calorimeter block and a source foil vertex to each track.

The gamma clustering: as gamma particles do not interact inside the tracker, the tracker clustering algorithm does not handle such particles. After the charged particle tracking algorithm, some calorimeter hits remain not associated with any track. The gamma clustering algorithm is dedicated to reconstruct the successive diffusions of gammas in scintillators using geometrical and time-of-flight informations.

The particle identification (PID): all previous algorithms have permitted the individual reconstruction of the different particles of an event. The particle identification module takes care of identifying and classify each particle as:

- Electron: negatively curved track with an associated calorimeter hit and a vertex on the source foil.
- Positron: positively curved track with an associated calorimeter hit and a vertex on the source foil.
- Alpha particle: short straight track with possible time delay.
- Gamma particle: unassociated calorimeter hit.

This last algorithm is not yet included in the official Falaise pipeline but were nonetheless widely used in the framework of the two analyses presented in Chapters 3 and 4.

The SuperNEMO software also provides a high precision visualisation, of which an example is given in Fig. 2.28. One electron and two γ's are simulated then reconstructed. One of the γ scatters in a first scintillator and deposits energy in a second one.

2.3.3 Analysis tools

Internal and external probabilities are extremely useful tools, widely employed in particular by the gamma clustering algorithm and particle identification module. They are also used for analysis purposes, to determine whether or not an event does come from inside or outside the source foils.

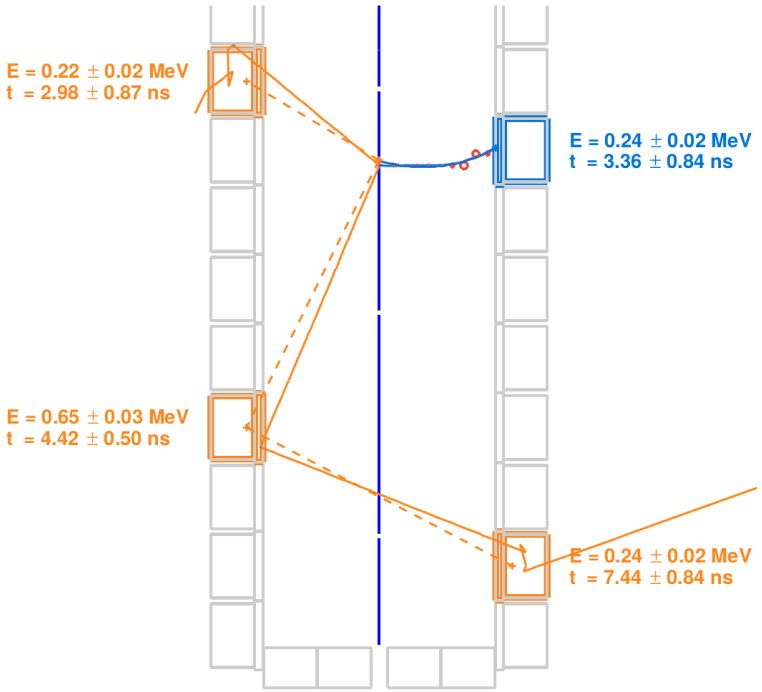

Figure 2.28: Display of an event with one electron (blue) and two γ's (orange) emitted. The simulated tracks are solid lines and reconstructed are dashed lines. The visualisation is provided by the Falaise software.

2.3.3.1 Internal probability

Internal probability is a mathematical tool used to quantify the probability that two particles were emitted simultaneously in the source foils. This tool is based on the particle Time-Of-Flight computation. Firstly, we define, for two particles, the internal χ^2

$$\chi^2_{int} = \frac{((t_1^{meas} - t_1^{exp}) - (t_2^{meas} - t_2^{exp}))^2}{\sigma^2_{tot}} \,. \tag{2.1}$$

t_i^{exp} is the expected time-of-flight of the particle i inside the calorimeter, t_i^{meas} the measured one, c is the speed of light, and σ_{tot} is the quadratic sum of all uncertainties. The expected time-of-flight, is defined as

$$t_i^{exp} = \frac{L_i}{\beta_i \, c} \,, \tag{2.2}$$

where L_i is the reconstructed track length, and β_i corresponds to

$$\beta_i = \frac{\sqrt{E_i(E_i + 2m_i)}}{E_i + m_i} \,, \tag{2.3}$$

E_i being the energy of the particle and m_i its mass. The total uncertainty, σ_{tot}, is defined as

$$\sigma_{tot} = \sqrt{\sigma^2_{t_1} + \sigma^2_{t_2} + \sigma^2_{\beta_2} + \sigma^2_{\beta_1} + \sigma^2_{l_1} + \sigma^2_{l_2}} \,. \tag{2.4}$$

The uncertainty σ_t on the measured time-of-fight This term is directly related to the phenomenon of absorption and re-emission of scintillation photons, as well as to the photomultiplier functioning. It is defined as

$$\sigma_t = \sqrt{\frac{\tau_{\mathrm{SC}}^2 + \left(\frac{\mathrm{FWHM_{TTS}}}{2\sqrt{2\ln 2}}\right)^2}{\mathrm{N_{PE}}}}\,, \tag{2.5}$$

where τ_{SC} is the scintillator characteristic time representing the scintillator de-excitation time. $\mathrm{FWHM_{TTS}}$ is the temporal dispersion linked to the photomultiplier: the transit time of the photoelectrons inside the photomultiplier can evolve, according to its point of creation on the photocathode. This transit time is unique for each photomultiplier, and has to be characterised experimentally. $\mathrm{N_{PE}}$ is the number of photo-electrons emitted after a particle has deposited all its energy E in the scintillator:

$$\mathrm{N_{PE}} = E \times \left(\frac{2\sqrt{2\ln 2}}{\mathrm{FWHM_E}}\right)^2\,, \tag{2.6}$$

where $\mathrm{FWHM_E}$ is the energy resolution of the PM, 8 % at 1 MeV for the SuperNEMO calorimeter. Therefore, for a particle of 1 MeV depositing all its energy inside a scintillator, $\mathrm{N_{PE}} \sim 866$ photo-electrons are emitted. Preliminary studies gave a first estimation of σ_t and found $\sigma_t = 342 \pm 10$ ps for 1 MeV gammas entering the front face of the scintillator, and $\sigma_t = 248 \pm 6$ ps for 1 MeV electrons [30]. On the occasion of the SuperNEMO detector commissioning, we complete this study and characterise the calorimeter time resolution in Chapter 6.

The uncertainty σ_β on the expected time-of-flight induced by the uncertainty on the particle energy This term is derived from Eqs. (2.2) and (2.3):

$$\sigma_{\beta_i} = \frac{t_i^{exp} \times m_i^2}{E_i \times (E_i + m_i) \times (E_i + 2m_i)} \times \sigma_E\,, \tag{2.7}$$

where $\sigma_E = \mathrm{FWHM_E} \times \sqrt{E_i}$ represents the energy resolution of the PM for the energy E_i.

The uncertainty σ_l on the expected time induced by the uncertainty on the reconstructed track length This corresponds to the typical uncertainty due to particle track reconstruction. It is induced mainly by the uncertainty on the interaction point inside the scintillator block, thus is greater for γ particles than for electrons. Indeed, thanks to the gaseous detector and the trajectory fitting, valuable information on the impact point inside the scintillator are provided for electrons crossing the tracker, while photons only deposit their energy inside the calorimeter, without ionising the tracker gas. In the framework of the optimisation of γ reconstruction in the SuperNEMO detector, a previous study has evaluated the uncertainty on the track length for γ's, by simulating mono-kinetic γ's, and

estimated $\sigma_L = 0.9$ ns [32]. The value used in the simulation/reconstruction pipeline, for the case of electrons, is inherited from the NEMO-3 analysis with $\sigma_L = 0.1$ ns. An optimisation of this parameter is given in Chapter 4.

We would translate the internal χ^2 distribution into the so-called *internal probability* through

$$P_{int} = \frac{2}{\sqrt{2\pi}} \int_{\chi_{int}}^{+\infty} e^{-\frac{u^2}{2}} du \,. \tag{2.8}$$

This formula transforms the χ^2 Gaussian distribution into a flat distribution between 0 and 1. One of the benefits of using the probability distribution rather than the χ^2 distribution is that it brings extra qualitative information, especially useful to check the estimation of the uncertainties. The shape of the probability distribution can bring out an overestimation or an underestimation of the uncertainties, which would translate into a positive or a negative slope, respectively. On the other hand, a flat distribution signifies an appropriate estimation of the errors and confirms the Gaussian distribution of the original quantity measured.

2.3.3.2 External probability

The external probability is built to test if one of the two particles (electron, γ) first deposited energy in the calorimeter, crossed the tracker to reach the source foil and triggered a second calorimeter module (with or without interacting inside the source foils when crossing it). The external χ^2 is defined in the same manner as the internal one:

$$\chi^2_{int} = \frac{(|t_1^{meas} - t_2^{meas}| - (t_1^{exp} + t_2^{exp}))^2}{\sigma^2_{tot}} \,. \tag{2.9}$$

The time experimental difference is compared to the time it would have taken a particle to travel from one calorimeter module to the other. The external χ^2 is translated into the so-called *external probability* the same way as in Eq. (2.8).

2.4 Summary

SuperNEMO demonstrator features have been exposed, and often compared with the ones of its predecessor, NEMO-3. This detector aims at demonstrating that the NEMO unique technology is scalable in order to explore previously unattained reaches in the search for the $0\nu\beta\beta$ decay. Previous studies have been led in order to estimate the sensitivity of SuperNEMO to this decay. The one presented in the next chapter follows them by evaluating the influence of several parameters.

The detector calibration has started and should be completed this year thanks to the involvement of all the collaboration.

Chapter 3

Sensitivity of the SuperNEMO experiment to the $0\nu\beta\beta$

> Never send a human to do a machine's job.
>
> Agent Smith
> *The Matrix*

A study aiming to evaluate the SuperNEMO sensitivity to the $0\nu\beta\beta$ decay, and the corresponding effective neutrino mass is presented. From previous studies, the final detector is expected to exclude half-lives up to 1×10^{26} y (90% CL), with an exposure of 500 kg.y with ^{82}Se sources[1] [39]. The SuperNEMO demonstrator was designed in order to assess the technical feasibility of such a large-scale detector and to show that background specifications can be achieved. With a reduced exposure of 17.5 kg.y, this demonstrator is expected to reach a sensitivity on the $0\nu\beta\beta$ process of 5.3×10^{24} y (90% CL) [32].

As it was the case with its predecessor, a copper coil was designed to deliver a magnetic field inside the wire chamber, to bend the charged particles trajectories, hence making it possible to discriminate between electrons and positrons. However, studies led by the collaboration determined that the intensity of this field could be modified by the photomultiplier magnetic shields. Photomultipliers energy resolution could also be impacted by the presence of this magnetic field [32, 33]. We aim to explore the impact, on both the demonstrator and final detector sensitivity, of the presence of this magnetic field. The findings of this study participate in better understanding the detector performances. In a context of investigating the demonstrator and final detector's capabilities, different internal source contamination levels are considered to estimate the sensitivity. The topology of interest is that of two electrons, and we use the total energy sum to discriminate the signal from the background events. Thanks to SuperNEMO tracking capabilities, extra topological informations are exploited to improve the final sensitivity. To go further, we also explore the possibility of studying the $0\nu\beta\beta$ decay of other $\beta\beta$ isotopes.

[1] Supposing the $0\nu\beta\beta$ decay of ^{82}Se occurs through the exchange of a light Majorana neutrino.

3.1 The $0\nu\beta\beta$ signal and background model

A full GEANT4 simulation of the demonstrator was performed to determine the lower limit on the $0\nu\beta\beta$ half-life that can be probed with SuperNEMO in case of the non-observation of the signal. Due to the time it would take to simulate every background contribution, we choose a simplified model where only the most harmful backgrounds to the $0\nu\beta\beta$ decay search are simulated. In addition, $0\nu\beta\beta$ signal decays inside the detector are simulated, to better understand all the aspects of this analysis.

3.1.1 The $0\nu\beta\beta$ signal

The SuperNEMO detector was designed to search for the yet never-observed $0\nu\beta\beta$ decay. In the following, we assume the underlying mechanism for this decay is the exchange of a light Majorana neutrino, the so-called mass mechanism (MM), as it is the most widespread. The hypothetical $0\nu\beta\beta$ signal would be detected as an excess of events at the end point of the $2\nu\beta\beta$ spectrum, with respect to the predicted background contamination levels.

3.1.2 Inside detector backgrounds

Numerous types of backgrounds that could mimic and hinder the search for the $0\nu\beta\beta$ signal were simulated.

3.1.2.1 Internal backgrounds

As explained is Chapter 2, internal backgrounds stand for decays occurring inside the source foils, presenting the same signature as the $0\nu\beta\beta$ signal. These backgrounds are mainly the $2\nu\beta\beta$ decay undergone by the source isotope, disintegrations of ^{208}Tl and ^{214}Bi contaminations inside the source foils, as well as ^{214}Bi disintegrations due to Radon deposited on the surface of the source foils.

The $2\nu\beta\beta$ process

In the full energy range, the allowed $2\nu\beta\beta$ decay of ^{82}Se stands as the dominant internal background type. The corresponding two-electrons energy sum spectrum is a continuum, whose ending point should stands at $Q_{\beta\beta} = 2.99$ MeV, but is subtly shifted by the detector's energy resolution due to energy losses inside the source foils and gaseous detector. A total of 10^7 events of this decay were simulated inside the source foils, in the full energy window. However, above a certain energy value, the number of $2\nu\beta\beta$ events decreases strongly, which can lead to a lack of statistics in a energy region favourable for the search for $0\nu\beta\beta$ signal. To offset this effect, additional 10^7 of this decay were simulated on a slightly reduced energy range, that is to say above 2 MeV. The second set of simulations is normalised with the first one. In this way, the lack of $2\nu\beta\beta$ simulated events in the high-energy tail is avoided, without requiring too high computational resources.

Source foils contamination by natural isotopes

As described in Sec. 2.2.1, after sources purification, residual natural isotopes such as ^{208}Tl or ^{214}Bi can still be present inside the foils, constituting the principal internal source of background, with the $2\nu\beta\beta$ decay.

3.1.2.2 Tracker contamination by natural isotopes

Radon, a descendant of ^{238}U, is present as a gas in the tracker. Its daughter isotopes, when deposited on the tracker wires, can produce events similar to internal ones. In fact, one of the progeny of ^{222}Rn, the ^{214}Bi, can decay on (or near) a foil, and appear with a two-electron topology, becoming hard to distinguish from a double beta decay candidate. As this isotope is distributed throughout the whole tracking detection volume, a large quantity of this decay were simulated on the tracker wires.

3.1.3 External backgrounds

This background category was described in detail in Sec. 2.2.2. As a reminder, it is populated by the external γ-ray flux produced by radioactive isotope decays (mostly ^{40}K, ^{214}Bi and ^{208}Tl) in detector components or surrounding laboratory rocks, as well as neutron interactions in the external iron shield. As simulating external backgrounds would be very consuming in terms of computing resources due to their very low probability to produce two electrons ($2e$) topologies, they were not simulated in the framework of this analysis. Nevertheless, a future study would consider their contribution, especially to evaluate the impact of the magnetic field on the sensitivity.

3.1.4 Expected number of decays

The number of natural isotope decay events expected in the $2e$ topology depends on their activities inside the source foils (for ^{208}Tl and ^{214}Bi), or on the tracker's wires (for ^{222}Rn decaying in ^{214}Bi). The amount of expected double β decays is driven by its half-life value: the higher the half-life, the lower its contribution in the total number of expected background. For this analysis, we consider the $2\nu\beta\beta$ half-life of ^{82}Se measured by NEMO-3, $T^{2\nu}_{1/2} = 9.39 \pm 0.17\,(\text{stat}) \pm 0.58\,(\text{syst}) \times 10^{19}$ years [40]. For the $0\nu\beta\beta$ process, we also take the best limit set by the NEMO-3 detector, $T^{0\nu}_{1/2} > 2.5 \times 10^{23}$ y [40]. This value is given for illustration purposes only, as it is not used to estimate the sensitivity of the detector.

Tab. 3.1 gives the expected number of background events, for the demonstrator and final detector exposures, assuming target background activities are reached: $\mathcal{A}^{\text{Tl}} = 10$ μBq/kg, $\mathcal{A}^{\text{Bi}} = 2$ μBq/kg and $\mathcal{A}^{\text{Rn}} = 0.15$ mBq/m^3. The expected number of disintegrations do not take into account any technique to reject background, and are given for the full energy range of the two measured electrons.

Process	Half-life/Activity	Expected decays	
		Demonstrator	Final detector
$2\nu\beta\beta$	$T^{2\nu}_{1/2} = 9.39 \times 10^{19}$ y	9.5×10^5	2.7×10^7
^{208}Tl	$\mathcal{A}^{\mathrm{Tl}} = 2\ \mu$Bq/kg	1.1×10^3	3.1×10^4
^{214}Bi	$\mathcal{A}^{\mathrm{Bi}} = 10\ \mu$Bq/kg	5.5×10^3	1.6×10^5
^{222}Rn	$\mathcal{A}^{\mathrm{Rn}} = 0.15$ mBq/m^3	1.8×10^5	7.2×10^6

Table 3.1: Expected number of background events, for the demonstrator (17.5 kg.y) and for the final detector (500 kg.y). We assume target background activities are reached: $\mathcal{A}^{\mathrm{Tl}} = 10\,\mu$Bq/kg, $\mathcal{A}^{\mathrm{Bi}} = 2\,\mu$Bq/kg, $\mathcal{A}^{\mathrm{Rn}} = 0.15$ mBq/m^3. The measured half-life $T^{2\nu}_{1/2} = 9.39 \times 10^{19}$ y for ^{82}Se is considered [40].

However, they are expected to be extremely reduced, notably by the application of event selections aimed at maximising the sensitivity to the $0\nu\beta\beta$ half-life. Especially, in the following, we focus on an optimised narrow energy window, called *region of interest*, whose usefulness is described in detail in the next section. This is also one of the reasons why it was necessary to simulate a large number of events, so that the signal and backgrounds are correctly represented in the region of interest.

3.2 Event selection

For SuperNEMO, the $0\nu\beta\beta$ signature is two-electrons events, emitted simultaneously from the same vertex on the source foils, with an energy sum compatible with $Q_{\beta\beta} = 2.99$ MeV for ^{82}Se sources. Therefore, we conducted this analysis selecting only events matching the $2e$ topology.

3.2.1 Electron definition

A reconstructed particle is tagged as an electron if it has:

- a vertex on the source foil,
- a reconstructed track inside the wire chamber,
- an associated calorimeter hit,
- and a final criterion applied only if the magnetic field is simulated inside the tracker.

About the last point, as announced, we aim at studying the influence of the magnetic field on the final sensitivity results. To this end, we are led to consider two separate cases, one where the magnetic field is switched on, aligned with the Z (vertical) axis of the detector, with a uniform value of 25 Gauss, and one where it is switched off. In the first case, particles such as electrons and positrons of a few MeV have a curved trajectory in the tracker. In the second case, the tracks of the particles may be similar to straight lines (not to mention the possible multiple

scattering on the tracker wires). It is then necessary to adapt the selection of events to each case. When the magnetic field is on, we consider a fourth criterion: a particle is identified as an electron if its track has a negative curvature[2]. In the following, we present results where the magnetic field is turned on. The off-field study is addressed in Sec. 3.5.

A two-electron ($2e$) topology is then defined as two reconstructed tracks with negative curvatures, each one associated with a vertex on the source foils and a calorimeter hit. These selections represent the so-called *first-order* cut-offs. The $2e$ topologies have been selected using the Particle Identification module at the end of the Falaise reconstruction pipeline [32]. I wrote my own module and added it to the collaboration software in order to store the selected events in a data format matching my off-line analysis chain. Second order selections taking into account topological information (time of flight, location of vertices on the source foils) are presented in Sec. 3.4.

3.2.2 Total energy spectrum

In Fig. 3.1, we present the total energy spectra for each simulated process in the $2e$ topology, after application of the first-order cut-offs. The distributions are given for the demonstrator (^{82}Se sources, 17.5 kg.y exposure), considering the specified activities are reached. Once again, the $0\nu\beta\beta$ spectrum is given only for illustrative purposes. If this decay is detected, its two-electrons energy sum distribution would be a peak, located at the end-point of the $2\nu\beta\beta$ energy distribution, that is to say at the total available energy, $Q_{\beta\beta} = 2.99$ MeV. As the two electrons of this decay would share the total available energy, this peak should be infinitely thin. However, a widening of this distribution is expected, mainly due to the calorimeter energy resolution as well as energy losses inside the dense source material. Indeed, the path of an electron in the source is more or less long, depending on the disintegration location and on the emission angle, leading to a degradation of the measured energy.

As explained in Sec. 3.1, two sets of $2\nu\beta\beta$ events were simulated: one on the full energy range, and one for which the two-electrons energy sum is greater than 2 MeV. After the normalisation of these two sets, we get the complete $2\nu\beta\beta$ energy spectrum displayed in the figure. These energy spectra confirm the $2\nu\beta\beta$ background is dominant in the total energy range.

The ^{208}Tl total energy spectrum extends up to high energies. It reveals two distinct peaks, one corresponding to a low-energy β particle, the other to the internal conversion of the 2.614 MeV gamma, emitted after ^{208}Tl β^- disintegrations (Sec. 2.2.1). Whatever their origin, either ^{222}Rn contaminations inside the tracker gas, or internal contaminations of the source foils, the two ^{214}Bi energy distributions have nearly the same shapes.

A widespread technique consists in constraining the $0\nu\beta\beta$ decay searches to a narrow energy range, the so-called *region of interest* (ROI). It allows to reduce the

[2] A trajectory is said by convention to be negative if it has the same curvature as that of an electron moving from the source to the calorimeter, in a magnetic field oriented according to $+Z$.

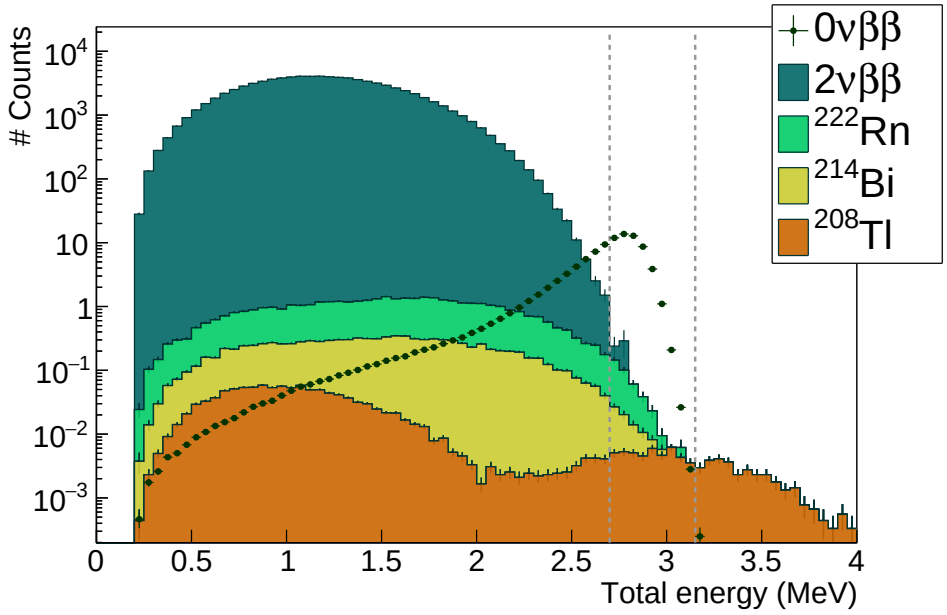

(a) Full energy range.

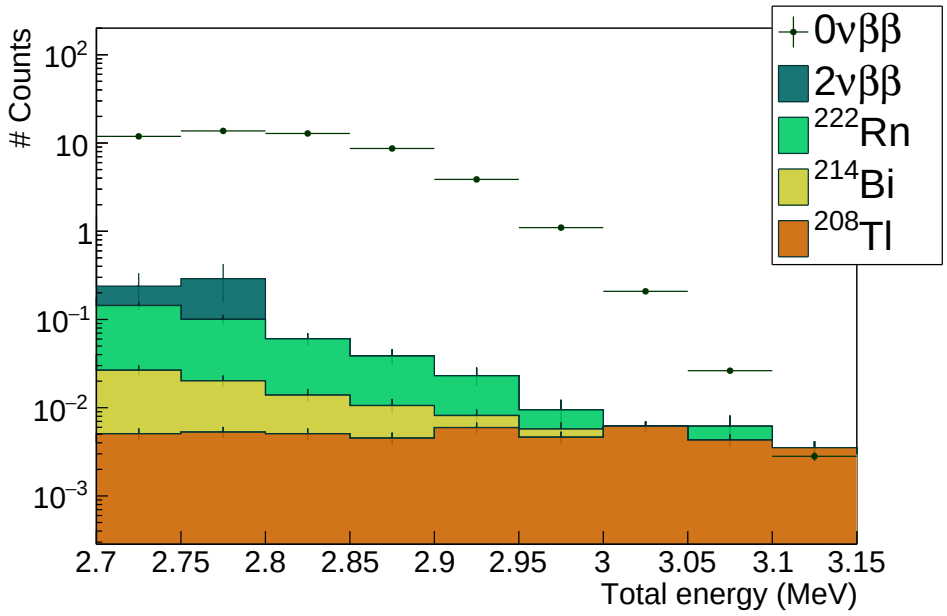

(b) Zoom on ROI.

Figure 3.1: Total energy spectra for the $0\nu\beta\beta$ signal and main backgrounds, for (a) the full energy range, and (b) for the [2.7;3.15] MeV energy range, whose optimisation is discussed in Sec. 3.3. The $2\nu\beta\beta$ spectrum is normalised to $T^{2\nu}_{1/2} = 9.39 \times 10^{19}$ y, and the specified activities are considered for ^{208}Tl,^{214}Bi and ^{222}Rn. The amplitude of the $0\nu\beta\beta$ is arbitrarily set at the limit obtained with NEMO-3.

expected number background decays, while improving the chances to observe the signal decay, then maximising the limit set on $T_{1/2}^{0\nu}$. A typical ROI is materialised in the figure by two vertical dashed lines, revealing ^{208}Tl, ^{214}Bi and ^{222}Rn could be harmful for the search for the $0\nu\beta\beta$ decay. The influence of the sources contamination by these natural isotopes, as well as optimised background rejection techniques are presented in Sec. 3.4.

In the following, we expose general principles leading to the determination of the best limit on $T_{1/2}^{0\nu}$, in the appropriate region of interest. We illustrate the reasoning by applying it on the demonstrator case, with specified activities, and on-magnetic field condition. However, the technique presented remain valid for all exposures, internal contamination levels and field conditions.

3.3 Demonstrator sensitivity to the $0\nu\beta\beta$ decay of ^{82}Se

The SuperNEMO demonstrator is designed to measure $\beta\beta$ decays of radioactive emitters. In case a the non-observation of the $0\nu\beta\beta$ process, the collaboration would set a lower-limit on the half-life $T_{1/2}^{0\nu}$, and an upper-limit on the effective neutrino mass $m_{\beta\beta}$.

3.3.1 Sensitivity to the $0\nu\beta\beta$ half-life

In case of the non-observation of a $0\nu\beta\beta$ signal, the expected lower limit on the half-life is provided for a given energy range $[E_{\min};E_{\max}]$ on the two electrons energy sum, and depends on the characteristics of the detector. Firstly, it depends on the signal detection efficiency, $\epsilon_{0\nu}$ in this energy window, which corresponds to the ratio of the number of selected signal events to the number of simulated ones. It also depends on the source isotope nature, as well as on the detector exposure $m \times t$, with m the mass of source material in the foils and t the data acquisition time period. It follows

$$T_{1/2}^{0\nu} > \frac{\mathcal{N}_{\mathrm{A}} \ln 2}{M} \times \frac{\epsilon_{0\nu} \times m \times t}{N_{0\nu}^{\mathrm{excl.}}}\,, \tag{3.1}$$

with $\mathcal{N}_{\mathrm{A}}$ the Avogadro number and M the $\beta\beta$ emitter molar mass. $N_{0\nu}^{\mathrm{excl.}}$ is the number of signal events excluded at a given confidence level (usually 90%), calculated with the Feldman-Cousins statistics from the total expected number of background events. The Feldman-Cousins statistics [41] is a wide-used method in rare events search experiments, providing confidence intervals for upper limits in the case of background events following a Poissonian probability law. We use this method in the framework of this analysis to provide a limit, at 90% CL, on the number of excluded signal events $N_{0\nu}^{\mathrm{excl.}}$, on the basis of the expected number of background events, given below.

- The $2\nu\beta\beta$ background
  Eq. (3.1) defines the lower limit on $T_{1/2}^{0\nu}$ from the number of excluded signal

events, and the signal selection efficiency $\epsilon_{0\nu}$. In a similar manner, we can define the number of expected $2\nu\beta\beta$ events, $N_{2\nu}$, from the half-life $T^{2\nu}_{1/2}$ and the $2\nu\beta\beta$ selection efficiency, $\epsilon_{2\nu}$, as

$$N_{2\nu} = \frac{\mathcal{N}_A \ln 2}{M} \times \frac{\epsilon_{2\nu} \times m \times t}{T^{2\nu}_{1/2}} \,. \tag{3.2}$$

- Natural radioactive backgrounds
  We consider the background selection efficiencies $\epsilon_{\text{rad.}}$ in a given energy window. The number of background events is therefore given, for the ^{208}Tl and ^{214}Bi internal contaminations, as

$$N^m_{\text{rad.}} = A^m_{\text{rad.}} \epsilon_{\text{rad.}} \times m \times t \,, \tag{3.3}$$

  where $A^m_{\text{rad.}}$ is the activity given in Bq/kg. Similarly, for the ^{222}Rn background,

$$N^V_{\text{rad.}} = A^V_{\text{rad.}} \epsilon_{\text{rad.}} \times V \times t \,, \tag{3.4}$$

  with $V = 15.3$ m^3 the total tracker volume, and $A^V_{\text{rad.}}$ represents here a volumic activity, given in Bq/m^3.

As we said, all equations from Eq. (3.1) to (3.4) are valid for a given energy range $[E_{\text{min}};E_{\text{max}}]$. To find the optimal energy interval for the search for the $0\nu\beta\beta$ decay, that is to say the one maximising the limit on $T^{0\nu}_{1/2}$, we must study the influence of the variations of E_{min} and E_{max} bounds on the final sensitivity. On Fig. 3.1, we observe that beyond the energy sum of 3 MeV, the total number of background events is highly reduced, and the ^{208}Tl background dominates, with 0.03 count expected for E> 3.2 MeV. This is why the upper limit E_{max} of the energy interval has only a limited impact on the search for the best ROI. It is then natural to study mainly the influence of the lower limit E_{min}.

In Fig. 3.2 is presented the variations of sensitivity with the ROI upper and lower bounds. We found that, for the demonstrator exposure, with ^{82}Se sources and a 25 Gauss magnetic field, and for the specified background activities, the best ROI is [2.7;3.15] MeV. As expected, as long as the upper bound is larger than 3.15 MeV, the sensitivity on the search for $0\nu\beta\beta$ is not affected. Therefore, this value is kept in order to enter into a future more general study, taking into account the neutron background of the experiment, which extends at high energies. In the optimised [2.7;3.15] MeV energy range, the sensitivity expected for the SuperNEMO demonstrator stands at

$$T^{0\nu}_{1/2} > 5.7 \times 10^{24}\,\text{y} \qquad (90\%\text{CL}) \,. \tag{3.5}$$

This result is compatible with the previous SuperNEMO analysis led by Steven Calvez [32].

Tab. 3.2 summarises the expected number of background events. As a matter of fact, the ROI would correspond to an energy range where background selection efficiencies are low, in order to maximise the $T^{0\nu}_{1/2}$. The dominating background in this range remains the $2\nu\beta\beta$ decay.

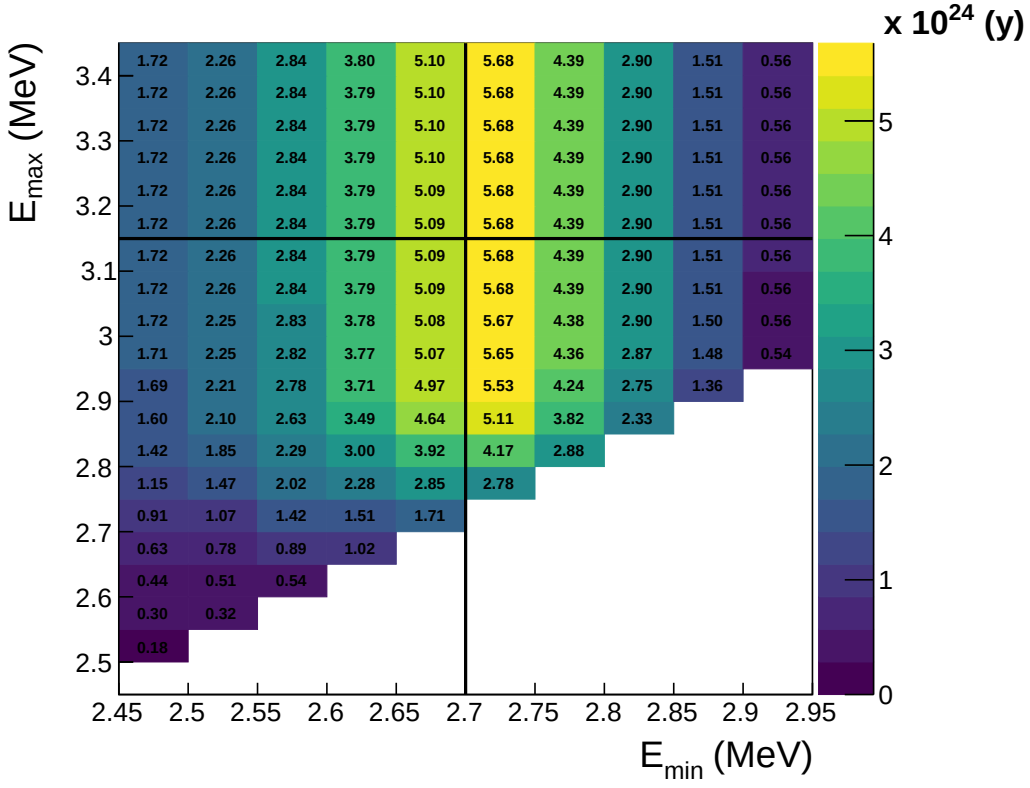

Figure 3.2: Two-dimensional histogram showing the evolution of the $T^{0\nu}_{1/2}$ 90% limit as a function of the ROI lower and upper energy bounds. The maximal lower limit of $T^{0\nu}_{1/2} > 5.7\times 10^{24}$ y (90% CL) is retained, in the [2.7;3.15] MeV region of interest.

Process	Event selection
$\epsilon_{0\nu}$	14.7%
$2\nu\beta\beta$	0.418
^{208}Tl	0.0475
^{214}Bi	0.0546
^{222}Rn	0.292
Total	0.394

Table 3.2: Selection efficiency of $0\nu\beta\beta$ events and expected number of backgrounds events in the optimised ROI [2.7;3.15] MeV, for the exposure of the SuperNEMO demonstrator (17.5 kg.y). The specified levels of contamination are considered.

3.3.2 Limit on the effective neutrino mass

The decay rate for the light Majorana exchange mechanism is reminded:

$$(T^{0\nu}_{1/2})^{-1} = g_A^4 G^{0\nu} |M^{0\nu}|^2 \left| \frac{m_{\beta\beta}}{m_e} \right|^2 . \tag{3.6}$$

where $G^{0\nu}$ is the two particles phase space factor, depending on $Q_{\beta\beta}$ and Z the number of protons, $M^{0\nu}$ is the nuclear matrix elements for the $0\nu\beta\beta$ process, and

$m_{\beta\beta}$ is the effective Majorana neutrino mass, defined as

$$\langle m_{\beta\beta} \rangle = \left| \sum_i m_i U_{ei}^2 \right| , \tag{3.7}$$

where m_i are the neutrino masses, and U_{ei}^2 is the mixing matrix. Therefore, the effective mass takes into account the neutrino mixing. Consequently, observing the $0\nu\beta\beta$ decay would not only prove the Majorana nature of neutrinos but, assuming the mass mechanism, could also help constraining the absolute neutrino masses. Given g_A, $G^{0\nu}$ and $M^{0\nu}$ [42, 43], we find the SuperNEMO demonstrator could reach a limit on the effective neutrino mass of

$$\langle m_{\beta\beta} \rangle < [0.24 - 0.47] \text{ eV} \qquad (90\%\text{CL}) . \tag{3.8}$$

Although this limit is not competitive with other current $0\nu\beta\beta$ experiments, this is an improvement compared to NEMO-3, demonstrating that SuperNEMO's technology would benefit from being adapted to larger scales.

In this section, we presented the general procedure leading to an optimised result on the $T_{1/2}^{0\nu}$ limit, and provided it for the SuperNEMO demonstrator, showing it is compatible with the previous studies led by the collaboration. Thereafter, we discuss the results obtained for different detector exposures (demonstrator and final detector), and different internal background activities. Also, and this is the main purpose of this study, we discuss the influence of the presence of the magnetic field on the final detector's sensitivity.

3.4 Impact of sources contamination levels on the sensitivity

We study the impact of the isotope contamination levels (inside the source foils, as well as on the tracker's wires) on the $0\nu\beta\beta$ sensitivity. We also optimise additional event selections aimed at improving it.

3.4.1 Contamination levels

Strict specifications have been defined for source foil contamination in order to achieve the target sensitivity for the final SuperNEMO detector (500 kg.y). BiPo detector and SuperNEMO collaboration measurements (Sec. 2.2.1) have shown that the ^{208}Tl level is not reached for the demonstrator source foils, being almost 27 times higher than expected, with $\mathcal{A}^{\text{Tl}} = 54$ μBq/kg [26 - 102]. Also, the ^{214}Bi contamination is not greater than 290 μBq/kg at 90% CL. If this upper limit was reached we would expect 1.6×10^5 internal Bismuth events in the total energy range. Fortunately, the Radon contamination does not exceed the specifications supposing a gas flow rate of 2 m^3/h inside the chamber. In the previous section we developed the general procedure allowing to set a 90% confidence interval limit on $T_{1/2}^{0\nu}$. The sensitivity limit computed for the SuperNEMO demonstrator, taking

into account the specified internal activities, could be affected by the higher-than-specified levels provided by BiPo.

In Fig. 3.3, $T^{0\nu}_{1/2}$ limits at 90 % CL and optimised ROI are compared for four distinct levels of internal contaminations, which are:

- the *zero activities* case, a hypothetical case where the source foils and the tracker are non contaminated at all by natural isotopes,
- the *specified activities* case, where the targeted level of contaminations would have been reached,
- and two *measured* cases. As the ^{214}Bi activity is provided by BiPo measurements as an upper limit, we choose to present the results either for sources that would not be contaminated by this isotope (the *without* ^{214}Bi case), or considering that the activity reached is 290 μBq/kg (*with* ^{214}Bi). The ^{208}Tl activity considered for these two measured cases is the limit at 90% CL.

Globally the sensitivity limit decreases with increasing background activities. However, no difference is observed in terms of half-life limits, or ROI, between the zero and specified activity cases. This is explained by an important phenomenon about the Feldman-Cousins statistics which is employed to determine the number of excluded signal events, $N^{\text{excl.}}_{0\nu}$, given the number of observed background events.

Clarifications on Feldman-Cousins statistics When the expected number of background events is negligible (which is the case for the zero and specified levels), the probability p to observe n_s signal events, expecting s events, is given by the Poisson distribution

$$p = \frac{e^{-s} s^{n_s}}{n_s!} \,. \tag{3.9}$$

Let's now put ourselves in the situation where no signal event is observed - that is what we assume to put a lower limit on the $0\nu\beta\beta$ half-life. Then $n_s \to 0$, and $p \to e^{-s}$. If zero signal event is *observed*, it is incorrect to assume that zero signal events were *produced* during the experiment. We only can say that no signal event has been observed *a priori*. To account for this particular case, the quantity s should no longer be viewed as the number of expected signal events, but as the number of excluded signal events, $N^{\text{excl.}}_{0\nu}$. In the end, for a negligible expected number of background events, and no signal event observed, we can set a lower limit on the number of excluded signal events, excluding values for which $p < \alpha$. Taking a 90% confidence interval, that is to say $\alpha = 10\%$, we obtain $s \leq 2.303$.

Therefore, no difference is observed between the two first activity cases presented because in both cases, the number of expected background events is too low compared with the 2.303 limit. For the two last activity cases, the number of background events in the ROI is no more negligible, and influences significantly the value of $T^{0\nu}_{1/2}$, decreasing the experiment's sensitivity by 23% (without ^{214}Bi) and 37% (with ^{214}Bi).

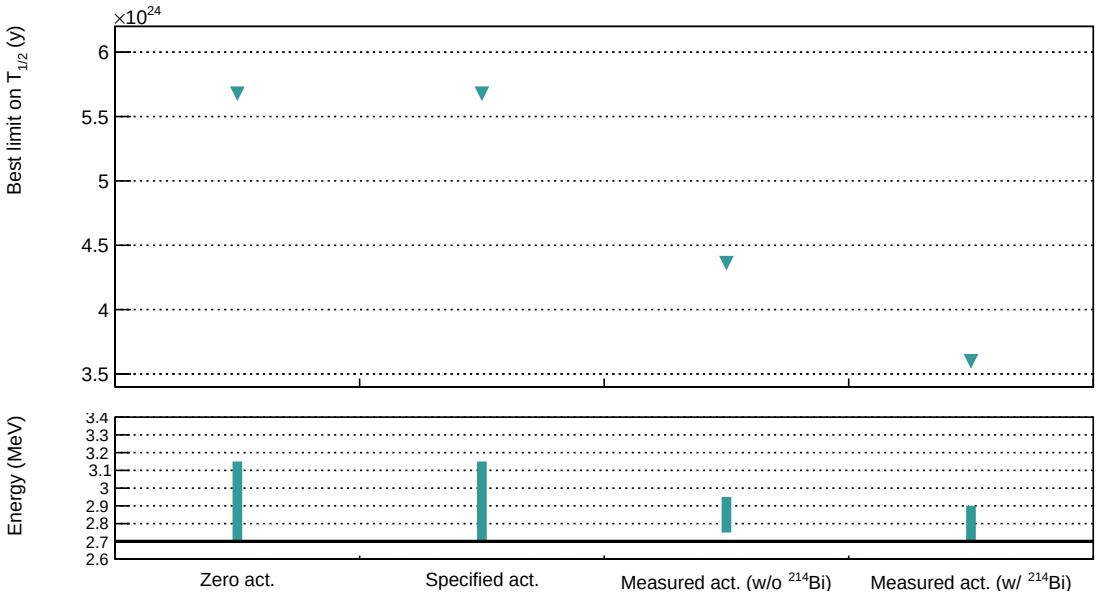

Figure 3.3: The 90% CL limit on the $0\nu\beta\beta$ half-life (top pad), and the corresponding ROI (bottom pad), as a function of the contamination level considered. For the *zero activities* case, we consider hypothetical contamination levels where $\mathcal{A}^{\mathrm{Bi}} = \mathcal{A}^{\mathrm{Tl}} = 0$ Bq/kg. The *specified activities* are presented in Tab. 2.3. The *measured activities*, provided by the BiPo detector [34], are presented in the same table. We consider successively a null ^{214}Bi contamination (*measured act. w/o* ^{214}*Bi*), or equals to the 290μ Bq/kg upper limit (*measured act. w/* ^{214}*Bi*).

Tab. 3.3 summarises the expected number of background events for the three non-zero contamination cases presented in Fig. 3.3. Regions of interest, optimised for each activity, are reminded. For the two measured cases, both optimised regions of interest are highly reduced, especially for the case without ^{214}Bi, where the lower bound is increased from 2.7 to 2.75 MeV. As this 50 keV wide energy region is populated with a non-negligible number of background events, this change in $\mathrm{E_{min}}$ usefully reduces the $2\nu\beta\beta$ background contribution, thereby limiting the increase of total expected number of background.

Activity ROI	Specified [2.7;3.15] MeV	Measured (w/o ^{214}Bi) [2.75;2.95] MeV	Measured (w/ ^{214}Bi) [2.7;2.9] MeV
$\epsilon_{0\nu}$	14.7%	11.3%	14.3%
$2\nu\beta\beta$	0.418	0.122	0.418
^{208}Tl	0.0475	0.688	0.699
^{214}Bi	0.0546	0	1.55
^{222}Rn	0.292	0.173	0.287
Total	0.812	0.983	2.95

Table 3.3: Selection efficiency of $0\nu\beta\beta$ events and expected number of backgrounds events in the optimised ROI, for the exposure of the SuperNEMO demonstrator (17.5 kg.y). Three levels of contamination are considered.

The degradation of the limit on the $0\nu\beta\beta$ half-life with the level of contamination remains acceptable. However, we can try improving the situation by exploring new background rejection techniques. This would be especially useful for the final detector case, where a slight increase in internal contaminations could be highly harmful, all the more so as the upper limit given for ^{214}Bi turns out to be the true contamination level.

3.4.2 Optimisation of event selection

Following the BiPo radiopurity measurements, we wish to implement additional event selections, to reject a higher quantity of background. Most of the double beta experiments are only sensitive to the total electron energy sum. The unique SuperNEMO tracko-calo technology confers the experiment the ability to characterise single particles (individual energies, emission angles...). Based on previous studies [32, 44], *topological cuts*, relying on these additional observables, can be set up. They are especially designed to reject events where the two electrons are not emitted simultaneously, or from the same location on the source foils.

3.4.2.1 The internal probability

Based on time-of-flight (TOF) computation, the internal probability (P_{int}) is derived from the internal χ^2_{int} (see details in Sec. 2.3.3). In Fig. 3.4 are presented the internal probability spectra for the $0\nu\beta\beta$ signal and all background processes, after the first-order selections. These distributions are normalised to the double beta half-lives, and the nominal activities. Equivalent distributions, but with different ^{214}Bi and ^{208}Tl contamination levels, can be derived for the case of measured activities. The internal probability distributions for the $0\nu\beta\beta$ and $2\nu\beta\beta$ processes follow the expected flat distribution for electrons emitted simultaneously from the source. As internal Bismuth disintegration actually takes place inside the sources, the ^{214}Bi distribution is also flat. The same could have been assumed for Thallium, however, the distribution is distorted at low internal probabilities. This might be explained by the existence of a metastable excited state ($\tau_{1/2} = 294ps$) of the daughter nuclei, which would slightly delay the second electron emitted via internal conversion. This feature is addressed in detail in Chap. 4. The Radon, being a non-internal background, presents a large peak at low internal probabilities.

We want to evaluate the influence of a cut-off on the simulations using internal probability as a rejection criterion: simulated events are selected only if their P_{int} value is upper than a given limit. The standard value applied in NEMO-3 analyses was $P_{int} > 4$ %. We wish to establish the most adequate P_{int} selection level for the SuperNEMO demonstrator. To do so, we vary the P_{int} minimal value applied on simulations, and for each we evaluate the limit reached on $T^{0\nu}_{1/2}$ (at a 90 % confidence interval), as well as the optimised ROI. The best internal probability cut-off value to be applied is the one maximising this sensitivity, and is specific for each contamination level.

We depict in Fig. 3.5 a set of four figures that help to better understand this optimisation. We consider two levels of contamination, the specified and measured

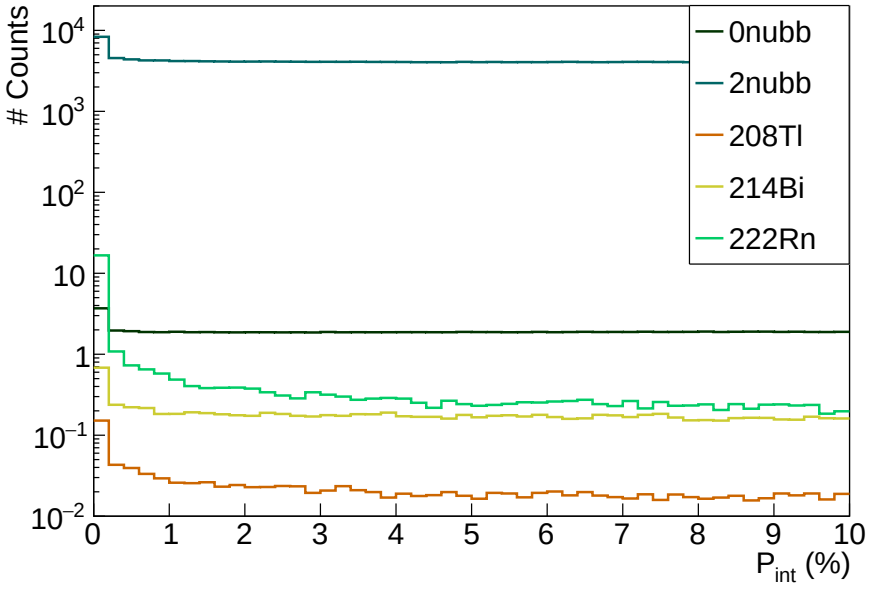

Figure 3.4: Internal probabilities for all processes. First-order cuts have been applied. $\beta\beta$ distributions are normalised to the half-lives, and background processes are normalised to the specified activities.

contamination levels (taking the upper limit for ^{214}Bi). We first detail these figures for the case of the specified activities and then explain what we observe for the measured activities.

Specified activities The total expected number of background in the ROI (Fig. 3.5a) is very low compared to one: it is smaller than 0.8 for $P_{int} > 0\%$, and slightly decreases when the minimal cut on P_{int} increases. Therefore, the number of excluded signal events, $N_{0\nu}^{excl.}$, is set to its minimal value of 2.303, regardless of the P_{int} level. As a consequence, the ROI bounds are stable (Fig. 3.5b) and thus $\epsilon_{0\nu}$ is only impacted by the P_{int} level applied which makes it decrease (Fig. 3.5c). All these observations allow to understand the evolution of $T_{1/2}^{0\nu}$ (Fig. 3.5d), decreasing with the P_{int} level applied on simulations. The sensitivities displayed for a 0% cut-off on P_{int} of course correspond to the results given in Fig. 3.3.

Measured activities The total number of expected background event in the ROI is higher than for the specifications. Nevertheless, this level is too low for the P_{int} cut-off to have an impact on it, and the number of expected background remains globally constant. When the minimal acceptable P_{int} is changed from 0 to 1 %, the ROI upper bound increases from 2.9 to 3.05 MeV. Usually, the variation of this bound does not have such a great impact on the event selection. Nevertheless, in the measured activities case, for a $P_{int} > 0$ % level, the ROI is optimised at the narrow [2.7;2.9] MeV interval, where the upper bound is located in an energy region still populated by signal. Therefore, even small variations of this upper bound has a great impact on the $0\nu\beta\beta$ selection efficiency, explaining its local increase for P_{int} cut-off between 0 and 1%. For P_{int} selections greater than 1 %,

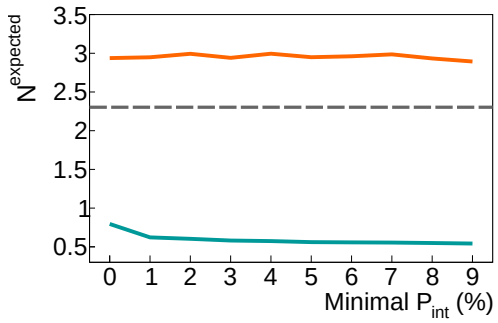

(a) Total expected number of background in ROI.

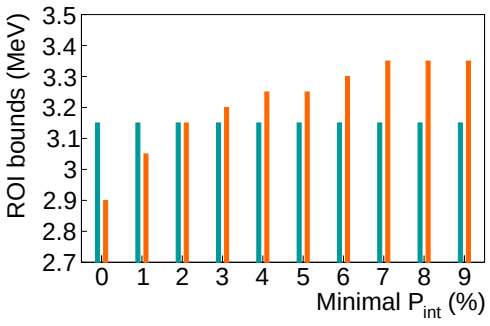

(b) ROI optimisation.

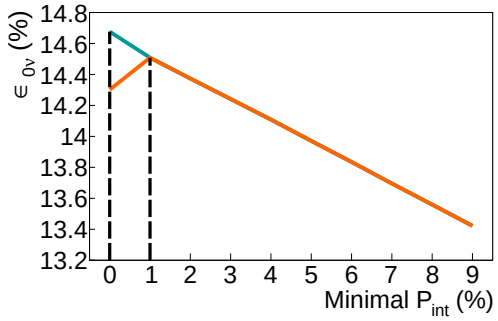

(c) $0\nu\beta\beta$ selection efficiency in ROI.

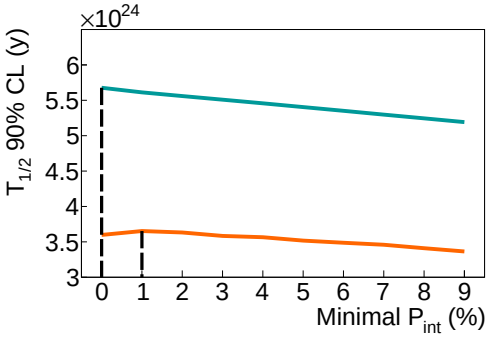

(d) Limit on $T^{0\nu}_{1/2}$.

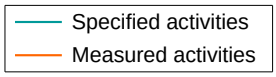

Figure 3.5: Total number of expected background in ROI (a), evolution of the regions of interest (b), $0\nu\beta\beta$ selection efficiency in ROI (c), and limit set on $T^{0\nu}_{1/2}$ at 90% CL (d), as a function of the cut-off applied on internal probability, P_{int}. The ROI is optimised for each P_{int} value. Results are displayed for two contamination levels: the specified (blue) and the measured (orange) activities (taking into account the upper limit provided for ^{214}Bi). An exposure of 17.5 kg.y is considered. Two vertical dashed lines in (c) and (d) display the best P_{int} selections to be applied in order to improve the $T^{0\nu}_{1/2}$ sensitivity of the experiment.

we come back in cases where the upper bound of the ROI no longer has an impact on $\epsilon_{0\nu}$. At this level, only variations of the total number of background events have an impact. As the limit set on $T^{0\nu}_{1/2}$ depends directly on $\epsilon_{0\nu}$, the variations presented in Fig. 3.5c fully explain the results displayed in Fig. 3.5d, presenting the evolution of $T^{0\nu}_{1/2}$ with the internal probability selection level.

The optimisation work we have just presented is of interest in the case of measured activities, where the cut-off on P_{int} is set at 1%. We will see in the following sections that this optimisation is also be useful, especially when studying the influence of the magnetic field. However, this rejection criterion has only a limited impact on the improvement of $T^{0\nu}_{1/2}$ sensitivity for the specified activities, because of the very low contamination levels considered. Indeed, paradoxically, the selection on internal probability worth it only if there is enough background

events to be rejected, as we can start observing for the measured activities case. Nevertheless, in that case, we recommend to keep at least a loose cut-off at $P_{int} > 4$ %. Indeed, this only slightly degrades the sensitivity (around 4%) while insuring the rejection of potential harmful external backgrounds for a more general study.

3.4.2.2 Vertices distance

NEMO-3 analyses also used the distance between the reconstructed vertices on the source foils as a background rejection criterion. As we have shown that the additional P_{int} cut-off is poorly adapted for the low activities of SuperNEMO sources, it is interesting to know if we can improve the results by using this second selection. Thanks to the trajectory fitting algorithm, we have access to the (Y, Z) coordinates of the latter, and by extension, to the distance between them. In the previous studies, the choice was made to look at the effect of this selection, separately on the Y (perpendicular to the wires) and Z (parallel to the wires) directions. We choose to follow the same approach, and we give the results for a cut along the Z axis, but the conclusions remain valid for the Y direction. Fig. 3.6 shows the distributions of the absolute value of the distance between foil vertices for each process studied. We would use this information in order to maximise the double β decays to be selected, while rejecting natural isotope disintegrations.

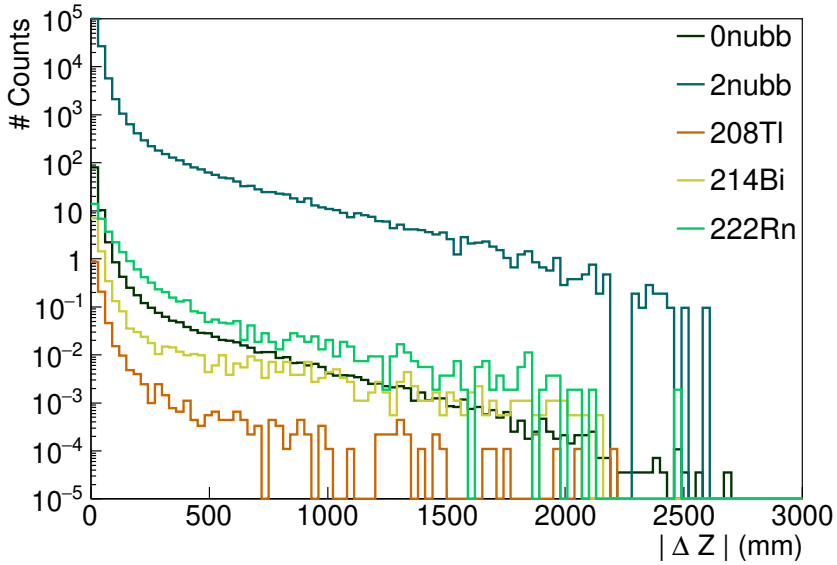

Figure 3.6: Distance along the Z direction between the vertices of the 2 reconstructed electrons, for each process considered. The $2\nu\beta\beta$ spectrum is normalised to $T^{2\nu}_{1/2} = 9.39 \times 10^{19}$ y, and ^{208}Tl, ^{214}Bi and ^{222}Rn backgrounds are normalised to the nominal activities. The amplitude of the $0\nu\beta\beta$ is arbitrarily set at the 90% limit obtained with NEMO-3. No energy cut is applied.

In the same way as the previous paragraph, Fig. 3.7 displays all informations leading to the maximisation of $T^{0\nu}_{1/2}$, allowing to study the impact of the vertices distance cut-off on the final sensitivity. Overall, these figures show us that too strict

cut-off on the distance between vertices would lead to a decrease in sensitivity. Because of the variations of the $0\nu\beta\beta$ selection efficiency and the total number of background events, the $T^{0\nu}_{1/2}$ distributions reaches a plateau, corresponding to the sensitivities achieved with the first-order cuts and optimised P_{int}. In practice, as it is done for P_{int}, a selection on vertex distance will always be applied, even if it is very loose, as such a cut-off could be useful for rejecting unexpected background (coincidence between independent events, for instance). We recommend to apply a loose cut-off level at $|\Delta Z| < 80$ mm, which does not degrade significantly the sensitivity. The same conclusions apply to the $|\Delta Y|$ cut-off.

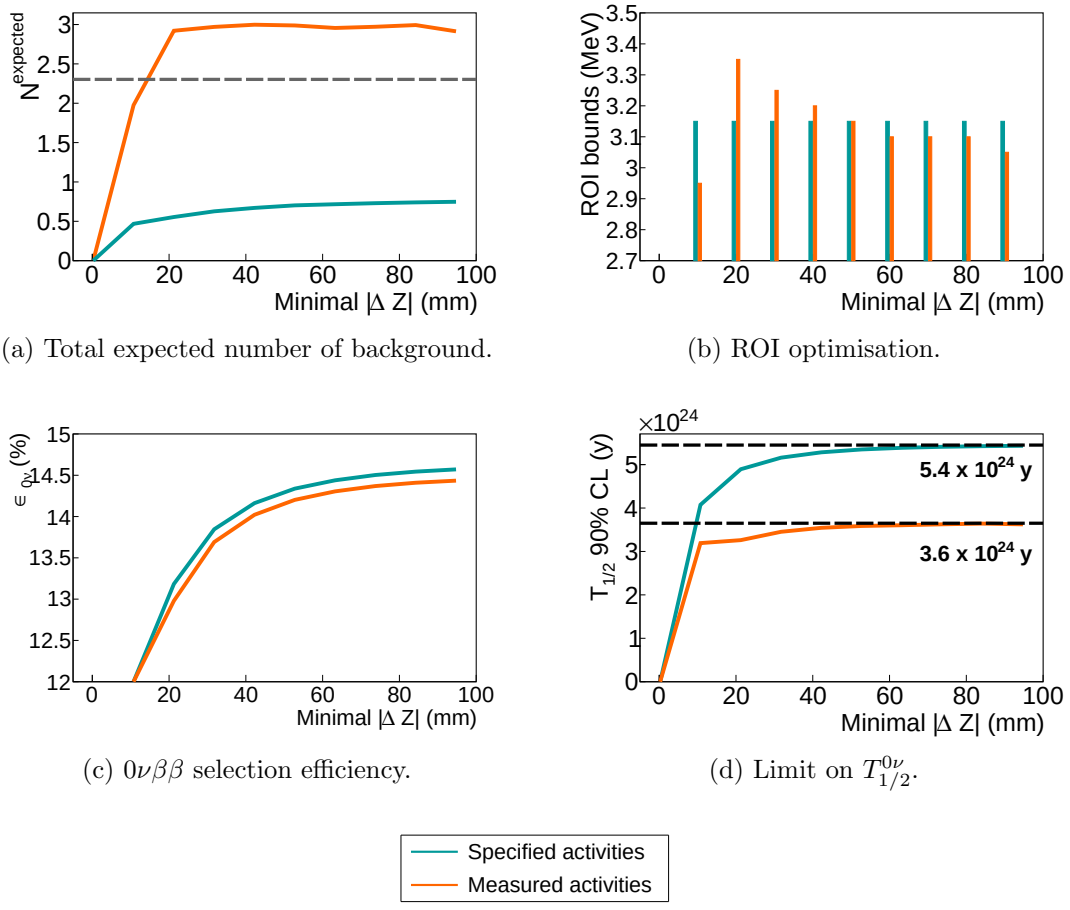

(a) Total expected number of background.

(b) ROI optimisation.

(c) $0\nu\beta\beta$ selection efficiency.

(d) Limit on $T^{0\nu}_{1/2}$.

Figure 3.7: Total number of expected background in ROI (a), evolution of the regions of interest (b), $0\nu\beta\beta$ selection efficiency in ROI (c), and limit set on $T^{0\nu}_{1/2}$ at 90% CL (d), as a function of the cut-off applied on distance between vertices, $|\Delta Z|$. The ROI is optimised for each $|\Delta Z|$ cut. Results are displayed for two contamination levels: the specified (blue) and the measured (orange) activities (taking into account the upper limit provided for ^{214}Bi). An exposure of 17.5 kg.y is considered.

The idea of having implemented these two selections (on the internal probability and on the distance between vertices) comes from a previous NEMO-3 analysis on the background rejection. For the SuperNEMO demonstrator case, the levels of

contaminations we are dealing with is remarkably low for most of the topological cut-offs to be worth applying. However, in practice, applying loose topological selections on the data remains necessary, especially to reject external background events. The minimal cut-off level to be applied is $P_{int} > 4\,\%$ and $|\Delta Z| < 80$ mm (similarly for $|\Delta Y|$), and can be optimised by taking into account the sources activity.

For future studies, it is useful to give the efficiencies of these loose selections, for the signal and for each background considered (Tab. 3.4a), as well as the expected number of background in the ROI (Tab. 3.4b). The selection efficiencies show topological cuts have a huge impact on Radon selection, as they are especially designed to reject non-internal events. The P_{int} cut-off is also efficient in rejecting Thallium internal events, because of the existence of a metastable exited state, described earlier. A special technique to reject efficiently ^{208}Tl background is also addressed in Chapter 4.

Cut-off	First-order cuts (%)	Internal probability (%) $P_{int} > 4\%$	Vertex distance (%) $\lvert \Delta Z \rvert < 80$ mm
$0\nu\beta\beta$	26.9	25.3	24.7
$2\nu\beta\beta$	9.15	8.56	8.21
^{208}Tl	0.106	0.0889	0.0846
^{214}Bi	0.168	0.151	0.144
^{222}Rn	0.0177	7.91×10^{-3}	5.34×10^{-3}

(a) Selection efficiencies for the three levels of selection (first-order, P_{int} and vertex distance), in the full energy range.

Activity	Specified		Measured (w/ ^{214}Bi)	
Cut-off	$P_{int} > 4\,\%$	$\lvert \Delta Z \rvert < 80$ mm	$P_{int} > 4\,\%$	$\lvert \Delta Z \rvert < 80$ mm
ROI (MeV)	[2.7;3.15]	[2.7;3.15]	[2.7;3.25]	[2.7;3.3]
$\epsilon_{0\nu}$	14.1%	13.9%	14.1%	13.9%
$2\nu\beta\beta$	0.392	0.383	0.392	0.383
^{208}Tl	0.0338	0.0323	1.08	1.09
^{214}Bi	0.0491	0.0491	1.42	1.42
^{222}Rn	0.115	0.0782	0.115	0.0782
Total	0.590	0.543	3.01	2.97

(b) Selection efficiency of $0\nu\beta\beta$ events and expected number of backgrounds events in the optimised ROI, for the exposure of the SuperNEMO demonstrator (17.5 kg.y), for successive application of topological selections. Specified and measured activities (taking into account the upper limit for ^{214}Bi contamination) are considered.

Table 3.4: The selection efficiencies and expected number of background events for the topological selections.

After the topological cut-off optimisation, the SuperNEMO demonstrator would reach a sensitivity of $T^{0\nu}_{1/2} > 5.4 \times 10^{24}$ y if specified activities are reached, corresponding to the effective neutrino mass range $\langle m_{\beta\beta} \rangle < [0.25 - 0.48]$ eV. For the measured activities, supposing ^{214}Bi activity reaches the measured upper limit, $T^{0\nu}_{1/2} > 3.6 \times 10^{24}$ y and $\langle m_{\beta\beta} \rangle < [0.31 - 0.59]$ eV.

In the following we review the influence of the 25 Gauss magnetic field inside the detector on the sensitivity reachable by the SuperNEMO demonstrator, and evaluate the usefulness of the topological cut-offs in that case.

3.5 Impact of the magnetic field on the sensitivity

The SuperNEMO demonstrator was originally designed with a copper coil, similarly to NEMO-3, delivering a magnetic field inside the tracker volume. This 25 Gauss magnetic field is high enough to bend the trajectory of the few MeV electrons and positrons of interest for SuperNEMO, without too strongly preventing them from reaching the calorimeter. In practice, this magnetic field is mainly used to identify and reject the electron-positron pairs created by high energy γ's, themselves emitted after a neutron capture. However, as explained in sub-section 3.1.3, we choose to not consider the contribution of this external background for this study's background model. We therefore focus on evaluating the influence of the presence of the magnetic field on the rejection of natural isotopes disintegrations and on the $0\nu\beta\beta$ selection efficiency.

3.5.1 Simulations of the magnetic field

In order to study the influence of the magnetic field on the demonstrator sensitivity to the $0\nu\beta\beta$ decay, the simulations and reconstructions of signal and backgrounds have been performed in two different conditions.

- Simulations with a uniform 25 Gauss magnetic field (following recommendations [32]). Results about the final sensitivity achieved in this condition have already been presented earlier in this chapter. The possible variations of the field intensity, mainly due to the calorimeter magnetic shields, are not taken into account for these simulations. This will be discussed in sub-section 3.5.4.

- Simulations where the magnetic field is turned off.

Each magnetic field condition has the same number of simulated events, as summed up in Tab. 3.1.

Depending on the case under consideration, the charged particles do not have the same trajectory curvature. In the first uniform on-field case, they are bended. The track fit algorithm then performs two distinct trajectory fittings: one with a helix and one with a line. The most accurate fit is chosen and provides information on the charge of the detected particle. In the second off-field case, the fitting algorithm is modified to fit only linear trajectories.

3.5.2 Impact of the magnetic field on signal and background selections

Among first-order event selection criteria considered in Sec. 3.2, the one on the trajectory curvature is of primary importance with regard to the influence of the magnetic field on the final sensitivity. Indeed, when the magnetic field is switched on, a particle is identified as an electron when the trajectory fitting results in a negative curvature. When the magnetic field is switched off, the trajectory of the charged particles takes place in a straight line[3]. This last selection criterion on the track curvature is then no longer applied.

Consequently, the number of identified $2e$ topologies selected by the first-order cuts is increased for the off-field case because the event selections are less strict. To illustrate this effect, we give in Tab. 3.5 the selection efficiencies of signal and background in the total energy range [0;4] MeV, for the two cases of magnetic field. The $0\nu\beta\beta$ efficiency increases, as well as the one of backgrounds. In particular, the Radon efficiency increases very significantly. Indeed, in some cases, the two electrons resulting from the decay of Bismuth on the tracker wires can be emitted back to back. One of the two electrons can subsequently pass through the source in the direction of the opposite calorimeter. When this decay takes place close to the source, it is arduous to reconstruct a helix in the presence of a magnetic field, and this type of event is easily rejected. Whereas without a field there is no selection of curvature so these events are more likely to be selected.

Field	On	Off
$0\nu\beta\beta$	26.9	31.4
$2\nu\beta\beta$	9.16	10.6
^{208}Tl	0.106	0.169
^{214}Bi	0.168	0.252
^{222}Rn	0.0177	0.0924

Table 3.5: Selection efficiencies (%) in the full energy range [0;4] MeV, for on and off-field cases. First-order cut-offs have been applied.

We compare the variations of selection efficiencies in the ROI these in Tab. 3.6 for the two field cases. The selection efficiencies of $\beta\beta$ decays are disadvantaged by the lower bound of the ROI for the off-field case. The slight variation of the ROI upper bound have a measurable impact on the expected number of ^{208}Tl events, as this background has a contribution at high energies. The increase of ^{222}Rn events, despite the ROI lower bound variation, is directly explained by the phenomenon, described above, of selecting $2e$ events issued back to back close to the source. These observations result in a decrease in sensitivity when the field is switched off, giving

$$T^{0\nu}_{1/2} > 4.8 \times 10^{24}\,\mathrm{y} \qquad (90\%\mathrm{CL})\,(\text{off-field}). \tag{3.10}$$

[3]In saying this, we do not take into account possible deviations in the trajectory of the particles, due in particular to multiple scattering in the tracker.

Field	On [2.7;3.15] MeV	Off [2.75;3.2] MeV
$\epsilon_{0\nu}$	14.7%	12.4%
$2\nu\beta\beta$	0.418	0.0353
^{208}Tl	0.0475	0.0600
^{214}Bi	0.0546	0.0452
^{222}Rn	0.292	0.553
Total	0.812	0.693

Table 3.6: Selection efficiency of $0\nu\beta\beta$ events and expected number of backgrounds events in the optimised ROI, for the exposure of the SuperNEMO demonstrator (17.5 kg.y). Specified activities are considered. The two on- and off-field cases are compared. First-order cut-offs have been applied.

As concluded in Sec. 3.4, topological selections are especially efficient in rejecting the Radon background. Therefore, the application of these additional cut-offs, for the off-field case, could be interesting, in order to increase the sensitivity. Following the work presented in the previous section, we optimise these selections for the particular off-field case, both for the specified and measured contamination levels[4]. Fig. 3.8 summarises the results obtained in sensitivity before and after application of these topological cut-offs. The left part of the panel gives information on the evolution of sensitivity, when only the first-order cut-offs are applied. We come back to the conclusions given above: when the magnetic field is switched-off, we lose sensitivity, regardless of the level of contamination considered. On the right side of the figure, we present the results when the topological cuts are applied. For the on-field case, the addition of these selections have almost no effect on the sensitivity, as concluded in sub-section 3.4.2. However, as predicted, we are beginning to see the usefulness of these selections in the off-field case, as a higher number of ^{208}Tl and ^{222}Rn events passed the first-order selections. For instance, for the specification case, $T^{0\nu}_{1/2}$ goes from 4.8×10^{24} y to 6.1×10^{24} y, an improvement of $\sim$ 30%.

In Tab. 3.7 are presented the expected number of background events in the ROI for the off-field condition, before and after application of topological cut-offs, for the specified and measured activities (taking into account the upper limit for the ^{214}Bi contamination). This selection allows to reject mainly ^{222}Rn background.

Finally, even if the absence of the magnetic field has the effect of reducing the sensitivity to the $0\nu\beta\beta$ decay, topological cuts allow this effect to be compensated for, making it possible to reach higher values of $T^{0\nu}_{1/2}$.

[4] As done in sub-section 3.4.2, for the Bismuth measured contamination, we consider here the upper limit where $\mathcal{A}^{\mathrm{Bi}} = 290$ μBq/kg.

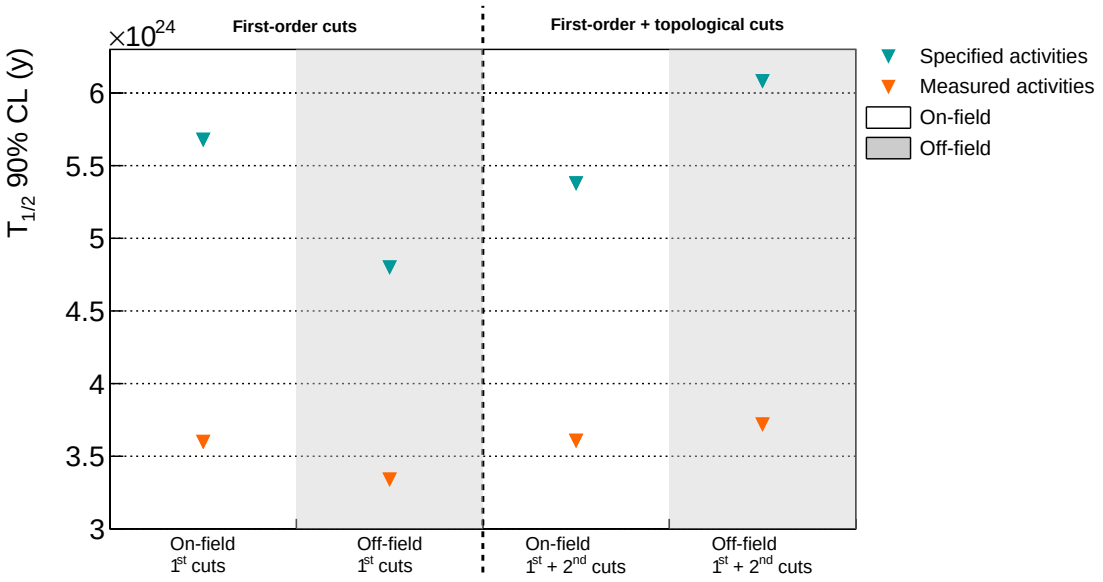

Figure 3.8: $T^{0\nu}_{1/2}$ (90% CL) considering various conditions: on- and off-field (white and grey stripes), first-order and addition of topological cut-offs (left/right parts of the panel), specified and measured activities (blue and orange triangle markers). The measured activities are $\mathcal{A}^{\mathrm{Tl}} = 54$ μBq/kg, $\mathcal{A}^{\mathrm{Bi}} = 290$ μBq/kg and $\mathcal{A}^{\mathrm{Rn}} = 0.15$ mBq/m^3.

Activity	Specified		Measured (w/ ^{214}Bi)	
Cut-off	First-order	Topological	First-order	Topological
ROI (MeV)	[2.75;3.2]	[2.7;3.2]	[2.65;2.9]	[2.7;2.9]
$\epsilon_{0\nu}$	12.4%	15.7%	19.1%	14.8%
$2\nu\beta\beta$	0.0353	0.453	1.56	0.440
^{208}Tl	0.0600	0.0506	1.01	0.613
^{214}Bi	0.0452	0.0706	2.94	1.84
^{222}Rn	0.553	0.0894	1.42	0.0689
Total	0.693	0.664	6.93	2.96

Table 3.7: Selection efficiency of $0\nu\beta\beta$ events and expected number of backgrounds events in the optimised ROI, for the exposure of the SuperNEMO demonstrator (17.5 kg.y), with off-field condition. Specified and measured (with ^{214}Bi) activities are considered. Topological cut-offs are optimised: $\mathrm{P}_{int} > 4\%$ and $|\Delta Z| < 80$mm (specified activities), $\mathrm{P}_{int} > 5\%$ and $|\Delta Z| < 80$mm (measured activities)

3.5.3 Influence of the magnetic field on optical modules and reconstruction efficiency

In the previous sub-section, a comparative study has been led to evaluate the influence of the presence of a magnetic field on the event selection, and thus on the final sensitivity. However, as things stand now, some features of the demonstrator are not yet implemented in the simulation software, and could have

a great impact on the results presented above. In particular, studies have been led by the collaboration to evaluate the influence a 25 Gauss magnetic field on the optical modules, as well as on the event reconstruction [32, 33].

SuperNEMO PMTs are protected from the external magnetic field by individual iron shields. Unfortunately, the latter do not perfectly protect the PMTs, and a residual magnetic field is measured inside the shieldings, leading to losses in charge collected by PMTs close to 8%. This study also revealed the energy resolution would be worsened with a relative decrease of 3% of the initial value of 8% at 1 MeV. Moreover, the PMTs shieldings could themselves severely impact the shape of the field lines, as well as its intensity. In fact, with a 25 Gauss magnetic field generated by the copper coil, the magnetic shields are responsible for the field strength decreasing, and barely 10 G is expected near the source foils. Worse, the magnetic field strength decreases very quickly as we get closer to the calorimeter walls, where nearly 0 G could be expected. The reconstruction efficiency could therefore be greatly impacted: the magnetic field intensity varying from the source foils to the calorimeter wall, electrons trajectory curvatures are not constant, and the track-fitting algorithm is less performing. An incorrect description of the distribution of the magnetic field would more strongly impact low-energy electrons.

In the light of these conclusions, it could be interesting to study the evolution of the sensitivity, considering field simulations with more realistic variations inside the detector.

3.5.4 Simulations with a non-uniform magnetic field

Simulations with a 25 Gauss *mapped* magnetic field have been performed, taking into account more realistic variations of the field inside the detector [45]. In this condition, the fitting algorithm follows the same steps as for on-field: a helix and linear fit are performed for each simulated event, and the most accurate is selected. Unfortunately, Radon isotope decays could not be simulated with this magnetic field configuration. Indeed, as it is present in the entire wire chamber, simulations would have required too many additional storing resources. Thus, strong conclusions on the sensitivity can't be given. However, it is possible to assess the selection efficiencies of the different processes, and then get an idea of the influence of realistic variations of the field on the final results.

Tab. 3.8 compares the selection efficiencies, for the three field cases (uniform on-field, mapped field and off-field), in the total energy range [0;4] MeV. The mapped field case has lower selection efficiencies, compared with uniform field simulations. As announced in the previous sub-section, the magnetic shields distort the field intensity across the detector. Therefore, the fitting algorithm is less efficient in identifying particles with a negative curvature inside the tracker, hence the number of selected $2e$ topologies is decreased.

Tab. 3.9 presents the expected number of background events in the energy range [2.7;3.2] MeV, for simulations using the realistic mapped field. As expected, the $0\nu\beta\beta$ selection efficiency is drastically decreased compared with the on-field case, as well as the expected number of background events. As explained above,

Field P_{int}	On $P_{int}> 4\%$	Off $P_{int}> 1\%$	Mapped $P_{int}> 4\%$
$0\nu\beta\beta$	24.7	29.3	19.1
$2\nu\beta\beta$	8.21	9.93	6.39
^{208}Tl	0.0846	0.140	0.0774
^{214}Bi	0.144	0.211	0.125

Table 3.8: Signal and background selection efficiencies (%) for on-field, off-field and mapped-field cases, in the energy range [0;4] MeV. The first-order and optimised topological cut-offs have been applied. Especially, for all field conditions, $|\Delta\ Z| < 80$ mm.

the selection on track curvature is still applied in this case, and the non-uniform magnetic field causes deviations in the particles trajectory, which are therefore more difficult to identify as electrons. Even if Radon simulation with such field conditions are unavailable, it is interesting to provide an order of magnitude of the $T^{0\nu}_{1/2}$ limit set with these realistic variations of the field. To do so, we extrapolate the expected number of Radon events in the [2.7;3.2] MeV energy range, from the ^{214}Bi one. Indeed, we postulate the ratio between these two numbers remains constant, and the on-field simulations give $N_{\mathrm{Bi}}/N_{\mathrm{Rn}} \sim 5$. Taking this into consideration, a limit of $T^{0\nu}_{1/2} > 4 \times 10^{24}$ y (90 % CL) would be reached with the demonstrator, a ~ 30 % decrease compared with the non-realistic uniform case.

This approximation should be examined with caution, however, as magnetic field conditions can greatly influence the selection of Radon and Bismuth events. To be specific, we have seen in Sec. 3.5.2 that between off-field and on-field conditions, the Radon and Bismuth efficiencies varied differently. So, to ensure that our approximation is valid, a more proper study would have to be made. In particular, it would be necessary to study how events where the two electrons are emitted back to back from a wire of the tracker when the field is no longer uniform are treated.

	Mapped field
$\epsilon_{0\nu}$	10.4%
$2\nu\beta\beta$	0.245
^{208}Tl	0.0279
^{214}Bi	0.0535
Total	0.326

Table 3.9: Selection efficiency of $0\nu\beta\beta$ events and expected number of backgrounds events in the [2.7;3.2] MeV optimised ROI, for the exposure of the SuperNEMO demonstrator (17.5 kg.y), for mapped field simulations. The specified background activities are considered. First-order and optimised topological cuts have been applied ($P_{int}>$ 4% and $|\Delta\ Z| < 80$ mm).

3.6 Searching for the ^{150}Nd $0\nu\beta\beta$ decay

This study was conducted jointly with the PhD student Axel Pin, from CENBG [46]. Although we mainly developed together the whole analysis, I presented in detail in the previous sections the results regarding the influence of the magnetic field. Meanwhile, Axel Pin focuses on the possibility of changing the ^{82}Se material by other $\beta\beta$ isotopes. Indeed, on the model of the NEMO-3 detector, which housed, among others, 6.914 kg of ^{100}Mo and 0.932 kg of ^{82}Se, the SuperNEMO detector possesses the technical possibility of exchanging the source material and study several $\beta\beta$ isotopes. Notably, in the case SuperNEMO demonstrates the feasibility of a large-scale tracko-calo experiment, it would be natural to evaluate the sensitivity of SuperNEMO to the $0\nu\beta\beta$ decay of other isotopes than ^{82}Se.

3.6.1 Searching for the $0\nu\beta\beta$ of other isotopes

One of the distinctive features of NEMO detectors is the gaseous detector, designed to track charged particles. Unluckily, this advantage is also a great inconvenience when it comes to Radon contamination. Indeed, Radon enters by diffusion or emanates from the detector materials. It is then interesting to consider $\beta\beta$ candidates with an energy transition value above the Q_β = 3.27 MeV of ^{214}Bi, a ^{222}Rn daughter. Another useful criterion is the natural isotopic abundance: typically, considering only isotopic abundances greater than 2% is a reliable basis when selecting potential $\beta\beta$ emitters. Two nuclei satisfy these two criteria: ^{96}Zr and ^{150}Nd (with respective $Q_{\beta\beta}$ values of 3.35 and 3.36 MeV, and respective isotopic abundances of 2.8 and 5.6 % [47]). As the ^{150}Nd isotope has the highest $Q_{\beta\beta}$ value, the current section focuses on evaluating the SuperNEMO sensitivity to the $0\nu\beta\beta$ decay of this isotope, supposing we have several kg at our disposal. Moreover, the ^{150}Nd has a more favourable phase space than the ^{82}Se, on which the half-life limit directly depends.

3.6.2 Sensitivity to the $0\nu\beta\beta$ of ^{150}Nd

Until recently, ^{150}Nd was not enrichable in large quantities. Recent developments have resulted in the production of several grams, making this $\beta\beta$ isotope interesting for the search for $0\nu\beta\beta$. Thanks to that, NEMO-3 had available 36.6 g of ^{150}Nd which were recovered by the collaboration, for a possible reuse for SuperNEMO. The best limit for the search for neutrinoless double β decay of ^{150}Nd was reached by the NEMO-3 detector with 5.25 years of data acquisition. The detector achieved $T^{0\nu}_{1/2} > 2.0 \times 10^{23}$ y (90 % CL), corresponding to a range on the effective neutrino mass of $\langle m_{\beta\beta} \rangle < [1.6-5.3]$ eV. The collaboration also measured the $2\nu\beta\beta$ half-life, with $T^{2\nu}_{1/2} = [9.34 \pm 0.22 \text{ (stat.)} \pm ^{0.62}_{0.60} \text{ (syst.)}] \times 10^{18}$ y [48].

We wish to determine the limit on the $0\nu\beta\beta$ of the ^{150}Nd that could be reached with the SuperNEMO demonstrator, with an exposure of 17.5 kg.y. We lead this study considering the activities specified for the ^{82}Se sources are reached. We use simulations with the 25 Gauss uniform magnetic field. Fig. 3.9 depicts the

normalised energy distributions for the $2e$ topologies selected after application of first-order and topological selections.

Signal and background selection efficiencies for ^{150}Nd sources, in the total energy range, are given in Tab. 3.10. The selection efficiencies of backgrounds are lower for ^{150}Nd sources than for ^{82}Se sources. In both cases, for the total energy range the background contribution is dominated by the $2\nu\beta\beta$ decay. This is caused by the more elevated number of protons in the ^{150}Nd nucleus which induces a stronger Coulombian effect. Indeed, the more the $\beta\beta$ emitter has a high atomic number Z, the more the electrons emitted from inside the source (or passing through it) are likely to interact electromagnetically with it. Despite this, for reasons of limited storage resources, we choose to consider this effect to be negligible for events outside the source, such as ^{214}Bi disintegrations (from ^{222}Rn) from the tracker wires, and we choose to use the Radon simulations already generated for the ^{82}Se sources study. Clearly, future studies would rather use a new set of simulations for ^{222}Rn events and evaluate its influence on the sensitivity.

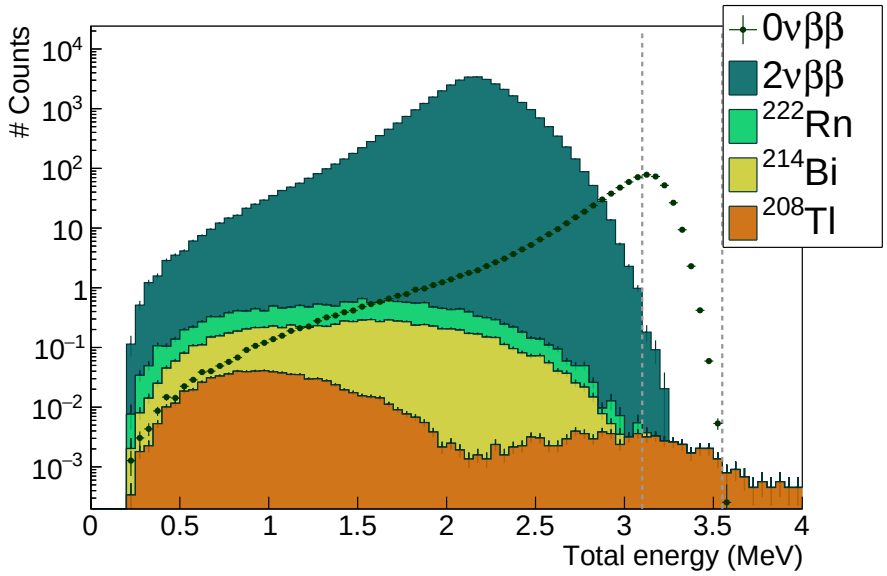

Figure 3.9: Total energy spectra for the $0\nu\beta\beta$ signal and main backgrounds, for ^{150}Nd sources and for a 17.5 kg.y exposure. The $2\nu\beta\beta$ spectrum is normalised to $T^{2\nu}_{1/2} = 9.34 \times 10^{18}$ y, and ^{208}Tl, ^{214}Bi and ^{222}Rn backgrounds are normalised to the nominal activities. The amplitude of the $0\nu\beta\beta$ is arbitrarily set at the limit obtained with NEMO-3 $T^{0\nu}_{1/2} = 2.0 \times 10^{23}$ y. First-order and optimised topological cuts have been applied. The ROI of [3.1;3.55] MeV is depicted by to vertical dashed lines.

In Tab. 3.11 we give the expected number of background events in the optimised ROI [3.1;3.55] MeV. The selection efficiency of the $0\nu\beta\beta$ decay in this energy range is also given. Although the $2\nu\beta\beta$ half-life of the ^{150}Nd is lower than that of the ^{82}Se by a factor $\sim$ 10, the number of $2\nu\beta\beta$ events in the ROI remains low. Indeed, thanks to the Coulombian effects described above, this process has a limited contribution at high energy. The high energy of transition $Q_{\beta\beta} = 3.36$ MeV

Isotope	^{82}Se	^{150}Nd
$0\nu\beta\beta$	25.8	25.5
$2\nu\beta\beta$	8.21	8.11
^{208}Tl	0.0846	0.0749
^{214}Bi	0.144	0.138
^{222}Rn	5.34×10^{-3}	5.34×10^{-3}

Table 3.10: Selection efficiencies in the full energy range [0;4] MeV, for ^{82}Se and ^{150}Nd sources. First-order and optimised topological cuts have been applied.

of ^{150}Nd implies that the contributions of ^{214}Bi and ^{222}Rn are very small, or even zero, because the ROI is optimised in a high energy range. The $2\nu\beta\beta$ and ^{208}Tl events are therefore the major contributors to the background. Consequently, if the choice of changing the source material with ^{150}Nd isotope was made, it would be conceivable to release the specifications on ^{214}Bi and ^{222}Rn backgrounds.

Isotope ROI	Selenium [2.7;3.15] MeV	Neodymium [3.1;3.55] MeV
$\epsilon_{0\nu}$	14.4%	10.3%
$2\nu\beta\beta$	0.39	0.28
^{208}Tl	0.044	0.029
^{214}Bi	0.053	5.6×10^{-4}
^{222}Rn	0.20	0.0
Total	0.687	0.309

Table 3.11: Selection efficiency of $0\nu\beta\beta$ events and expected number of backgrounds events in the optimised ROI, for the exposure of the SuperNEMO demonstrator (17.5 kg.y), for ^{82}Se and ^{150}Nd sources. The specified background activities are considered. First-order and optimised topological cuts have been applied.

The SuperNEMO demonstrator, with 7 kg of ^{150}Nd and 2.5 years of data acquisition, would achieve a $T^{0\nu}_{1/2} > 2.2\times 10^{24}$ y sensitivity, one order of magnitude higher than the best limit ever reached. The corresponding limit on the effective neutrino mass is $\langle m_{\beta\beta}\rangle = [0.15 - 0.50]$ eV. This is a better result than for ^{82}Se sources, as the ^{150}Nd has a more favourable phase space factor.

3.7 The final detector sensitivity

The ultimate goal of the SuperNEMO demonstrator is to show that the NEMO technology is scalable to probe unprecedented half-life on the $0\nu\beta\beta$ decay. The final detector would consist in building 20 modules similar to the demonstrator. In this context, we estimate the final detector sensitivity to the $0\nu\beta\beta$ decay.

We suppose the specified activities of $\mathcal{A}^{\mathrm{Tl}} = 2$ μBq/kg, $\mathcal{A}^{\mathrm{Bi}} = 10$ μBq/kg and $\mathcal{A}^{\mathrm{Rn}} = 0.15$ mBq/m^3 are reached. The simulations with an uniform magnetic field are used.

Tab. 3.12 shows the number of expected events in the optimised ROI for first-order and topological cut-offs. The total expected number of background events is high enough for the optimised cut-offs to be worth it, with $P_{int} > 4$ % and $|\Delta Z| < 80$ mm (similarly for $|\Delta Y|$). They allow primarily to reduce the Radon background by a factor 3. Due to the optimisation of the ROI, especially to the raising of the upper bound, the ^{208}Tl background is a little increased, without important consequences, as the $2\nu\beta\beta$ and ^{222}Rn dominate the total number of background in this energy range.

Cut ROI	First-order [2.75;2.95] MeV	Topological [2.75;3.1] MeV
$\epsilon_{0\nu}$	11.3%	10.7%
$2\nu\beta\beta$	3.48	3.36
^{208}Tl	0.728	0.756
^{214}Bi	0.945	0.835
^{222}Rn	6.93	2.16
Total	12.1	7.11

Table 3.12: Selection efficiency of $0\nu\beta\beta$ events and expected number of backgrounds events in the optimised ROI, for the exposure of the SuperNEMO final detector (500 kg.y). The specified background activities are considered. The topological selections have been optimised: $P_{int} > 4\%$ and $|\Delta Z| < 80$ mm.

With an exposure of 500 kg.y, the SuperNEMO final detector would reach a sensitivity of $T^{0\nu}_{1/2} > 5.4 \times 10^{25}$ y, with ^{82}Se sources, corresponding to $\langle m_{\beta\beta} \rangle = [0.079 - 0.15]$ eV. By comparison, with the same exposure and background specifications but with ^{150}Nd sources, the final detector would achieve a sensitivity of $T^{0\nu}_{1/2} > 2.2 \times 10^{25}$ y, in the [3.1;3.75] MeV ROI, corresponding to $\langle m_{\beta\beta} \rangle = [0.046 - 0.15]$ eV.

3.8 Conclusion

Latest measurements of source activities by BiPo-3 show that the specified background level for Thallium isotope is not reached, although it is improved on average by a factor 2, compared to NEMO-3. An upper limit is given for the internal Bismuth isotope activity. In addition, not all sources were measured and a precise measurement is expected to be provided by the SuperNEMO demontrator when data acquisition will begin. C-sections measurements with a concentration line showed the Radon targeted activity can be achieved for the demonstrator, with an gas flow rate of 2 m^3/h inside the chamber. Topological selections, designed to reject non-internal and non-simultaneous $2e$ events, have been optimised, and allowed to reduce the Radon background by a factor 3 for the final demonstrator. Assuming the target background activities are reached, the SuperNEMO demonstrator, running for two and half years with 7 kg of ^{82}Se, would be able to a set a limit on the $0\nu\beta\beta$ process $T^{0\nu}_{1/2} > 5.4 \times 10^{24}$ years,

translating into a limit on the neutrino effective mass $\langle m_{\beta\beta}\rangle < [0.25-0.48]$ eV[5]. Taking into account the measured activities (with 290 μBq/kg of ^{214}Bi), the limit on $T^{0\nu}_{1/2}$ would be decreased by a factor 33% with $T^{0\nu}_{1/2} > 3.6\times 10^{24}$ years ($\langle m_{\beta\beta}\rangle < [0.31-0.59]$ eV). This limit could be enhanced by using a multivariate analysis, similarly to what is done in other double beta decay experiments, taking advantage of the several topological variables offered by SuperNEMO.

Recent studies have shown that the 25 Gauss magnetic field would be distorted by detector materials, especially the calorimeter magnetic shields. In this context, we studied the influence of this field on the demonstrator sensitivity. Switching-off the field would enhance the expected number of $2e$ topologies, especially for background processes, and decrease the sensitivity. This effect is compensated by applying optimised topological cut-offs which are useful with such a level of background. Finally, without magnetic field, the SuperNEMO demonstrator would set a limit on the sensitivity of $T^{0\nu}_{1/2} > 6.1\times 10^{24}$ years ($\langle m_{\beta\beta}\rangle < [0.24-0.46]$ eV), taking into account the specified activities, a 13% increase on $T^{0\nu}_{1/2}$ compared with the on-field case. With the measured activities, $T^{0\nu}_{1/2} > 3.7\times 10^{24}$ years ($\langle m_{\beta\beta}\rangle < [0.30-0.58]$ eV), an improvement of 3% compared with the on-field case. Simulations with a mapped field have shown that the signal and background selection efficiencies would be degraded by a non-uniform, more realistic magnetic field.

Like its predecessor, the SuperNEMO demonstrator was designed to study several isotopes, such as the ^{150}Nd. Assuming the target background activities are reached for ^{150}Nd sources, the SuperNEMO demonstrator would achieve a $T^{0\nu}_{1/2} > 2.2\times 10^{24}$ years ($\langle m_{\beta\beta}\rangle < [0.15-0.51]$ eV).

Finally, assuming we reach the target background levels, the SuperNEMO final detector would achieve an unprecedented limit of $T^{0\nu}_{1/2} > 5.4\times 10^{25}$ years for ^{82}Se sources, corresponding to $\langle m_{\beta\beta}\rangle < [0.079-0.15]$ eV. For ^{150}Nd sources, the half-life $T^{0\nu}_{1/2} > 2.4\times 10^{25}$ years would be reached. This corresponds to $\langle m_{\beta\beta}\rangle < [0.046-0.15]$ eV, better than for ^{82}Se sources, thanks to its higher phase-space factor.

To go further in this study, the SuperNEMO collaboration would study the influence on the sensitivity of external backgrounds, coming from detector materials as well as the laboratory. Also, more realistic performances of the detector, as well as field variations have to be implemented in the software for the simulations to reproduce more accurately the demonstrator performances.

As the ^{208}Tl background is higher than specified, and topological cut-offs are not strongly efficient to reduce its contribution, the next chapter focuses on setting up a specific technique to reject this internal background.

[5]The real mass of isotope is 6.23 kg, then to achieve a 17.5 kg.y exposure, the demonstrator should run a little more than two years and a half.

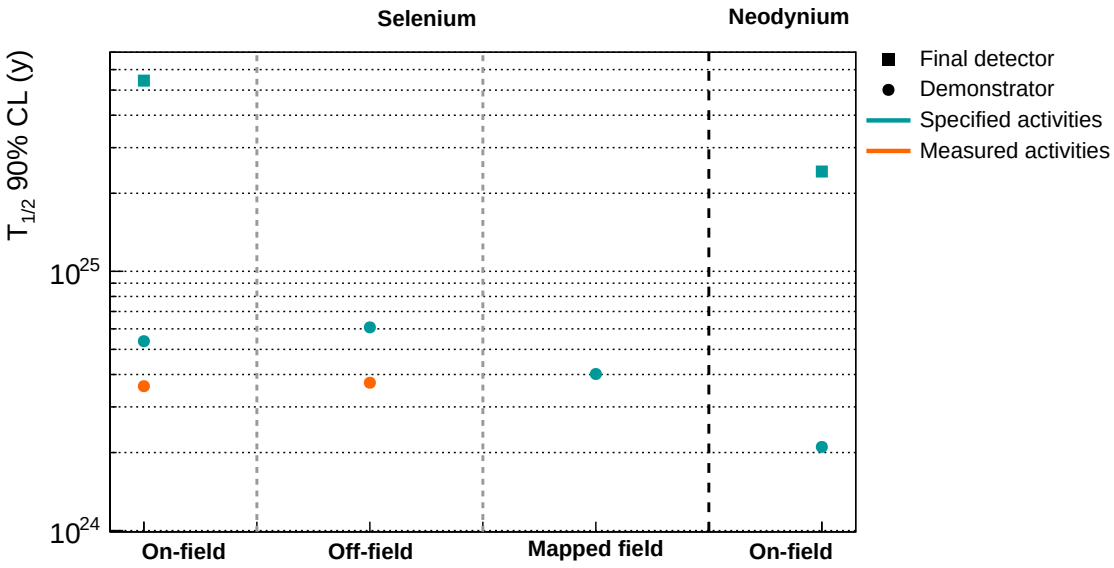

(a) $T^{0\nu}_{1/2}$ (90% CL) limits.

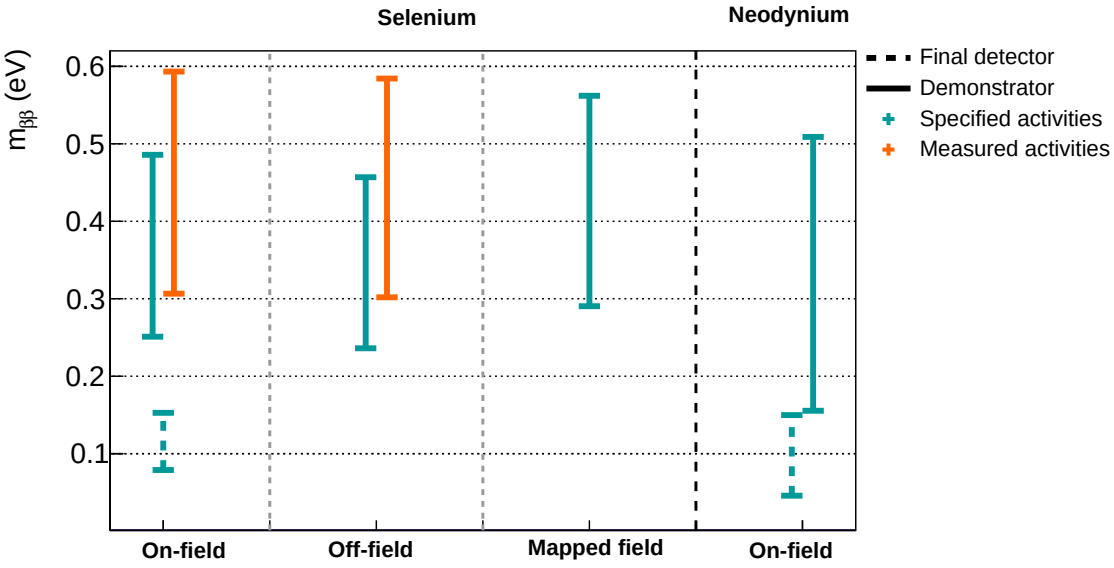

(b) $m_{\beta\beta}$ limits.

Figure 3.10: Summary of limits set on $T^{0\nu}_{1/2}$ (a) and $m_{\beta\beta}$ (b) for each case dealt with in this chapter. First-order and optimised topological cut-offs have been applied. Regions of interest have been optimised for each case.

Chapter 4

Improvement of the internal ^{208}Tl background rejection

> Le bien et le mal vont de pair,
> vous ne pouvez pas les séparer.
>
> Marilyn Manson

At the end of September 2018, the 34 enriched-Selenium source foils were installed on the demonstrator. At this time, the internal ^{208}Tl and ^{214}Bi activities of these sources had already been measured by the BiPo detector, as well as ^{222}Rn contamination inside the tracker. We described in the previous chapter the impact of these activities on the final detector sensitivity to the $0\nu\beta\beta$ decay, and set up optimised topological selections adjusted to reject the ^{222}Rn background.

However, ^{208}Tl disintegrations in the sources also remains a troublesome background, even for $\beta\beta$ emitters with a high $Q_{\beta\beta}$. Indeed, it contributes at high energies (up to 4 MeV on the two electrons energy sum spectrum), because of the internal conversion of the 2.615 MeV γ-ray. In a context where the ^{208}Tl contamination is higher than expected inside the sources, we focus in the current chapter on rejection techniques peculiarly adapted to reject internal ^{208}Tl events. We study the influence of these additional techniques on $0\nu\beta\beta$ events selection, and evaluate the impact on final detector sensitivity. Impact of the calorimeter timing performances on these techniques are also addressed in this chapter.

4.1 Motivations

In Chapters 2 and 3, we presented the specifications set on the background activities, in order to reach the target limit on the $0\nu\beta\beta$ process half-life of the ^{82}Se in 5 years, with 100 kg of isotope. The Tab. 2.3 given in Chapter 2 summarises the target ^{208}Tl, ^{214}Bi and ^{222}Rn activities, and provides a comparison with those measured by the collaboration. The BiPo measurements showed that the ^{208}Tl contamination is about 30 times greater than expected on average. We give in Tab. 4.1 the number of expected background events for the measured activities

(taking the upper limit for ^{214}Bi contamination), for the demonstrator and final detector. With an activity fixed to the measured one, the ^{208}Tl background does not affect significantly the sensitivity of the demonstrator (17.5 kg.y exposure) as only one event is expected in the optimised [2.7;3.3] MeV energy region, after first-order and topological cut-offs were applied. On the other hand, this background could be harmful for the final detector (500 kg.y exposure), with 21 events expected in the region of interest [2.6,2.95] MeV. To overcome this effect, it is interesting to set a specific method designed to reject ^{208}Tl events.

Exposure	Demonstrator 17.5 kg.y	Detector 500 kg.y
ROI (MeV)	[2.7;3.3]	[2.6;2.95]
$2\nu\beta\beta$	0.383	104
^{208}Tl	1.09	21.2
^{214}Bi	1.42	110
^{222}Rn	0.0782	6.11

Table 4.1: Expected number of background events in the $2e$ topology, in optimised energy ranges for the SuperNEMO demonstrator (17.5 kg.y) and the final detector (500 kg.y exposure). The $2\nu\beta\beta$ half-life is taken as $T^{2\nu}_{1/2} = 9.39 \times 10^{19}$ y, and the measured background activities are considered (with the upper limit for ^{214}Bi contamination). The topological selections have been optimised: $P_{int} > 4\%$ and $|\Delta Z| < 80$ mm. ROI are optimised to maximise the $T^{0\nu}_{1/2}$ limit at 90% (see Chapter 3).

In the next section, we describe the specific features of the ^{208}Tl internal background. We develop a new technique of rejection, especially designed to identify internal ^{208}Tl events, based on several Time-of-flight computations.

4.2 The internal ^{208}Tl background

As described in Chapter 2, radioactive isotope disintegrations inside the source foils can occasionally produce two-electron events, and thus can mimic $\beta\beta$-decay events. The ^{208}Tl, a progeny of ^{232}Th, is one of the largest contribution to the internal background. Two electrons can be emitted from the source via a β-decay followed by a Møller scattering, β-decay to an excited state with the subsequent internal conversion, or due to Compton scattering of the de-excitation photon.

The disintegration scheme of ^{208}Tl isotope is presented in Fig. 4.1. This shows that ^{208}Tl always β-decays to an excited state of the ^{208}Pb daughter nuclei. In more than 99 % of the decays, at least 2 γ's are expected after the β emission. For $0\nu\beta\beta$ detection of isotopes with high $Q_{\beta\beta}$, the most dangerous mode of $\beta\beta$-like events production comes from the internal conversion of the 2.615 MeV-γ, resulting in one electron with an energy of 2.5 MeV approximately and a beta-electron with a continuous spectrum between 0 and $\sim$ 1.5 MeV. Thus ^{208}Tl events with a total energy greater than 2.7 MeV can populate the region of interest.

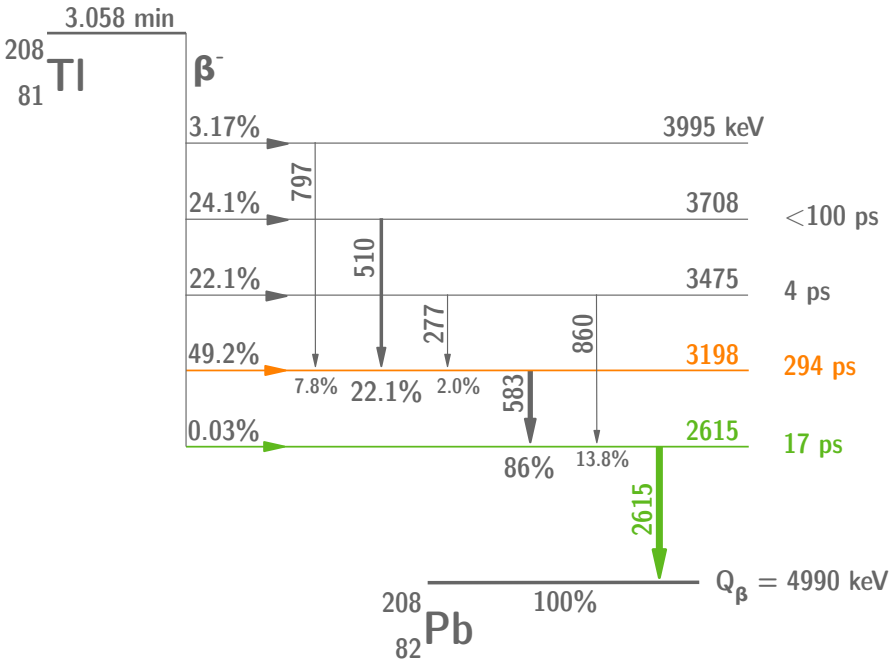

Figure 4.1: A simplified disintegration scheme for the ^{208}Tl isotope. 81 % of the disintegration pass through the 294 ps metastable energy level (orange). All disintegration go through the 2.615 MeV energy level (green), where an orbital electron is ejected in 0.246 % of the cases through the internal conversion process.

4.2.1 The internal conversion process

An excited nucleus will practically constantly achieve a transition to a lower state by one of two processes: the emission of a γ-ray, or the ejection of one of the orbital electrons. The latter, called *internal conversion* (frequently abbreviated IC), is a second-order process, where an electron couples to a proton inside the excited nucleus. Thus, in such a radioactive decay, the de-excitation energy of the nucleus is transferred *directly* to a j-shell electron ($j = K, L, M...$). A high-energy electron is therefore emitted from the atom, and carry off the energy

$$E_{IC} = E_\gamma - E_j \qquad (j = K, L, M...)\,, \tag{4.1}$$

where E_j is the binding energy of the electron in the j-shell, and E_γ is the energy of the γ-ray.

This mechanism is possible because there is a non-zero probability of finding the electron within the nucleus, that is to say, the wave-function of the electron can penetrate the volume of the nucleus. Consequently, due to their high nuclear penetration, electrons coming from the $1s$ state are more likely to be ejected (this transition is called K internal conversion). Although electrons coming from $2s$, $3s$ and $4s$ states (L, M or N internal conversions) have also a non-zero probability to undergo this process. After the electron ejection, the hole in the corresponding shell is filled by an electron from a higher energy level, emitting characteristic X-rays, Auger electrons, or both.

For a given transition, the internal conversion coefficient of the electron in the j-shell, is defined by

$$\alpha_j = \frac{P_{IC,j}}{P_\gamma}\,, \tag{4.2}$$

where $P_{IC,j}$ is the j conversion electron emission probability, and P_γ is the γ-ray emission probability. The total coefficient is

$$\alpha_T = \sum_{j=K,L,M\cdots} \alpha_j\,. \tag{4.3}$$

These coefficients are given in Tab. 4.2 for the 2.615 MeV energy level of ^{208}Tl isotope. Therefore, in 0.246 % of the cases, the ^{208}Pb excited nucleus will undergone an internal conversion corresponding to the 2.615 MeV energy level.

j-shell	K	L	M	Total
IC coefficients (%)	0.1708	0.0292	0.00685	0.246

Table 4.2: Internal conversion coefficients for the 2.615 MeV γ-ray of the ^{208}Tl decay scheme.

4.2.2 ^{208}Tl disintegrations in the 2e channel

Finally, a ^{208}Tl decay can present a two-electrons topology when, after the β emission, an electron is ejected from the atom through internal conversion. Especially, when this energy transfer corresponds to the 2.615 MeV γ-ray, the ejected electron carry off a significant energy, depending on its initial binding energy with the nucleus. For instance an orbital electron from the K-shell is ejected with an energy $E_{IC,K} = 2.526$ MeV ($\alpha_K = 0.17\%$). This decay is therefore likely to contribute in the region of interest for the $0\nu\beta\beta$ search of ^{82}Se, or even ^{150}Nd.

In the $2e$ channel, optimised topological cut-offs, based on time-of-flight computation and the distance between vertices, were presented in the previous chapter. They are mostly efficient in rejecting the non-internal ^{222}Rn events. After a brief presentation of the simulations carried out as part of this analysis, we remind and specify the internal probability computation, and present a new selection, also based on the time-of-flight computation, to reject the ^{208}Tl background.

4.3 Simulated demonstrator performances

The background model used in the framework of this study has already been described in detail in the previous chapter. Nevertheless, calorimeter performances implemented in the Falaise software have been modified in this study. Indeed, one of the main goal is to evaluate the influence of the calorimeter timing performances on the ^{208}Tl background rejection.

Such a characterisation was led before the commissioning phase of the calorimeter, and few optical modules' timing performances had been characterised before their installation at Modane [30]. An encouraging value for the uncertainty on the calorimeter time measurement of 248.3 ps for incoming electrons and 341.8 ps for photons were provided for the best optical module tested (Fig. 4.2).

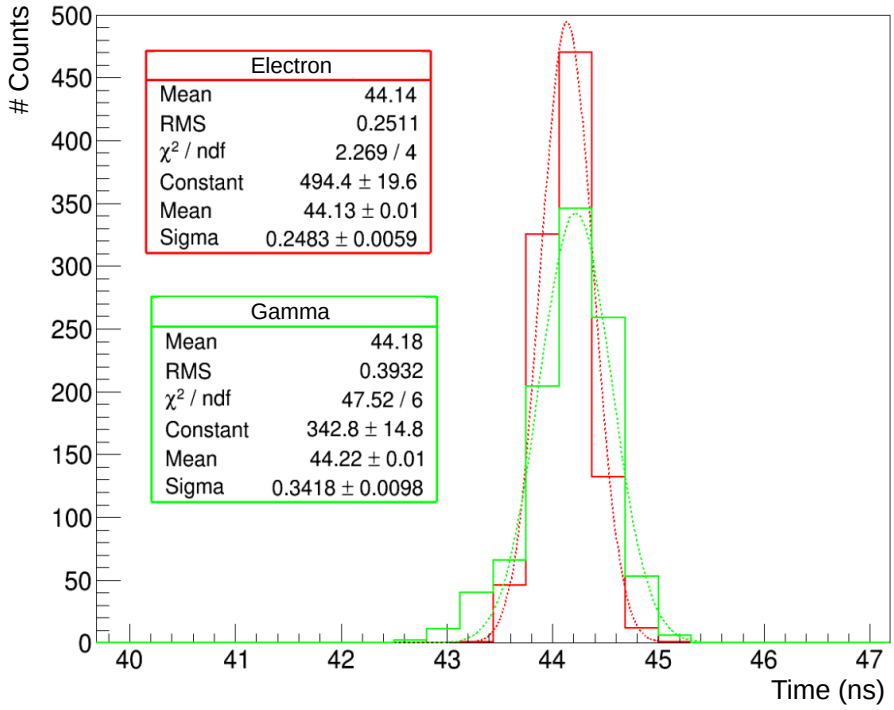

Figure 4.2: Time distribution of the trigger time of an optical module in the case of electrons (red) and gamma radiation (green) depositing an energy of 1 MeV in the scintillator. The trigger threshold is set at 45 mV and corresponds to an energy of 0.150 MeV. Adapted from [30].

In this context, before the full calorimeter calibration in Modane, we would give an overview of the influence of these performances on the ^{208}Tl background rejection. To do so, signal and background simulations were performed supposing the optical modules measure perfectly the particle time-of-flights, by setting to zero the time uncertainty at the level of the calibration module in the Falaise pipeline. I wrote a Root code allowing to degrade the precision on time measurements for it to be set by the user to the desired accuracy.

All of the simulations produced for this analysis were generated using the official Falaise pipeline, and are made available to the collaboration in the common SuperNEMO repository at the IN2P3 computing centre platform. The same code described in the previous chapter has been used for this study, including the Particle Identification module, the module I wrote and the Root code pipeline. An additional set of codes have been developed in order to degrade the simulated calorimeter resolution as well as to compute the analysis tools described in the following.

In the first instance we set the reasonable value of 200 ps for the measurement uncertainty. In Sec. 4.5.4 the influence of this parameter on the ^{208}Tl rejection is provided, and we give final sensitivity results according to it in Sec. 4.6.

4.4 Analysis tools to describe the ^{208}Tl internal background

The internal probability, based on time-of-flight computation, quantifies the likelihood that two particles were emitted inside the source foils, from the same vertex. Unless it is a useful tool, we would implement a new one, also based on time-of-flight, taking into account the possible delay between the two incoming electrons due to the ^{208}Pb metastable state.

4.4.1 The internal probability

As part of the analysis pipeline, this tool is widely employed in NEMO-3 and SuperNEMO, for background rejection purposes. We present it in detail in Chapter 2 and examine an example of its usefulness in Chapter 3. Nevertheless, in the framework of this analysis we need to perform our own calculation of internal probability, after the reconstruction pipeline, because the simulations are performed for an ideal value of the optical module performances. That is an opportunity to come back to this tool and to clarify certain points.

The expression of the internal χ^2 is reminded in Eq. (4.4), for two detected electrons, a depends of the expected time-of-flights, t^{exp}, the experimentally measured time-of-flights, t^{meas}, as well as the total uncertainty on the time-of-flight measurement written on the denominator:

$$\chi^2_{int} = \frac{((t_1^{\text{meas}} - t_1^{\text{exp}}) - (t_2^{\text{meas}} - t_2^{\text{exp}}))^2}{\sigma_{t_1}^2 + \sigma_{t_2}^2 + \sigma_{\beta_2}^2 + \sigma_{\beta_1}^2 + \sigma_{l_1}^2 + \sigma_{l_2}^2} \,. \tag{4.4}$$

σ_{t_i} is the uncertainty on the measured time-of-flight. σ_{β_i} and σ_{l_i} are the uncertainties on the expected time-of-flight brought by the uncertainty on particle energies and track lengths, respectively. The denominator square root corresponds to the total uncertainty, whose measured time-of-flight uncertainty is simulated as zero and degraded afterwards.

In the official SuperNEMO reconstruction pipeline, $\sigma_l = \sigma_{l_1} = \sigma_{l_2} = 70$ ps for electron particles. As we simulated perfect calorimeters, we check that this parameter is correctly evaluated in order to implement it in the off-line Root code pipeline.

Optimisation of σ_l

One way to examine if σ_l is well-evaluated is to look at the flatness of the internal probability distribution for $0\nu\beta\beta$ events in the $2e$ topology, for which a flat distribution is expected. Indeed, the slope of this distribution provides pertinent information to check the estimation of uncertainties. The flatter the distribution, the more correctly uncertainties are estimated.

For this optimisation, we use $2e$ topologies of signal simulations inside the source foils. Discrete values of σ_l running from 0.01 to 0.1 ns are used to compute the internal probability distributions of these events. For each distribution, a linear fit is performed on the reduced range $P_{int} \in [0.1; 1]$ in order to avoid the peak at low internal probabilities. The *flatness parameter* a_F is defined as the slope parameter of the linear fit. The optimisation then consists in finding the value of σ_l for which the parameter a_F is cancelled, which corresponds to the best estimate for σ_l.

In Fig. 4.3 is given the slope a_F as a function of σ_l. For $\sigma_l = 70$ ps, $a_F > 0$, revealing an overestimation of uncertainties in the computation of the internal χ^2 in the SuperNEMO reconstruction pipeline, at the Particle Identification module level. The optimised value, kept for the further analysis, is $\sigma_l = 27.8 \pm 0.8$ ps. In Fig. 4.4 is displayed the internal probability distributions for these two values of the σ_l parameter, $\sigma_l = 70$ ps and $\sigma_l = 27.8$ ps.

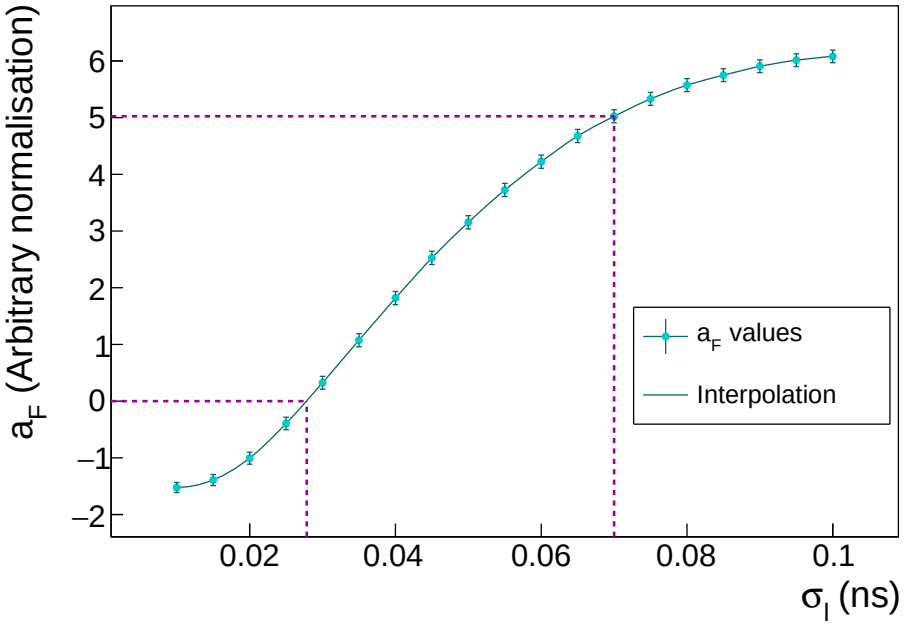

Figure 4.3: Flatness parameter a_F as a function of the time uncertainty due to the reconstructed track length σ_l. Data points (blue markers) are interpolated (black solid line). The former value used in the SuperNEMO reconstruction pipeline is pointed out by pink dashed lines, as well as the optimised value $\sigma_l = 27.8 \pm 0.8$ ps. P_{int} is calculated for $0\nu\beta\beta$ decays simulated inside the source foil, with first order cut-offs applied.

Let us notice that normally σ_l should depend on the track length as well as the energy, especially as multiple scatterings in the tracker have a more notable impact for low energy electrons. A more complete analysis would then compare the simulated track lengths with the reconstructed ones, for different energy simulated sets of mono-kinetic electrons, to evaluate this dependence. Nevertheless, our optimisation is good enough for the current analysis. Discussions are in progress to modify this parameter in the SuperNEMO software.

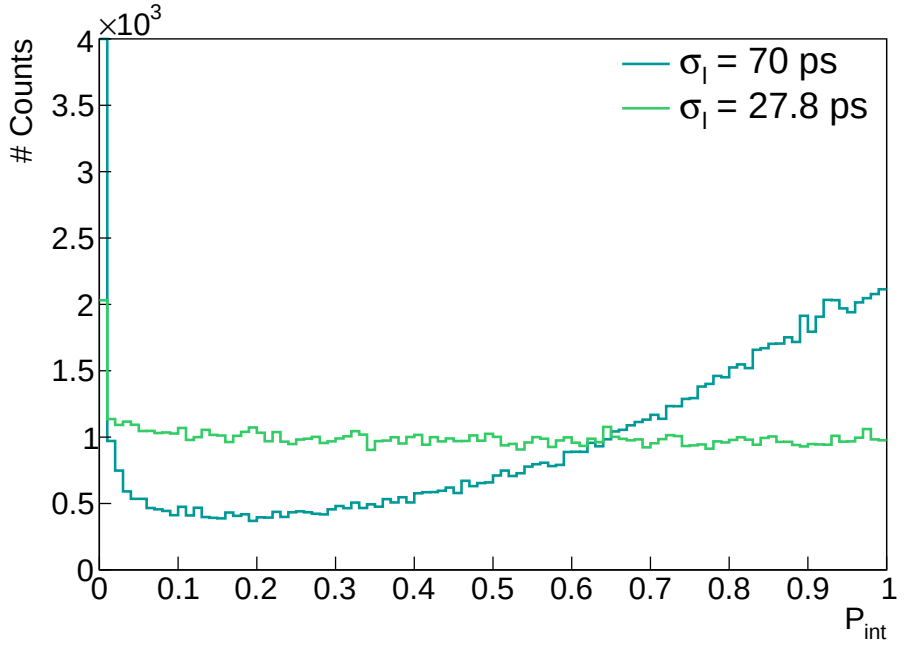

Figure 4.4: Internal probability distributions for $\sigma_l = 70$ ps (blue) and $\sigma_l = 27.8$ ps (green). P_{int} is calculated for $0\nu\beta\beta$ decays simulated inside the source foil, with first order cut-offs applied.

The internal probability is principally designed to reject non-simultaneous events coming from the source foils. Therefore, it is extremely effective in rejecting ^{222}Rn events produced far from the source foils. Even if it is less, this criterion is also effective in rejecting ^{208}Tl events, due to the existence of a metastable state for the daughter nucleus of ^{208}Tl. Therefore the emission of the 2.615 MeV-γ is in most of the cases delayed. But to describe even better these internal conversion events we would set up a new probability law expressing the hypothesis that a given event is from a β+IC delayed ^{208}Tl disintegration.

4.4.2 The exponential probability

According to the disintegration scheme of the ^{208}Tl isotope (Fig. 4.1), there is an 81 % probability of passing through the 294 ps metastable level. After that, to reach the ground state of ^{208}Pb, the excited nucleus has 100% of probability to decay through the 2.615 MeV energy level. At this occasion, in 0.246% of cases (Tab. 4.2), one of the orbital electrons is ejected from the atom following the internal conversion process. To summarise, for 0.20 % of the total ^{208}Tl decays, a β particle is emitted, and a delayed orbital electron is ejected through internal conversion of the 2.6 MeV-γ. Furthermore, 75% of these events have an energy sum greater than 2.7 MeV (the ROI low bound), and could be harmful for the $0\nu\beta\beta$ search. We aim to use this delayed electron to discriminate ^{208}Tl internal background from the $0\nu\beta\beta$ signal.

4.4.2.1 Probability density function

For a given detected $2e$ topology, we define the Δt^{meas} parameter as

$$\Delta t^{meas} = t_1^{meas} - t_2^{meas}\,, \tag{4.5}$$

where t_1^{meas} and t_2^{meas} are the two measured time-of-flights, respectively for the electron with the highest energy, and the one with the lowest energy. If this $2e$ topology corresponds to a delayed ^{208}Tl event, then the electron of lowest energy is a β particle and the one of highest energy an electron coming from an internal conversion, delayed on average of 294 ps. Assuming an ideal calorimeter perfectly measuring time-of-flights and energies, the Δt distribution for such delayed events would be a decreasing exponential, with the decay parameter $\tau = 294$ ps. However, in actual conditions, this exponential is degraded by the uncertainties on time-of-flight measurements detailed in Eq. (4.4). These are embedded by a Gaussian distribution centred around $\mu = 0$ ps with a given width σ. Therefore, to each $2e$ topology is associated a probability density function which is the convolution between an exponential and a Gaussian distribution, written down as $(E \otimes G)_{\tau,\mu,\sigma}(\Delta t)$. The corresponding value of Δt^{meas} is then found somewhere on this distribution, and will serve us to define the so-called *exponential probability*, $P_{exp}(\Delta t^{meas})$, which represents the probability that this event comes from a β+IC delayed decay.

4.4.2.2 Exponential probability

We wish to define this probability following the same principle as for the internal probability, for comparison purposes. Therefore, we would obtain the maximal value $P_{exp} = 1$ when the value of Δt is the most probable, i.e. when Δt is of the order of the mean of the $(E \otimes G)_{\tau,\mu,\sigma}(\Delta t)$ distribution. On the other hand, minimal values for P_{exp} would be reached for less probable values of Δt, so $P_{exp} \xrightarrow[|\Delta t| \to +\infty]{} 0$. To do so, the $(E \otimes G)_{\tau,\mu,\sigma}(\Delta t)$ distribution is normalised and the exponential probability is defined as

$$P_{exp}(\Delta t^{meas}) = \int_{-\infty}^{\Delta t^{meas}} (E \otimes G)_{\tau,\mu,\sigma}(t)\, dt + \int_{\Delta t_{sym}^{meas}}^{+\infty} (E \otimes G)_{\tau,\mu,\sigma}(t)\, dt\,, \tag{4.6}$$

where Δt_{sym}^{meas} is defined such that $(E \otimes G)_{\tau,\mu,\sigma}(\Delta t_{sym}^{meas}) = (E \otimes G)_{\tau,\mu,\sigma}(\Delta t^{meas})$. A graphical representation is given in Fig. 4.5. In this example the distribution corresponds to $(E \otimes G)_{\tau,\mu,\sigma}(\Delta t)$ with $\tau = 294$ ps and $\mu = 0$ ps and the total time uncertainty is calculated taking $\sigma_l = 27.8$ ps and $\sigma_t = 200$ ps for 1 MeV electrons. The two integrals whose sum is given in the Eq. (4.6) are represented by two red-coloured areas. As explained, each probability density function is defined for a single 2-electrons event, because the time-of-flight uncertainty depends on the electron measured energy and on the track length. In the given example, we considered two particles interacting inside the calorimeter with an energy of 1 MeV each.

In fig. 4.6 are presented exponential probability distributions for $2e$ topologies selected of ^{208}Tl and $0\nu\beta\beta$ simulations inside the source foils. As expected,

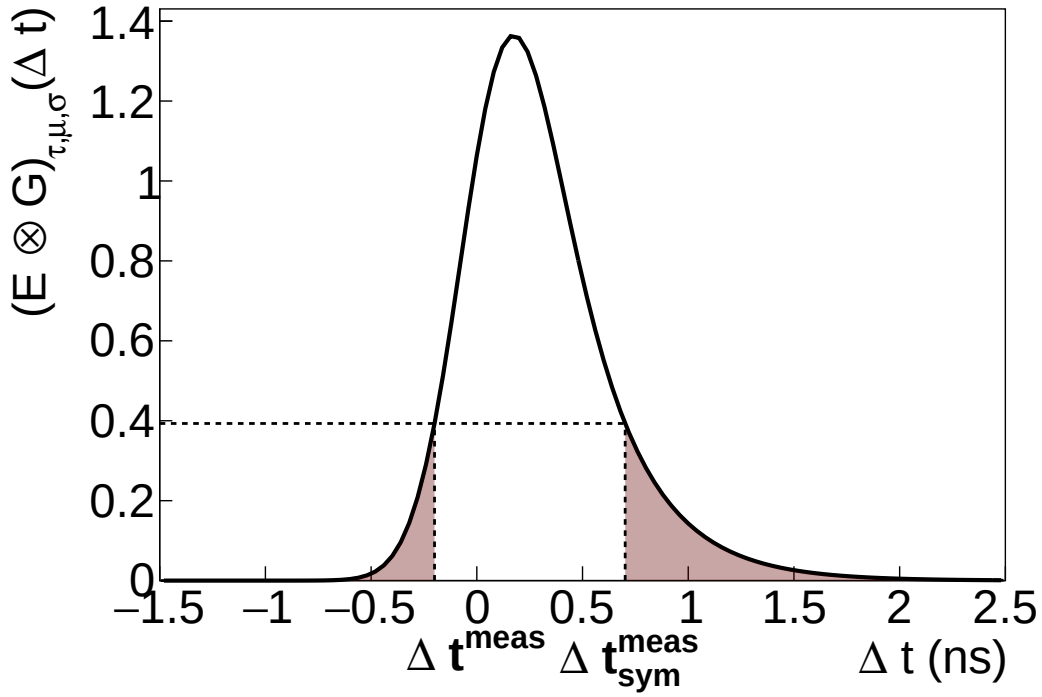

Figure 4.5: Normalised convolution distribution $(E \otimes G)_{\tau,\mu,\sigma}(\Delta t)$. The parameters are $\tau = 294$ ps, $\mu = 0$ ps and $\sigma = \sigma_{tot}$, computed with $\sigma_l = 27.8$ ps and $\sigma_t = 200$ ps.

the distribution for ^{208}Tl is flat. However, we would have expected a non-flat distribution for $0\nu\beta\beta$ events, but the time resolution is too degraded for such variations to be observable.

Now analysis tools are defined, the following sections focus on the event selections using them, the way to optimise them and their influence on the final detector sensitivity.

4.5 Event selection

Now the exponential probability tool has been defined, the aim of this analysis is to set up event selections focusing on delayed ^{208}Tl events rejection. Simple time-of-flight cut-offs are described, and compared with a more elaborated selection using these two probabilities. The influence of the uncertainty σ_t on time measurement is discussed at the end of the section.

4.5.1 Energy selection

Based on the conclusions given in the previous chapter, the lower bound of the region of interest optimising the search of $0\nu\beta\beta$ decay stands at the electron energy sum of 2.7 MeV for the demonstrator. Beyond this energy, $2e$ topologies for ^{208}Tl are populated at 75% by β decays followed by the internal conversion of the 2.615 MeV γ-ray. In the following, we therefore focus only on events with a sum in energy of the two detected electrons greater than 2.7 MeV.

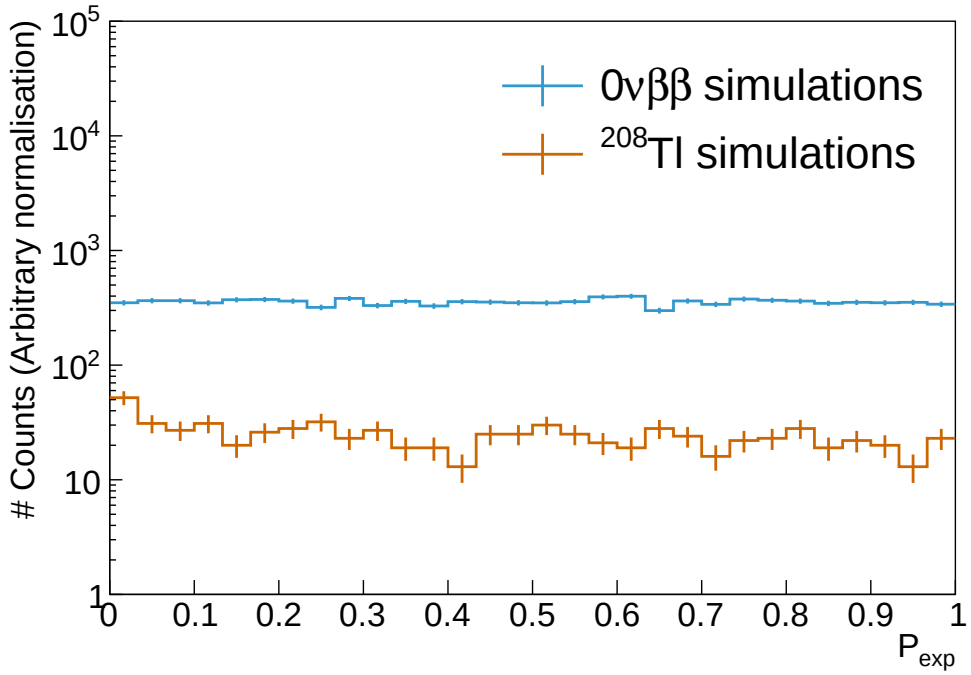

Figure 4.6: Exponential probability distribution for ^{208}Tl (orange) and $0\nu\beta\beta$ simulations (blue), for $2e$ topologies with an electron energy sum greater than 2.7 MeV (discussed in Sec. 4.5). $\sigma_t = 200$ ps, $\sigma_l = 27.8$ ps.

4.5.2 Time-of-flight cut-off

Before using the two internal and exponential probabilities, a simple cut-off using the electron time-of-flight is explored. Indeed, we are especially focused on rejecting the internal ^{208}Tl events for which the successive β and γ-rays emissions went through the 294 ps metastable state. For these decays, we are expecting the particle of highest energy to be delayed compared with the one of lowest energy. Each term in Eq. 4.5 corresponds to what it took for a particle to travel from the source to the calorimeter and depends on the time it spent in the source after emission, as well as how long it took to cross the tracker. In order to remove from Δt^{meas} the dependency on travel time in the tracker, we define the corrected time difference as

$$\Delta t^{\text{corr}} = t_1^{\text{corr}} - t_2^{\text{corr}} \tag{4.7}$$

$$= (t_1^{\text{meas}} - t_1^{\text{exp}}) - (t_2^{\text{meas}} - t_2^{\text{exp}}) \,, \tag{4.8}$$

where t_i^{corr} are the corrected time-of-flights and t_i^{exp} the expected ones calculated with the particle energy and track length.

The two distributions Δt^{meas} and Δt^{corr} are presented in Fig. 4.7, for $0\nu\beta\beta$ and ^{208}Tl simulations inside the source foils. For $0\nu\beta\beta$ simulations, the Δt^{corr} distribution is centred around zero, as the two electrons are emitted simultaneously inside the source. Then, the correction on time difference only lowers the standard deviation of the distribution. For ^{208}Tl simulations, the mean of the distribution is

slightly shifted towards positive values. Once corrected by the expected times, the mean difference between the two electrons time-of-flights stands at 296 $\pm$ 18 ps. This is a direct consequence of the existence of β+IC delayed events, for which the particle of highest energy is expected to hit a calorimeter block at a time $t_1^{\text{corr}} > t_2^{\text{corr}}$. The set up calorimeter time uncertainty at 200 ps allows to be sensitive to this decay as the mean of the distribution is near 294 ps. Therefore, a simple way of rejecting the ^{208}Tl delayed events is to consider the sign of Δt^{corr} and to reject events for which $\Delta t^{\text{corr}} > 0$.

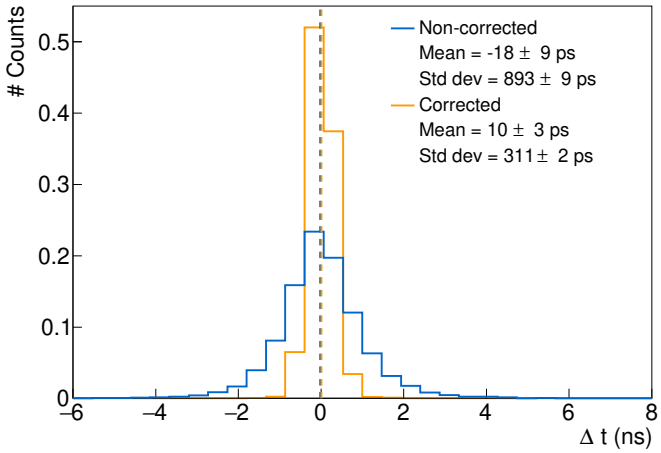

(a) $0\nu\beta\beta$ simulations.

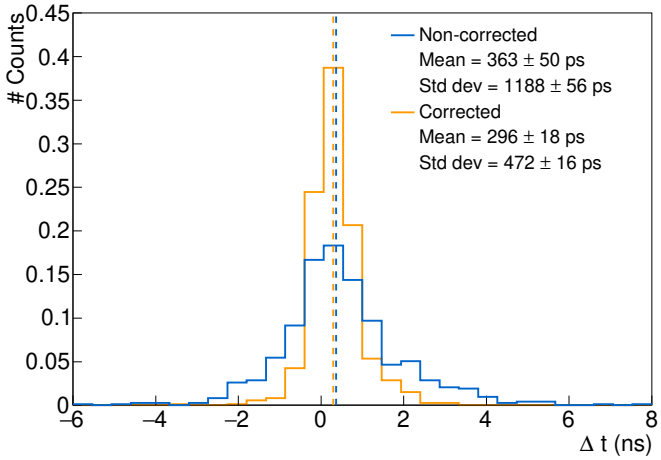

(b) ^{208}Tl simulations.

Figure 4.7: Corrected (orange) and non-corrected (blue) time-of-flight difference between the two electrons. (a) $0\nu\beta\beta$ simulations inside the source foils. (b) ^{208}Tl simulations inside the source foils. The first-order selections have been applied. The two distributions are normalised. $\sigma_t = 200$ ps and $\sigma_l = 27.8$ ps.

By applying this selection on $2e$ topologies of $0\nu\beta\beta$ and ^{208}Tl simulations for which $E > 2.7$ MeV, we are able to reject 76 % of ^{208}Tl while selecting 49 % of the $0\nu\beta\beta$ ($\sigma_t = 200$ ps). The selection of half of the signal events was expected as the corresponding Δt^{corr} distribution is symmetrical, unlike the one for ^{208}Tl

events. Although we manage to reject a significant fraction of ^{208}Tl events, the impact of this cut is too high on $0\nu\beta\beta$ events. Moreover, the uncertainties on time-of-flights are not taken into account in the rejection criterion. Later in this chapter we consider different levels for this selection and optimise them according to the σ_t value set up.

4.5.3 Probability cut-off

At this level it is interesting to consider the internal and exponential probabilities to describe $2e$ topologies and attempt to obtain a higher ^{208}Tl background rejection. They seem to be better tools notably because, unlike the Δt^{corr} rejection criterion, they do take into account the time-of-flight uncertainties. The first one was already used in Chapter 3, and is a widely-used tool to reject non-internal events. The second was designed specifically for this analysis to identify delayed ^{208}Tl events, and also depends on the time of flight resolution through the convolution with a Gaussian function.

The idea is this section is to reject ^{208}Tl events taking into account their two values of internal and exponential probabilities. Then it is interesting to represent them with a two-dimensional binned histogram of P_{exp} as a function of P_{int}, as done is Fig. 4.8. In this particular example, we picture the variations of P_{int} and P_{exp} applying $\sigma_t = 200$ ps. In order to better understand these variations, we give in Fig. 4.9 three examples of $(E \otimes G)_{\tau,\mu,\sigma}(\Delta t)$ distributions, each of them illustrating one of the three zones observed on the two-dimensional histogram.

1. $\mathrm{P}_{int} \in [0;1]$ and $P_{exp} \in [0;0.65]$, with $\mathrm{P}_{int} > P_{exp}$ (Fig. 4.9a):
   This region corresponds to events for which $\Delta t^{\text{corr}} < 0$. As the internal χ^2_{int} distribution is symmetrical, such events can have a value of P_{int} varying from 0 to 1. Small values of P_{int} correspond to events with a large negative Δt^{corr} value. Conversely, the exponential distribution is not centred in zero. Therefore, if we limit to events for which the time difference is negative, we reach an upper bound for the value of the integral (0.65 in that case). This bound directly depends on the variations of the exponential distribution, therefore on the σ_t value applied.

2. $\mathrm{P}_{int} \in [0;0.65]$ and $P_{exp} \in [0;1]$, with $P_{exp} > \mathrm{P}_{int}$(Fig. 4.9b):
   These events have positive values for Δt^{corr}, beyond the $(E \otimes G)_{\tau,\mu,\sigma}(\Delta t)$ distribution maximum. The smaller the value of P_{int}, the lower the probability that both particles were emitted at the same time into the source. Besides, for values of Δt^{corr} highly positives, the value of the exponential probability can reach high values, up to 1. The larger the value of Δt^{corr} in positives, the smaller the value of P_{exp}.

3. $\mathrm{P}_{int} \in [0.65;1]$ and $P_{exp} \in [0.65,1]$ (Fig. 4.9c):
   This region is also populated by events for which $\Delta t^{\text{corr}} > 0$. Unlike the previous case, these events have small Δt^{corr} values, meaning below the maximum of the exponential distribution. Also, these events have high internal probability values, as the probability that these two particles were

emitted simultaneously is high. In the same way as the first bullet, the value of P_{exp} is bounded: the lower bound corresponds to the value of the integral when $\Delta t^{\text{corr}} = 0$ (here 0.65). Once again, this bound is deeply related to the value considered for σ_t. The exponential probability can be equal to 1 when Δt^{corr} reaches the maximum of the exponential distribution.

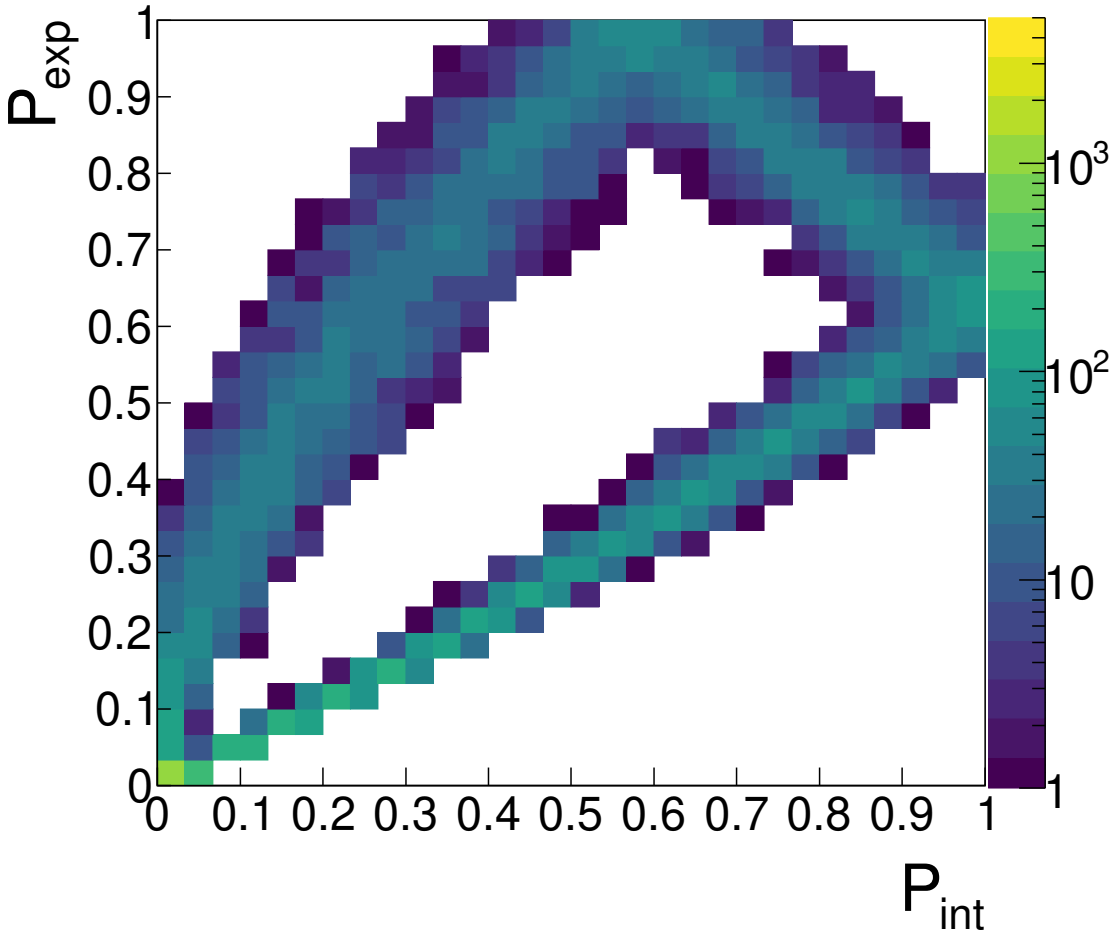

Figure 4.8: Two-dimensional histogram showing the P_{exp} variations as a function of P_{int} for ^{208}Tl $2e$ topologies. $\sigma_t = 200$ ps and $\sigma_l = 27.8$ ps.

As discussed, the exponential probability quantifies the likelihood that two particles were emitted with a delay corresponding to the radioactive exponential decay with $\tau = 294$ ps, taking into account the time of flight resolution. Therefore, we are interested in rejecting events for which values of P_{exp} are high compared with the P_{int} values. Regarding the biplot presented in Fig. 4.8, the goal is to reject events located in the area 3 and a part of the events located in area 2. Therefore, an adapted cut-off is to reject events for which $P_{exp} > 0.65$ and $\mathrm{P}_{int} \in [0.4, 0.7]$. For this selection and $\sigma_t = 200$ ps, we reject 20% of ^{208}Tl and keep 84% of $0\nu\beta\beta$ events. The proportion of signal events kept with this selection is satisfying. Nevertheless

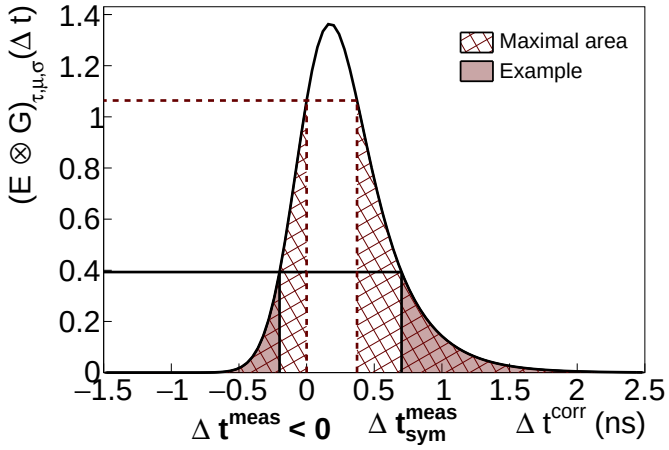

(a)

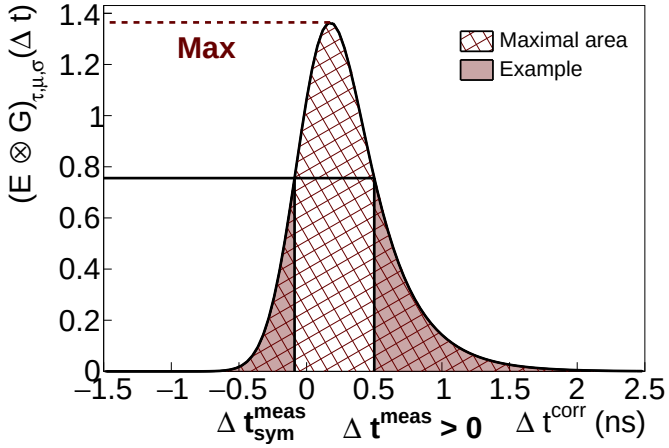

(b)

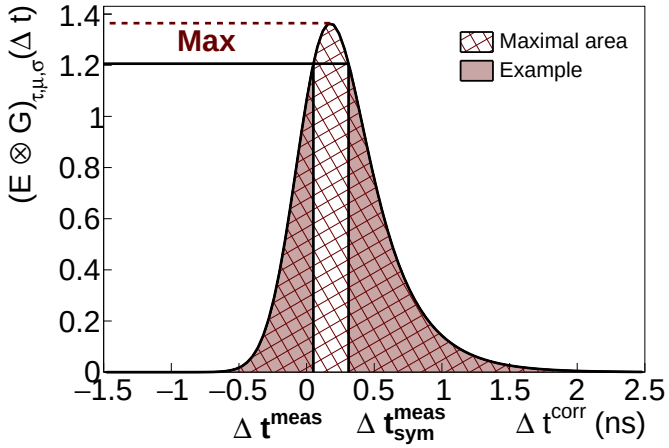

(c)

Figure 4.9: $(E \otimes G)_{\tau,\mu,\sigma}(\Delta t)$ distributions describing the three areas observed in Fig. 4.8. (a) $\Delta t^{\text{corr}} \in]-\infty; 0]$. (b) $\Delta t^{\text{corr}} \in]\Delta t_{max}; +\infty]$. (c) $\Delta t^{\text{corr}} \in]0; \Delta t_{max}]$.

the efficiency of ^{208}Tl rejection is almost 4 times lower than for the time-of-flight selection presented in Sec. 4.5.2.

4.5.4 Influence of the calorimeter time resolution

We study in this subsection the influence of the calorimeter timing resolution on event selections, using the cut-offs presented above. We consider values for σ_t in the [0 - 400] ps range.

In Sec. 4.5.2 we presented rejection efficiencies for a $\Delta t^{corr} > 0$ ps selection, with $\sigma_t = 200$ ps. In Fig. 4.10 is presented the $0\nu\beta\beta$ selection efficiency with the rejection efficiency of ^{208}Tl, for values of σ_t running from the ideal 0 ps, to 400 ps. Each point corresponds to a Δt^{corr} level applied on the selected $2e$ topologies, from $\Delta t^{corr} > 0$ to $\Delta t^{corr} > 650$ ps. For $\Delta t^{corr} > 0$ and $\sigma_t = 200$ ps, we get back to the result given previously. For this time uncertainty, a better value for the Δt^{corr} cut level, allowing to reject more ^{208}Tl while keeping a great proportion of $0\nu\beta\beta$ events, is found at $\Delta t^{corr} > 250$ ps.

Such an optimal selection/rejection point can be found for each of the five σ_t values presented. The more precisely the time-of-flight is measured in the calorimeter, the better this point is determined. Indeed, the poorer the resolution in time, the more linearly the distribution evolves, and therefore the more difficult it is to discriminate delayed events from those emitted simultaneously such as those of $0\nu\beta\beta$. Especially, for an ideal calorimeter where the timing measurement would be perfect, we could reach 80% of ^{208}Tl rejection, while keeping 90% of signal events.

As discussed, the variations of P_{int} and P_{exp} are bound to the value of σ_t, thus the levels applied on P_{int} and P_{exp} must be adapted to match these variations. Eight P_{int}/P_{exp} biplots are given in Fig. 4.11, for $\sigma_t = 0$, 100, 300 and 400 ps both for $0\nu\beta\beta$ and ^{208}Tl $2e$ selected topologies (the $\sigma_t = 200$ ps case is already given in Fig. 4.8). Depending on σ_t, the area to be rejected moves towards higher values of P_{int}. Taking this into consideration, optimised values for P_{int} have been set up, summarised in Tab. 4.3. To find an optimal value of P_{exp} to be applied, several cut-offs are set up from $P_{exp} > 0$ to 0.95, and associated with the P_{int} cut-offs presented in the previous table, in order to reject the required area.

Following the work done for the Δt^{corr} cut-off, results are presented in Fig. 4.12 on an efficiency selection diagram. The calorimeter timing measurement has a great influence, especially on ^{208}Tl events rejection. Evolution of selection efficiencies for $\sigma_t < 200$ ps are very similar, reaching a plateau for $\sim P_{exp} > 0.25$ allowing to reject 20% of ^{208}Tl while keeping 85% of $0\nu\beta\beta$.

For calorimeter time uncertainty better than 100 ps the background rejection is improved despite a loss in signal selection efficiency, up to reaching $\sim$ 45% of ^{208}Tl rejection and $\sim$ 80% signal selection for an ideal calorimeter. The plateau is reached at $P_{exp} > 0.2$ for $\sigma_t = 100$ ps and $P_{exp} > 0.15$ for $\sigma_t = 0$ ps.

A better ^{208}Tl rejection can be obtained with the simple selection on time-of-flights, but the probability one has the main advantage to be more accurate as it takes into account the calorimeter time measurement uncertainties. Moreover, even if variations of selection/rejection of this diagram are not as pronounced as

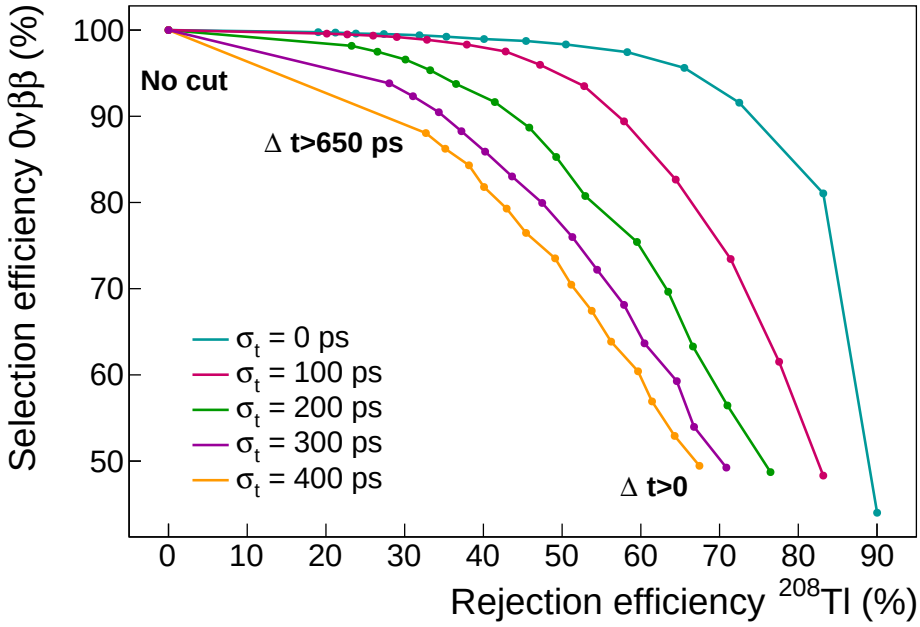

Figure 4.10: $0\nu\beta\beta$ selection efficiency as a function of ^{208}Tl rejection. Each curve corresponds to a given value of σ_t from 0 to 400 ps. Each data point corresponds to a minimum value for Δt^{corr} applied on selected 2 topologies from 0 to 650 ps. The optimised value of $\sigma_l = 27.8$ ps is applied.

σ_t (ps)	0	100	200	300	400
P_{int} cut-off	[0.05 - 0.3]	[0.25 - 0.6]	[0.4 - 0.7]	[0.5 - 0.8]	[0.55 - 0.85]

Table 4.3: Range of P_{int} for which events are rejected. An additional cut-off with $P_{int} < 0.01$ and $P_{exp} < 0.01$ is also applied.

for the Δt^{corr} cut-off, a strong assumption can be made: the more we are precise on time-of-flight measurements, the more we are able to reject ^{208}Tl events while keeping a satisfying part of signal. During the calorimeter R&D, a great effort has been made to improve the optical modules energy resolution compared to NEMO-3, notably because it allows to have a better background rejection, and thus to decrease its contribution to the $0\nu\beta\beta$ search. Finally, in view of these results, a good timing precision in calorimeter blocks is also important when it concerns background rejection, and especially the identification of β+IC delayed ^{208}Tl decays. Nevertheless, to give a final conclusion on the usefulness of the Δt^{corr} and probability cut-offs, one have to study its impact on the final sensitivity of the detector, which is dealt with in the next section.

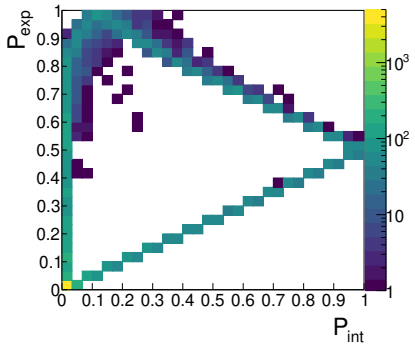

(a) ^{208}Tl simulations, $\sigma_t = 0$ ps.

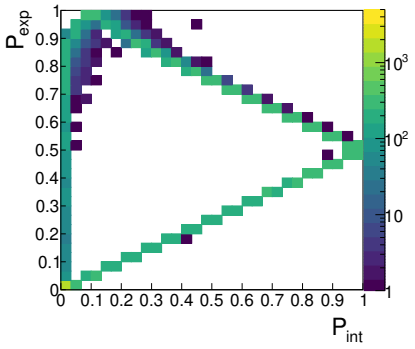

(b) $0\nu\beta\beta$ simulations, $\sigma_t = 0$ ps.

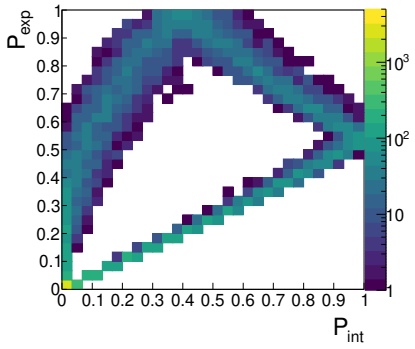

(c) ^{208}Tl simulations, $\sigma_t = 100$ ps.

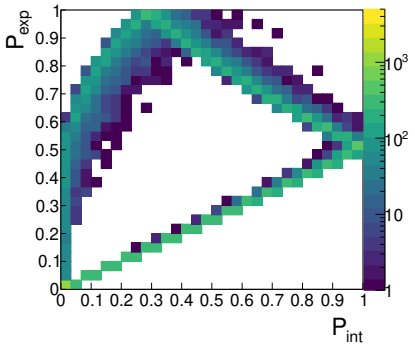

(d) $0\nu\beta\beta$ simulations, $\sigma_t = 100$ ps.

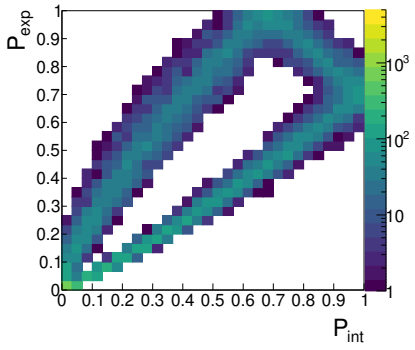

(e) ^{208}Tl simulations, $\sigma_t = 300$ ps.

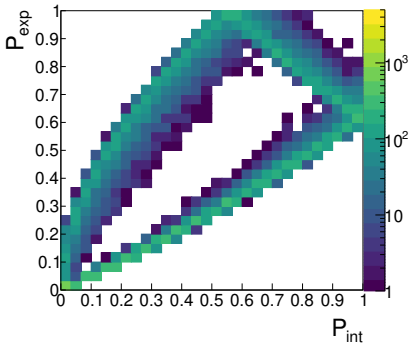

(f) $0\nu\beta\beta$ simulations, $\sigma_t = 300$ ps.

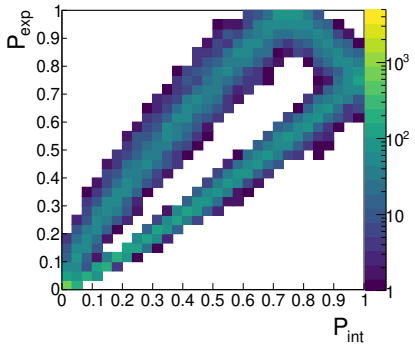

(g) ^{208}Tl simulations, $\sigma_t = 400$ ps.

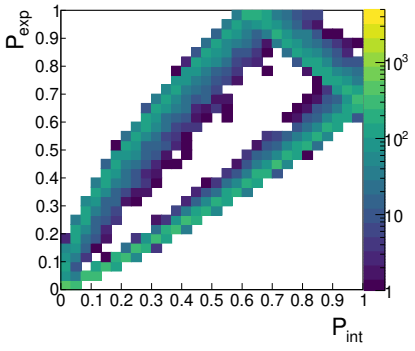

(h) $0\nu\beta\beta$ simulations, $\sigma_t = 400$ ps.

Figure 4.11: P_{int}/P_{exp} biplots for different σ_t values for ^{208}Tl and $0\nu\beta\beta$ simulations.

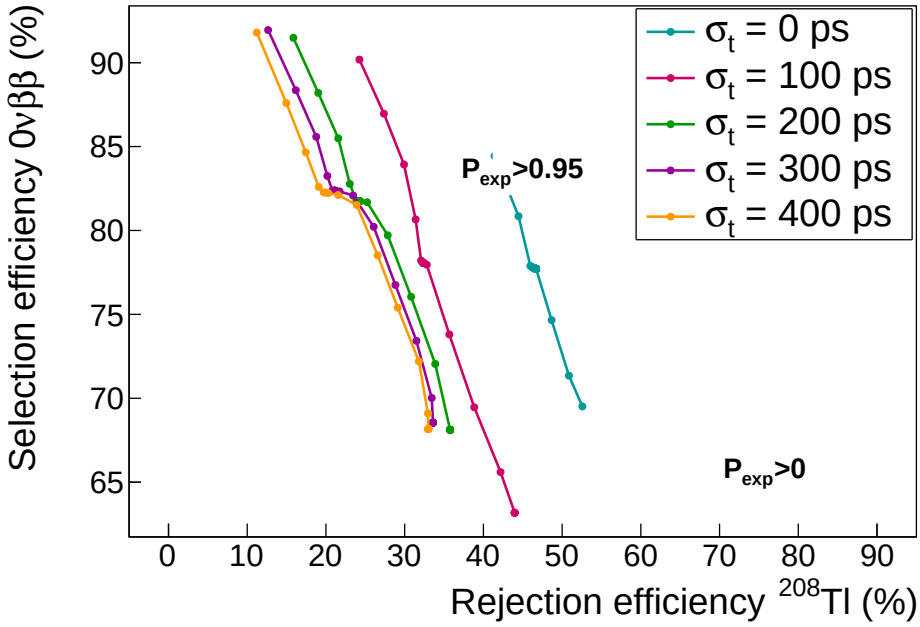

Figure 4.12: $0\nu\beta\beta$ selection efficiency as a function of ^{208}Tl rejection. Each point corresponds to a minimal P_{exp} value applied on the selected $2e$ topologies. P_{int} selections are also applied, their value depending on the σ_t value (Tab. 4.3). $\sigma_l = 27.8$ ps.

4.6 Impact of ^{208}Tl rejection on the experiment's sensitivity

In the previous section were presented results for Δt^{corr} and optimised probability cut-offs, and the influence of the calorimeter time resolution on these rejection techniques was reviewed. Nevertheless, to properly quantify the effectiveness of these cut-off, one have to study their impact on the final detector sensitivity (500 kg.y exposure). To do so, the procedure described in Chapter 3 is applied to the $2e$ topologies selected (after the application of Δt^{corr} or probability cut-offs), for signal and backgrounds considered ($2\nu\beta\beta$, ^{214}Bi, ^{208}Tl and ^{222}Rn).

4.6.1 Sensitivity results

The variations of the sensitivity are presented in Fig. 4.13 for three values of σ_t at 1 MeV, as a function of the Δt^{corr} and probability cut-off levels applied. For these two figures, the more the x-values increase, the more the applied cut is released. In both cases sensitivity results converge towards $\sim 2.4 \times 10^{25}$ years, for very loose values of the selection.

Regarding the influence of Δt^{corr} selection, a sensitivity improvement can eventually be obtained by applying this selection, depending on the value of σ_t considered for the calorimeter (Fig. 4.13a).

- $\sigma_t = 0$ ps at 1 MeV: an improvement of 12% on the sensitivity is observed for events rejected if $\Delta t^{corr} > 200$ ps. This is consistent with the ^{208}Pb

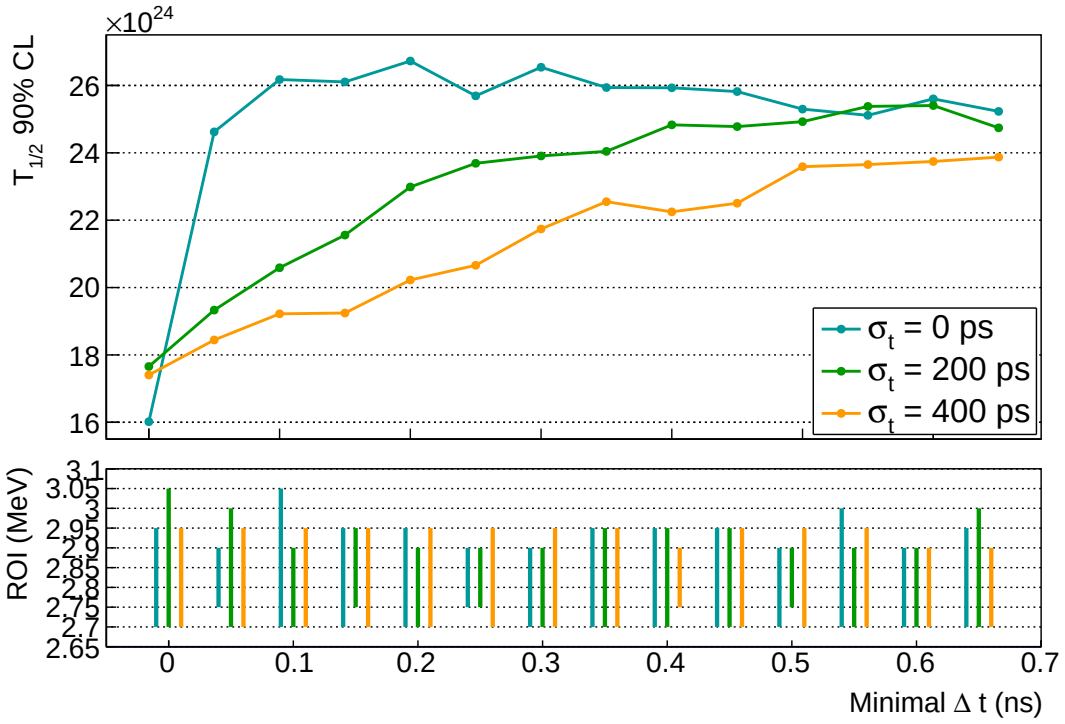

(a) Δt^{corr} cut-off.

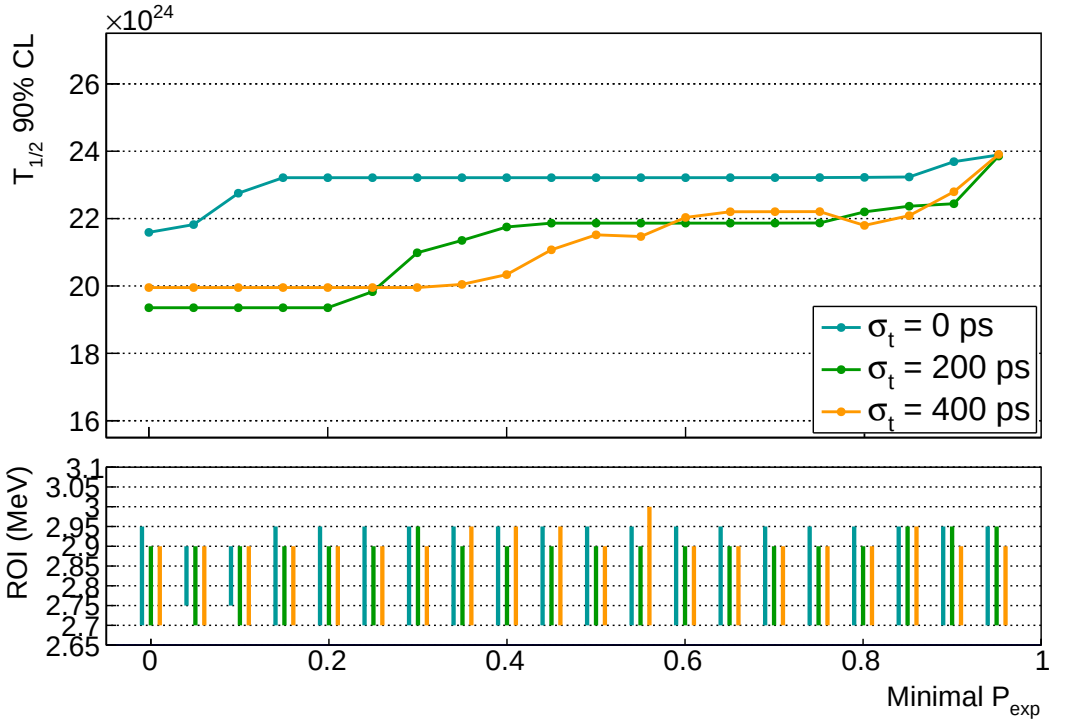

(b) Probability cut-off.

Figure 4.13: (Top pad) $T^{0\nu}_{1/2}$ at 90% CL and (bottom pad) optimised ROI, as a function of the minimal value of Δt applied on the selected $2e$ topologies. Results are given for $\sigma_t = 0$, 200 and 400 ps at 1 MeV, and $\sigma_l = 27.8$ ps.

metastable level of 294 ps to which we are very sensitive with such ideal value of the calorimeter resolution.

- σ_t = 200 ps at 1 MeV: a slighter improvement of 6% is reached for $\Delta t^{corr} > 550$ ps.

- $\sigma_t = 400$ ps at 1 MeV: the resolution is too degraded for an improvement to be obtained with such a time-of-flight cut-off.

In conclusion, we can expect to see an improvement in sensitivity by rejecting delayed ^{208}Tl events with the Δt^{corr} criterion only if the time resolution is good enough, above 200 ps.

Concerning the influence of P_{int}/P_{exp} selection, values of $T^{0\nu}_{1/2}$ also converge towards a unique value, attained for $P_{exp} > 1$, meaning all the events are selected for such a level. In other words, the more restrictive this cut is, the more the sensitivity is reduced. The least unfavourable case is obtained for the ideal calorimeter resolution case, with stagnation of the values on a plateau, for most of the applied cut-off levels. Even if it is less wide, a plateau is also reached for $\sigma_t = 200$ ps. Finally, this selection is not adapted to reject ^{208}Tl events, but the same conclusion as above can be made: the better the time resolution, the higher the sensitivity increases. A future study could investigate other selection levels to reject a more favourable area on the P_{int}/P_{exp} biplot.

4.6.2 Expected number of background

The influence of the Δt^{corr} selection on the number of expected background events in the optimised ROI is presented in Tab. 4.4. Three values of σ_t are considered, and for each of them the best level for this cut, determined in the previous sub-section, is applied. The best rejection of ^{208}Tl is reached for the ideal calorimeter time resolution, as the two electrons time-of-flights are measured precisely. For $\sigma_t = 200$ ps, a smaller amount of ^{208}Tl background is rejected, but the $0\nu\beta\beta$ selection efficiency remains stable. This selection efficiency is affected for σ_t = 400 ps, because the delayed events are badly discriminated compared with the simultaneous ones. As expected, other background events ($2\nu\beta\beta$, ^{214}Bi and ^{222}Rn) are not significantly affected by this selection. We understand the final sensitivity is degraded because the $0\nu\beta\beta$ selection efficiency is reduced.

As discussed, the P_{int}/P_{exp} cut-off applied on $2e$ topologies highly degrades the final sensitivity to the $0\nu\beta\beta$ process. To quantify its impact on the background rejection, we present in Tab. 4.5 the expected number of background in the optimised ROI, for two different levels for the P_{exp} selection, one at 0.5 and the other one very loose. Even if it affect the $0\nu\beta\beta$ selection efficiency, this selection allows to reject 5 events of ^{208}Tl inside the ROI for the SuperNEMO final detector.

These two selections were implemented in order to reject ^{208}Tl events and they have fulfilled this role. However the probability selection degrades too strongly the $0\nu\beta\beta$ efficiency to improve the final sensitivity. The Δt^{corr} selection allowed to improve the sensitivity by 12% for a perfect calorimeter time resolution.

σ_t (ps)	0	200	400
ROI (MeV)	[2.7;2.95]	[2.7;2.9]	[2.7;2.95]
Minimal Δt^{corr} (ps)	200	550	650
$T^{0\nu}_{1/2}$ (90% CL) ($\times 10^{25}$ y)	2.7	2.5	2.4
$m_{\beta\beta}$ (90% CL) (eV)	$[0.11 - 0.22]$	$[0.11 - 0.22]$	$[0.12 - 0.23]$
$\epsilon_{0\nu}$	14.6%	14.2%	12.9%
$2\nu\beta\beta$	10.8	10.8	9.58
^{208}Tl	9.52	13.3	13.4
^{214}Bi	42.9	42.0	39.2
^{222}Rn	1.12	1.12	1.04
Total	64.4	67.2	63.2

Table 4.4: Expected number of background events in the optimised ROI, for the exposure of the SuperNEMO final detector (500 kg.y). Three values of σ_t are considered for which the best Δt^{corr} is applied.

ROI (MeV)	[2.7;2.9]	[2.7;2.9]
Minimal P_{exp}	0.5	0.95
$T^{0\nu}_{1/2}$ (90% CL) ($\times 10^{25}$ y)	2.2	2.4
$m_{\beta\beta}$ (90% CL) (eV)	$[0.12 - 0.24]$	$[0.12 - 0.23]$
$\epsilon_{0\nu}$	12.1%	13.9%
$2\nu\beta\beta$	9.83	10.8
^{208}Tl	16.3	21.0
^{214}Bi	38.4	42.0
^{222}Rn	0.596	0.596
Total	65.1	74.4

Table 4.5: Expected number of background events in the optimised ROI, for the exposure of the SuperNEMO final detector (500 kg.y). The time resolution is taken as $\sigma_t = 200$ ps. Two levels of P_{exp} cut are compared, 0.5 and 0.95.

Finally, the final detector sensitivity is greatly affected by this timing measurement precision.

4.7 Conclusion

During this chapter we have defined or specified analysis tools adapted to the rejection of the delayed ^{208}Tl background. In particular, a so-called exponential probability law has been set up to match the 294 ps decay time. Not only the cut-off based on the electron time-of-flight is very satisfactory for rejecting this last background, but also the associated cut-off in internal and exponential probability makes it possible to be more precise since it takes into account the errors made on the time-of-flight measurements in the calorimeter. These two rejection techniques could be tested on site using a ^{232}U calibration source, a parent of ^{208}Tl nucleus, set inside the calorimeter to check the ^{208}Tl rejection using time-of-flight.

We have determined the influence that the time resolution has on the various defined cut-off efficiencies. The poorer this resolution is, the more difficult it is to discriminate ^{208}Tl events from signal events. Improving the time resolution of the calorimeter was not a direct purpose of the R&D programme, however it has benefited from the high light output achieved to meet the energy resolution goals. The time resolution of the optical modules has been monitored at every stage of the R&D programme but remains to be precisely determined. This is actually the purpose of the next chapter, which describes how the time resolution of the optical modules of the demonstrator calorimeter can be determined with a ^{60}Co calibration source.

Chapter 5

Calorimeter commissioning

> There's a difference between knowing the path and walking the path.
>
> Morpheus
> *The Matrix*

The commissioning of the SuperNEMO demonstrator has begun in 2019 and calibration acquisitions were taken and analysed by the collaboration.

The first two sections describe the start-up of the calorimeter, with the first data acquisitions and the various calibration operations carried out by the collaboration. Studies led to characterise the waveform baseline and pulse shape are presented. Optical modules have are aligned in gain and a general procedure for their energy calibration is given.

The rest of the chapter deals with the work done within the framework of this PhD in order to verify the operating state of the calorimeter and its signal cables, after integration. All cable lengths are measured by an innovative technique, and the corresponding time offset of each electronic channel is characterised. An additional time offset brought by the electronic boards is also measured.

5.1 Optical modules calibration

It is necessary to check the correct operation of the whole calorimeter as well as each individual optical module, in order to repair and correct it if necessary.

5.1.1 Pulse shape studies

It is interesting to study the shape of the pulses sampled by the electronic boards, as it allows the identification of the presence of pre- or post-pulses. This may be caused by undesired interactions, such as contamination of photomultipliers' vacuum by Helium, or the interaction of photons from the laboratory lighting, due to defects in the detector's light tightness. A study performed by William Queen, a PhD student at UCL, allowed to determine a reference model for the expected

shape of calorimeter waveforms. An example of an awaited waveform is given in fig. 5.1. The pulses received by the calorimeter can then be compared with this standard waveform, allowing any issues to be detected and resolved.

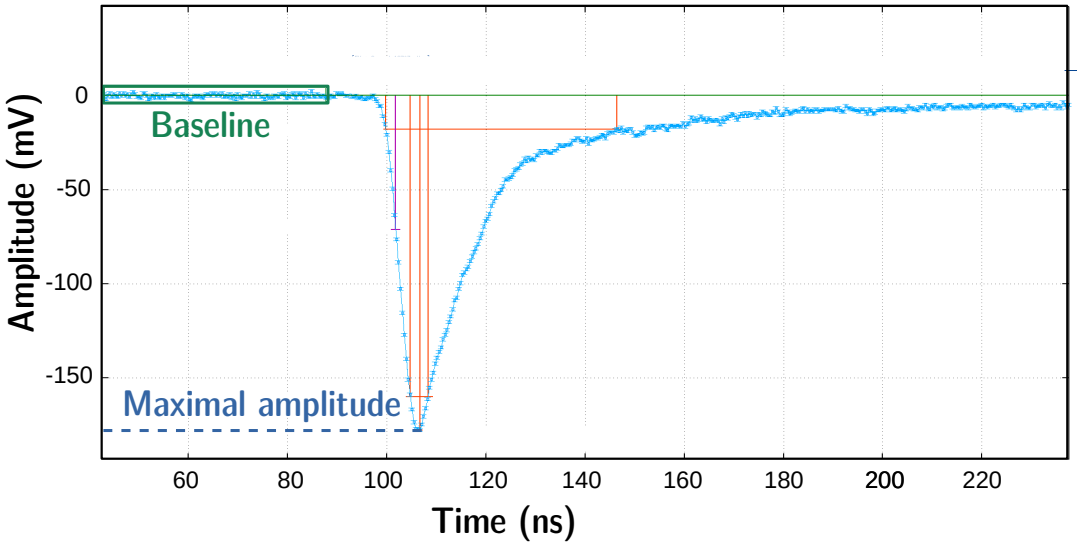

Figure 5.1: Calorimeter waveform visualisation with the SNFee software.

5.1.2 Baseline studies

The baseline is the part of the signal located before the signal rising edge. Slight signal fluctuations can be observed in this area due to electronic noise, for example. By averaging the amplitude value in this area, a reference can be defined to calculate the pulse amplitude. This average is calculated by default directly by the calorimeter front-end boards, over the first 6.25 nanoseconds of the signal. In order to minimise the impact of statistical fluctuations on the baseline calculation, a more efficient analysis has been developed by Hichem Tedjditi, a PhD student at the CPPM, allowing to calculate it over an extended time. The calculation of this average starts at the opening of the acquisition window, up to the rising edge of the signal pulse, which is detected automatically. The presence of pre-pulses is also automatically characterised. This analysis is done off-line and participates in the verification of the optical modules condition, after the installation of the calorimeter, and throughout the data acquisition of the demonstrator.

5.1.3 Gain studies

When a particle deposits energy as it interacts in the scintillator, the detection chain that follows enables a quantity of charge to be recovered at the PM voltage divider, that is proportional to the first energy deposited and depends on the high voltage applied to the photomultiplier. In the SuperNEMO detector, these voltages can be adjusted individually for each block. Charge and amplitude spectra can be obtained for each optical module and therefore depend on the high voltage

applied. As the optical modules are triggered by a signal amplitude threshold, it is necessary that the gains of all the optical modules of the calorimeter are equalised, in order to have comparable threshold values. For the SuperNEMO calorimeter, this value has been set at an amplitude of 200 mV for 1 MeV deposited. Each optical module has then to be calibrated after installation, in order to reach this standard value and equalise all the PM responses. The current study has been led by Axel Pin, a PhD student from CENBG.

This calibration consists in the optical module gains alignment, by obtaining a new high voltage value to be applied. To determine the current gain of an optical module, one must first obtain its amplitude (or charge) spectrum and then locate a particular point on this spectrum. For this study, the chosen point is located at the end of the spectrum, where the only contribution of ^{208}Tl is expected. To obtain these spectra with a reasonably large statistics, long runs (few hours) have been taken with the demonstrator, without the ^{207}Bi calibration sources. Once this gain is obtained, a reference gain is computed using simulations of ^{208}Tl decays. The same particular point is determined, which corresponds to a given energy, as simulations allow to construct energy spectra. Therefore, two gains are obtained one for real data and the other for simulations, allowing to determine the optimal high voltage value to apply for each photomultiplier. The gains distributions after equalisation are presented in Fig. 5.2. The gain adjustment method have been effective as the distribution mean stands at 606.5 ± 1.4 mV at 3 MeV, considering a 8 % FWHM at 1 MeV, for the 440 8 inches photomultipliers.

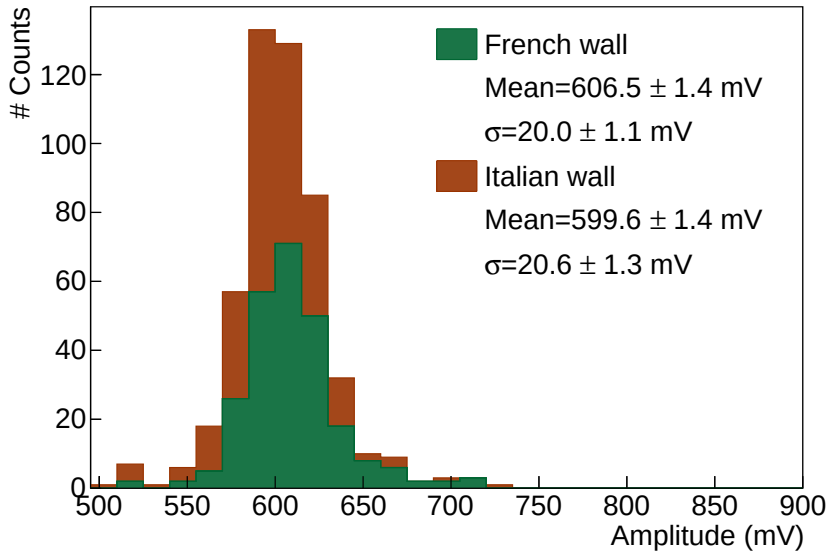

Figure 5.2: Amplitude spectra for French and Italian main wall after gain equalisation.

Now the optimal high voltages have been determined for each optical module, the collaboration will have to monitor their gain, in order to insure the stability of the SuperNEMO calorimeter over time.

5.1.4 Energy calibration

As described in Sec. 6.1, the collected charge at photomultiplier voltage divider is proportional to the amount of incident photoelectrons, thus to the initially deposited energy inside the scintillator. Once optical modules were assembled (optical coupling, packing, shielding integration), they were individually tested at Bordeaux laboratory, CENBG, with an electron spectrometer [30]. Their energy resolutions for 1 MeV-electrons at the centre of scintillator front face were determined. For optical modules assembled with 8 inches photomultipliers, this value is on average of 8.19%. Supply high voltages were characterised and set individually for each optical module to their to optimal values.

However, after the calorimeter integration, due to possible modifications of optical module characteristics, amplitude spectra of each optical block have to be re-aligned. This work was also performed by Axel Pin, PhD student at CENBG. The energy calibration method consists to find a particular point of a charge or amplitude spectrum, the Compton edge of ^{208}Tl for this study. Looking for the same location on simulated ^{208}Tl energy spectra, a charge-energy or amplitude-energy correspondence can be made and applied to calibrate each optical module in energy. I also performed another energy calibration using the data acquisition and simulations with a ^{60}Co source, using the ^{60}Co peak at 1 MeV. This is discussed in Chapter 6.

5.2 Light Injection System

The LIS is a calibration method sending light pulses in optical modules for energy calibration purposes. It has been detailed in Chapter 2. In the framework of this PhD, I took part in the analysis of the first commissioning data of this system. All results presented in this sub-section are currently being improved by the collaboration.

In Fig. 5.3 is displayed the light intensity received by each optical module of the French main wall, for a data acquisition of $\sim$ 20 minutes. Optical modules on the same main wall are divided into 5 distinct groups, each illuminated via optical fibers by the light of one LED. In the figure each of the 5 area is represented. Optical modules from area 1 do not receive light from their associated LED, denoting a possible connection problem at the bundle (all fibers coming from one LED are grouped together in one bundle before being distributed on the calorimeter wall), or an issue with the LED itself. It has been determined that this issue is intermittent, and sometimes affect other areas, possibly showing a more general problem related to the power supply of the LEDs. This issue does not seem to be serious and is currently under investigation.

After checking the LED operation and quantity of light received, the amplitude spectra for each area have been studied and are presented in Fig. 5.4. These spectra are very discontinuous and above all very spread out in amplitude. The fact that the distributions are wide is not surprising, as the amount of light received by an optical module depends on many parameters, such as the location of the optical fibre in the bundle, which determines how close the fibre is to the LED. The angle

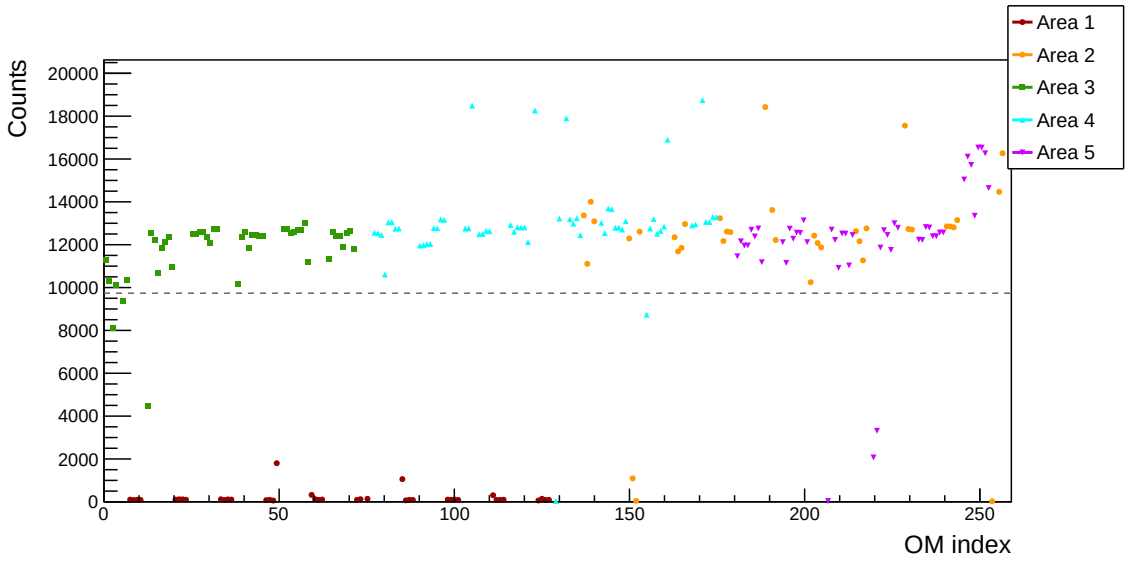

Figure 5.3: Quantity of light received by each OM (labelled with OM index) of the French main wall. Each coloured marker represents counting rates for one area of the detector, that is to say one group of optical modules lighted by the same LED. The area 1 (dark red dots) is not receiving light from its corresponding LED.

at which the optical fibre enters the scintillator can also greatly influence this quantity. But the potentially worrying thing is that the amplitudes can go up to very high values. In practice, the acquisition does not record signal amplitudes above a few hundred mV. When the amplitude is even slightly too high, the signal is simply truncated. It is then the SNFee off-line analysis software which, when trying to determine the location of the waveform peak, performs an extrapolation and gives such saturated amplitudes. So even if these values do not correspond to the actual amount of light received by the optical modules, the amplitude is still too high compared to what is expected. This work is currently being pursued by the collaboration. Especially, calibration operations are underway to harmonise the measured amplitude.

In the following, the work achieved on the calorimeter commissioning, especially on timing performances, is discussed.

5.3 Calorimeter cabling network

In this section is presented an analysis performed in order to check the status of the calorimeter signal cables installed at Modane. I was involved in most of the stages of the detector cabling, from cutting the calorimeter HV and signal cables at LAL, to their installation in Modane on the various walls of the calorimeter, via their welding to the PM voltage dividers and their organisation on the patch panel. Although not covered in this analysis, I was also involved in the connection (under the detector) of the tracker cables and their routing from the detector to the electronics. These steps were crucial and gave me a good knowledge of the detector I am working on.

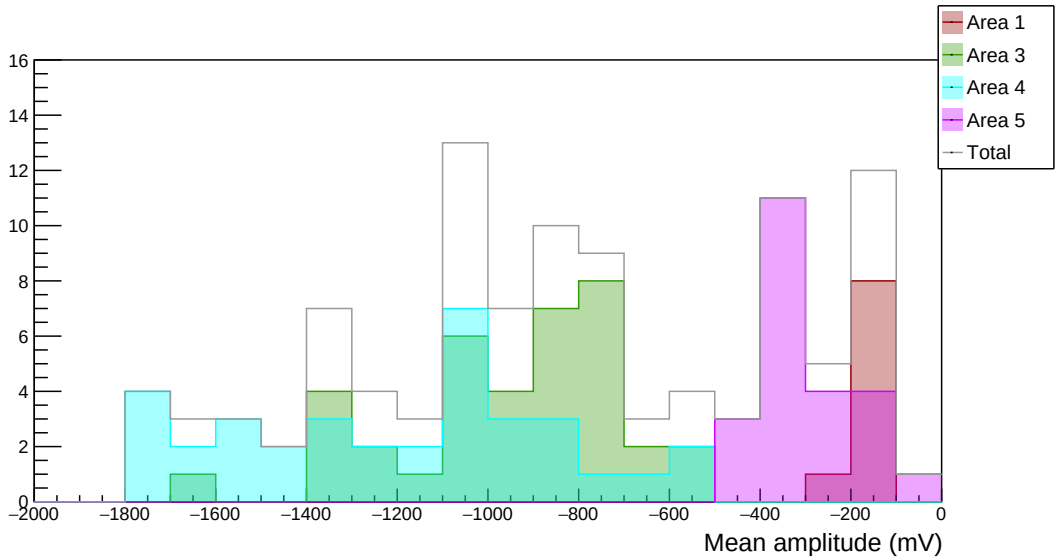

Figure 5.4: The mean signal amplitude distribution for each optical module is presented. One colour represents one area of the French main wall. In Grey is the total mean amplitude distribution.

5.3.1 Motivations

The cabling network of SuperNEMO is described in detail in Chapter 2. In particular, the calorimeter is segmented in 712 optical modules, each connected to the electronics by the photomultiplier divider through 2 cables. The first one provides the high voltage (HV) necessary for its operation. The other one, the so-called signal cable, is a coaxial cable collecting and transporting the charge corresponding to the optical module signal. Regarding only the last category, 1424 coaxial cables were cut, assembled, connector-mounted, transported and installed at LSM.

Each coaxial cable length was determined by taking into account the demonstrator design. All external coaxial cables were designed to be 7 meters-long – the distance between electronic boards and patch panel being the same for all channels – and internal cable lengths have been adapted to fit the distance from the patch panel to each optical module. Cutting and labelling all cables lasted several weeks. After all cables were transported and installed at LSM, we have to check each coaxial cable condition, for several reasons:

- making sure that cables have not been damaged during the transport and the installation,
- controlling if no swap between signal channels has been made during cable labelling or calorimeter cabling,
- checking if the coaxial cables were cut at right lengths,
- estimating time delays induced by the signal transit time inside the coaxial cables.

The last point is essential: knowing that the electron velocity in a coaxial cable is a determined constant value, the longer the cable, the longer it takes for the

signal to reach the electronics. As coaxial cables have different lengths, each calorimeter signal channel is characterised by a delay degrading the calorimeter time-of-flight resolution. Therefore, each coaxial cable length has to be precisely characterised, and the transit time has to be stored in a database made available to the collaboration.

5.3.2 Experimental setup

In order to control each cable status, we used a feature provided by the SuperNEMO's electronics, where an electrical signal, called *primary* pulse, is generated by the calorimeter front-end boards and sent independently to each channel. The electric signal reflects when it encounters a high impedance, and travels back to the electronics where it is recorded, after a more or less long cable distance. This back signal is naturally called *secondary* pulse. The Fig. 5.5 summarises the three most probable scenarios when such a pulse is sent in the SuperNEMO calorimeter cables.

- Fig. 5.5a: under normal cable operating conditions, the pulse travels along the coaxial cable until it reaches the photomultiplier and reflects on the divider.

- Fig. 5.5b: it may happen a cable is not (or badly) connected to the PM divider. In that case the signal reflects at the end of the internal cable. In this scenario, the time it took for the signal to travel this distance is the same as in the first case, but since the impedance is different, the amplitude and shape of the reflected pulse are also different. This scenario is addressed in Sec. 5.3.3.

- Fig. 5.5c: if the cable is not connected at the patch panel level, the signal undergoes a reflection at the end of the external cable. This scenario is addressed in Sec. 5.3.4.

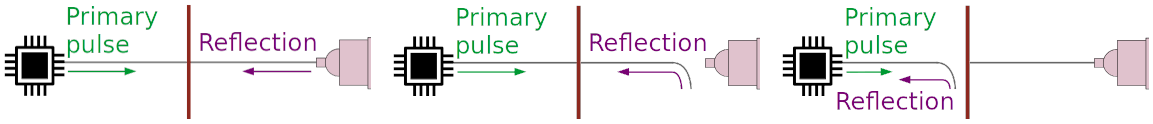

(a) Normal reflection at PM divider.

(b) Cable not connected at PM.

(c) Cable not connected at the patch panel.

Figure 5.5: Three possible scenarios occurring when a signal is sent in the SuperNEMO coaxial cables. The electronic boards are symbolised by black chips, and the patch panel by red vertical bars. The coaxial cable, pictured by horizontal lines, connects the electronics to the PM divider. (a) The cable is well connected at the patch panel and at the PM. The signal reflects at the PM divider. (b) The cable is not connected (or badly connected) at the PM divider. The signal is reflected at the end of the internal cable. (c) The cable is not connected (or badly connected) at the patch panel. The signal is reflected at the end of the external cable.

An example of a set of primary and secondary pulses, under normal cable operating conditions, for 8 inches PMs, is displayed in Fig. 5.6. All primary pulses are sent almost simultaneously inside different electronic channels, so they appear all superimposed. Depending on the cable length they travelled through, secondary pulses return to the electronics with more or less delay. Secondary pulses are deformed by their passage through the cable, which acts as a transfer function on the signal.

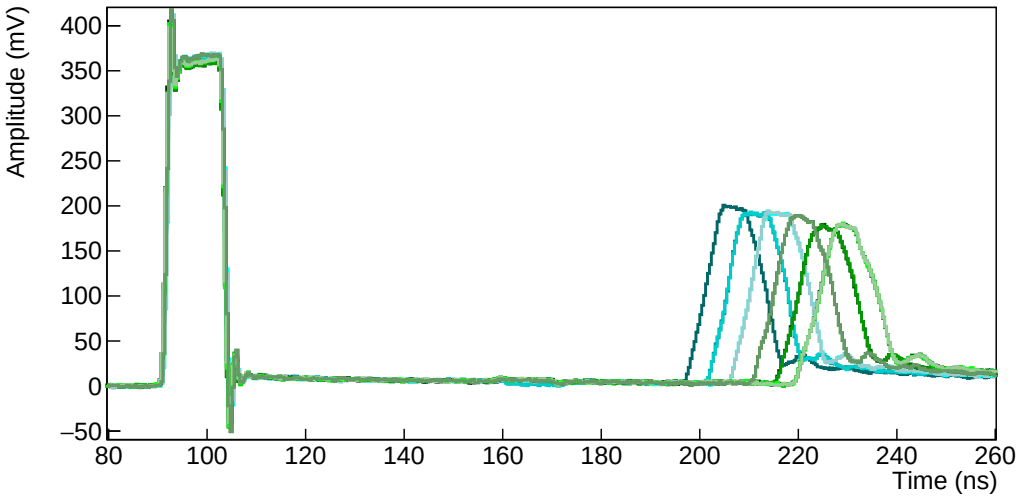

Figure 5.6: Primary (left) and secondary (right) pulses for different cable lengths under normal cable operating conditions, for 8 inches PM. Such pulse shapes are used as a reference to detect abnormal pulses and thus identify possible defaults.

In order to accumulate enough statistics, we send thousands of pulses in each coaxial cable. The analyses of the shape and arrival times of those secondary pulses for each electronic channel is called *reflectometry*, and allow to check the coaxial cable conditions and to control their lengths. Mathieu Bongrand (LAL) and me took care of the data acquisition at Modane.

5.3.3 Pulse shape analysis

By analysing the shape of secondary pulses, one may gather information about the cable state and connection. This analysis was conducted jointly with Mathieu Bongrand.

In Fig. 5.7 are displayed three examples of expected secondary pulse shapes, taken as reference in order to compare them with other reflected signals. These are obtained by averaging all pulses sent in a given electronic channel. The first one corresponds to a normal recorded pulse for a signal reflected on a 5 inches PM divider. The shape is modified compared with the one of 8 inches, because the impedances at 8 and 5 inches dividers are not the same. The second one is observed when the coaxial cable is misconnected (typically when signal and ground connectors are inverted at PM divider). The last one stands for a disconnected cable, at the patch panel or photomultiplier, as the signal is being reflected at the

end of the coaxial cable. A reflection at the patch panel level can also be tagged by using pulse timing: the secondary pulse would be detected highly earlier than expected. Then, a simple check onsite can confirm this observation, and the coaxial cable can be connected again.

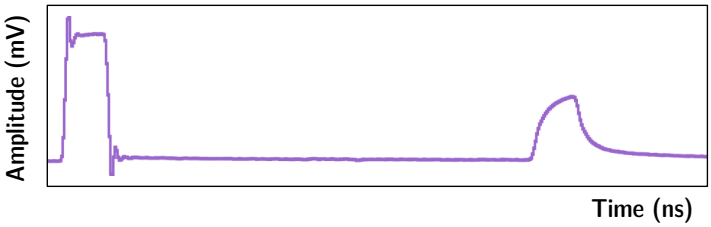

(a) Expected secondary pulse for 5 inches PM.

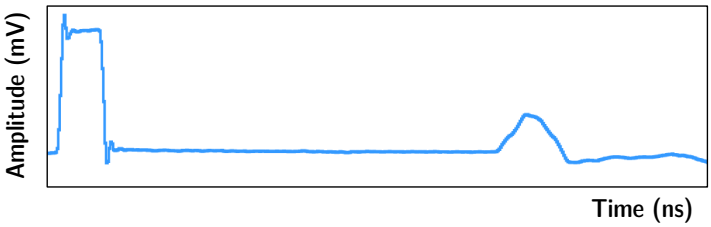

(b) Expected secondary pulse for swapped cables at PM.

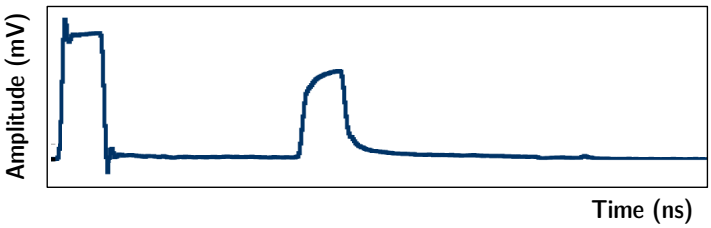

(c) Expected secondary pulse for disconnected cable (PP or PM).

Figure 5.7: Expected secondary pulse shapes obtained by averaging the thousands of pulses sent in one cable.

In order to identify cabling issues, secondary pulses are averaged for each channel and visually analysed. If an averaged pulse is identified as abnormal, then the problem affecting the cable can be characterised by comparing the averaged waveform with the references presented. Thanks to this analysis, some cable de- or misconnections at the patch panel and PM divider have been identified and fixed.

A last issue, which is not pictured in the previous figure, would be if a coaxial cable is damaged in the middle of its length. In that case, we expect to see pre-pulses between the primary and secondary pulses, stating that a part of the signal is reflected on a cable defect. The time difference between the initial pulse and the pre-pulse would make it possible to locate the defect. Such signal has not been observed, leading to the conclusion that no cables have been damaged during transport.

For a future study, it would be interesting to automate this process, as it was done for the analysis presented in Sec. 5.1.1. Many manipulations still take place

at Modane, some of them close to the calorimeter, which is not yet protected. It is therefore important to do again these tests before encapsulating the detector.

5.3.4 Pulse timing

Coaxial cable lengths have been designed to match the cable routing plan from the electronics to optical modules. Using the reflectometry tests performed at Modane, we are able to measure precisely each cable length and to compare it with the designed one.

The measured length l_j^m of a cable j can be defined as

$$l_j^m = 0.5\, t_j\, v_p\,, \tag{5.1}$$

where t_j is the time taken by the signal to make a back and forth trip in the cable, and v_p is the signal velocity in coaxial cables. The time t_j corresponds to the averaged timing difference between primary and secondary pulses and is written as

$$t_j = \langle t_{\text{sec}} - t_{\text{prim}} \rangle_p\ , \tag{5.2}$$

$\langle\rangle_p$ being the average over all pulses sent in one single cable j. The velocity v_p can be expressed as a fraction of light speed in vacuum, c, as

$$v_p = \frac{c}{\sqrt{\epsilon_r}}\,,$$

with ϵ_r the relative dielectric constant of the material, indicating that the signal velocity depends on the cable components. For coaxial cables chosen for SuperNEMO, the manufacturer supplies $v_p = 0.69\, c$.

Definition of the pulse timing

Both analyses of chapters 3 and 4 have been performed on simulated data. The reconstruction software of SuperNEMO does not offer the possibility to reconstruct signal waveforms, and only observables such as the measured energy and time are available. Nevertheless, as we analyse real data in this chapter, it is an opportunity to describe how the time of an event is defined from the waveform sampling.

The SNFee software, developed by the team in LPC Caen, provide a timing measurement called Constant Fraction Discriminator (CFD), furnishing an amplitude-independent definition of waveform timing. This algorithm aims at tracking a signal and defining its time at a given fraction f_{CFD} of its maximal amplitude. The main advantage of this technique is that it provides a good resolution on the measured time. A graphic representation of the CFD method is given in fig. 5.8 for $f_{CFD} = 40\%$, applied on a secondary pulse.

In order to have the best precision on the time measurement, it is important to investigate the possible influence of the f_{CFD} parameter. An easy operation has been set up at Modane: the coaxial cable connected at a given PM has been split in two parts, connected to two different channels, and electronic pulses were sent through one of the two connected channels. Therefore, the electronic signal sent in

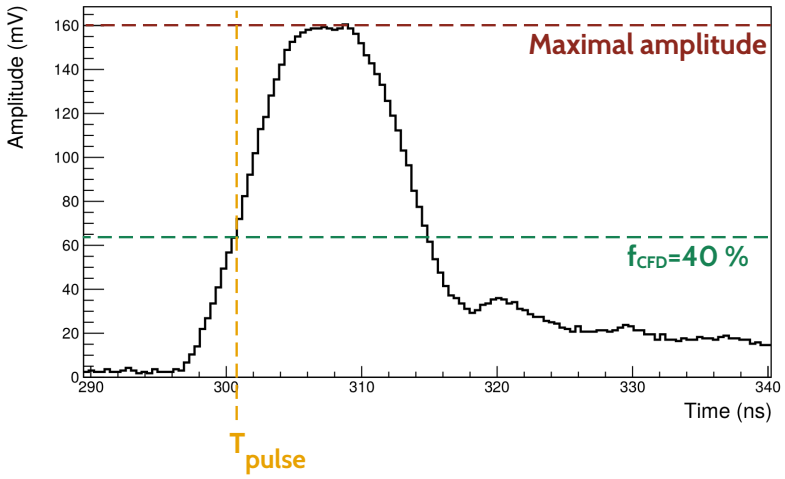

Figure 5.8: Graphical representation of the Constant Fraction Discriminator (CFD) method. The pulse maximal amplitude (red dotted line) and the fraction $f_{CFD} = 40\%$ (green dotted line) are displayed. The time T_{pulse} (orange dotted line) represents the time defined with this technique.

that channel travels through the split cable to the PM and come back to the front-end board. The signal then slits up to trigger both the two connected channels. As the signal takes two paths of slightly different lengths, the time difference Δt between the two channels can be defined as

$$\Delta t = t_{ch1} - t_{ch2} \,, \tag{5.3}$$

where t_j are defined with Eq.(5.2) and depends on the f_{CFD} fraction. In Fig. 5.9 is displayed such distributions: three different values of the f_{CFD} parameter are used to compute the t_j times, thus giving three different Δt distributions. The means and widths of these distributions depend on f_{CFD}. The distribution width expresses the precision with which time is measured, so this parameter has to be minimised. In Fig. 5.10 is displayed the distribution width with the value of f_{CFD}. It arises the value giving the best precision on timing measurement is $f_{CFD} = 50\%$ with $\sigma \sim 70$ ps, and we adopt this value for the following analysis.

The signal travels the same path from the PM to the point of cable separation. The phase shift that occurs between the two paths is caused by the length difference between the two strands of the split cable, as well as the signal path difference within the FEBs calo. The measurement of the shift for each calorimeter FEB is addressed in Sec. 5.4.

Signal velocity in coaxial cables

The value supplied by the manufacturer for signal velocity in coaxial cables is experimentally verified, in order to provide robust and precise results for the reflectometry analysis.

To control this velocity, three coaxial cables of different lengths are measured, with a precision of 1 cm. A thousand of electronic pulses are sent in each of the three cables and secondary pulses are recorded. The time t_j is then measured,

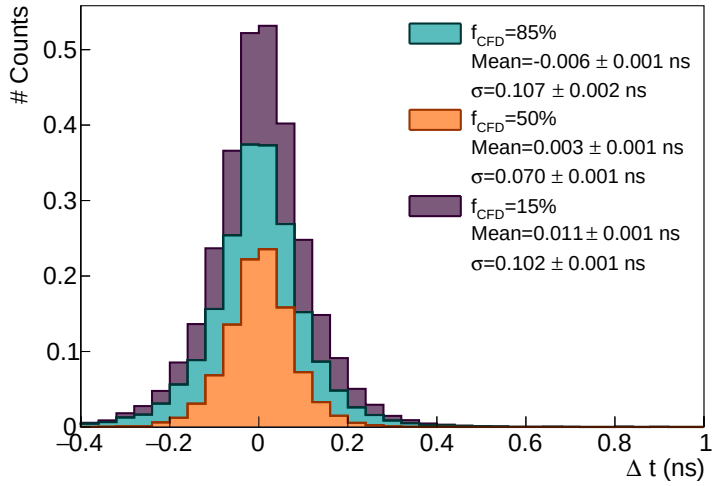

Figure 5.9: Δt distributions for three different f_{CFD} parameter value.

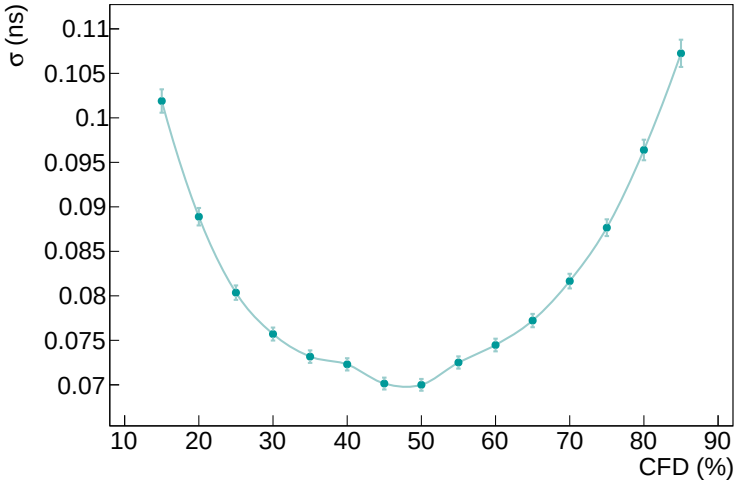

Figure 5.10: Δt distribution width as a function of f_{CFD}.

using the CFD method. In Fig. 5.11 is displayed the lengths l_j as a function of the times t_j. This procedure allows to have three independent measurements for the signal velocity by fitting these points. The value of $v_p/c = 0.697 \pm 0.0011$ is found, showing a compatibility up to 7σ with the data sheet. Certain conditions during data acquisition may explain this difference, such as the frequency of the signal. This velocity is kept for the current analysis.

Cable lengths

One of the principal goal of this study is to measure the cable lengths l_j^m using reflectometry data, in order to check if they were cut at designed lengths l_j^d. Results are presented for main wall cables.

Coaxial cables are tested by sending pulses in front-end boards electronic

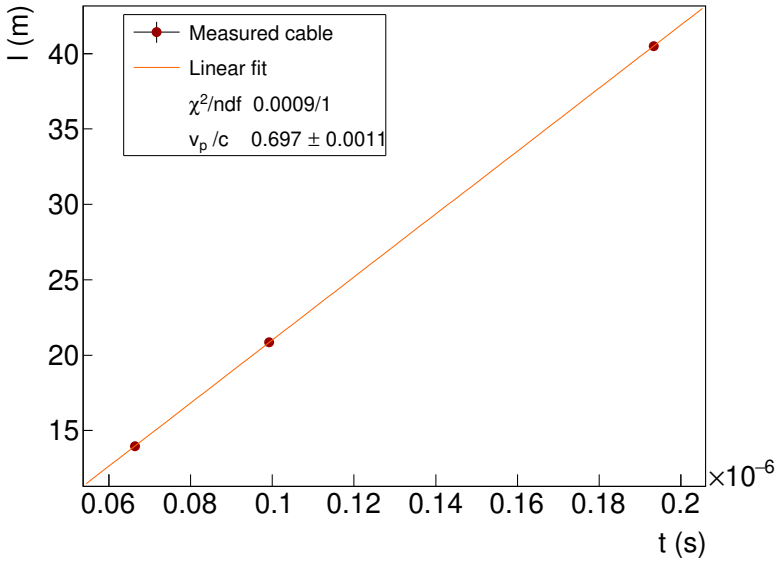

Figure 5.11: Three different lengths l_j of cables are measured. Pulses are sent inside all cables. The lengths l_j are plotted as a function of the time differences t_j between primary and secondary pulses. The value of v_p/c fitted from the data points is displayed. This value of 0.697 ± 0.0011 shows the compatibility with the one supplied by the constructor, of 0.69 c.

channels, and by measuring the secondary pulse times. The length difference ΔL_j between measurements and expectations is defined as

$$\Delta L_j = l_j^m - l_j^d \,. \tag{5.4}$$

Knowing the signal velocity inside cables, each cable length is determined precisely. In Fig. 5.12 is displayed the distribution ΔL of lengths measured by reflectometry. In hypothetical perfect conditions, all tested cables should have the designed length, in other words, $l_j^d = l_j^m \; \forall j$. In that case, the ΔL distribution would be a Dirac peak at zero. However, in real conditions, the measured lengths are different from the designed one, leading an enlargement of the distribution. This width gives access to the cutting device precision, measured at $\sigma = 5.0 \pm 0.3$ cm, which is an acceptable value for the cable length accuracy required. A few cables have been cut too short by mistake, the worse of them being 80 centimetres shorter than expected. A verification has been made on site to check a possible disconnection at the patch panel, but it turned out that this cable had indeed been cut too short. Fortunately, this cable was successfully connected to PM despite this deficit. On the contrary, few cables have a large extra length. This probably is due to human punctual mistakes, but without any strong consequences for the calorimeter operation.

Surprisingly, the distribution is also shifted towards positive values, with the mean at $+10.9 \pm 0.3$ cm, meaning that cables are longer than expected, in average. This may reveal a bias coming from the cable cutting device. Indeed, during the cutting process, the device had a tendency to slip, probably leading to extra lengths of cable. If that is the case, we assume the device has a determined probability to slip, for one meter of cable. Therefore, the probability for the device to provide

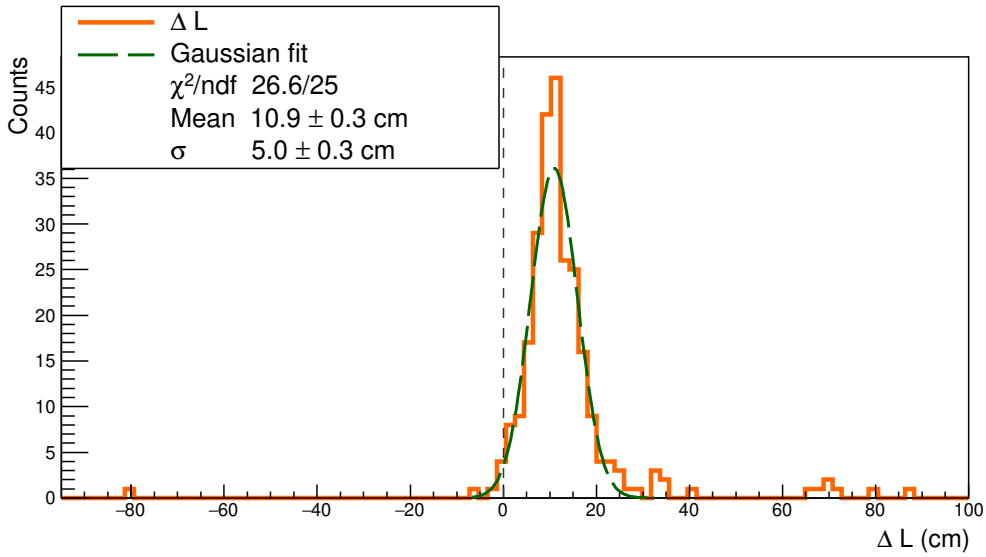

Figure 5.12: The ΔL distribution for coaxial cables of the two main calorimeter walls (orange). The ideal case for which $l_j^m = l_j^d \ \forall j$ is displayed (grey dashed line). Some data points considered as outliers are beyond 3σ.

extra length should increase with the cable length. To verify this assumption, Fig. 5.13 displays the length difference ΔL as a function of the initial design length l^d. A linear fit, parameterised as $y = \alpha x + \beta$, reveals that the cutting device presents two different biases. The value of β shows that it systematically takes away 3.4 cm of each cable. As it was planned in the design to add a few tens of centimetres per cable, for safety reasons, this bias is absorbed and is not a cause of concern. Besides, the slope $\alpha = 0.010 \pm 0.002$ of the linear fit reveals that one extra centimetre is added for every meter of cable, being compatible with the hypothesis on the cutting device sliding. Hopefully this bias is not problematic as it makes most of the actual cable lengths longer than the design, while shorter lengths could have led to systematic connection issues to PMs. In conclusion, no important mistakes have been made when cutting cables, and we had no issue for connecting the only problematic cable.

The analysis of reflectometry data allowed to find and repair damaged coaxial cables, as well as to measure their length, thus taking part in the commissioning effort that has been provided by the whole collaboration. Measuring the real cable lengths give also access to the time taken by the signal to go from a PM to the electronics, which is an important characteristic of the demonstrator, that has to be characterised.

Signal time delay

Once the signal velocity is measured, the time needed for the signal to travel from one given PM divider to the electronic boards can be deduced. This time travel induces a signal delay, specific to each electronic channel. Therefore, one of the greatest implication of this study was to provide for the collaboration a database containing time delays for each electronic channel of the two main walls. This

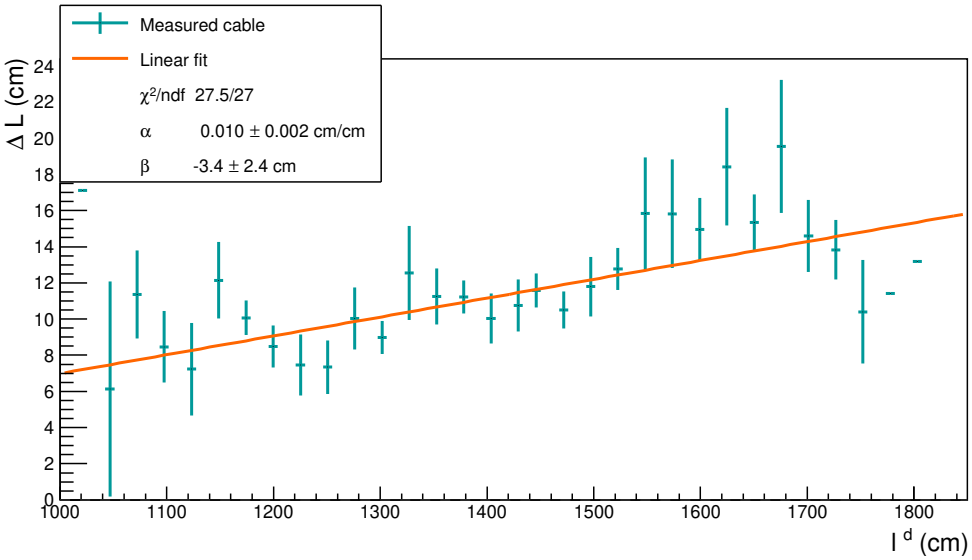

Figure 5.13: ΔL values as a function of l^d (cyan), where l^d are averaged in each bin. Data points are fitted by $\alpha x + \beta$, with $\alpha > 0$ and $\beta < 0$, revealing the two biases of the cutting device.

document is available on the Lyon computing platform.

5.3.5 Signal attenuation

The attenuation of an electric signal is a problem common to all electronic fields, and comes from the charge absorption of an electromagnetic wave travelling in a medium. For a coaxial cable, this attenuation mainly depends on the signal frequency f in MHz and on the cable characteristics. For the coaxial cables, the theoretical linear attenuation $\alpha_{\text{att}}^{\text{th}}$ corresponds to the attenuation by metre of cable in dB/m. It is supplied by the constructor as

$$\alpha_{\text{att}}^{\text{th}} = f\sqrt{\epsilon}\left(\frac{a}{\sqrt{f}} + b\right), \tag{5.5}$$

where the factor a depends on the diameter of the dielectric material on one side, and of the diameter of the conductor material on the other side, and where b is function of the dielectric loss factor, characterising the material's dissipation of electromagnetic energy. For the used coaxial cables, and with a frequency f of few GHz for the signal pulses sent in cables, we calculate this attenuation as $\alpha_{\text{att}}^{\text{th}} = 1.22$ dB/m. In a more general manner, the attenuation of a signal in dB is defined with the decimal logarithm of a power ratio. We use this definition to determine the attenuation in the framework of the reflectometry analysis, defining the attenuation $\mathcal{A}$, for a given length of cable l, as

$$\mathcal{A} = 10 \log_{10} \frac{V_{\text{prim}}}{V_{\text{sec}}}, \tag{5.6}$$

where V_i is a quantity representing the intensity of the signal. It corresponds either to the maximal amplitude of the pulse A or to the pulse charge Q, defined

as the amount of signal received by the acquisition, integrated over the acquisition time window. As the provided data sheet does not specify the attenuation of which quantity (amplitude or charge) represents $\alpha_{\text{att}}^{\text{th}}$, we decide to investigate both in the following. Then, we define the linear attenuation $\alpha_{\text{att}}^{\text{R}}$, measured by reflectometry in dB/m, with

$$\mathcal{A} = f_r + \alpha_{\text{att}}^{\text{R}}\, l\,, \tag{5.7}$$

with $f_r = -10 \log_{10} R$, where R is the reflection factor characterising the pulse reflection on the PM divider. In fact, as the circuit is opened, the pulse is reflected at the PM divider, but only partially. A part of the signal is not reflected but lost through the divider. This reflection is characterised by R, which is function of the impedance Z_c of the cable, and of the impedance Z_d at the divider level, where the pulse is reflected. It is written as

$$R = \frac{Z_d - Z_c}{Z_d + Z_c}\,, \tag{5.8}$$

where we have the limit

$$\lim_{Z_d \to \infty} f_r = 0 \text{ and } R = 1\,, \tag{5.9}$$

expressing a total reflection occurring when the impedance at the PM divider is infinite. The main goal here is to determine the value of $\alpha_{\text{att}}^{\text{R}}$, using the reflectometry data, and to compare it with $\alpha_{\text{att}}^{\text{th}}$. Moreover, the impedance Z_d value at PM divider can be estimated from the determination of f_r. In Fig. 5.14 is shown the linear dependence (on a logarithmic scale) between the attenuation $\mathcal{A}$ and the cable length l, for amplitude and charge. The amplitude A is given in mV and the charge Q in mV.ns. The values of $\alpha_{\text{att}}^{\text{R}}$ and f_r, for both amplitude and charge cases, are displayed in the legend. Firstly, the two linear fits reveal that, whether calculated with the amplitude, or with the charge, the linear attenuation $\alpha_{\text{att}}^{\text{R}}$ is smaller than the calculated one $\alpha_{\text{att}}^{\text{th}}$ (for the amplitude case, $\alpha_{\text{att}}^{\text{th}} \simeq 5 \times \alpha_{\text{att}}^{\text{R, amp}}$, and for the charge case $\alpha_{\text{att}}^{\text{th}} \simeq 7 \times \alpha_{\text{att}}^{\text{R, ch}}$). That means the signal is less affected, when transmitted by the cable, than expected. Secondly, the attenuation in charge is less important that the attenuation in amplitude. This can be easily explained: as it is integrated over time, the charge is a quantity less affected by amplitude variations that the amplitude itself. For the same reason, the charge data set points are less spread than the amplitude ones, confirming we are less sensitive to cable length variations when using the charge quantity.

The study of signal attenuation allows us to conclude that coaxial cables do not significantly degrade the signal transmission, especially if we look at the waveform charge. However, looking at the shape of the secondary pulses compared to the primary ones, it is clear that the pulse shape, and especially its rising edge, is affected by the path in the cable. It would then be interesting to conduct a study investigating the influence of these cables on the rising edge time, and thus on the accuracy of time measurement of calorimeter data due to the coaxial cables.

5.3.6 Summary

Analysis of reflectometry data allowed to control the coaxial cables status after the calorimeter cabling operations. All possible misconnections and damaged

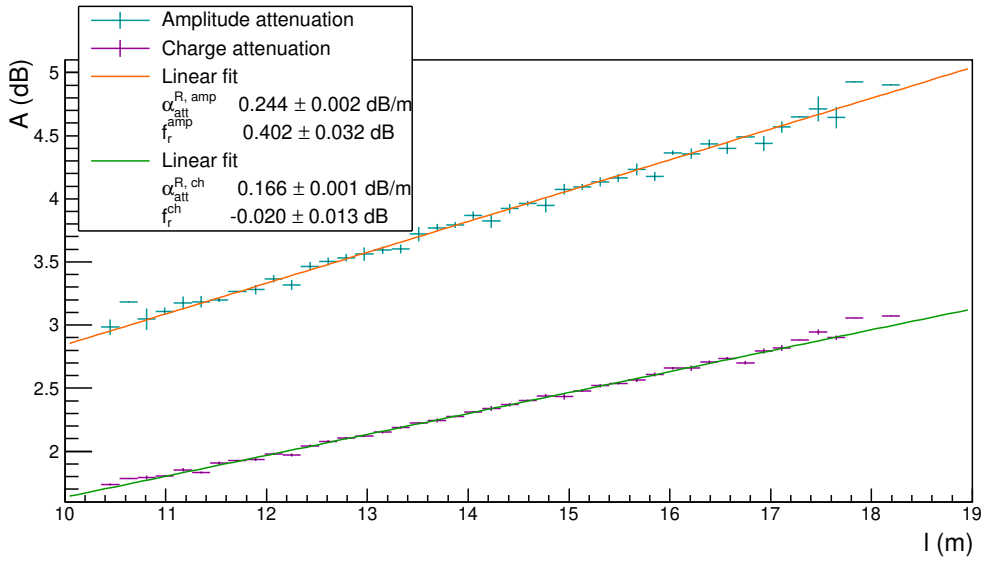

Figure 5.14: The amplitude $\mathcal{A}$ is displayed as a function of the measured cable length l. The data set calculated with the amplitude (charge) is given in cyan (magenta) and fitted by a linear function in orange (green). The values of the slope, which represent the linear attenuation of the coaxial cables in dB/m, are respectively $\alpha_{\text{att}}^{\text{R, amp}} = 0.241 \pm 0.000\text{dB/m}$ and $\alpha_{\text{att}}^{\text{R, ch}} = 0.166 \pm 0.000\text{dB/m}$. The two y-intercept values, which represent the reflection of the pulse on the PM divider, are $f_r^{amp} = 0.402 \pm 0.032$ dB and $f_r^{ch} = -0.020 \pm 0.013$ dB.

connectors have been fixed. The time measurement, using the CFD method, was optimised in order to have a better timing precision. All cable lengths were checked and revealed the cutting device is biased, producing cables longer than designed. The corresponding time delay induced by the signal time travel are stored in a database made available for the collaboration. This study was the occasion to understand some properties of the cables, as velocity and attenuation of a signal travelling in coaxial cables.

Apart from the coaxial cables, the calorimeter FEBs themselves can have an impact on the signal timing delay, which is addressed in the next section.

5.4 Synchronisation of calorimeter FEBs

One of the parameters that can also delay and de-synchronise the signal collected from optical modules is the path difference of the electronic signal inside the calorimeter FEBs, which is pictured in Fig. 5.15. Indeed, the CB manages the distribution of the clock in all calorimeter FEBs. The further away the CB is from an FEB on the crate, the longer it will take for this information to be transmitted. The scheme given is highly simplified and in practice even each electronic channels of a given board has an individual delay. This de-synchronisation has to be characterised in order to calibrate each electronic channel of each FEB, which is primordial for analysis of coincidence events with the calorimeter.

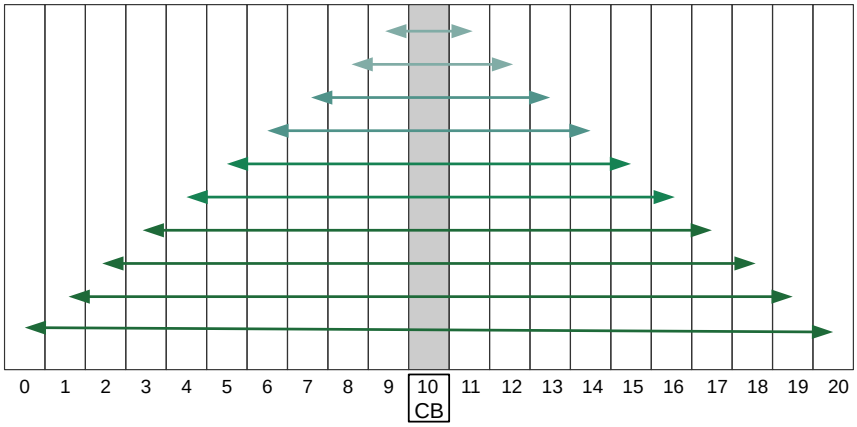

Figure 5.15: Sketch of the electronic paths from the central CB to each FEB.

The set up used to measure this de-synchronisation was provided by the electronics team at LAL. A wave-catcher is set up to produce an electronic impulse (of same shape as the one used for reflectometry) and split it in two channels. By connecting this device on pairs of FEB channels, one can measure the time offset existing between them. The general principle consists then in choosing a channel taken as a reference by connecting one cable of the device to it. Then data acquisitions are taken by connecting successively the other cable to all other channels from the same crate, allowing to measure the offset existing between them and the reference channel. Three examples of Δt distributions are given in Fig. 5.16, for three different channels belonging to the same FEB, in coincidence with the reference channel. The distributions σ stand around $\sim 20 - 30$ ps and represent the resolution on time measurements brought by the calorimeter FEBs. The distributions mean represents the time offset of each of the three channels with the channel taken as a reference.

The goal of this analysis is to characterise the time offset of each channel of each FEB. In Fig. 5.17 is given the mean of the Δt distributions as a function of the distance between the corresponding FEB and the central CB. The more distant an FEB is from CB, the greater its time offset will be in relation to the reference taken, confirming the description given in Fig. 5.15.

More than 800 channels were calibrated: 3 crates, 20 FEBs for the two firsts and 12 for the last one, each having 16 electronic channels. All time offsets have been stored in a database and made available for the collaboration.

5.5 Conclusion

On this early autotumn 2020, the calorimeter commissioning is almost complete, and a huge effort have been provided by the whole collaboration to calibrate it. Automated codes have been developed to monitor changes in calorimeter characteristics over time (pulse shape, baseline, optical modules gain...). The reflectometry analysis allowed us to control and record the lengths of all coaxial

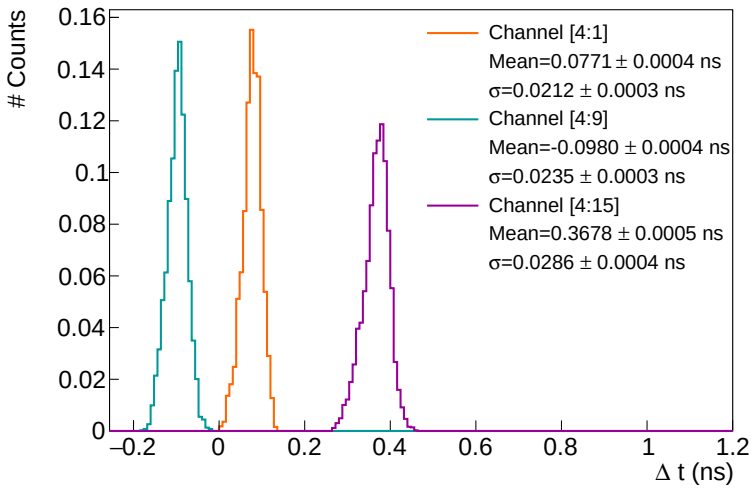

Figure 5.16: Δt distributions between the reference channel and three channels on the same FEB. Data taken with a waveform digitiser.

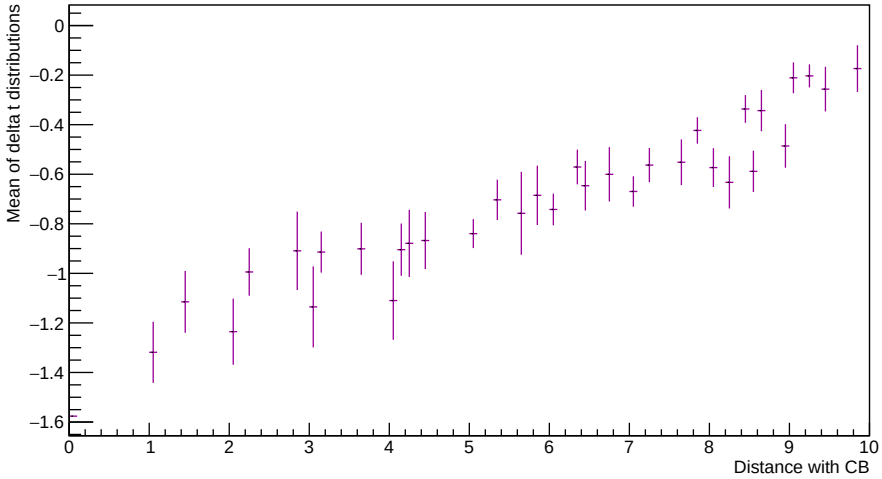

Figure 5.17: Δt distribution mean as a function of the distance of the corresponding FEB with CB.

cables installed on the SuperNEMO demonstrator at LSM, and gave information on the status of cable connections at the patch panel. We also have understood the main results on measured cable lengths. The signal time delay induced by coaxial cables and front-end boards have been characterised and made available in databases. In a subsequent analysis, the entire calibration chain will have to be calibrated in time, from the optical modules to the FEBs, using for example the LIS system sending light pulses in each scintillator.

All the work done to calibrate the calorimeter, and especially its time calibration, opens the door to the first physical data acquisition with the calorimeter. Coincidence measurements of particle time-of-flights are therefore made possible by the characterisation of the time delay specific to each channel. In the following chapter, we describe an experiment carried out with a ^{60}Co source

to determine the time resolution of the optical modules, which follows the work presented in Chapter 4.

Chapter 6

Characterisation of the calorimeter time resolution

I suppose every second counts.

Alice
Alice through the looking glass

The precise knowledge of the different particle interaction times in the optical modules of the SuperNEMO calorimeter is important to better understand and reject the background. For example, the study of electron time-of-flight allows us to distinguish internal events (occurring within the source foils) from external events (radioactive decays occurring outside the source foils, for example in the PMs or in the iron shielding).

During the commissioning phase, a lot of work, presented in the previous chapter, was achieved to calibrate the detector. Following on from this task and completing it, a part of my PhD was allocated to determine the time resolution of the SuperNEMO calorimeter, and to provide tools to the collaboration to purchase this analysis.

In this chapter a study conducted in order to characterise the time response of the SuperNEMO optical modules with a ^{60}Co source is presented. Some detector adjustments were still ongoing at the time of the acquisition and could influence the results discussed. However, all the work presented here is necessary in the framework of the first calorimeter calibration. Moreover, I provide all the analysis tools for the collaboration, with a view to doing a possible update, once the whole demonstrator calibration will be achieved.

6.1 Time response of optical modules

In order to characterise the energy and time-of-flight of incoming particles (photons, electrons), each calorimeter block of SuperNEMO is composed of a scintillator and a photomultiplier. As detailed in Chapter 2, the purpose of the scintillator material is to transfer the kinetic energy of incoming particles through the production of the so-called optical photons. Those reaching the photomultiplier

photocathode are then converted into electrons, with an efficiency called quantum efficiency. After amplification, electrons are collected by the anode which delivers an electric signal whose charge is proportional to the initial amount of incident photoelectrons. This signal is then transmitted, via the PM voltage divider, to the electronic readout, where the signal is sampled. The particle energy, as well as the time-of-flight, can be extracted from the signal waveform analysis. Each step of the particle detection process, from the incident particle interaction inside the scintillator, to the signal sampling at the electronic readout, can have an impact on the precise time measurement of the charged particle. In Chapters 2 and 4 we introduced the so-called calorimeter time resolution σ_t, which encapsulates the global uncertainty on the time-of-flight measurement of particles into the calorimeter (Eq. (2.5)). The squared time-resolution can therefore be expressed as the sum of two contributions: the scintillator resolution $\sigma^2_{t,\mathrm{sc}}$, and the PM resolution $\sigma^2_{t,\mathrm{PM}}$,

$$\sigma_t^2 = \sigma^2_{t,\mathrm{sc}} + \sigma^2_{t,\mathrm{PM}}\,. \tag{6.1}$$

In the following, we detail in depth the physical origins of these terms.

6.1.1 Scintillator time dispersion

The scintillator temporal dispersion $\sigma_{t,\mathrm{sc}}$ in Eq. (6.1) receives contributions mainly from two important characteristics of the scintillator operating principle.

Interaction point

The incoming particle's interaction point location inside the scintillator block highly contributes to the scintillator temporal uncertainty, and depends on the incident particle type. In fact, this effect will not have the same impact on time dispersion, depending on whether the incident particle is a photon or an electron. In Fig 6.1 are schemed the interactions of a photon and that of an electron for the specific case of a SuperNEMO plastic scintillators. In Sec. 2.1.5, we exposed the different interaction types of photons and electrons. We have also explained the origin of the differences that exist in terms of interaction depth between these two types of particles. To remain consistent with these conclusions, we represent the electron as interacting in the first millimetres, while the photon stops deep inside the scintillator. When a particle (photon or electron) interacts in the scintillating material, the absorbed energy leads to the isotropic emission of scintillation photons: they propagate inside the scintillator, in all directions from the interaction point, at the speed of c/n_{sc}, with n_{sc} the optical index of polystyrene, and c the light speed in vacuum. Depending on their initial direction, some of those photons propagate straight to the PM (we name them the *direct* photons), while others are at least reflected once on the scintillator surface, before reaching the PM glass. This mechanism leads to time delays between direct and reflected photons.

In order to illustrate, and give an order of magnitude of this delay, let us consider an example where an incoming electromagnetic particle enters a scintillator from the front face, and interacts right in the centre of the scintillator

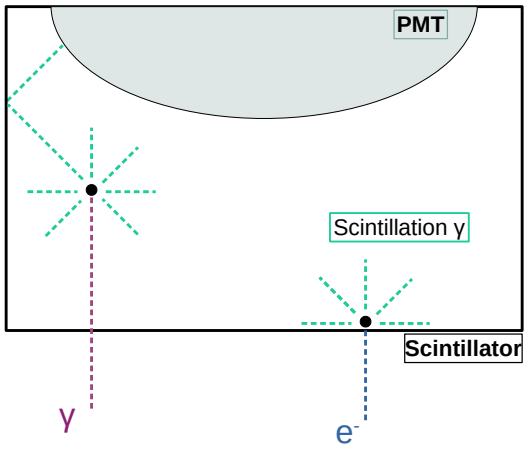

Figure 6.1: A scheme of interaction of particles in a scintillator. The photon case is displayed on the left in pink dotted line, and the electron case is on the right in dark blue dotted line. Both particles enter in the scintillator through the front face. Examples of interaction points inside the scintillator are represented by the black dots. The photons of scintillation emitted isotropically after the interaction are materialised by the bright green dotted lines. Due to different interaction probabilities in matter, the two particles interact at different depths inside the scintillator. The photon can interact deeply inside the volume, while the electron has a high probability to stop within the first few millimetres.

volume. After the scintillation emission process, a direct photon will reach the PM glass surface at time

$$t_s = \frac{L}{2c/n_{sc}}\,, \tag{6.2}$$

L being the scintillator width. Now, let us consider another photon, that we name *backward reflected*, emitted in the opposite direction. It will propagate, reflect on the front scintillator surface, and finally reach the PM at

$$t_r = \frac{3L}{2c/n_{sc}}\,. \tag{6.3}$$

This reflected photon is therefore delayed compared to the direct photon, with a time-shift of

$$\Delta t^{r,s} = t_r - t_s = \frac{L}{c/n_{sc}}\,. \tag{6.4}$$

In the case of a SuperNEMO scintillator, the length L has been designed to 25 cm, and the optical index is the one of polystyrene with $n_{sc} = 1.5$. Finally, for an incoming particle interacting at the centre of a SuperNEMO scintillator volume, a backward reflected scintillation photon will reach the PM glass 1.25 ns later than a direct photon. And this delay is even more important as the incident particle interacts deep inside the scintillator.

In view of the conclusions given in Sec. 2.1.5, we know that photons have a higher probability of interacting far into the scintillator block, compared with electrons. Therefore, this time-shift effect is all the more important for incoming

photons, while it is quite negligible for incoming electrons, for which reflected photoelectrons reach the PM glass almost as the same time as the direct ones.

This mechanism increases the signal collection rising time at the PM anode, and boosts the scintillator time dispersion $\sigma_{t,\mathrm{sc}}$, with $\sigma^{\gamma}_{t,\mathrm{sc}} > \sigma^{\mathrm{e}^-}_{t,\mathrm{sc}}$. This geometrical uncertainty does not contribute to σ_t and contributes to the time uncertainty brought by the track length.

Scintillating light emission

When a particle interacts in a SuperNEMO scintillator, two successive mechanisms of light absorption/re-emission take place. Firstly, the excitation of scintillator molecules leads to the creation of fluorescence photons. Afterwards, those optical photons are absorbed, then re-emitted by the POPOP agent, at higher wavelengths. The characteristic times of these two processes contribute to increase the scintillator time dispersion $\sigma_{t,\mathrm{sc}}$.

6.1.2 Photomultiplier time dispersion

A photomultiplier is a photodetector: after the light is collected and converted at the photocathode, the photoelectrons are multiplied. The transit time for the photoelectrons emitted at the photocathode to reach the anode after being multiplied is not constant for every photoelectron, due to a varying path for electrons emitted by the different dynodes. This results in time dispersion. This fluctuation is called transit time spread (TTS). It leads to an uncertainty on the time measurement and so has an influence on the photomultiplier time dispersion $\sigma_{t,\mathrm{PM}}$.

As discussed in Chapter 4, the time uncertainty brought by the scintillator light emission process and the photomultiplier was characterised for few optical modules before the calorimeter assembly. It is possible that the optical modules time resolutions may have changed during the phases following their measurement, so they must be measured again. To do so, data acquisitions were taken with the calorimeter, behind which a ^{60}Co calibration source was set, allowing to detect in coincidence two emitted γ's.

6.2 Description of ^{60}Co nucleus

The ^{60}Co is a man-made isotope, with a 5.27 years half-life, of which we provide the main interesting properties in the simplified decay scheme of Fig. 6.2. This unstable nucleus spontaneously decays, through the β^- process, into an excited state of Nickel 60. To reach the ground state of the Nickel 60, the nucleus goes through two successive energy levels, emitting in 99.83% of the cases two photons of 1.17 MeV and 1.33 MeV, respectively. The life-time of the second energy level is under the picosecond, thus very short with respect to the expected timing precision of the calorimeter. Therefore, the two photons are considered as emitted in coincidence.

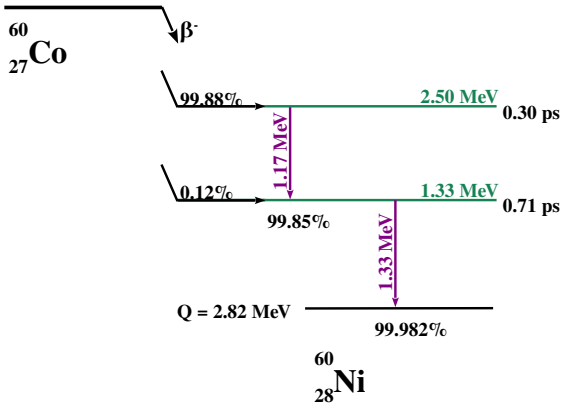

Figure 6.2: A simplified decay scheme for ^{60}Co [49]. The ^{60}Co decays, through β^-, predominantly to the 2.50 MeV state. Then, two successive γ's (whose energy levels are represented in green) are emitted in 99.83% of the cases. The two photons have an energy of 1.17 MeV and 1.33 MeV, respectively. As the life-time of the 1.33 MeV energy level is short ($<$ 1 ps) with respect to the timing precision of the calorimeter, the two photons can be considered as emitted in coincidence. We use this property to calibrate in time the demonstrator optical modules.

We aim to detect these two photons and look for coincidences between pairs of optical modules to determine their time resolutions.

6.3 Experimental design

The idea to use a ^{60}Co source to characterise the time response of the calorimeter part of SuperNEMO had never been tested on the full calorimeter before the current analysis. Therefore, all the experimental design had to be implemented.

6.3.1 Setting up the experimental design

The initial activity of the ^{60}Co source we used for this experimental set-up was 447.4 kBq in February 2014. Given the half-life of this isotope, it was reduced to 232 kBq at the time of the data-taking. In order to determine the best design, and later to monitor and compare the results obtained in the framework of this analysis, I performed simulations of ^{60}Co disintegrations for the demonstrator configuration. The characteristics of those simulations are detailed later in this section.

As described in Chapter 2, the SuperNEMO calorimeter is composed of two main walls (called *French* and *Italian* sides), as well as the so-called X-Walls (on the detector sides) and γ-Vetos (on top and below the detector). At the time of the data-taking, X-Walls and γ-Vetos were not yet operational, hence the current analysis only applies on the French and Italian main calorimeter walls. As the demonstrator was closed at this time, it was impossible to set the ^{60}Co source inside the detector, at the source foils level. Hence, the calibration source was

placed behind the calorimeter, as displayed in Fig. 6.3, where sketches of side and back views of the calorimeter are drawn. In order for all PMs to detect γ's from ^{60}Co decays, several bunches of data acquisitions were taken: the source was placed at 9 different positions on each of the 2 main calorimeter walls, approximately one meter behind. Therefore, in total, 19 data acquisitions have been taken, of which:

- 18 with the ^{60}Co source set behind the wall. The 9 different positions for one wall are represented in Fig. 6.3b.
- 1 acquisition have been taken without the ^{60}Co source, with the Italian main wall, to characterise the background detected with the current calorimeter settings.

Each data acquisition lasted about 25 minutes, for a total of 10 hours of on-site activities, taking into account the time needed to move the ^{60}Co source from spot to spot.

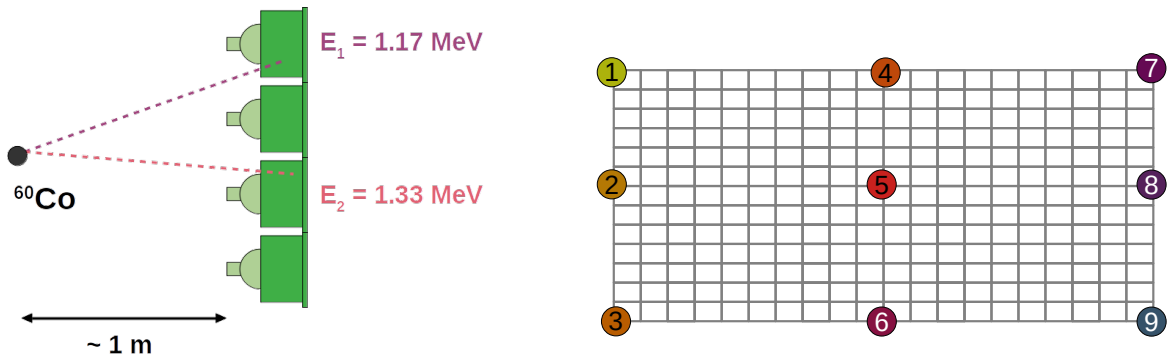

(a) (b)

Figure 6.3: (a) Side view example of the ^{60}Co source positioning behind a calorimeter main wall, schemed by 4 optical modules (green). The emissions of the 2 γ's of interest are displayed in coloured dotted lines. (b) Back view of the nine source positions behind a main wall. Each grey box represents an optical module.

Currently, the demonstrator is not protected from the laboratory lights by the anti-radon tent. As those would damage the SuperNEMO photomultipliers under tension, two removable black curtains are deployed on top of the detector (that does not interfere with data collection), and acquisitions are taken in dark laboratory. With this way of doing, all data acquisitions can be performed, while eventual necessary repairs remain possible during the detector commissioning.

Taking acquisitions in the dark is a big constraint. Moreover, the ^{60}Co source, initially used for teaching purposes, was loan by IPN laboratory (Orsay), for only two weeks, mainly because of legal constraints. Therefore, to not disturb LSM on-site activities by plunging the whole laboratory into darkness, and to make the loan time profitable, a SuperNEMO team and I performed night shifts to take data. The acquisition took place during two weeks, at the summer break 2019.

6.3.2 Simulations and analysis pipelines

As for the data acquisition, the simulated source has been placed behind the calorimeter walls. Hopefully, there was no need to simulate all the 18 positions. In fact, at this time, the detector implemented in simulations is symmetrical in terms of detection performances. Therefore, simulations of ^{60}Co events behind the two main walls are equivalent, and we only need to simulate events from 4 locations (positions 1, 2, 4 and 5, according to the Fig. 6.3b numbering system), other being obtained by symmetry operations. Four bunches, for a total of 10^9 ^{60}Co events, were simulated with the official Falaise pipeline and stored at the IN2P3 computing centre platform, making them available to the collaboration.

As the objective is to determine the optical modules time resolution, σ_t, due to the scintillator light emission process and to the photomultiplier, all simulations were performed with an ideal calorimeter, setting up $\sigma_t = 0$ ps. In that case, the only remaining contribution of optical modules to the time resolution is geometrical and comes from the interaction point uncertainty inside the scintillator. The idea behind that is to compare simulated and real data in order to bring out the contribution of σ_t to the total calorimeter time uncertainty.

The entire experimental set-up was designed and carried out by me and a group of physicists from LAL, Orsay and LPC, Caen. I developed a complete set of ROOT codes for data processing and analysis, available on the GitHub platform [50]. As the tracker is not yet operational for data collection at Modane, we are only interested in the part of the simulations with the calorimeter. Several criteria described in the following section were used to select the ^{60}Co events of interest. A single off-line analysis pipeline has been developed to handle the different output data models of the simulations and real data, in order to ensure the consistency of the analysis.

6.4 Signal events selection

We aim to use the two γ's of 1.17 MeV and 1.33 MeV from ^{60}Co β^- decay, to characterise the time resolutions of individual optical modules. Thus, the signal we are looking for is two particles detected in coincidence in distinct optical modules. In order to maximise the signal to background ratio, some selections have been applied on data.

- Trigger criteria:
  in the two calorimeter hits channel, the trigger condition is defined so as one of the two hit has to trigger the low energy (or amplitude) threshold, of 50 keV for the data acquisition. As we look for two calorimeter hits, we set an additional off-line selection on events whose two hits passed both the high amplitude threshold, corresponding to approximately 150 keV.

- Coincidence time criterion:
  we define the coincidence time-window by events occurring in a 62.5 ns-long time interval. This allows to avoid accidental coincidence events (interactions of two gammas, produced by different sources, in two optical modules), while

keeping events where two γ particles interact at both ends of the wall. This time-window was set for the data-taking and can be improved for eventual future acquisitions.

- Individual energy selection:
  in Fig. 6.4 is displayed the highest energy deposit as a function of the lowest energy deposit, for simulations with the ^{60}Co source in position 5. The high energy threshold is represented by two black dotted lines. The topology of interest is observable with two hits around 1 MeV. Also, events where two successive Compton interactions of a single photon from ^{60}Co occur in two different optical modules are characterised by a high energy hit ($\sim$ 0.8 MeV), and a low energy hit ($\sim$ 0.2 MeV). This topology constitutes a background for this analysis because the time difference between the hits has a different distribution. In order to reject them, given the energies of the two interesting ^{60}Co photons, we only select individual calorimeter hit energies greater than 0.7 MeV. This individual energy selection is pictured by two black dashed lines. It naturally highly depends on the calorimeter energy calibration.

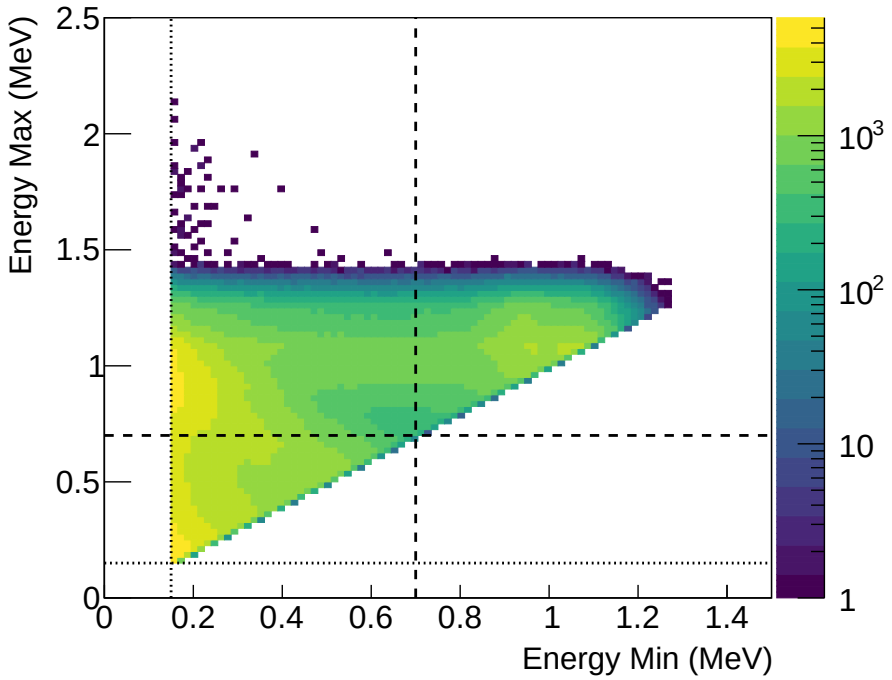

Figure 6.4: Maximal energy with minimal energy, for simulated ^{60}Co events, with source in position 5 (see Fig. 6.3b). High threshold is represented in black dotted line. Dashed lines materialise the individual energy selections.

- Geometrical selection: with a detector well calibrated in energy, the previous selection is sufficient to prevent double Compton interactions to be selected. But, at the time of the data-taking, the detector was not fully calibrated. The energy of some reconstructed particle hits then might be badly estimated and some background events could pass this energy

selection. As such interactions occur predominantly in two close scintillators, we reject topologies where two neighbouring optical modules detect signal in the coincidence window. The detector energy calibration is discussed in Sec. 6.5.

These four selections are intended to improve the signal to background ratio. The coincidence time selection is only applied to real data, while others are applied both to simulations and real data. Indeed, what we call an *event* does not have the same meaning depending on whether we are talking about simulation or real data. We simulate a given amount of disintegrations at given location(s) of the detector, so the definition of a Monte Carlo event is straightforward, and concepts such as the pile up make no sense. For real data acquisitions, a set of criteria have to be established in order to define what an event is, as the time coincidence window for example.

We remind the signification of the selection efficiency ϵ which is

$$\epsilon = \frac{\text{Number of selected events}}{\text{Total number of counts}} . \tag{6.5}$$

Selection efficiencies for cut-offs applied successively are presented in table 6.1. Significant differences are observed between simulations are real data, mainly due to the energy calibration. Indeed, at the time of the data taking, the gain equalisation and energy calibration were preliminary and had to be improved. Therefore, this statement directly affects the reconstructed energies of calorimeter hits. We address this question in Sec. 6.5.

Successive cut-offs	Simulations	Data
High threshold	35.7%	98.0%
Individual energy	17.0%	70.2%
Geometrical	16.5%	61.0%

Table 6.1: Selection efficiencies for simulations and real data.

6.5 Energy calibration

The charge collected at each PM divider is correlated to an energy initially deposited inside the scintillator. It is important to provide a robust calibration, allowing to provide a relation between these two observables, for any analysis to be valid. At the time of the data acquisition with the ^{60}Co source, only an incomplete energy calibration was provided. Indeed, as the calorimeter was at the beginning of the commissioning phase, several tests were performed, in particular manipulations that required changing the values of the high voltages. The equalisation of gains was therefore not yet implemented, which had an impact on the resolution in terms of energy. In this context, I developed a temporary energy calibration using the data taken with the ^{60}Co source.

In Fig. 6.5a is displayed charge spectra for two optical modules located in front of the ^{60}Co calibration source. In order to have a sufficient statistics, only trigger

selection have been applied on data, allowing to select events for which exactly two optical modules triggered (at least one must have triggered the high amplitude threshold). The first peak is mainly populated by double Compton interactions inside the scintillator, and the second by simple Compton interaction of the two ^{60}Co γ's of interest. For this energy calibration, the second peak is used as the particular point of the distribution. An automatic research of the two peaks is performed and, if exactly two are detected, the second one is fitted with a Gaussian function. This point has been chosen because it is less statistics-dependent than the end point of the distribution. In the figure, an example of an optical module with an appropriate gain is given, and the fit is well-performed. An example of an optical module with a too low gain (because it was under a too low high voltage) is also displayed, and shows only one peak. These kinds of distributions were thus not fitted and no energy calibration was provided for them.

The same work is performed on simulated energy distributions for all optical modules. The fits provide an average of the energy location point corresponding to the second peak, of 0.927 ± 0.009 MeV. This work allowed to calibrate 172 optical modules, in total, for the French main wall. An energy spectrum of a successfully calibrated optical module is given in Fig. 6.6 after event selection has been applied. We find the results obtained in the previous section concerning the difference in efficiency between simulations and real data. As all optical modules are now equalised in gain, this result will be improved by the new data acquisitions planned for the end of October 2020. We also notice that the data spectrum extends at higher energies than simulations, corresponding to the ^{208}Tl background.

Selection efficiencies for each cut-off, after the energy calibration, are given in Tab. 6.2. We notice an improvement at the level of individual energy cut, where the selection efficiency is reduced compared with the previous case using the energy calibration provided by the collaboration.

	Simulations	Data
High threshold	35.7%	94.0%
Individual energy	17.0%	58.0%
Geometrical	16.5%	51.9%

Table 6.2: Selection efficiencies for simulations and real data. Energy calibration with ^{60}Co data have been applied.

This is a temporary calibration, only use in the framework of this analysis, and does not replace the more complete one accomplished for later data acquisitions. An amelioration could be brought with a double fit of the two peaks. Nevertheless, this improvement is not necessary since the gains were not yet aligned but it would be interesting to try this method again with the new ^{60}Co data.

6.6 Background estimation

The signal for this analysis is composed two γ's of 1.17 MeV and 1.33 MeV, emitted after ^{60}Co disintegrations. After application of the four selections, it is primordial

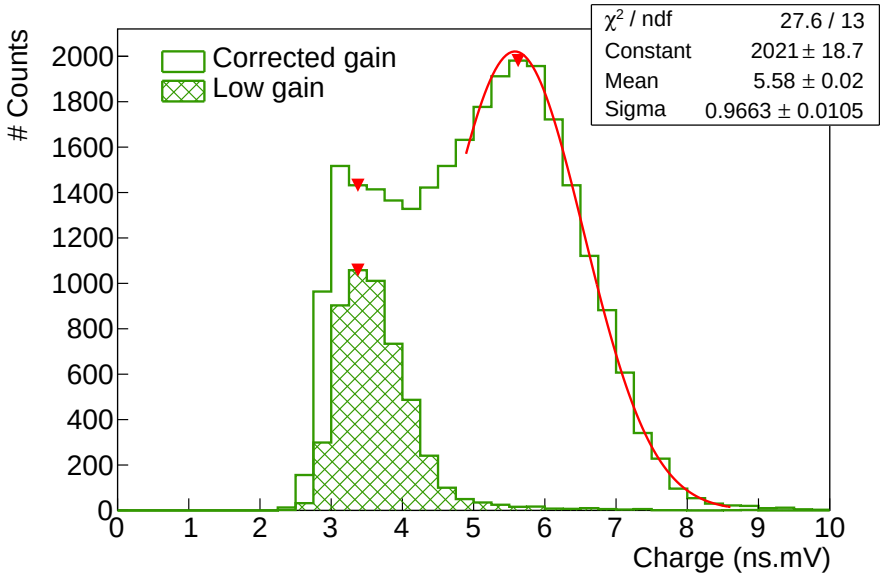

(a) Data acquisition.

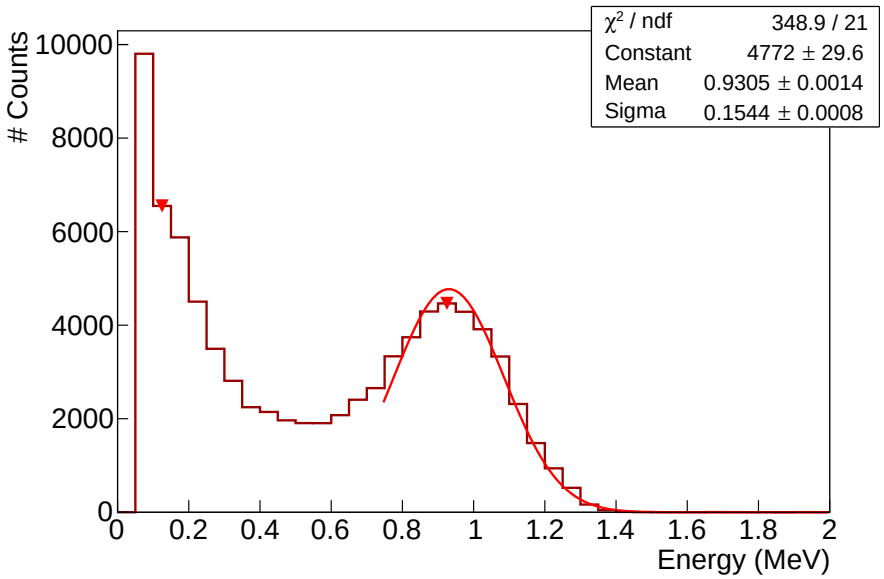

(b) Simulated data.

Figure 6.5: Data acquisition charge (a) and simulated energy (b) spectra. If two peaks are detected, the second one is fitted with a Gaussian. When the OM gain is too low, the lower energy peak, due to a double Compton interaction of a ^{60}Co gamma in two scintillator blocks, is less likely to be detected an the OM is not calibrated.

to estimate and characterise the remaining background in the selected topology, detected by the calorimeter during the data acquisition.

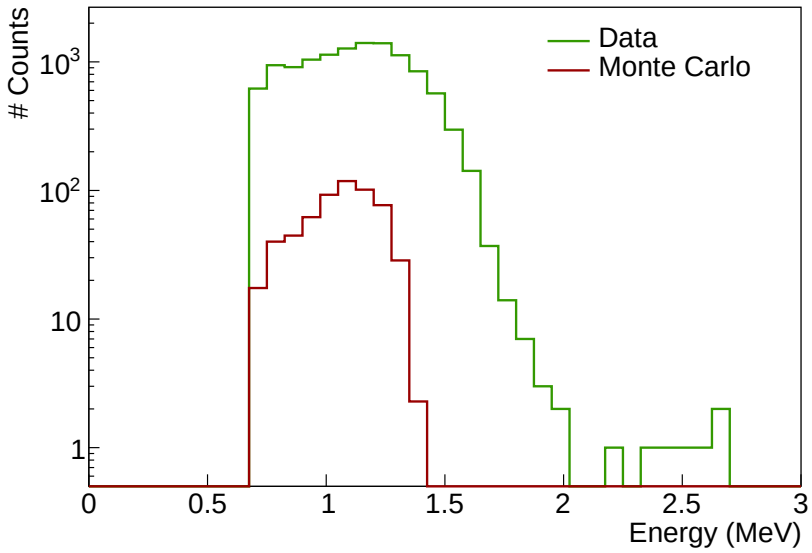

Figure 6.6: Energy spectrum for a calibrated optical module of the French wall, using ^{60}Co data acquisition. The simulations have been normalised to the source activity and data acquisition time.

6.6.1 Types of background

Mainly three different types of background can be harmful for this analysis, all pictured in Fig. 6.7.

- Through a double Compton interaction, a single ^{60}Co γ particle can deposit energy in two scintillator blocks (see Fig. 6.7b). As described in Sec. 6.4, the geometrical and individual energy selections have been set up to reject these background events.

- Photons coming from the natural radioactive decay chains of ^{238}U, ^{232}Th and ^{40}K isotopes. Typically, the 2.615 MeV-γ, from ^{208}Tl decay, can interact successively in two scintillators through Compton scatterings and produce high energy events (see Fig. 6.7a). These disintegrations can occur in the source foils or in the detector's components (mainly PM glass).

- At the time of the data acquisition, the calorimeter was in commissioning phase, and the iron shielding was not yet installed. Therefore, the calorimeter was not properly protected from external particles, coming from outside the detector (radioactive isotope contamination of laboratory rock). Accidental events where two decorrelated γ particles, can be detected in two scintillator blocks (see Fig. 6.7c). The coincidence time window should avoid these accidentals to be selected.

All these three topologies can mimic the ^{60}Co two-γ's signal. In order to characterise the two last types of background (decorrelated from the ^{60}Co source), a background data acquisition, without the ^{60}Co calibration source, has been performed. Unfortunately, be owing to optical modules gain issues, these data

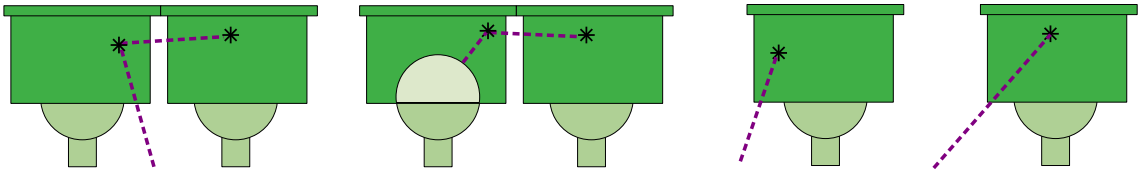

(a) (b) (c)

Figure 6.7: Background types for the ^{60}Co study. Interactions of photons in scintillators are represented by black stars. (a) Interaction of a single ^{60}Co photon in two scintillators through double Compton scattering. (b) Interaction of a photon coming from natural radioactive isotopes contamination (PM glass...), through double Compton scattering. (c) Interactions of two uncorrelated photons, coming from the demonstrator outside (natural radioactivity of laboratory rock...), in two scintillator blocks

are not usable. Therefore, we use the data acquisition taken with the ^{60}Co source set behind the wall to estimate this background.

6.6.2 Background characterisation

When the ^{60}Co source is set behind the wall, collected data may contain signal events coming from it as well as background events. Let us assume these background events are dominated by radioactive decays and external γ's, by considering the background coming from double Compton interactions of ^{60}Co γ's have been efficiently removed by application of the individual energy cut. We choose to model the ^{60}Co data as a linear combination of signal events s and background events b

$$\hat{d} = s + b\,, \tag{6.6}$$

where s and b are thus considered as uncorrelated. The question is how to extract informations about the background, using the ^{60}Co data acquisitions? We remind the ^{60}Co source was placed at different positions behind the calorimeter wall. We aim to take advantage of those different configurations to reach our goal. In the following, we make use of the positions 2 and 8 for the ^{60}Co source.

Therefore, depending on whether the source is in one of the two positions, some optical modules are *close* to it, others are *far*. More precisely, we consider as *close*, the optical modules that are separated from the source by less than 10 optical modules (i.e. less than half the wall-length), the others being *far* from it[1]. Considering that, we distinguish two categories of data, $\hat{d}^{\,\text{close}}$ and $\hat{d}^{\,\text{far}}$, defined as the estimations of data events detected by an optical module when the source is close to, or far from it, respectively. Then, we precise our data model with

$$\hat{d}^{\,\text{close}} = b + s^{\,\text{close}}\,, \tag{6.7}$$

where $s^{\,\text{close}}$ is naturally the number of ^{60}Co signal events detected by a given optical module for which the distance from the source, D_{source}, is lower than 10.

[1]For example, an optical module located on the left (right) of the calorimeter wall, is considered as far from (close to) the source, if the source is in position 8.

In the same way, considering $s^{\,\mathrm{far}}$ as signal events detected by an optical module from which the source is far, we have

$$\hat{d}^{\,\mathrm{far}} = b + s^{\,\mathrm{far}}\,. \tag{6.8}$$

Estimations of $s^{\,\mathrm{close}}$ and $s^{\,\mathrm{far}}$ (respectively noted $\tilde{s}^{\,\mathrm{close}}$ and $\tilde{s}^{\,\mathrm{far}}$) are provided using simulations of ^{60}Co events in positions 2 or 8. Indeed, as we consider the double Compton interaction background as negligible, the number of signal events received for optical modules far or close from the source can be established with ^{60}Co simulations. Then, the coefficient α defined as

$$\alpha = \tilde{s}^{\,\mathrm{far}}/\tilde{s}^{\,\mathrm{close}}\,. \tag{6.9}$$

It depends on the distance D_{source} and is found to be $0.05\% < \alpha < 5\%$, meaning that the number of simulated signal events detected by optical modules distant from the source is greatly lower than for close optical modules, for a given source position.

In order to provide a non-biased estimation of b given the data model in Eq. (6.8), we would remove $\tilde{s}^{\,\mathrm{far}}$, estimated through simulations, from $\hat{d}^{\,\mathrm{far}}$, which can be estimated with ^{60}Co data acquisition. To do so, we display in Fig. 6.8 the number of calorimeter hits, after event selection, counted by each optical module, as a function of the distance to the ^{60}Co source. The 10 optical modules limit is materialised by a vertical dashed line. Calorimeter hits that occurred in coincidence above and below this limit are displayed both for simulated and real data. Therefore, events where the two hits occur in two optical modules, each located in one half of the calorimeter, are not represented. This explains the observable gap at the 10 optical modules limit level.

We first focus on simulation results. Calorimeter hits for which $D_{\mathrm{source}} < 10$ represent the estimation of the number of signal events detected close to the source, $\tilde{s}^{\,\mathrm{close}}$. Similarly, hits for which $D_{\mathrm{source}} > 10$ embed for $\tilde{s}^{\,\mathrm{far}}$, the number of signal events remaining for optical modules far from the calibration source site. As expected, the number of ^{60}Co signal events decreases with the distance to the source. Moreover, this decrease is linear, showing the same slope beyond and above the 10 optical modules limit.

Regarding real data acquisition, calorimeter hits for which $D_{\mathrm{source}} < 10$ materialise the number of data events estimation $\hat{d}^{\,\mathrm{close}}$. Apart from slight differences due to the detector efficiency, these data events follow the same linear evolution as signal events with the distance to the source. This leads us to conclude that optical modules close to the source are dominated by ^{60}Co signal events. Similarly, $D_{\mathrm{source}} > 10$ events stand for $\hat{d}^{\,\mathrm{far}}$. We observe that $\tilde{s}^{\,\mathrm{far}}/\hat{d}^{\,\mathrm{far}} \ll 1$, which is compatible with the α coefficient values, being 5% in the worse case, explaining the few amount of $\tilde{s}^{\,\mathrm{far}}$ events remaining for optical modules far from the source. Moreover, we find that the amount of $\hat{d}^{\,\mathrm{far}}$ events is globally stable with the distance to the source, which confirms the assumption made that, at such distances from the source, radioactive contaminant decays and external γ's interactions dominate the background contribution and are decorrelated from the ^{60}Co source. Therefore, for a 25 minutes run, each optical module detects around 10^2 external background events.

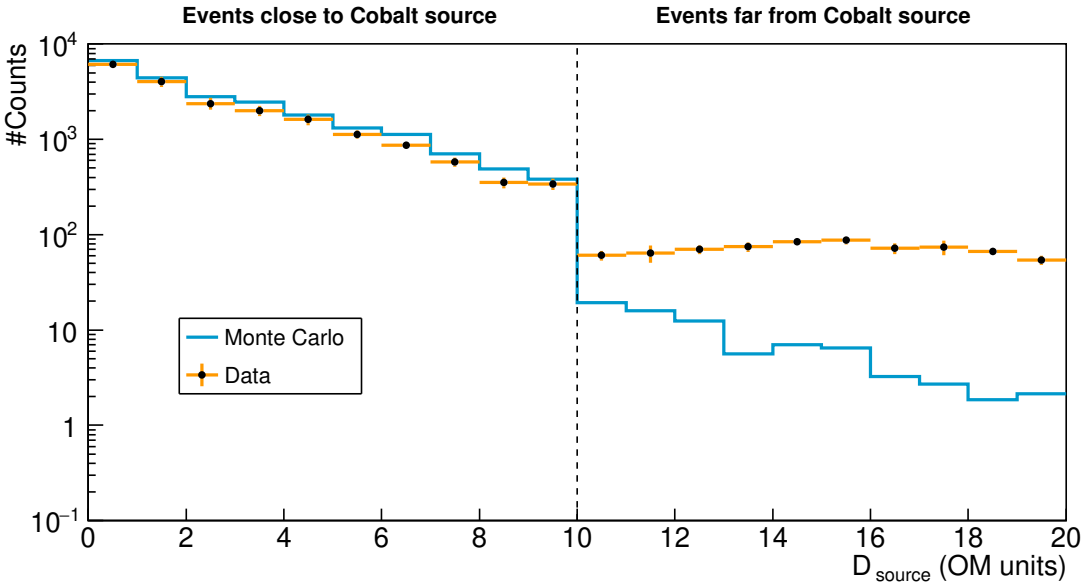

Figure 6.8: Number of events for pairs of OMs close and far from the source, for real data (orange) and simulated data (blue), as a function of the distance to the source (in units of number of OM). The vertical dashed line materialises the distance limit of 10 OMs from the source.

To sum up these results, calorimeter hits for optical modules close to the ^{60}Co calibration source are, for the most part, signal events. Besides, hits occurring far from the source are predominantly background events. As we moved the source in different positions, we have access to the estimation of background rate $\hat{b}$ for each optical module (when the source is far), and to the estimation of $\hat{s}$ (when the source is close). Therefore, we can compute the signal to background ratio, as a function of the distance to the ^{60}Co source, displayed in Fig. 6.9. The number of signal events in each optical module depends on the distance to the source, which is not the case for the number of background events, explaining the decreasing of S/B with D_{source}. For this reason, the distribution stabilises at high D_{source} ($\sim$ 8 OM units) as these optical modules are more sensitive to the flat background contribution than those right in front of the source.

To summarise, in this subsection, we gave information on background events for the whole French wall, using data taken with the ^{60}Co source set at different positions. We confirmed our assumption that the more one optical block is far from the source, the less it detects γ particles emitted after ^{60}Co disintegrations, then the more the signal to background ratio decreases.

6.7 Determination of the optical modules timing resolution

The final goal of this analysis is to determine σ_t, the time resolution of optical modules. As displayed in Fig. 6.2, given the time resolution of SuperNEMO, the

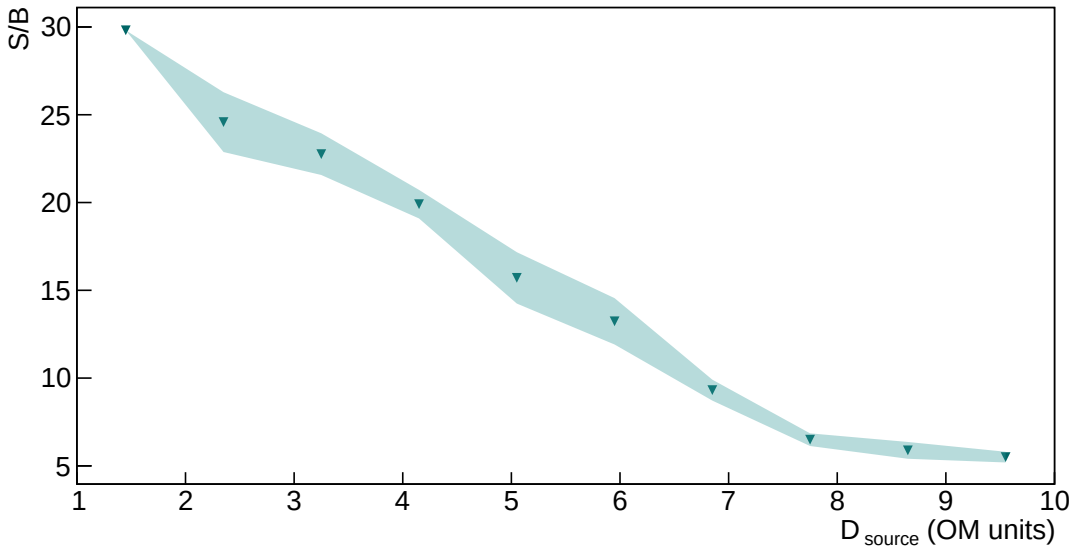

Figure 6.9: Signal to background ratio for each optical module, as a function of the distance to the ^{60}Co source.

two photons emitted from ^{60}Co can be considered as emitted in coincidence. The selections described in Sec. 6.4 aim to maximise the signal to background ratio, the signal being the detection of two γ's interacting in two different optical modules.

6.7.1 Time difference distributions

The speed of the two γ's travelling in the air is considered as equal to that in vacuum, c, and reach the two optical modules at two different times t_i^γ. These time-of-flights are defined from the sampling of the collected charge, using the CFD method described in Chapter 5. These topologies are likely to happen for all combinations of pairs of optical modules. Therefore, for each pair of calorimeter optical module, A and B, we can construct a time difference distribution between two hits, defined as $\Delta t^{\text{pair}} = t_A^\gamma - t_B^\gamma$. The two time-of-flights t_A^γ and t_B^γ are corrected from the time offset determined in the precedent Chapter 5, due to the signal travelling inside coaxial cables and to the FEBs time offsets. For a given pair, one of the two optical modules is chosen as reference, here A.

In Fig. 6.10 is presented an example of a Δt^{pair} distribution, for a given pair of optical modules, both for the simulated and real data, with the ^{60}Co source set in position 5. The two distributions present different behaviours in terms of means and standard deviations. This can be explained by two distinct reasons. Firstly, as exposed in Sec. 6.1 the simulation are processed with perfect optical modules in terms of time-of-flight measurement. It is thus expected that the standard deviation is higher for real data than for simulations. Even though the case presented is just an example for a given pair of optical modules, this is a general result for all pairs. Secondly, we notice the mean of the real data distribution is shifted towards negative values. This is induced by a systematic time delay of particle time-of-flight value for real data. This result is observed for all pairs of

optical modules. As the time-of-flights are corrected from the coaxial cables and FEBs time offsets, this difference could be caused by a difference between simulated and real location of the ^{60}Co source. Moreover, the shift of the mean could also be the consequence of an incorrect energy calibration, that can lead to the selection of background events such as double Compton interactions in two successive optical modules. The average time-of-flight difference for such background events is different from that if signal events, and therefore their accidental selection could be the cause of the observed discrepancy.

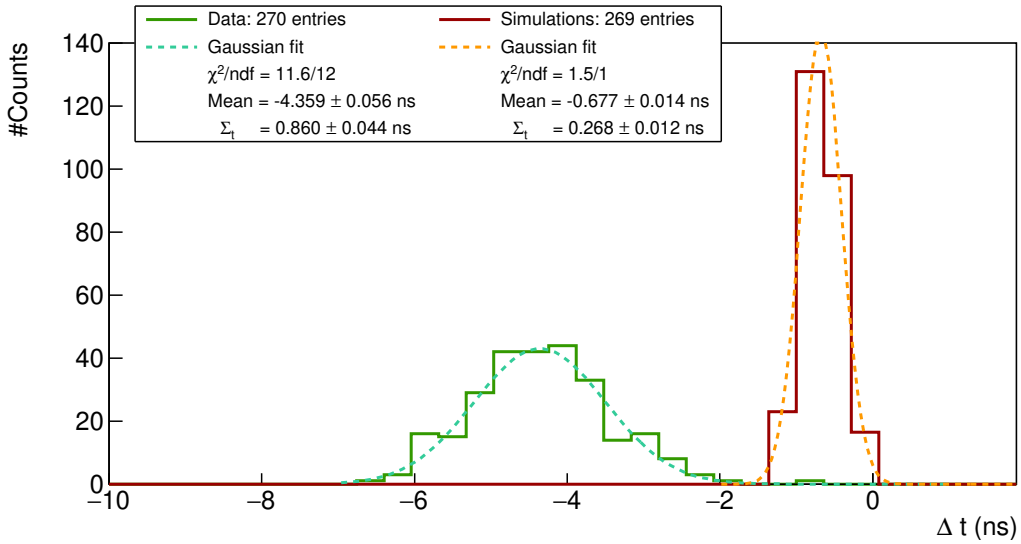

Figure 6.10: Δt^{pair} distributions for real data (green solid line) and simulated data (dark red solid line). Two Gaussian fits (dotted line) are displayed and fit parameters are given in the legend box.

Such Δt^{pair} distributions are defined for each pair of optical modules detecting events in coincidence. The least square method is used to fit the distributions, which minimises the difference between the measured value and the fitted value. A mean and a standard deviation is then defined for each pair of optical modules whose fitted data has $\chi^2/\text{dof} < 4$. Therefore, due to a lack of statistics, some distributions cannot be fitted properly, and are rejected by the algorithm. At the end, each pair of optical modules whose Δt^{pair} distribution fit is selected is characterised by the mean and standard deviation of this fit. The distribution's standard deviation, noted Σ_t, is called *coupled time uncertainty* and corresponds to the uncertainty on time measurement for this peculiar pair of optical modules. It was checked graphically that the Σ_t distributions were Gaussian, so the variance of Σ_t^2 is noted

$$\text{Var}[\Sigma_t^2] = \frac{2\,\Sigma_t^4}{N-1}\,, \tag{6.10}$$

where N is the number of events detected in coincidence for this pair of optical modules.

6.7.2 Coupled time uncertainties

The data acquisition was taken with 254 optical modules from French wall instead of 260: at this time three optical modules were out of order, and three photomultipliers whose gain were too low were removed from the analysis. Moreover, in the framework of this study, we intend to characterise timing resolution of 8 inches optical modules only. At the end 214 optical modules were considered, representing more than 2×10^4 different pairs of optical modules.

With this method, we succeed to provide Σ_t values for 26% of pairs of optical blocks for real data, against 87% for simulations. This difference is due to a lack of statistics for real data. In Fig.6.11 is displayed the number of characterised optical blocks, with the distance between the reference block and the ^{60}Co source, in OM units. The further away an optical module is from the source, the less likely the fit successes. Moreover, for a given distance from the source, the number of characterised optical modules is lower for the real data case than for the simulated one, explaining the lower amount of provided Σ_t values for real data.

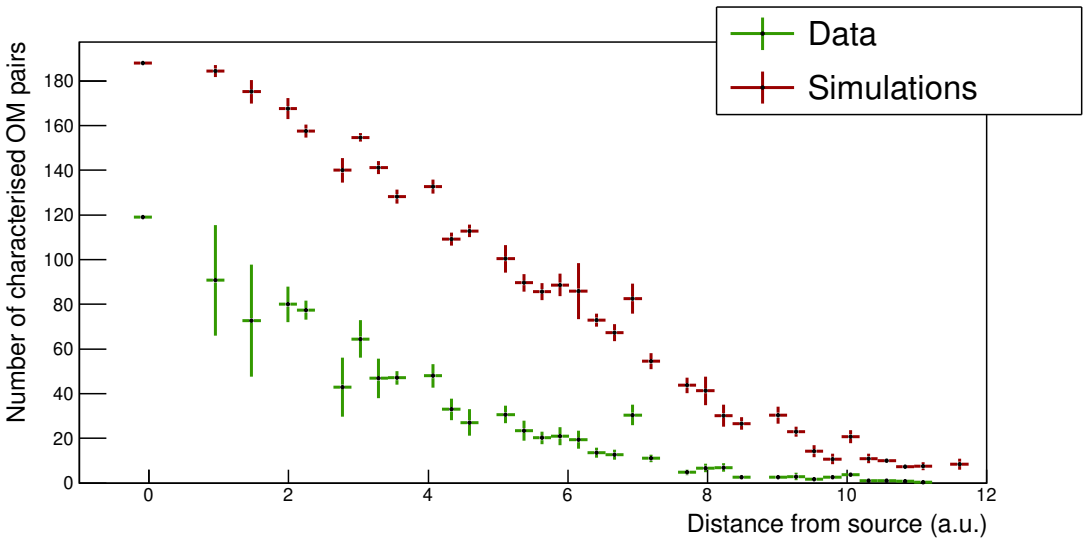

Figure 6.11: Number of characterised OM pairs, as a function of the distance between reference OM and source.

We presented results on the uncertainty on time measurement for pairs of optical modules, Σ_t. However, we are interested in providing the individual uncertainty of each optical module, noted σ_t. In the following, we present the algorithm we used to compute such value.

6.7.3 Decoupling the Σ_t uncertainties

The Σ_t values that have been determined are defined for pairs of optical modules and can therefore be expressed in terms of the individual time resolutions for each module. In the framework of this study, we decide to consider trios of optical modules detecting coincidental events two by two. Therefore, the pair uncertainty, Σ_t, can be considered as a linear combination of the individual optical module

uncertainties, σ_t:

$$\begin{aligned}(\Sigma_t^{0,1})^2 &= \frac{(\sigma_t^0)^2}{\bar{E}_0} + \frac{(\sigma_t^1)^2}{\bar{E}_1} \\ (\Sigma_t^{0,2})^2 &= \frac{(\sigma_t^0)^2}{\bar{E}_0} + \frac{(\sigma_t^2)^2}{\bar{E}_2} \\ (\Sigma_t^{1,2})^2 &= \frac{(\sigma_t^1)^2}{\bar{E}_1} + \frac{(\sigma_t^2)^2}{\bar{E}_2}\,,\end{aligned} \tag{6.11}$$

where $\bar{E}_i$ is the averaged energy measured by the optical module i, and σ_t^i is its individual time uncertainty at 1 MeV, so-called *decorrelated time uncertainty*, the quantity we are seeking to determine. Consequently, determining the three individual time resolutions is equivalent to solving this set of equations. In the end, each decorrelated σ_t is expressed as a linear combination of each Σ_t of the optical modules trio.

In practice, this has to be done for all the optical modules for which the Δt^{pair} distribution fit has provided a Σ_t value. With this in mind, the Σ_t values are sorted by order of the number of coincidental events. The work presented above is therefore applied to the first trio of this list. Then the next trio is selected, etc. In the end σ_t is computed for each optical module.

The variance of a given σ_t^2 value, noted $\mathrm{Var}[\sigma_t^2]$, depends on the variance of the three Σ_t defined in Eq. (6.10). For instance, for a trio optical modules we have

$$\mathrm{Var}[(\sigma_t^0)^2\,] = \mathrm{Var}\left[\frac{1}{2\bar{E}_0}(\Sigma_t^{0,1} + \Sigma_t^{0,2} - \Sigma_t^{1,2})^2\right] \tag{6.12}$$

$$= \frac{1}{4\bar{E}_0{}^2}\left(\,\mathrm{Var}[(\Sigma_t^{0,1})^2\,] + \mathrm{Var}[(\Sigma_t^{0,2})^2\,] + \mathrm{Var}[(\Sigma_t^{1,2})^2\,]\,\right), \tag{6.13}$$

where we assume the Σ_t values are uncorrelated.

In some cases, when an optical module has detected events in coincidence with more than two other optical modules, it can belongs to more than one trio. Thus, it is selected several times to participate in the de-correlation process of several different trios. Each optical module can then have many decorrelated σ_t values associated to it. The mean of these values, $\bar{\sigma}_t$, then stands as the final time uncertainty for each optical module. It is defined as the weighted average:

$$(\bar{\sigma}_t^i)^2 = \sum_n^N \frac{(\sigma_{t,n}^i)^2}{\mathrm{Var}[(\sigma_{t,n}^i)^2]} \left(\sum_n^N \mathrm{Var}[(\sigma_{t,n}^i)^2]\right)^{-1} \tag{6.14}$$

with i the optical module index and n The nth estimate made of σ_t.

The work presented in the current section can be applied to real and simulated data. For each optical module, the simulated time uncertainty is subtracted in quadrature from the real-time uncertainty, allowing to bring out the optical module time uncertainty defined in Eq. (6.1). The distribution of $\bar{\sigma}_t$ for 8 inches optical modules of the French wall is given in Fig. 6.15. On average, the time uncertainty stands at 570 ± 130 ps while few optical modules show large values, beyond 900 ps. Although these values are higher than expected, it should be borne

in mind that they have been characterised under rather complicated conditions, where the detector was not yet fully calibrated. In particular, the double Compton background, possibly poorly rejected due to imperfect energy calibration, can widen the Δt^{pair} distributions and degrade the final results.

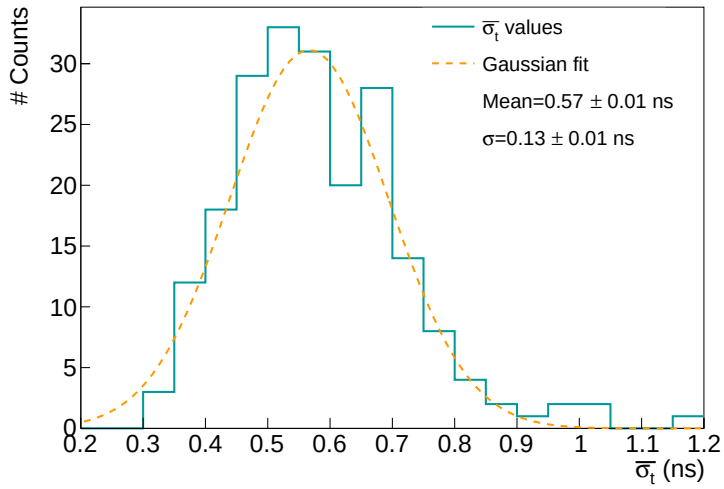

Figure 6.12: Decorrelated time uncertainties $\bar{\sigma}_t$.

However, it is important to keep in mind that we made strong assumptions about the properties of the system. Thus, while the mean of this distribution should be well-estimated, the standard deviation may not be. Indeed, we provided a very rough and naive estimate of the optical module time uncertainty σ_t, assuming Gaussian statistics, and uncorrelated estimate of the coupled time uncertainties Σ_t, as well as uncorrelated individual estimate of $\sigma_{t,n}$. This is, of course, not the case. In practice, we can do much better, by solving an over-determined system of equations that include all the Σ_t and σ_t at once. Nevertheless, our naive estimate is sufficient for this preliminary analysis, and provides encouraging results, opening the door to a full calorimeter timing characterisation.

6.8 Conclusion

This study has provided the first analysis of the resolution of the SuperNEMO demonstrator's calorimeter since its installation at Modane, where 26% of the demonstrator's optical modules could be characterised, representing more than 40% of the 8 inches PMs. It is an end to end work, from the experimental set up design, to the creation of the code and the analysis algorithm, through the acquisition of the calibration source and all the necessary administrative and security procedures, as well as the data acquisition at Modane. An estimation of the background detected was also given, and it was the opportunity to perform a quick energy calibration of the French main wall using the ^{60}Co source. This preliminary study aims to be improved, and new data, taken in Modane at the end of October 2020, will allow to purchase this work.

Conclusion

The search for the neutrinoless double beta decay is one of the doorways to physics beyond the Standard Model. If the neutrino is a Majorana particle, in addition to providing an explanation for the matter/anti-matter asymmetry observed in the universe, the existence of $0\nu\beta\beta$ decay could explain the fact that neutrinos have a very low mass compared to other fermions, through the see-saw mechanism.

NEMO technology, which has already set limits on the effective neutrino Majorana mass for several isotopes, has given birth to the SuperNEMO detector. We determined that with 100 kg of ^{82}Se this detector based on the unique tracko-calo technology would achieve $T^{0\nu}_{1/2} > 5.4 \times 10^{25}$ years, corresponding to $\langle m_{\beta\beta} \rangle = [0.079 - 0.15]$ eV, for 5 years of data acquisition. The SuperNEMO demonstrator, which is nearing the end of installation at the Modane Underground Laboratory with 6.23 kg of ^{82}Se, will complete its commissioning phase by the end of 2020 and will take data for slightly more than two years and a half. With the measurement of SuperNEMO source activities by BiPo-3 detector, we also found that the demonstrator should achieve a sensitivity at $0\nu\beta\beta$ of $T^{0\nu}_{1/2} > 3.6 \times 10^{24}$ years, corresponding to $\langle m_{\beta\beta} \rangle < [0.31 - 0.59]$ eV. The 25 Gauss magnetic field that will be applied in the detector has very limited impact on the sensitivity if optimised topological selections are applied on the event. Nevertheless, it is necessary to wait for simulations of external background before a more complete study can be carried out and a final conclusion can be drawn on the influence of this magnetic field. When the demonstrator starts taking data, these activities can be measured more accurately and the sensitivity results will be updated. In particular, it is conceivable that the contamination of sources in ^{214}Bi is lower than the upper limit provided by BiPo-3.

A way to improve this sensitivity is to reject more efficiently the background coming from ^{208}Tl isotope decays in the sources. When this isotope performs a beta decay to an excited level of ^{208}Pb followed by internal conversion of the 2.615 MeV metastable level, the event can be rejected by measuring the times of flight of the two detected electrons. A 6% improvement in sensitivity was achieved by setting up optimised time-of-flight rejection.

It was demonstrated that this improvement in sensitivity is deeply related to the actual time uncertainty of optical modules, and beyond $\sigma_t = 200$ ps, no improvement can be reached on the ^{208}Tl rejection. A mission was then conducted at Modane to determine this parameter using a ^{60}Co source whose two prompt gamma rays can be detected coincidentally by pairs of calorimeter blocks. An algorithm has been developed in order to characterise the individual time uncertainties, standing at 570 ± 130 ps for the first preliminary result. This value would have to be updated using the data acquisition planned at Modane by the end of October 2020, that will be taken now the calorimeter is fully equalised in

gain and calibrated in energy. This would be the occasion to perfect the algorithm developed in the framework of this PhD.

During my PhD, I was also given the opportunity to participate in commissioning data collection and analysis, thus characterising the detector's performances. In particular, by sending electronic pulses through the signal cables of the calorimeter, the condition of each cable and connector could be checked and corrected if necessary. The time offset induced by the coaxial cables and calorimeter FEBs has been conducted and two databases were made available to the collaboration. These two preliminary analyses will have to be completed by a more complete study aimed at characterising the entire signal transmission chain, from the calorimeter to the DAQ.

The commissioning of the calorimeter is now almost complete, and the next step in characterising the detector will be to study the performance of the tracker. This phase will begin by the end of November, allowing energy calibration of the calorimeter using Bismuth sources, and should be completed by the end of 2020.

Bibliography

[1] E. Fermi. Tentativo di una teoria dei raggi ? *La Ricerca Scientifica*, 1933.

[2] B. Pontecorvo. Mesonium and antimesonium. *Soviet Phys. JETP*, 1958.

[3] Y. Fukuda et al. Evidence for Oscillation of Atmospheric Neutrinos. *Phys.Rev.Lett.*, 81:1562–1567.

[4] F. Capozzi et al. Status and prospects of global analyses of neutrino mass-mixing parameters. *Journal of Physics: Conference Series*, 888:012037, sep 2017.

[5] C. Giuntin and C. W. Kim. *Fundamentals of neutrino physics and astrophysics*. Oxford, 2007.

[6] P. Minkowski. $\mu \to e\gamma$ at a rate of one out of 109 muon decays? *Physics Letters B*, 67:421–428, 1977.

[7] M. Ernest. Pathways to naturally small neutrino masses. *Physical Review Letters*, 81:1171, 1998.

[8] R. Marshak and R. Mohapatra. Invited talk given at orbis scientiae, 14-17 Jan 1980.

[9] M. Drewes. The phenomenology of right handed neutrinos. *International Journal of Modern Physics E*, 22, 2013.

[10] M. Goeppert-Mayer. Double beta-disintegration. *Physical Review*, 48:512, 1935.

[11] S. Dell'Oro et al. Neutrinoless Double Beta Decay: 2015 Review. *Advances in High Energy Physics*, 2016:37, 2015.

[12] W.H. Furry. On transition probabilities in double beta-disintegration. *Physical Review*, 56:1184, 1939.

[13] M. Agostini, A.M. Bakalyarov, et al. Upgrade for Phase II of the GERDA experiment. *Eur. Phys. J. C*, 2018.

[14] M. Agostini et al. Final Results of GERDA on the Search for Neutrinoless Double-β Decay. *Phys. Rev. Lett.*, 125:252502, Dec 2020.

[15] N. Abgrall et al. The MAJORANA DEMONSTRATOR Neutrinoless Double-Beta Decay Experiment. *Advances in High Energy Physics*, 2014.

[16] S.I. Alvis et al. Search for Neutrinoless Double-Beta Decay in ^{76}Ge with 26 kg-yr of Exposure from the MAJORANA demonstrator. *Phys. Rev. C*, 100, 2019.

[17] *LEGEND: The Large Enriched Germanium Experiment forNeutrinoless Double-Beta Decay*, 2018.

[18] C. Brofferio et al. Neutrinoless Double Beta Decay Experiments With TeO2 Low-Temperature Detectors. *Frontiers in Physics*, 7:86, 2019.

[19] D.Q. Adams et al. Improved Limit on Neutrinoless Double-Beta Decay in 130Te with CUORE. *Phys. Rev. Lett.*, 2020.

[20] CUPID Interest Group. CUPID: CUORE (Cryogenic Underground Observatory for Rare Events) Upgrade with Particle IDentification. 2015.

[21] M. Auger et al. The EXO-200 detector, part I: detector design and construction. *Journal of Instrumentation*, 7(05):P05010–P05010, may 2012.

[22] G. Anton et al. Search for Neutrinoless Double-β Decay with the Complete EXO-200 Dataset. *Phys. Rev. Lett.*, 123:161802, Oct 2019.

[23] nEXO Collaboration. nEXO Pre-Conceptual Design Report, 05 2018.

[24] J.J. Gomez-Cadenas et al. The NEXT experiment. *Phys. Rev. Lett.*, pages 1732–1739, Apr-Jun 2016.

[25] X. Chen et al. PandaX-III: Searching for Neutrinoless Double Beta Decay with High Pressure 136Xe Gas Time Projection Chambers. 2016.

[26] A. Gando et al. Search for Majorana Neutrinos Near the Inverted Mass Hierarchy Region with KamLAND-Zen. *Phys. Rev. Lett.*, 117:082503, Aug 2016.

[27] A. Chopra. C0 Commissioning Results. Internal presentation, 2015.

[28] C. Cerna. Tracker review conclusions. Internal presentation, 2014.

[29] Estar database (nist). http://physics.nist.gov/PhysRefData/Star/Text/ESTAR.html.

[30] A. Huber. *Recherche de la nature du neutrino avec le détecteur SuperNEMO : Simulations optiques pour l'optimisation du calorimètre et performances attendues pour le ^{82}Se.* PhD thesis, Université Bordeaux, 2017.

[31] Xcom database (nist). http://physics.nist.gov/PhysRefData/Xcom/html/xcom1.html.

[32] S. Clavez. *Development of reconstruction tools and sensitivity of the SuperNEMO demonstrator.* PhD thesis, Université Paris Sud, 2017.

[33] M. Bongrand and X. Garrido. Hamamatsu 8" PMT Test in Magnetic Shield. Internal presentation, 2014.

[34] P. Loaiza. Source foils measurement with BiPo. Internal presentation, 2017.

[35] F. Perrot. Radiopurity measurements for 8" PMTs and preliminary budget for the SN demonstrator. Internal presentation, 2017.

[36] R. Arnold et al. Technical design and performance of the NEMO3 detector. *Nucl. Instrum. Meth. A*, pages 79–122, 2005.

[37] R. Arnold et al. Results of the search for neutrinoless double-β decay in ^{100}Mo with the NEMO-3 experiment. *Phys. Rev. D*, 2015.

[38] Xin Ran Liu. Radon Mitigation Strategy and Results for the SuperNEMO Experiment. IoP APP / HEPP Conference, 2018.

[39] R. Arnold et al. Probing new physics models of neutrinoless double beta decay with SuperNEMO. *Eur. Phys. J. C*, 2010.

[40] R. Arnold et al. Final results on ^{82}Se double beta decay to the ground state of ^{82}Kr from the NEMO-3 experiment. *Eur. Phys. J. C*, 2018.

[41] G. Feldman and D. Cousins. A Unified Approach to the Classical Statistical Analysis of Small Signals. *Phys.Rev.*, pages 3873–3889, 1999.

[42] J. Kotila and F. Iachello. Phase-space factors for double-β decay. *Phys. Rev. C*, 85:034316, Mar 2012.

[43] Dong-Liang Fang, Amand Faessler, Vadim Rodin, and Fedor Šimkovic. Neutrinoless double-β decay of deformed nuclei within quasiparticle random-phase approximation with a realistic interaction. *Phys. Rev. C*, 83:034320, Mar 2011.

[44] A. Chapon. *Mesure des processus de double désintégration bêta du Mo vers l'état excité 0_1^+ du Ru dans l'expérience Nemo3, Programme de R&D SuperNEMO : mise au point d'un détecteur BiPo pour la mesure de très faibles contaminations de feuilles sources.* PhD thesis, Université Caen Basse-Normandie, 2011.

[45] S. Snow. A magnetic field map for the tracker. Internal presentation, 2015.

[46] A. Pin. *Recherche de la nature du neutrino via la décroissance double bêta sans émission de neutrinos. Caractérisation et optimisation du calorimètre SuperNEMO et impact sur la recherche de la décroissance du 82Se Développement du premier prototype LiquidO.* PhD thesis, Université Bordeaux-Gradignan, 2020.

[47] G. Audi and A. H. Wapstra. The 1995 update to the atomic mass evaluation. *Nucl. Phys. A*, 595:409–480, feb 1995.

[48] R. Arnold et al. Measurement of the $2\nu\beta\beta$ decay half-life of ^{150}Nd and a search for $0\nu\beta\beta$ decay processes with the full exposure from the NEMO-3 detector. *Phys. Rev. D*, 94, oct 2016.

[49] Nucleid database.

[50] My GitHub page. https://github.com/girardcarillo.

Résumé

Il est toujours intéressant d'adopter une approche historique lorsque l'on aborde une découverte scientifique. Cela permet de mettre en perspective des connaissances aujourd'hui considérées comme acquises.

L'existence du *neutrino* a été postulée pour la première fois par W. Pauli en 1930 comme un "remède désespéré" à la non-conservation de l'énergie totale observée lors de la désintégration β. Ce sont F. Reines et C. Cowan qui, en 1956, confirment expérimentalement l'existence de l'antineutrino électronique. Le neutrino est une des particules élémentaires décrite aujourd'hui dans le Modèle Standard de la Physique des Particules (MS).

Sans trop prendre de risques, l'on peut avancer qu'une des raisons de la découverte si tardive du neutrino dans l'histoire de la physique réside dans la manière dont le neutrino "parle" ou interagit avec la matière qui nous entoure et donc qui compose nos détecteurs (essentiellement des nucléons et des électrons). En effet, le neutrino étant neutre sous les interactions électromagnétique et forte, il interagit uniquement avec les autres particules via l'interaction faible, une force à courte portée – on ne parle pas ici de la gravité, cette force n'étant pas décrite par le MS, et négligeable dans le cas des neutrinos.

Aujourd'hui encore, des scientifiques du monde entier travaillent à comprendre et à déterminer certaines des propriétés de cette particule. Notamment, le neutrino peut être décrit dans le Modèle Standard soit comme un fermion dit de *Majorana* (neutrino et antineutrino seraient alors la même particule), soit comme un neutrino dit de *Dirac* (où neutrino et anti-neutrino seraient des particules bien distinctes, comme c'est le cas pour les autres fermions). Les expériences NEMO (pour Neutrino Ettore Majorana Observatory) font partie de l'effort mondial mené dans l'optique de déterminer la nature de la relation entre neutrino et anti-neutrino. La thèse que je présente dans ce manuscrit a été menée au Laboratoire de L'Accélérateur Linéaire (renommé IJCLab) dans l'expérience SuperNEMO, successeur de NEMO-3, installée au Laboratoire Souterrain de Modane (LSM).

Le démonstrateur SuperNEMO

NEMO est une collaboration scientifique internationale à la recherche de la double désintégration β sans émission de neutrino (abrégé comme $0\nu\beta\beta$) théorisée par H. Furry en 1939, mais jamais observée jusqu'à présent. Lors de cette désintégration, deux désintégration β ont lieu simultanément, mais les deux neutrinos attendus ne sont pas émis, violant ainsi la loi de conservation du nombre leptonique. L'observation de cette désintégration prouverait la nature de Majorana du neutrino et aurait de grandes implications dans différents domaines de la physique. Plusieurs noyaux instables seraient capables d'effectuer cette désintégration, et il est possible d'exprimer la découverte de ce processus en terme de demie-vie radioactive pour un noyau donné. En cas de non-observation, une limite sur cette demie-vie, correspondant à la sensibilité à la $0\nu\beta\beta$, peut donc être déterminée. C'est d'ailleurs une des observables permettant de caractériser les expériences cherchant à observer la $0\nu\beta\beta$.

Le détecteur SuperNEMO est attendu avec une sensibilité de $T^{0\nu}_{1/2} > 1\times 10^{26}$ ans (90% CL) avec 100 kg de Sélénium enrichi (^{82}Se) en 5 années d'acquisition de données. C'est le seul détecteur à allier à la fois une technologie de traçage des particules (chambre à fils) et de mesure de leur énergie (calorimètre segmenté), présentant des couches de détection successives décorellées de la source radioactive. Cette source est répartie au centre du détecteur sous forme de fines feuilles sources. L'ensemble du détecteur est placé dans un champ magnétique externe, permettant ainsi de courber la trajectoire des particules chargées. Les deux électrons émis lors d'une désintégration double-β peuvent être reconstruits séparément.

Afin de prouver que la technologie NEMO est extensible à de telles masses d'isotope, tout en restant un détecteur ultra-bas bruit de fond, le démonstrateur SuperNEMO a été conçu avec une masse réduite d'isotope double-β, soit 6.23 kg de ^{82}Se. L'installation du détecteur au LSM a débuté en 2015. Depuis, les sources ont été installées, le traceur et le calorimètre ont été assemblés et tous les systèmes d'étalonnage ont été déployés. Un schéma du détecteur est présenté sur la Fig. 6.13.

J'ai été impliquée dans le travail qui a été effectué depuis 2017 sur le démonstrateur, notamment en menant plusieurs missions à Modane en salle blanche, sur diverses parties du détecteur (câblage, tests de l'électronique, installation des feuilles sources, étanchéité du détecteur...). Au cours de la première année de mon doctorat, j'ai passé toutes les formations de sécurité et de secourisme nécessaires afin de devenir l'une des personnes responsables de la sécurité de l'équipe sur site. J'ai également participé à la fermeture du détecteur, le 22 Novembre 2018, une étape cruciale dans la construction du détecteur. Le démonstrateur est actuellement en phase de mise en service et est presque entièrement étalonné – le début de la phase d'étalonnage du traceur débutera au cours de l'année 2020, après la fin de mon doctorat.

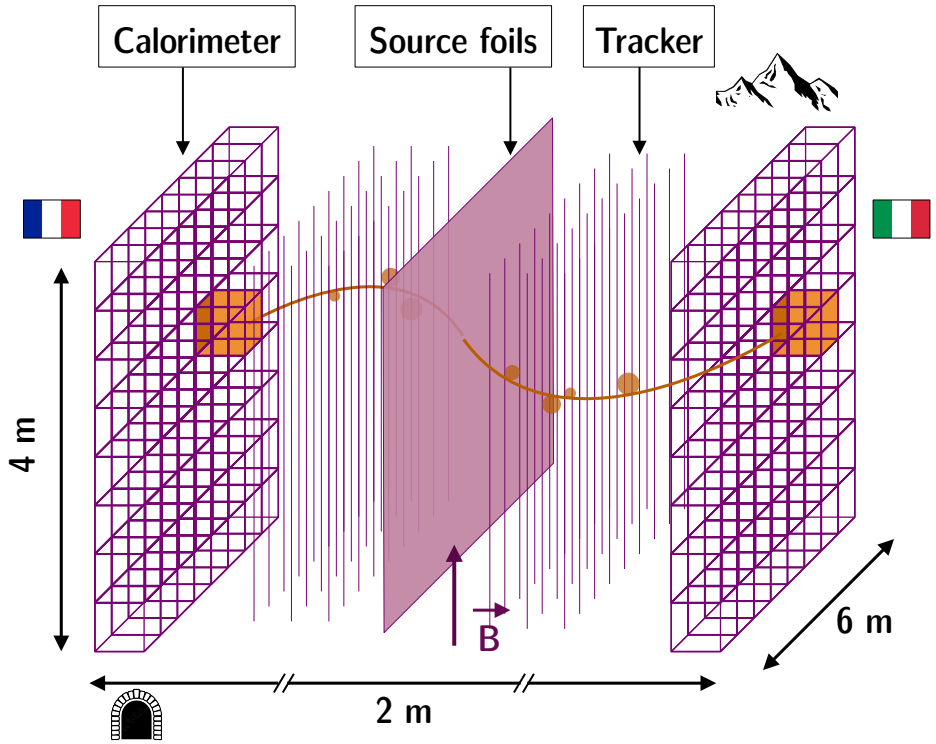

Figure 6.13: Schéma d'une vue ouverte du détecteur SuperNEMO.

Sensibilité de SuperNEMO à la $0\nu\beta\beta$

La sensibilité attendue pour le détecteur final SuperNEMO a été déterminée à travers des simulations, en utilisant les paramètres de conception du détecteur. Grâce aux précieuses informations obtenues après le montage et la calibration, nous étudions l'influence de plusieurs paramètres sur cette sensibilité. Entre autres, la présence du champ magnétique visant à courber la trajectoire, et donc à discriminer les particules chargées, peut avoir un impact non-négligeable sur l'efficacité de reconstruction des événements. Également, la contamination des sources par certains isotopes radioactifs naturels ont un impact direct sur la sensibilité du détecteur. Certaines de ces contaminations ont été mesurées par le détecteur BiPo3 et sont utilisées pour cette étude. Enfin, les sources du détecteur SuperNEMO ont été conçues afin d'être interchangeables, dans l'optique de pouvoir à terme rechercher la $0\nu\beta\beta$ pour différents isotopes. Nous avons donc complété cette étude en analysant les sensibilités du détecteur pour d'autres noyaux effectuant des doubles désintégrations β. Cette étude a été réalisée grâce à des simulations d'événements dans le détecteur, et menée conjointement avec le doctorant Axel Pin du laboratoire CENBG.

En cas de non-observation d'un signal $0\nu\beta\beta$, la limite inférieure attendue sur la demie-vie est fournie pour un intervalle d'énergie optimisé $[E_{\min}; E_{\max}]$ sur la somme des énergies des deux électrons reconstruits, et dépend des caractéristiques du détecteur (efficacité de détection du signal $0\nu\beta\beta$ dans cette fenêtre d'énergie déterminé par la simulation, nature de l'isotope source, masse d'isotope, temps

d'acquisition). Une sélection simple des événements est mise en place afin de pouvoir sélectionner la topologie d'intérêt, qui est ici deux électrons émis depuis les feuilles sources – un électron étant défini comme un vertex reconstruit sur la source, associé à une trace de courbure négative dans le traceur et à une énergie reconstruite dans le calorimètre.

La contamination des sources et du traceur en isotopes naturels radioactifs (^{208}Tl et ^{214}Bi) induit une dégradation de la sensibilité de 37% par rapport à la valeur initiale. Plusieurs pistes pour améliorer la sélection des événements ont donc été explorées, en se servant des différentes informations topologiques apportées par la configuration en couche du détecteur. Un outil statistique, appelé *probabilité interne*, est calculé à partir du temps de vol des deux particules reconstruites, quantifiant la vraisemblance qu'elles aient été émises en même temps depuis les feuilles sources. L'écart entre les deux vertex reconstruits est également utilisé pour déterminer si les deux particules ont été émises au même point depuis les sources. Des niveaux de coupures des événements ont donc été optimisés afin d'améliorer la sensibilité finale. Finalement, nous avons pu limiter la dégradation de la sensibilité à 5%, ce qui est très encourageant et qui pourra être poursuivi après de futures mesures des sources en contaminant radioactifs.

Des simulations d'événements du détecteur plongé dans différentes configurations de champ magnétique ont été implémentées et ont notamment permis de mettre en évidence certaines caractéristiques du logiciel de reconstruction. En effet, la sensibilité attendue du détecteur a été déterminée en utilisant des simulations de lignes de champ magnétique constantes à travers le détecteur. Après des analyses de l'influence de différents composants du détecteur sur le champ magnétique lui-même – menées au LAL – des simulations plus réalistes, dites avec "champ cartographié" ont été implémentées. La sensibilité avec une telle configuration du détecteur est dégradée d'environ 30% par rapport au cas où le champ magnétique est considéré comme uniforme. Effectivement, dans ces conditions, l'algorithme de reconstruction des trajectoires dans le traceur a plus de mal à reconstruire les traces puisque leur courbure varie le long de leur parcours de la source vers le calorimètre. L'efficacité de sélection des courbures correspondant à des électrons diminue, affectant ainsi directement la sensibilité. Une mise à jour de ce module de reconstruction devra donc être implémentée afin de pallier ce problème. Le champ magnétique a également un impact sur la résolution en énergie du calorimètre. Malgré cela, pour les mêmes coupures appliquées sur les événements, l'analyse des simulations a montré que la sensibilité à la $0\nu\beta\beta$ est dégradée en absence de champ magnétique.

Enfin, l'utilisation de ^{150}Nd dans les sources du détecteur pourraient nous permettre d'atteindre des sensibilités sans précédent pour cet isotope. Sur la Fig. 6.14 est présenté un graphe récapitulatif des résultats pour une exposition de 500 kg.an.

Amélioration de la réjection du bruit de fond ^{208}Tl

Lors de la précédente analyse, nous avons pu quantifier l'influence de la contamination des sources en isotope ^{208}Tl sur la sensibilité finale du détecteur.

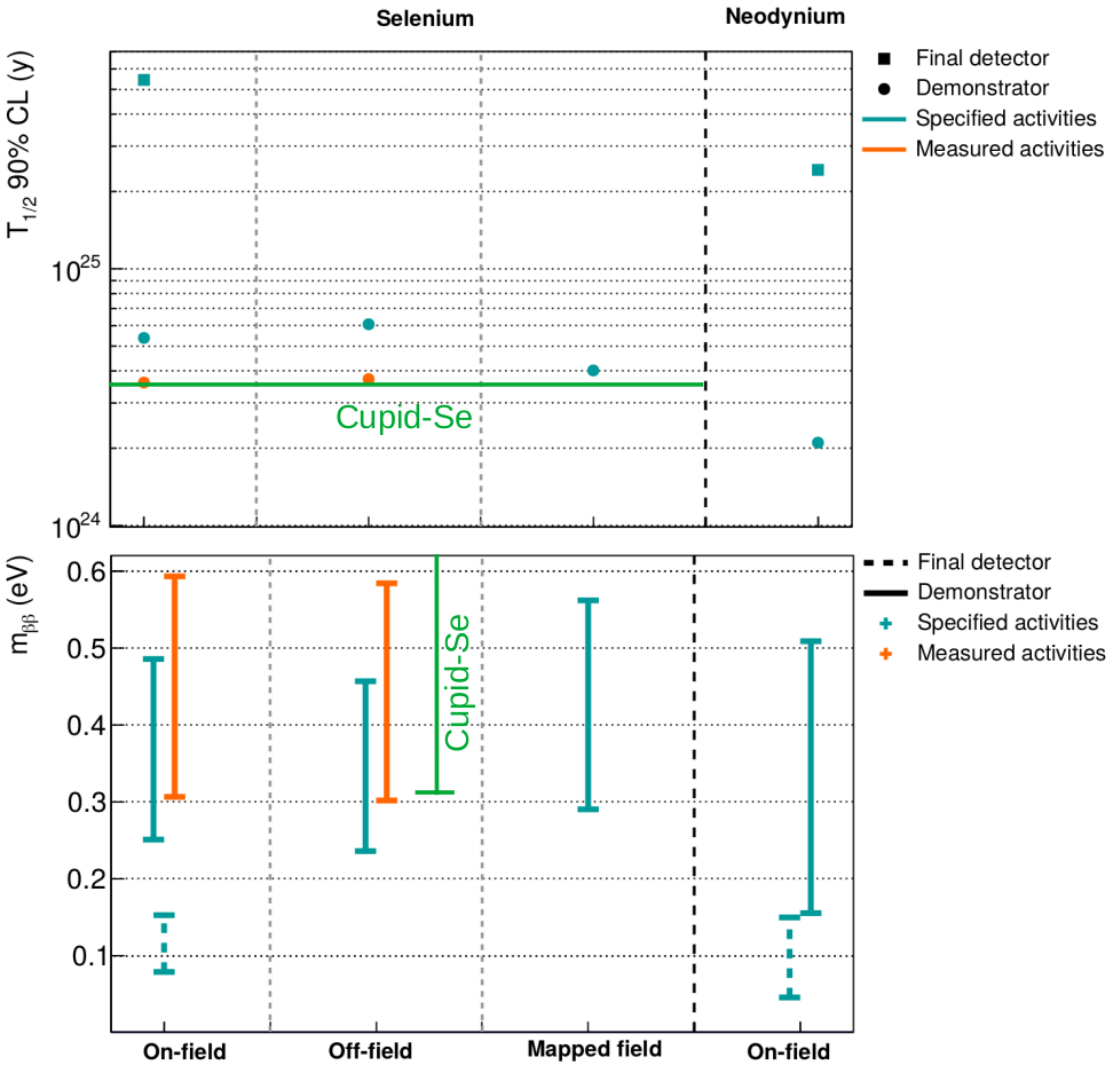

Figure 6.14: Récapitulatif des limites obtenues sur la $T^{0\nu}_{1/2}$ ainsi que sur la $m_{\beta\beta}$ pour chaque cas étudié.

Nous voulons donc implémenter une technique de réjection spécialement adaptée pour ce bruit de fond. L'idée ici est d'utiliser une particularité du schéma de désintégration β du ^{208}Tl vers le ^{208}Pb afin de le discriminer des autres bruits de fond pour la recherche de la $0\nu\beta\beta$. En effet, un des niveaux d'énergie de ce schéma de désintégration est métastable, et suivi de l'émission d'un photon de 2.615 MeV. Un électron de conversion de haute énergie a donc une certaine probabilité d'être émis lors de la désintégration β du ^{208}Tl. Et cet électron sera retardé dû au niveau d'énergie métastable. L'étude des simulations de désintégration β de ^{208}Tl dans la source ont montré que 75% des topologies à deux électrons dans la région d'intérêt de SuperNEMO (entre 2.7 et 3.2 MeV) sont composées d'un électron β et d'un électron retardé de haute énergie.

Cette étude est également l'occasion d'évaluer l'impact de la résolution en temps du calorimètre sur la réjection du bruit de fond. Le calorimètre a donc été simulé avec une résolution en temps parfaite, qui a ensuite été dégradée dans

un module à la fin du pipeline de simulation, pour nous permettre de faire varier facilement ce paramètre et ainsi évaluer son influence sur la sensibilité finale du détecteur. Les études préliminaires sur simulations ont montré que cette résolution est attendue à 250 ps pour la détection d'électrons.

Afin de rejeter de façon optimale les événements de ^{208}Tl, nous utilisons la différence entre le temps d'émission – dans la source – de l'électron de plus haute énergie et celui de plus basse énergie. Ces temps d'émission sont calculés à partir du temps de détection de la particule dans le calorimètre, corrigé du temps de vol dans le traceur. Pour des simulations de $0\nu\beta\beta$ dans la source, la distribution d'une telle grandeur après sélection des événements à deux électrons est, comme attendu, piquée autour de 0 ps. En revanche, pour des simulations de ^{208}Tl, la moyenne de cette distribution est décalée vers les positifs, jusqu'à 296 ps. Pour une résolution en temps du calorimètre simulée à 200 ps, une simple coupure rejetant les événements pour lesquels la différence des temps d'émission est supérieure à 0 ps permet alors de rejeter un niveau encourageant de 76% de ^{208}Tl, tout en gardant la moitié des événements $0\nu\beta\beta$. Nous remarquons que plus la résolution en temps du calorimètre s'améliore, plus cette coupure est favorable à la sélection d'événements $0\nu\beta\beta$ et à la réjection des événements ^{208}Tl. Cette sélection a également pu être optimisée en faisant varier la hauteur de la coupure au-delà de 0 ps, montrant des résultats encourageants sur la sensibilité finale du détecteur.

Une sélection plus élaborée a été mise en place, tenant compte non seulement de la différence des temps d'émission, mais cette fois-ci normalisée par la résolution en énergie elle-même, afin de décrire de façon plus fidèle les événements ^{208}Tl. Cet outil statistique permet de quantifier la vraisemblance que deux électrons aient été émis au même endroit dans la source et que l'électron de haute énergie soit retardé. Pour une résolution en temps de 200 ps pour le calorimètre, une sélection optimisée permet de rejeter 20% des événements ^{208}Tl, tout en sélectionnant 80% des événements $0\nu\beta\beta$. Nous avons cependant montré que cette réjection des événements ^{208}Tl peut-être améliorée avec la résolution en temps du calorimètre.

Finalement, le fait d'utiliser le niveau métastable de la désintégration β du ^{208}Tl est efficace en vue d'améliorer la sensibilité du détecteur à la désintégration $0\nu\beta\beta$, avec une amélioration de 12% pour une résolution idéale du calorimètre, et de 6% pour une résolution réaliste de 200 ps. La coupure sur la probabilité exponentielle devra cependant être optimisée en fonction de la contamination en isotope radioactif mesurée pour les sources et le traceur.

Mise en service du calorimètre

Après le montage des différentes parties du détecteur, un effort conséquent a été fourni par toute la collaboration afin de vérifier son bon fonctionnement et de mettre en place les premiers outils d'analyse du signal (calibration en énergie, égalisation des gains, analyses de waveform et baseline du signal...). Lors de mon doctorat, j'ai participé à la plupart des étapes de câblage du détecteur, de découpe des câbles coaxiaux et haute tension du calorimètre, ainsi qu'à leur installation à Modane sur les différentes parois du calorimètre, en passant par leur soudage aux

ponts diviseurs de tension des photomultiplicateurs (PM) et leur organisation sur le panneau de raccordement.

Après le travail d'installation sur site, il était primordial de vérifier le bon fonctionnement de chaque câble. Dans cette section, est présentée une analyse effectuée afin de vérifier l'état des câbles de signal du calorimètre installés à Modane (s'assurer que les câbles n'ont pas été endommagés pendant le transport et l'installation, contrôler s'il n'y a pas eu d'échange entre les canaux pendant l'étiquetage ou le câblage du calorimètre, vérifier si les câbles coaxiaux ont été coupés à la bonne longueur, estimer les délais induits par le temps de transit du signal dans chaque câble). Pour ce faire, des milliers de signaux électriques ont été envoyés individuellement dans chaque voie électronique, ce qui a été rendu possible grâce aux cartes d'acquisition construites par l'équipe électronique du LAL. Ce signal se propage dans le câble jusqu'à être réfléchi sur le pont diviseur de tension du PM auquel il est relié. Au cours de son trajet, le signal va être modifié par le câble, qui agit comme une fonction de transfert sur l'impulsion initiale. Pour chaque câble, les impulsions retours sont enregistrés. Leur analyse systématique permet de détecter d'éventuels dommages ou mauvaises connexions le long du parcours du signal.

Au cours de cette analyse, j'ai pu définir et optimiser la mesure du temps de la waveform en utilisant un Constant Fraction Discriminator (CFD) et ainsi évaluer l'influence de la présence des câbles sur le temps total de propagation du signal et son atténuation. J'ai programmé tout l'environnement d'analyse pour pouvoir surveiller l'état des câbles en direct au LSM. Grâce à cette étude, j'ai pu mettre en évidence différents dommages subis par les câbles et les réparer sur place lors de la prise de données. Afin de préparer de futures études d'événements en coïncidences, une base de données a été créée et mise à disposition de la collaboration regroupant le retard induit par les différentes longueurs de câbles.

Etude de la résolution en temps du calorimètre

Afin d'atteindre la sensibilité qui a été fixée pour le détecteur final de SuperNEMO, le calorimètre de l'expérience doit avoir une résolution en temps inférieure à 400 ps pour des électrons qui déposent une énergie de 1 MeV dans un scintillateur. La première étude sur simulation a montré menée par A.Huber au CENBG montre un résultat encourageant de 250 ps. J'ai mené une manipulation sur site qui a permis de fournir un résultat expérimental préliminaire sur cette résolution en temps.

L'incertitude sur la mesure du temps dans les calorimètres de SuperNEMO a différentes origines. Une contribution est liée à la fluctuation de la profondeur d'interaction de la particule dans le scintillateur, et dépend donc de la nature de la particule incidente (électron ou photon). La deuxième contribution vient de la technique de détection et dépend des fluctuations du temps d'émission de la lumière de scintillation ainsi que du temps de transit des photo électrons dans le photomultiplicateur. Cette dernière contribution a pu être déterminée grâce à une source de ^{60}Co.

Le ^{60}Co est un isotope qui, après une désintégration bêta, émet simultanément deux raies gamma de 1.17 et 1.33 MeV. J'ai placé une source de ^{60}Co de

232 kBq, prêtée par un laboratoire voisin (IPN) et acheminée à Modane, à différentes positions derrière le calorimètre de l'expérience. Au total, les différentes acquisitions de données ont duré plus d'une semaine, et ont permis la détection des deux raies gamma en coïncidence par des paires de modules optiques.

J'ai développé tout l'ensemble de code qui a permis d'analyser ces données et de donner un résultat préliminaire sur la résolution en temps du calorimètre de l'expérience de 570 ± 130 ps (Figure 6.15). Cette valeur est plus grande que la valeur préconisée, ce qui est consistant avec le fait que la caractérisation est faite avec des gammas qui interagissent plus profondément dans le scintillateur que les électrons. Au total, une résolution temporelle a pu être obtenue pour 26% des modules optiques de l'expérience grâce à cette méthode. Une plus grande proportion sera bientôt caractérisée avec l'étude d'une nouvelle campagne de prise de donnée, qui permettra d'avoir plus de statistiques. Ces résultats ainsi que ceux du commissioning du calorimètre feront l'objet d'un article qui est actuellement en cours de préparation.

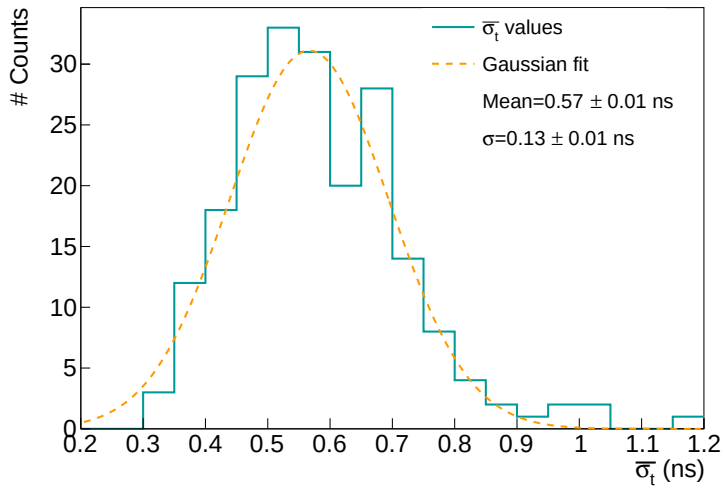

Figure 6.15: Distribution des incertitudes en temps pour 26% des modules optiques.

université PARIS-SACLAY | ÉCOLE DOCTORALE PHENIICS

Titre: Étude de l'influence de la réjection du bruit de fond ^{208}Tl sur la sensibilité à la $0\nu\beta\beta$, caractérisation des performances en temps du calorimètre du démonstrateur SuperNEMO.

Mots clés: Neutrino, Double désintégration bêta, SuperNEMO, Simulation Monte-Carlo, programmation et développement, mise en route du détecteur, réjection de bruit de fond, performances temporelles.

Résumé: La physique du neutrino est une des portes possibles pour aller au-delà du Modèle Standard (MS). En particulier, cette particule est décrite avec une masse nulle par le Lagrangien du MS. Le mécanisme étant à l'origine de la génération de leur masse n'est pas connu et dépend de leur nature, que le neutrino soit de Dirac (particules et antiparticules sont différentes) ou de Majorana (le neutrino est son propre antineutrino).

Les expériences NEMO font partie des expériences actuelles qui cherchent à mettre en évidence cette nature, avec une technologie unique alliant reconstruction de trace dans un trajectographe et mesure des énergies et temps de vol dans un calorimètre. La dernière génération de ce projet est le détecteur SuperNEMO, dont le premier des 20 modules, faisant office de démonstrateur, est en cours d'assemblage au Laboratoire Souterrain de Modane.

Le présent manuscrit décrit le travail de thèse effectué dans cette expérience. Après avoir rappelé certaines notions liées à la physique du Modèle Standard et au-delà, notamment concernant la physique des neutrinos, le manuscrit présente le démonstrateur SuperNEMO en détail. Le travail de cette thèse est ensuite décrit dans 4 chapitres d'analyse.

La sensibilité du démonstrateur à la décroissance $0\nu\beta\beta$ est étudiée dans différentes conditions de champ magnétique, qui est délivré dans le trajectographe au moyen d'une bobine. L'influence de la contamination des sources en isotopes naturels est également étudiée. Il est montré que des coupures sur les données, en particulier dans le canal de détection deux électrons, peuvent améliorer le résultat final de la sensibilité. Pour les sources ^{82}Se, la sensibilité du détecteur final est trouvée supérieure à $5,4 \times 10^{25}$ années, correspondant à $\langle m_{\beta\beta}\rangle < [0,079 - 0,15]$ eV. Pour des source ^{150}Nd la sensibilité sur la demie-vie est supérieure à 2.4×10^{25} années serait atteint. Cela correspond à $\langle m_{\beta\beta}\rangle < [0.046 - 0.15]$ eV, ce qui est meilleur que pour les sources ^{82}Se, grâce au meilleur facteur de phase.

Le bruit de fond interne le plus dangereux reste le ^{208}Tl, dont l'activité est mesurée comme étant supérieure aux spécifications. Deux techniques améliorées de réjection de ce fond sont développées, en utilisant notamment le temps de vol mesuré par le calorimètre, et son impact sur la sensibilité de l'expérience est discuté. Une amélioration de la sensibilité de 6% est obtenue en tenant compte des performances raisonnables du calorimètre en matière de temps de vol.

Une description détaillée de la mise en service du calorimètre est donnée, auquel j'ai activement participé pendant mon doctorat. En particulier, le travail effectué pour vérifier le fonctionnement du calorimètre et de ses câbles de signal est décrit. La longueur de chaque câble a été mesurée avec précision à l'aide d'une méthode de réflectométrie. Cela permet d'estimer les retards des signaux, qui ont un impact sur la résolution temporelle évoquée ci-dessus.

Une étude finale visant à déterminer la résolution en temps des modules optiques du calorimètre a été menée, ce qui est crucial pour comprendre et rejeter le bruit de fond de l'expérience. L'utilisation d'une source ^{60}Co pour caractériser le calorimètre complet est une idée originale développée dans le cadre de cette thèse, avec la prise en charge à la fois du dispositif expérimental et du développement de l'analyse. Une caractérisation d'une grande partie du calorimètre a été réalisée, ce qui ouvre la voie à l'étalonnage complet du détecteur avec cette méthode. En moyenne, la résolution en temps des modules optiques est 570 ± 130 ps.

université PARIS-SACLAY | ÉCOLE DOCTORALE PHENIICS

Title: Study of ^{208}Tl background rejection influence on the $0\nu\beta\beta$ decay sensitivity, characterisation of SuperNEMO demonstrator calorimeter timing performance

Keywords: Neutrino, Double beta decay, SuperNEMO, Monte-Carlo simulation, software development, commissioning, background rejection, timing performances.

Abstract: The physics of the neutrino is one of the possible doors to go beyond the Standard Model (SM). In particular, they are described with zero mass by the Lagrangian of the SM. The mechanism responsible for their mass is not known and depends on their nature, whether the neutrino is of Dirac (particles and antiparticles are different) or Majorana (the neutrino is its own antineutrino).

The NEMO experiments are part of the current experiments that seek to highlight this nature, with a unique technology combining trace reconstruction in a tracking detector and measurement of energies and times of flight in a calorimeter. The latest generation of this project is the SuperNEMO detector, of which the first of 20 modules, acting as a demonstrator, is currently being assembled at the Modane Underground Laboratory.

This manuscript describes the PhD work carried out in this experiment. After recalling certain notions related to the physics of the Standard Model and beyond, notably concerning neutrino physics, the manuscript presents the SuperNEMO demonstrator in detail. The work of this PhD is then described in 4 analysis chapters.

The sensitivity of the demonstrator to $0\nu\beta\beta$ decay is studied under different magnetic field conditions, which is delivered into the tracker by means of a coil. The influence of the contamination of sources by natural isotopes is also studied. It is shown that cuts in the data, especially in the two electron detection channel, can improve the final sensitivity result. For ^{82}Se sources, the final sensitivity is greater than $5.4\times\ 10^{25}$ years corresponding to $\langle m_{\beta\beta}\rangle\ <\ [0.079\ -\ 0.15]$ eV. For ^{150}Nd sources the sensitivity on half life e=is greater than $2.4\times\ 10^{25}$ years would be reached. This corresponds to $\langle m_{\beta\beta}\rangle\ <\ [0.046 - 0.15]$ eV, better than for ^{82}Se sources, thanks to its higher phase-space factor.

The most dangerous internal background remains ^{208}Tl, whose activity is measured to be higher than the specifications. Two improved rejection techniques of this background is developed, using in particular the time-of-flight measured with the calorimeter, and its impact on the experiment's sensitivity is discussed. An improvement of the sensitivity of 6% is obtained considering reasonable calorimeter timing performance.

A detailed description of the commissioning of the calorimeter is given, in which I had an important role during my PhD. In particular, the work done to verify the operation of the calorimeter and its signal cables is described. The length of each cable has been accurately measured with a reflectometry method. This allows to estimate the signal delays, which have an impact on the time resolution discussed above.

A final study to determine the time resolution of the optical modules of the calorimeter was conducted, which is crucial for understanding and rejecting the background of the experiment. The use of a ^{60}Co source to characterise the full calorimeter is an original idea developed in the context of this thesis, with the handling of both the experiment setup and the analysis framework. A characterisation of a large part of the calorimeter has been performed, which paves the way for the full detector calibration with this method. On average, the time uncertainty stands at 570 ± 130 ps.

Université Paris-Saclay
Espace Technologique / Immeuble Discovery
Route de l'Orme aux Merisiers RD 128 / 91190 Saint-Aubin, France